



HAL
open science

Anisotropic magnetoresistive sensor based on manganite oxide targeting biomedical application

Luiz Guilherme Enger

► **To cite this version:**

Luiz Guilherme Enger. Anisotropic magnetoresistive sensor based on manganite oxide targeting biomedical application. Automatic Control Engineering. Normandie Université, 2021. English. NNT : 2021NORMC257 . tel-03609152

HAL Id: tel-03609152

<https://theses.hal.science/tel-03609152v1>

Submitted on 15 Mar 2022

HAL is a multi-disciplinary open access archive for the deposit and dissemination of scientific research documents, whether they are published or not. The documents may come from teaching and research institutions in France or abroad, or from public or private research centers.

L'archive ouverte pluridisciplinaire **HAL**, est destinée au dépôt et à la diffusion de documents scientifiques de niveau recherche, publiés ou non, émanant des établissements d'enseignement et de recherche français ou étrangers, des laboratoires publics ou privés.



Normandie Université

THÈSE

Pour obtenir le diplôme de doctorat

Spécialité ELECTRONIQUE, MICROELECTRONIQUE, OPTIQUE ET LASERS,
OPTOELECTRONIQUE MICROONDES

Préparée au sein de l'Université de Caen Normandie

Anisotropic Magnetoresistive Sensor Based on Manganite Oxide Targeting Biomedical Application

Présentée et soutenue par
LUIZ GUILHERME ENGER

Thèse soutenue le 14/12/2021
devant le jury composé de

MME CLAIRE BARADUC	Chercheur HDR, CEA	Rapporteur du jury
MME MYRIAM PANNETIER-LECOEUR	Chercheur HDR, CEA	Rapporteur du jury
MME SUSANA CARDOSO DE FREITAS	Maître de conférences HDR, INESC MN	Membre du jury
M. HERVÉ GILLES	Professeur des universités, Université Caen Normandie	Membre du jury
MME LAURENCE MECHIN	Directeur de recherche au CNRS, ENSICAEN	Membre du jury
M. PAOLO PERNA	Chercheur, IMDEA Nanoscience	Membre du jury
M. LAURENT DANIEL	Professeur des universités, CentraleSupélec	Président du jury
M. STEPHANE FLAMENT	Professeur des universités, Université Caen Normandie	Directeur de thèse

Thèse dirigée par **STEPHANE FLAMENT**, Groupe de recherche en informatique, image, automatique et instrumentation



UNIVERSITÉ
CAEN
NORMANDIE



Abstract

This work presents the design, fabrication, characterization and ultimately the optimization of single layer magnetic field sensors based on the anisotropic magnetoresistance (AMR) effect present in $\text{La}_{2/3}\text{Sr}_{1/3}\text{MnO}_3$ (LSMO) thin films. The magnetic and electrical properties of this manganite oxide are linked through the double exchange mechanism. Thanks to the very low intrinsic noise of the material in the low frequency region, it presents itself as a competitive candidate for sensing magnetic fields targeting biomedical applications, such as the one envisioned by the European project ByAxon. The sensor must be of small size, operate at body temperature and achieve detectivity values in the range of hundreds of $\text{pT Hz}^{-1/2}$ below 1 kHz. The fabrication of this AMR sensor is quite simple when comparing to giant magnetoresistance and tunneling magnetoresistance devices, and its operation is based on a step-induced uniaxial magnetic anisotropy explained using the Stoner-Wohlfarth model. This is obtained by growing epitaxial films with Pulsed Laser Deposition (PLD) technique on top of vicinal SrTiO_3 (STO) substrates. To have the dominant contribution for the total electrical noise of the whole system coming from the sample itself, a low noise amplifier adapted to sample characteristics was built. Two Wheatstone bridge structures were etched in the LSMO thin films, presenting different current density directions regarding the easy magnetization axis. One structure is ruled by the planar Hall effect and presents a linear operation around zero magnetic field, whereas the second depends on standard AMR terms and requires a static bias field for correct operation. The operation mode of both structures was validated with Magneto-optical Kerr Effect imaging and fitting a numerical physical model to experimental data, which also allows the extraction of physical parameters. Several studies were performed in order to achieve lower detectivity values, thus improved performance: effect of thin film thickness, vicinal angle of the STO substrate, PLD deposition temperature and lithography masks designs variations. The sample with best low frequency performance presents $1.4 \text{ nT Hz}^{-1/2}$ detectivity at 1 Hz and $240 \text{ pT Hz}^{-1/2}$ at 1 kHz, while working at 310 K. Some samples were mounted on printed circuit boards with wire bonding, and covered with polydimethylsiloxane, a biocompatible polymer. Characterization with alternating and inhomogeneous magnetic fields was performed, and different gradiometer arrangements were validated. No live records of magnetic fields emitted by spontaneous activity of incubated neuronal cells were obtained by the time this thesis was concluded, however this work presents a real application of a spintronics device based on a functional oxide and pushes further development in this growing area of new technologies.

Résumé

Cette thèse est dédiée au design, à la fabrication, la caractérisation et finalement l'optimisation de capteurs de champ magnétique monocouche, basés sur l'effet magnéto-résistif anisotrope (AMR) dans des couches minces de $\text{La}_{2/3}\text{Sr}_{1/3}\text{MnO}_3$ (LSMO). Les propriétés magnétiques et électriques de cet oxyde sont liées par le mécanisme de double échange. Grâce à son très bas bruit intrinsèque dans le domaine basse fréquence, ce matériau se présente comme un candidat compétitif pour détecter des champs magnétiques avec pour cible potentielle des applications biomédicales, comme cela est par exemple envisagé dans le projet européen ByAxon. Dans ce projet, le capteur doit présenter une taille réduite, fonctionner à la température du corps humain et atteindre des valeurs de détectivité de quelques centaines de $\text{pT Hz}^{-1/2}$ en dessus de 1 kHz. La fabrication de ce capteur AMR est simple comparée aux dispositifs basés sur la magnétorésistance géante ou la magnétorésistance à effet tunnel, et son mode opératoire utilise l'anisotropie magnétique uniaxiale et est décrite par le modèle de Stoner-Wohlfarth. Une telle anisotropie uniaxiale est obtenue via la croissance épitaxiale par ablation laser pulsé de couches minces sur des substrats SrTiO_3 vicinaux. Afin d'avoir un bruit de mesure inférieur au bruit propre de l'échantillon, un circuit de pré-amplification à très bas bruit et adapté aux caractéristiques des échantillons a été conçu. Deux structures de pont de Wheatstone ont été gravées sur les couches minces de LSMO, avec différentes orientations pour la densité de courant par rapport à l'axe facile. Une structure est régie par l'effet Hall planaire et présente une opération linéaire en champ nul, et la deuxième structure est régie par la magnétorésistance anisotrope classique et a besoin d'un champ statique de polarisation. Le principe physique qui régit les deux structures a été validé par imagerie magnéto-optique à effet Kerr et par ajustement d'un modèle numérique à des données expérimentales. Ce qui permet aussi l'extraction des paramètres physiques du dispositif. Plusieurs études ont été réalisées pour réduire la détectivité, c'est-à-dire améliorer la performance: étude de l'effet de l'épaisseur des couches, de l'angle vicinal du substrat, de la température de dépôt et de la géométrie des dispositifs. L'échantillon le plus performant en basse fréquence atteint une détectivité de $1.4 \text{ nT Hz}^{-1/2}$ à 1 Hz, et $240 \text{ pT Hz}^{-1/2}$ à 1 kHz. Des échantillons sélectionnés ont été connectés sur des plaques de circuit imprimé par *wire bonding* et recouverts de *polydimethylsiloxane*, un polymère biocompatible. Des caractérisations sous champs magnétiques alternatifs et inhomogènes ont été réalisées, et différentes configurations gradiométriques ont été validées. L'enregistrement en direct du champ magnétique émis par l'activité spontanée de cellules neuronales n'a pas été obtenu à la date de rédaction de ce manuscrit. Cependant ce travail présente une application réelle d'un dispositif spintronique basé sur un oxyde fonctionnel et constitue une contribution au développement de ces nouvelles technologies.

Acknowledgements

First of all, I thank my parents Flávio Guilherme Acuña Enger and Adriana Pretto Enger for giving me education, health, amusement and most importantly love. What I conquered is because you were able to put me in places that provided me such opportunities, and fortunately I had the capacity to make use of all that. You are responsible for my achievements. I also want to thank my sisters Maira Enger and Elena Enger and my brother Pedro Enger, for all the moments we shared. Both through video calls when farther apart and together when we could meet. I am proud to be part of this family and ever grateful for everything. I love you all.

To my thesis supervisor, Professor Stéphane Flament. Who helped me to set up my new life when I arrived in Caen, shared his knowledge and expertise and provided insightful and crucial guidance for the development of this work, always with good spirits. Your supervision was essential to perform this research, and thanks to our discussions there were substantial improvements in its quality. Also thank you for the light-hearted conversations and even one training session on a common passion: Karate. To Dr. Laurence Méchin, who provided an enormous contribution with fruitful discussions and teachings on device fabrication, driving several experiments that were conducted during this thesis. Thank you for acting as the Director of the Electronics team during my time at GREYC and supervising our participation in ByAxon project. I also thank Dr. Bruno Guillet, Dr. Marc Lam Chok Sing, Sylvain Lebargy and Dr. Olivier Rousseau for their work and help in ByAxon project and the development of this thesis.

To cleanroom engineer Victor Pierron. Laboratory colleague, neighbour, friend. I am grateful for the support in sample fabrication processes and for the very important friendship. Thanks to you and Romane Mirgaine, the period during the SARS-CoV-2 crisis was way less harsh than what it could have been. I also thank my colleagues in the pursuit of a PhD at GREYC, Laryssa Mirelly Carvalho de Araújo and Olivier Haas. I wish you the best of luck in the new chapter of your lives. To Dr. Yoann Lechaux, Dr. Vanuza Nascimento, and Dr. Alexandre Esper, thank you for the advice, help and friendship.

To Professor Pierre Langlois, with whom I shared the office and had tasteful musical exchanges. To Matthieu Denoual, who helped me with PDMS covering and 3D modeling with FreeCAD, and also lent some reading material out of the thesis subject to clear the mind. To Julien Gasnier, for his technical assistance and building the custom made amplifier PCB. I also would like to thank Dr. Bernadette Domenges for her willingness and assistance in performing morphological analysis with electronic microscopy. To Arielle Perrette, Sophie Rastello, Gaëlle Picquenot and Phillipe Poupard for taking care of the administrative work and kindness.

I am grateful to Dr. Isidoro Martinez, Arturo Vera, Dr. Ruben Guerrero, Dr. Paolo Perna, Dr. Maria Teresa González and Professor Julio Camarero for the discussions on sensor development and characterization and receiving me at IMDEA Nanociencia. To Ana Arché-Núñez, Claudia González and Beatriz González for showing me a little more of Madrid. To Dr. Ivo Calaresu, Dr. Giada Cellot and Professor Laura Ballerini for the experiments at SISSA. I acknowledge everyone involved with ByAxon, a project I am happy and proud of having participated. I would like to thank everyone I met during the duration of my PhD. Each and every interaction, no matter the duration, added something to make the last three years a much richer experience.

It's the questions we can't answer that teach us the most. They teach us how to think. If you give a man an answer, all he gains is a little fact. But give him a question and he'll look for his own answers.

— Patrick Rothfuss, *The Wise Man's Fear*

There is nothing like looking, if you want to find something. You certainly usually find something, if you look, but it is not always quite the something you were after.

— J. R. R. Tolkien, *The Hobbit*

No man is brave that has never walked a hundred miles. If you want to know the truth of who you are, walk until not a person knows your name.

— Patrick Rothfuss, *The Wise Man's Fear*

"It's a dangerous business, Frodo, going out your door. You step onto the road, and if you don't keep your feet, there's no knowing where you might be swept off to."

— J. R. R. Tolkien, *The Lord of the Rings*

Have the Courage to seek the Wisdom that will grant you Power.

Contents

I	Introduction	15
1.1	ByAxon	16
1.2	Sensor Technologies	18
1.2.1	Induction coils and fluxgate sensors	19
1.2.2	Hall effect sensor	20
1.2.3	SQUID sensor	21
1.2.4	Optical pump magnetometers	23
1.2.5	GMR sensor	25
1.2.6	TMR sensor	26
1.2.7	AMR sensor	28
1.3	Conclusion	29
	Bibliography	31
II	AMR LSMO Sensor	37
2.1	$\text{La}_{2/3}\text{Sr}_{1/3}\text{MnO}_3$	37
2.1.1	Double-exchange mechanism and epitaxial strain	38
2.2	Uniaxial magnetic anisotropy in LSMO	40
2.2.1	Stoner-Wohlfarth model	40
2.2.2	Uniaxial anisotropy with vicinal substrate	43
2.3	Anisotropic Magnetoresistance	45
2.3.1	Resistance of single stripes	45
2.4	Considerations on Electrical Noise	50
2.4.1	Measuring noise	50
2.4.2	Preamplifier Circuit Design	51
2.4.3	LSMO noise sources	55
2.5	Wheatstone Bridge working principle and device validation	58
2.5.1	45° Wheatstone Bridge	60
2.5.2	90° Wheatstone Bridge	61
2.5.3	Device validation	62
2.5.4	Noise in Wheatstone Bridge	66
2.5.5	Detectivity	66
2.6	Conclusion	67
	Bibliography	67
III	Sensor Optimization	75
3.1	Effect of bias voltage and operation temperature	75
3.1.1	Operating temperature	78
3.2	Effect of thin film thickness	81
3.2.1	Characterization at IMDEA Nanociencia	82
3.2.2	Second batch of samples	84
3.3	Vicinal Angle	86
3.3.1	Electron Microscopy	88
3.3.2	Substrate temperature during deposition	92
3.4	Optimized sample	94

3.5	Masks geometry	95
3.5.1	Gold pad geometry	97
3.5.2	Effect of demagnetizing energy	102
3.5.3	Comparison in size	106
3.6	Samples reaching sub-nT	108
3.7	Comparison with commercially available sensors	109
3.8	Conclusions	110
	Bibliography	111
IV	Applications in Real Environment	115
4.1	Sensor mounting and Packaging	115
4.2	Characterization with alternating magnetic field	118
4.2.1	Inhomogeneous magnetic field	121
4.3	Gradiometer operation	122
4.3.1	45WB structure	123
4.3.2	90WB structure	123
4.3.3	Hybrid 90WB and 45WB	126
4.4	Experiments with living cells at SISSA	129
4.5	Conclusion	132
	Bibliography	133
V	General Conclusions and Future Perspectives	135
5.1	Conclusions	135
5.2	Future Perspectives	137
5.3	Scientific Contributions	138
A	Fabrication Procedure	139
A.1	Thin film deposition	139
A.2	Lithography and etching	140
A.3	List of fabricated samples	142
B	Characterization Procedure	143
B.1	Electrical transport and noise	143
B.2	Magneto-optical Kerr Effect imaging	145
B.3	Numerical fit to experimental curves	149
C	Résumé long en Français	151
C.1	Introduction	151
C.2	LSMO et validation du capteur	152
C.2.1	Mécanisme de double échange	153
C.2.2	Uniaxialité magnétique anisotrope	153
C.2.3	Magnétorésistance anisotrope	155
C.2.4	Validation du dispositif en pont de Wheatstone	157
C.2.5	Bruit d'un pont de Wheatstone LSMO et détectivité	160
C.3	Optimisation de la performance	162
C.3.1	L'effet de la tension de polarisation et de la température d'opération	162
C.3.2	L'effet de l'épaisseur de la couche mince	165
C.3.3	Angle vicinal du substrat	166
C.3.4	L'échantillon optimisé	167
C.3.5	Masques pour lithographie laser	167
C.4	Applications dans des environnements réels	170
C.4.1	Configuration gradiométrique	171
C.5	Conclusions	172

D Sub-nT resolution of Single Layer Sensor Based on the AMR Effect in $\text{La}_{2/3}\text{Sr}_{1/3}\text{MnO}_3$ Thin Films	173
D.1 Introduction	173
D.2 Film and samples characteristics	173
D.3 AMR curves and Detectivity of sensors	174
D.4 Conclusion	175
Bibliography	175

Chapter I

Introduction

When humans first found lodestones - rocks rich in magnetite Fe_3O_4 and naturally magnetized due to lightning strikes - the property of interacting at a distance with ferrous objects was regarded as magic. Even without a complete understanding of its nature, suspended pieces of this rock were used as guiding tool to navigation as early as 1088 [1]. In fact, the name lodestone can be translated from Old English to “leading stone”, from a now obsolete use of lode as “way, journey” [2]. One of the first steps taken in experimental science was by William Gilbert, when he proposed that Earth itself was a great magnet, and compasses weren’t affect by the stars or a strong magnetic island as previously thought. Later work and advances by Daniel Bernoulli, Hans-Christian Oersted, André-Marie Ampère, Dominique-François Arago and Michael Faraday culminated in the formulation of a unified theory of electricity, magnetism and light by James Clerk Maxwell (1864). But a satisfactory explanation as to why some materials present magnetic properties while others don’t only presented itself in the first half of twentieth century on modern Physics, with quantum mechanics. Nowadays, Magnetism is part of our daily lives, even if some may not acknowledge it and a strong mysticism surrounds it still. From fridge magnets to Magnetic Resonance Imaging, passing through electric motors, telecommunications, audio speakers, data acquisition and storage, personal electronics and so much more. A deeper understanding of Magnetism and its application is directly linked with the development of sources of magnetic field and the tools necessary to detect and measure this physical quantity: magnetic field sensors. The importance of such field can also be verified by its economical value. The market size of permanent magnets alone was valued in 2019 to reach USD 20.74 billion [3], while the magnetic sensors market was valued at USD 2 billion [4]. Both present an estimated annual growth of 6% until at least 2026.

Such big and expanding market for magnetic sensors alone owns to a wide range of applications for such devices. While different technologies such as fluxgate and Superconducting Quantum Interference Devices (SQUIDs) will be presented, this work is focused mainly on magnetoresistive (MR) devices, as for devices that present a change in electric resistance when exposed to a magnetic field. The influence of a magnetic field over electric resistance on a conductor specimen was first brought to our attention in 1857 by William Thomson, also known as Lord Kelvin [5]. More recently, the ever growing potential presented by MR sensors led the Technical Committee of IEEE Magnetics Society to develop a roadmap to guide research and development in such field, with future perspectives up to 2030 [6]. Flexible electronics, navigation and transportation, position sensing and human-computer interactions, non-destructive evaluation and monitoring and biomedical is a non-exhaustive but wide-range list of applications. Furthermore, with the miniaturization and low power consumption of magnetoresistive devices and optimization of performance, and ever increasing number of sensors is expected to be in operation. This growth is directly linked to all that is related to Internet of Things (IoT), where magnetic sensors already occupy a 10% slice of sensing devices for smart living [7]. Thanks to increasing performance, low cost and small footprint, the use of magnetoresistive sensors

in Industry 4.0 and IoT is expected to grow [8]. This work presents the effort made to optimize anisotropic magnetoresistive sensors based on a manganite oxide, a material not commonly used for such devices, with a target performance allowing the use in biomedical application.

In this first Chapter, a brief introduction of the ByAxon project and the related constraints regarding the sensor to be used are given. Then different magnetic field sensor technologies are discussed, along with the presentation of a general expression for detectivity, the main figure of merit of a sensor. While some technologies do achieve very high performance, they do not comply to the target application as an implantable device. It will be shown why, with current technologies, only MR sensors can be considered. Finally, some projections regarding this class of devices are presented, and it is clear that there is still much potential for further development.

Chapter II introduces the reader to the properties of the manganite oxide LSMO. It presents how the magnetic and electrical behavior are linked by the double-exchange mechanism and are affected by film strain, how epitaxial deposition on vicinal substrates provokes a step-induced uniaxial anisotropy and how the Stoner-Wohlfarth model for magnetic energy explains the operation of the device. The latter is confirmed with Magneto-optical Kerr Effect imaging. Expressions for the electrical resistance of single LSMO stripes as a function of magnetization direction are developed, according to the direction of current density that is defined when the thin film is etched. Experimental curves present the expected behavior. Then the discussion moves to noise analysis and measurement. The development of a low noise preamplifier circuit is presented, adapted to LSMO sample characteristics. Noise sources in LSMO thin films are discussed and confirmed with experimental data. Finally, the sensor device is presented: LSMO thin films etched in two different Wheatstone bridge designs, according to the direction of current density. Their working principle based on supporting theory is developed and validated with experimental data.

Based on the obtained equation for detectivity, Chapter III presents the strategies followed to achieve an improved performance. The effect of voltage bias and operating temperature is studied. Several samples were fabricated, either with different thin film thickness, vicinal angle of the substrate, temperature during deposition and variations in lithography mask design. Electrical and magnetic characterization shows how performance is affected, and results highlight the very nature of the material, ruled by the double-exchange mechanism. The distribution of current density is also verified. The chapter ends with a list of samples that are able to reach sub-nT detectivity values at 310 K temperature.

Chapter IV is dedicated to the use of LSMO sensors in real world environment. It starts by presenting how samples can be mounted on a printed circuit board for characterization and use outside of a station equipped with probes, and shows the possibility to cover samples with polydimethylsiloxane for protection and biocompatibility. Measurements with alternating and inhomogeneous magnetic fields are presented, and different gradiometer arrangements to suppress ambient noise are validated. The chapter closes with the presentation of the first trial to measure magnetic fields originated from the spontaneous activity of incubated neuronal cells.

This thesis is concluded with Chapter V, giving an overview of general conclusions and future perspectives.

1.1 ByAxon

The European project ByAxon (from January 2017 to December 2020) was a research and innovation work funded by the Horizon 2020 programme, under the Future and Emerging Technologies framework. With a consortium composed of SISSA, SESCAM, ICMC-CSIC, CNRS-GREYC, mdf-Diagnostics and IMDEA Nanociencia, the goal of the project was to develop an active bypass based on nanotechnology to perform neural

reconnection at the level of spinal cord injury [9]. The device to be implanted should act as a bridge for the neural signal, as presented in Fig. C.1(a). The re-injection of such signal using nanotechnology electrodes and their compliance to constraints was the subject of several PhD studies in our partner laboratories. But for a signal to be bypassed, it must first be detected. The electric activity of the brain and bundles of neurons generate a magnetic field, as there is displacement of electric charge. The generated fields are very low in amplitude and of low frequency (few Hz to kHz), but thanks to great effort and technology development it is nowadays possible to use magnetic field sensors to detect such activity. This allows a contactless detection of biological signals, as it occurs in magnetoencephalography and Magnetic Resonance Imaging equipment. As the bypass proposed in the ByAxon project is to be implanted, this imposes some constraints for the components of the device, as shown in Fig. 1.1(b). Not only the magnetic field sensor must reach excellent performance in the range of signals of interest (low amplitude and low frequency), but it must also be of small size and operate at body temperature. This is

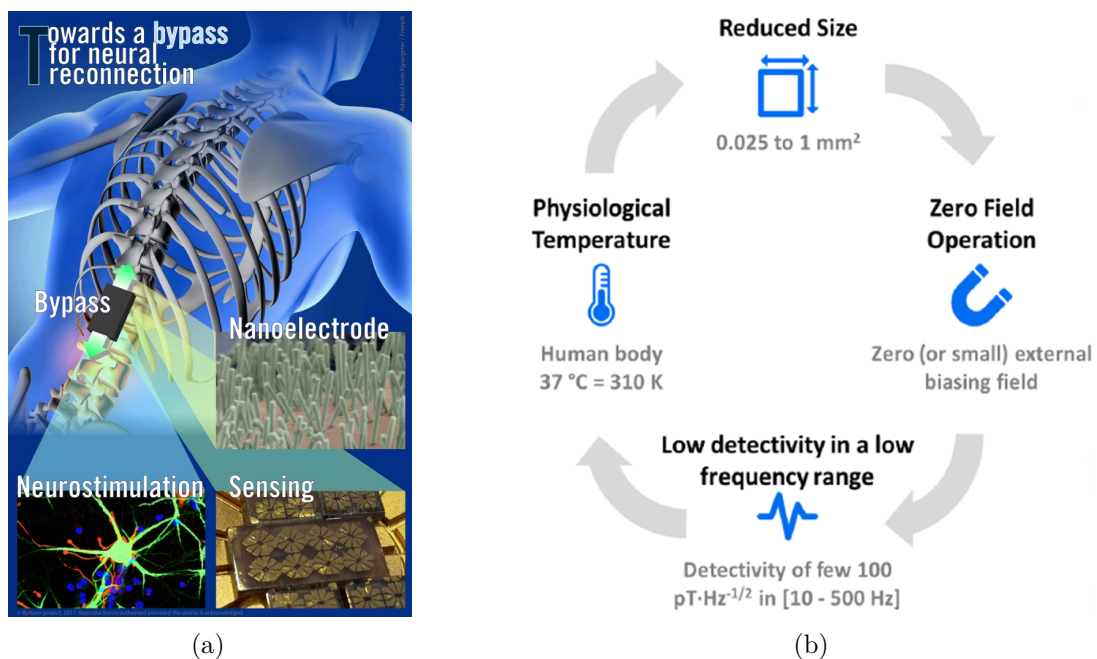


Figure 1.1: a) Poster presenting the goal and main areas of the ByAxon project. b) Constraints related to the magnetic field sensors to be employed in the device.

where the GREYC-CNRS laboratory plays its role. The laboratory was tasked with the fabrication and optimization of a magnetic field sensor that ought to present a high enough performance capable of detecting neural signals. Previous work on the magneto and electric transport properties of $\text{La}_{1-x}\text{Sr}_x\text{MnO}_3$ (LSMO), some already conducted in cooperation between GREYC and IMDEA Nanociencia, showed the opportunities of employing such material in the development of high performance magnetic sensors. Thanks to the intrinsic properties of this manganite oxide such as presenting AMR effect and very low noise in the low frequency range, LSMO was shown to be a proper candidate to achieve the goals set by the project. Thus, the design and optimization of a magnetic field sensor based on LSMO was the subject of this thesis and consists the main body of the present work.

Magnetic field originated from the transmembrane potential of a crayfish medial giant axon was measured by Roth and Wikswo [10]. The electric signal of the transmembrane potential and the corresponding magnetic signal were simultaneously measured. Magnetic signal with a peak to peak amplitude above 200 pT was measured with a toroidal pick-up coil. Using the volume conductor model, the resulting magnetic signal can be calculated and fitted to the experimental data, as showed in Fig. 1.2. Although there is still more study needed to understand biomagnetic signals, a signal of similar shape is expected when

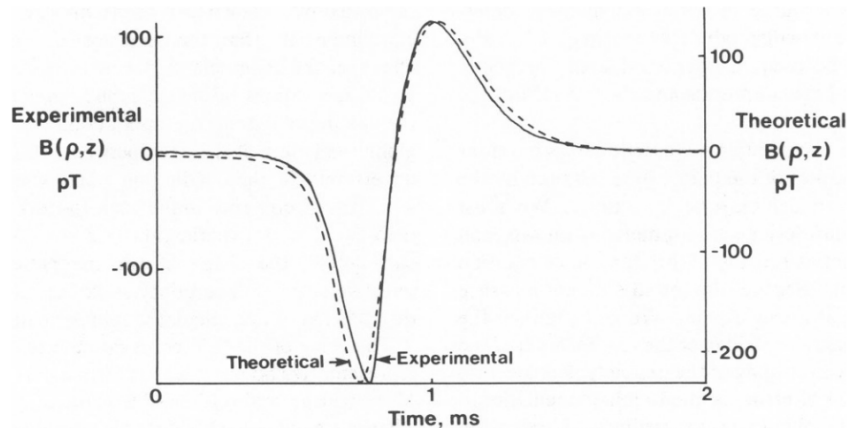


Figure 1.2: Experimental magnetic signal from crayfish axon and calculation using transmembrane potential and volume conductor model. From [10].

measuring the activity of bundles of neurons, as in the spinal cord. The inverse path is thus also possible: calculating the transmembrane potential using the measured magnetic field. This is the basis of the working principle of the ByAxon device. *In-vivo* measurements of a cat brain's stimulated activity have been measured using a magnetoresistance-based sensor [11]. Detection of magnetic signals originated from the spinal cord were detected with an array of sensors made of superconducting material [12]. As biological magnetic signals typically present frequencies below 1 kHz, the sensing device must present a high performance in the low frequency region. The next section will discuss on different magnetic sensor technologies, and why some are not compatible with the constraints imposed by the ByAxon project.

1.2 Sensor Technologies

Devices that detect the presence or variation of magnetic fields, i.e. magnetic sensors, deliver an electrical signal preferably proportional to the field acting at the sensor. The majority of sensors exploit either Hall effect, magnetoresistance properties or detect variations in magnetic flux. In this work, more attention is given to magnetoresistive devices and even more specifically to anisotropic magnetoresistance (AMR) sensors. While Hall effect sensors work with a surge of direct voltage difference, magnetoresistive sensors are based on electrical resistance change with the application of a magnetic field. The magnetoresistance ratio is a percentage given by $\Delta R/R_0 \times 100$, where R_0 is the average resistance between minimum and maximum values and ΔR is the resistance change, both in ohms (Ω).

Each sensing device has two essential parameters associated to it: sensitivity and noise. The sensitivity indicates how strongly the sensor will respond for a variation of the physical quantity of interest. A high sensitivity means that even weak signals will produce large variations in sensor's output. Noise is the name given to the random fluctuations that are present in the system, responsible for setting a minimum detectable level. If a variation in the physical quantity of interest produces through the sensor's sensitivity an electric signal lower than the sensor's noise, it won't be detected. Ultimately, the main figure of merit of a sensor is its detectivity, informing the lowest detectable signal amplitude at a given frequency. It is the ratio of sensor's total electrical noise by its sensitivity. The general expression of detectivity is presented in Eq. (1.1), with units corresponding to a magnetic field sensor. A low detectivity corresponds to a high sensor performance, as it will be able to detect weaker magnetic fields. The detectivity can be seen as the case when signal to

noise ratio equals to one.

$$\text{Detectivity [nT}/\sqrt{\text{Hz}}] = \frac{\text{Total electrical noise [nV}/\sqrt{\text{Hz}}]}{\text{Sensitivity [V/T]}} \quad (1.1)$$

The ideal sensor would present the lowest noise and highest sensitivity, thus detecting very weak signals. While some technologies own their performance to high sensitivity values, others present lower intrinsic noise. Sensitivity and noise concerning the device fabricated in this work will be further developed through this thesis. Firstly, some comparisons between different magnetic field sensor technologies are introduced, and more attention is given to magnetoresistance devices.

1.2.1 Induction coils and fluxgate sensors

Probably the simplest magnetic sensors, induction coils consist of a electrically conductive wire wound in n turns. The output signal comes from the Faraday's law of induction, with Φ the magnetic flux, B the magnetic flux density, t time and μ_0 the magnetic permeability in vacuum:

$$V = -\frac{d\Phi}{dt} = -nA\frac{dB}{dt} \quad (1.2)$$

for a coil with an area A [13]. Clearly, a higher output is obtained for an increased number of turns n and sensor area A . Such coils can be presented with an air-gap or a core made of soft magnetic material to increase its sensitivity. The presence of a magnetic core complicates the system, and a careful design both in terms of material used and geometry are essential. With proper design, detectivity values down to 20 pT Hz^{-1/2} at 1 Hz and 50 fT Hz^{-1/2} at 1 kHz have been reported at room temperature, with $A = 5 \text{ mm}^2$, $n = 10000$ and a coil/core length of 150 mm [14]. But although high performance can be achieved, this type of sensor also comes with drawbacks: miniaturization is difficult and the output depends on the variation rate of external field over time, so it does not detect DC fields and sensitivity varies with field frequency. In fact, it was due to miniaturization issues that induction coils were replaced by magnetoresistance read heads in hard drives. While further development allowed smaller-sized inductive coils that can achieve a 0.8 nT Hz^{-1/2} at 10 Hz detectivity value, magnetoresistance sensors presented better performance [15]. Experiments performed *in vivo* show that inductive coils can be made biocompatible, but the detected magnetic field was from a second coil and not of biological origin [16].

Fluxgate sensors can be seen as a natural evolution of induction coils that allow for DC and low frequency AC measurements. A soft magnetic core is wrapped with two coils, the drive coil and the pick-up coil. A sinusoidal current at frequency ω flows through the drive coil, creating a drive magnetic field $H_{drive}(t)$ which periodically saturates the core when it reaches peak values of $\pm H_S$. This modulates the magnetization of the core, becoming a function of time $M(t)$, that at saturation has the value M_S . An imbalance of the duration in positive versus negative saturated states is provoked by the external field H_{ext} . Figure 1.3 shows the basic schematic of a fluxgate and the behavior of the soft magnetic core. Following Faraday's law, the voltage induced between the terminals of the pick-up coil is the time derivative of the magnetic flux $\Phi(t) = \mu_0 n A (H(t) + M(t))$, where H is the total magnetic field. The field H is the sum of the field induced by the drive coil $H_{drive}(t)$ and the external field H_{ext} . The magnetization can be modeled as

$$M(t) \approx M_S \tanh(2H(t)/H_S) \approx M_S(2H/H_S - \frac{8}{3}(H/H_S)^3 + O\left(\frac{H}{H_S}\right)^5) \quad (1.3)$$

Explicitly writing $H(t)$, we have

$$H(t) = H_{ext} + H_S \sin(\omega t) \quad (1.4)$$

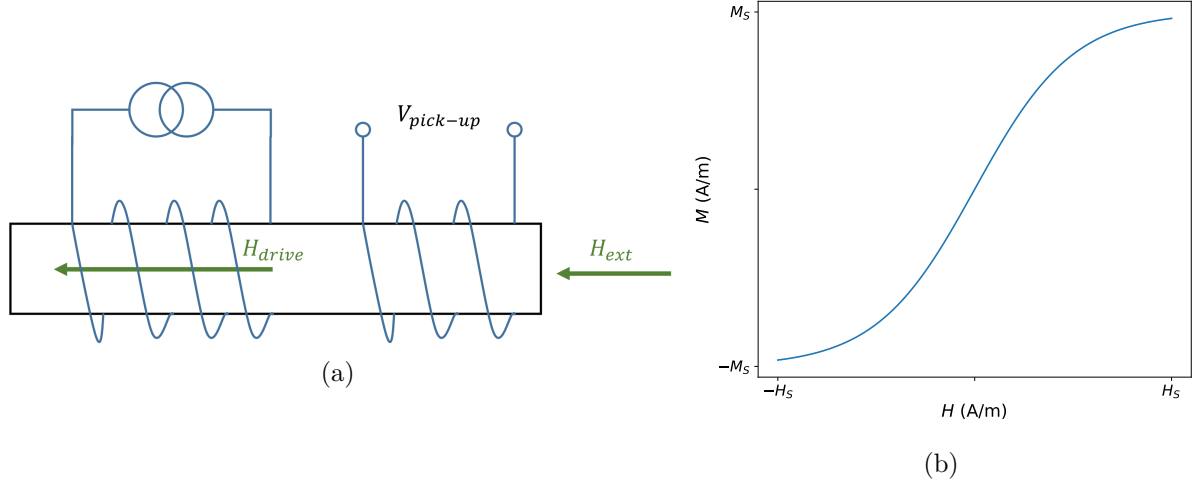


Figure 1.3: a) The drive coils generate a magnetic field to periodically saturate the soft magnetic core, and output signal is measured between the terminals of a pick-up coil. b) The dependence of core magnetization M can be modeled by a hyperbolic tangent of the total magnetic field H .

and the voltage induced in the pick-up coil is

$$\begin{aligned}
 V_{pick-up} &= -\mu_0 N A \frac{dH(t)}{dt} \left(1 + \frac{dM(t)}{dH} \right) \\
 &= -\mu_0 N A \omega \cos(\omega t) \left(1 + 2 \frac{M_S}{H_S} - 8 \left(\frac{H}{H_S} \right)^2 \right) \\
 &= -\mu_0 N A \omega \cos(\omega t) \left(1 + 2 \frac{M_S}{H_S} - \frac{8}{H_S^2} (H_{ext}^2 + H_S^2 \sin^2 \omega t + 2 H_{ext} H_S \sin(\omega t)) \right)
 \end{aligned} \tag{1.5}$$

When distributing the $\cos(\omega t)$ contribution, with the last term on the right hand side of Eq. (1.5) we obtain

$$V_{pick-up} \propto \frac{H_{ext}}{H_S} \sin(2\omega t) \tag{1.6}$$

By following the second harmonic signal of the voltage induced in the pick-up coil, after demodulation we obtain a linear dependence on the amplitude of the external field H_{ext} [17]. Although reaching very low detectivity values at room and body temperature, the geometry of such sensors is not suitable for use in ByAxon.

1.2.2 Hall effect sensor

Charged particles in movement under the influence of a electromagnetic field experience the known Lorentz force, given by

$$F = q(E + v \times B)$$

where q is the particle charge, E the electric field, v the particle's velocity and B the magnetic flux density. The presence of such field deflects the trajectory of an electrically charged body. This is exploited in particle accelerators and mass spectrometers. If charge carriers (electrons or holes) are flowing in a conductor in the y-direction and a magnetic field is applied along z-direction, they will sense a force pushing them along the x-direction, and will accumulate at the edge. This will generate an electric field perpendicular to the passage of current, increasing until the new electrostatic force balances the Lorentz force. This gives rise to a voltage difference perpendicular to current direction and proportional

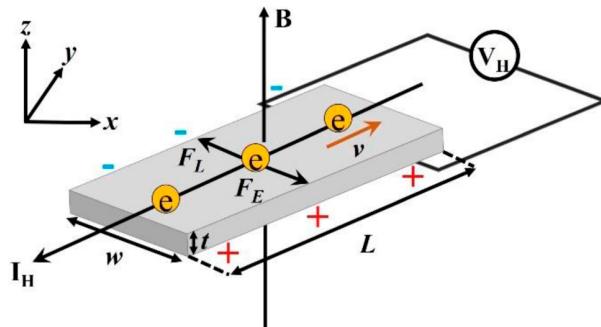


Figure 1.4: Representation of the classical Hall effect. The Lorentz force and electric field force are F_L and F_E , respectively. A current I_H generates a transverse voltage difference V_H . From [18].

to magnetic field intensity considering a fixed current density, as presented in Fig. 1.4. As a robust and cost effective technology, Hall effect sensors still dominate the market [4]. This technology is mainly used for electric current, proximity, speed and position sensing, specially in automotive applications. As such devices can be made out of semiconductor materials, a direct integration in silicon wafers is possible. This allows for fabrication using the same techniques for CMOS technology and mass production, which lowers final product cost. Hall effect devices can present a linear response to magnetic flux density or be made as transistors, effectively acting as switches [19]. More adapted for operation in mT, down to μT operation, linear Hall effect sensors with current technology do not present the magnetic resolution required by the ByAxon project. More recently, there is a progress in the development of Hall effect sensors based on graphene [18], with very promising results that call for further investigation.

1.2.3 SQUID sensor

Superconducting Quantum Interference Devices (SQUIDs) [20] are based on the Meissner effect found in superconductors and in Josephson junctions. Already in 1911, it was verified that when cooled below 4.2 K, mercury presents a huge drop in its electrical resistance [21]. This transition to a superconducting state below a critical temperature is present in several materials. The source of electrical resistance is the scattering of electrons as they propagate in a material. The Bardeen-Cooper-Schrieffer [22] (BCS) theory states that below this transition temperature, electrons condense into pairs (known as Cooper pairs) due to phonon exchange. The bond is a weak one, and can be broken by thermal, magnetic or kinetic interactions [23]: a rise in temperature, in magnetic field or current density, respectively. Meissner verified that when a material suffers superconducting transition, it causes an expulsion of any magnetic flux line that was going through the material. If a ring geometry is formed, flux lines will be trapped inside the ring, as exemplified in Fig. 1.5. When the source of magnetic flux is removed, an electric current is induced in the ring, keeping the trapped flux constant. A variation in magnetic flux provokes a variation in the current circulating in the ring. Currently, SQUIDs present the highest sensitivity to detect variations in magnetic flux. They can be employed in biomagnetism, geomagnetism, detection of gravitational waves and observation of spin noise. To do so, SQUIDs make use of tunneling through Josephson junctions [24] and the fact that flux φ is quantized in a superconduction loop in units of $\varphi_0 = h/2e$ [25], where h is Planck's constant and e the electron charge. A Josephson junction is formed by a thin insulating layer separating two superconductors. When tunneling through this barrier, the Cooper pair of electrons maintain phase coherence. For a current bias I below one given threshold I_0 , the maximum current the junction sustains, there is no voltage difference across the junction. But when $I > I_0$ a voltage appears. Shunting the junction with an external shunt resistance makes the voltage return to zero when applied bias is

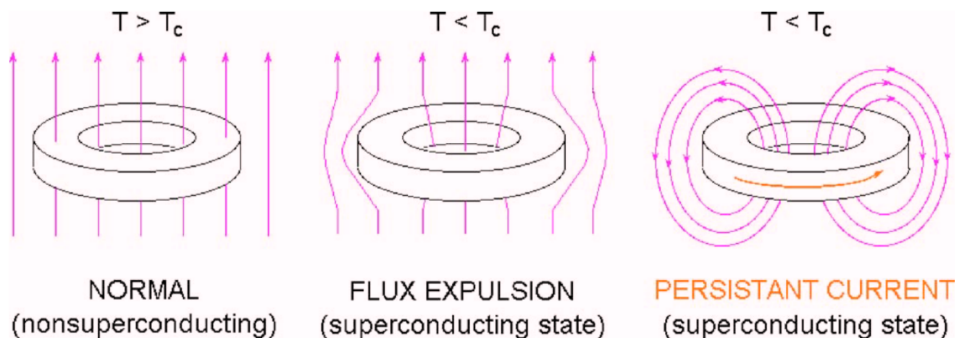


Figure 1.5: Ring-shaped conductor cooled below its transition temperature. Magnetic flux trapped inside the ring is quantized and gives rise to a circulating current. Adapted from [23].

reduced, avoiding an hysteric behaviour. As explained by John Clarke [26], there are two main types of SQUID devices: DC SQUIDS and RF SQUIDS. An oversimplified method of operation is as follows: DC SQUIDS present one superconducting loop with two parallel connected Josephson junctions, biased at a constant current above the critical current I_0 . With no applied flux φ , current is perfectly divided in both junctions and there is no net current circulating in the loop. When magnetic flux is applied, the flux will be quantized generating a circulating current $J = -\varphi/L$. This adds to the current flowing through one junction and subtracts from the other junction, with an oscillation with period φ_0 . Thus the voltage across the SQUID oscillates with the increase of φ . Signal is then coupled to a low-noise amplifier. For an increased performance, a feedback circuit can be employed. One coupled coil modulates the magnetic flux in the SQUID, at the same frequency of detection of a lock-in detector after the coupled amplifier. RF SQUIDS on the other hand have a superconducting loop with only one Josephson junction, and no bias current. The only current through the loop originates from magnetic flux φ . The SQUID is inductively coupled to a resonant circuit via mutual inductance. This tank circuit is excited at RF frequency. If the excitation current is correctly adjusted, the voltage across the tank circuit will be periodic in φ after demodulating the signal. Figure 1.6 shows schematics of both DC and RF modes of operation. As also done for DC SQUIDS, a modulating

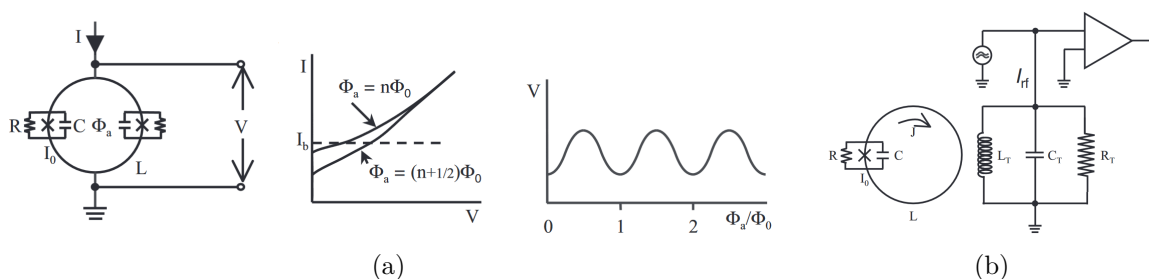


Figure 1.6: The cross symbol represents the Josephson junction in the superconducting loop, with an associated resistance and capacitance. a) DC SQUID with two Josephson junctions, biased at I_b above the threshold current. Variations in quantized flux at fixed current provoke an alternating output voltage. b) RF SQUID, with a single Josephson junction coupled to a tank circuit and its preamplifier. From [26].

flux is used along with lock-in detection and feedback, in a flux-locked loop. Although SQUID sensors present very low noise and high sensitivity, reaching detectivities of fT/Hz , they are complex devices, with a cumbersome mounting. First, for the material to be in superconducting state it needs to operate at cryogenic temperature. Even with the advance of High Temperature Superconductors, it is still well below 100 K. So the SQUID device must be isolated from the studied sample. This also imposes a requirement of a coupled pick-up coil, that does not required low temperature and can be placed closer

to the studied specimen. Indeed, it is not possible to obtain direct readings without a more complex supporting electronics and infrastructure when compared to other magnetic sensors. High performance commercially available SQUID magnetometer weight around 400 kg and occupy more than 1.7 m³ while consuming 4 liters of liquid helium and liquid nitrogen per day at typical use [27]. Thanks to their very low detectivity values, SQUIDS have been successfully used to perform magnetoencephalography (MEG) imaging, a tool that is now vital for neuroscience [28, 29]. Magnetic signals originated from the spinal cord activity have also been measured using an array of SQUIDS [12]. While their use in biomedical applications have already been proven due to very high performance, the need for cryogenic cooling makes SQUIDS not viable for use in an implantable device such as the one envisioned by the ByAxon project.

1.2.4 Optical pump magnetometers

A more recent alternative to MEG is the use of optical pump magnetometers (OPMs), as they also present very low detectivity levels and do not require cryogenic cooling [30]. Therefore they can be placed much closer to the patient. OPMs are based on changes in the atoms population at different energy levels by optical irradiation. This method, proposed by Dr. Alfred Kastler in 1950, is known as optical pumping [31]. Such variations can be verified by the changes of intensity of transmitted light or polarization of scattered light. Besides energy, angular momentum is also transferred from polarized light to atoms, producing an alignment of spin vectors and a macroscopic magnetization of the medium. In the presence of a magnetic field, the Zeeman splitting [32] breaks even further the hyperfine structure degeneracy of the system, as shown in Fig. 1.7. The schematic in Fig. 1.7(a) represents possible energy transitions of ⁸⁷Rb when a laser with 795 nm wavelength and circularly polarized is used. As explained by Tierney *et al* [33], the laser can provoke a

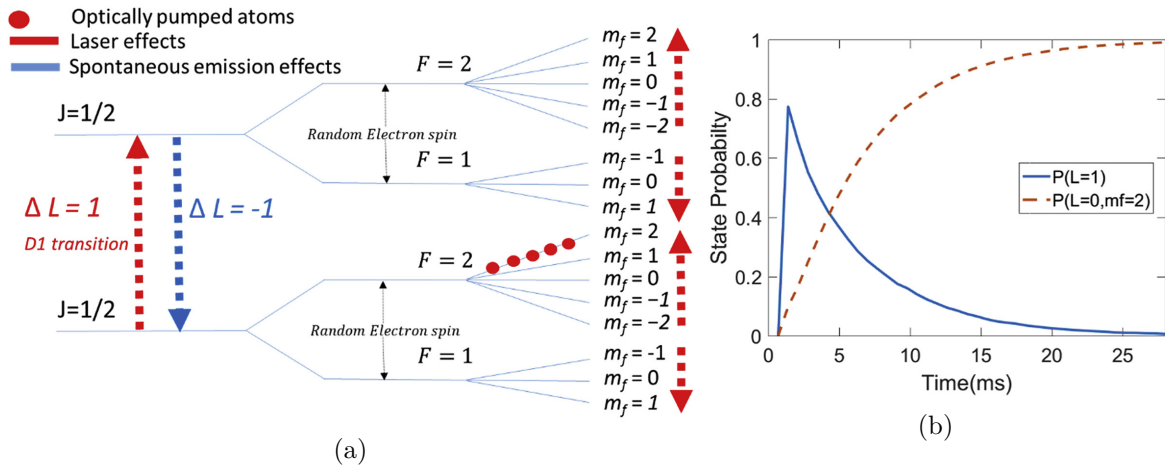


Figure 1.7: Energy diagram for ⁸⁷Rb ground and first excited states. a) J is the total angular momentum of the atom, F is a dimensionless quantum number defining possible hyperfine states and m_f represents the Zeeman splitting by the component of angular momentum along the laser axis. b) Evolution with time of population in first excited state (blue curve) and the state “locked” by optical pumping (dashed orange). From [33].

transition from ground to excited state, resulting in a spontaneous emission of a photon when the atom returns to ground state. But the laser will also provoke an increase in m_f of 1. When spontaneous emission occurs, the variation in m_f can be -1, 0 or 1, all with equal probabilities. So one third of the atoms that were excited to the first state will end up in ground state with $F = 2$ and $m_f = 2$. As 2 is the maximum value for m_f and the energy transfer from laser to atom has to increase its value, eventually all atoms become trapped in this energy level and no longer interact with the laser, becoming completely transparent to it. Figure Fig. 1.7(b) illustrates the occupation of the first excited state

and of the optically pumped state. In this configuration, the ^{87}Rb vapor becomes highly polarized, producing a strong net magnetization. This induced magnetic polarization of the vapor is very sensitive to external magnetic field.

The operation of OPMs as detection devices can be simply explained as follows: a vapour, usually of alkali metal due to simple atomic structure and low melting point, is contained in an electrically heated glass cell. A laser at a specific wavelength is shined through the cell, transferring energy and causing a transition in energy state of the atoms. Due to Zeeman effect, energy levels split into sub-levels when a magnetic field is applied, thus enabling new energy transitions and changes in the occupation of states. There are two modes of operation for OPMs: with a single laser or with the use of a pump laser and a second probe laser. In both cases, a photodiode is used to detect the optical signal. Once the vapour is completely polarized, the pump laser no longer interacts with it and its intensity can be detected at the other side of the glass cell. With the presence of a magnetic field, the energy state of the vapour atoms will change and they will once again absorb the pump laser, thus reducing the incoming intensity at the detector. If a secondary probe laser is used, it is its variation in intensity, due to absorption, or polarisation due to Faraday effect, that gives the information of the magnetic field. The greater the volume of the vapour, the higher the sensitivity to external magnetic fields [33]. Commonly, Rb vapour with a 795 nm pumping laser is used. Figure 1.8 shows the basic working principle and an example of a OPM cell. At a given magnetic flux density B , the magnetic moments

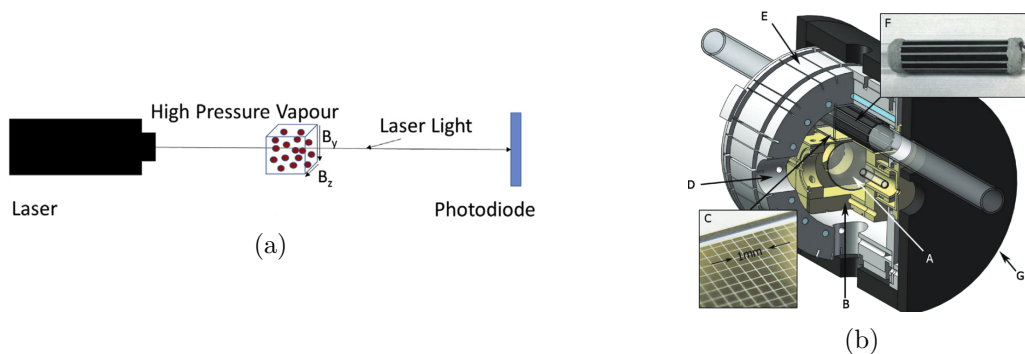


Figure 1.8: a) Laser light is detected after going through a high pressure vapor cell. From [33]. b) OPM system, indicating A: alkali-metal cell, B: boron-nitride oven, C: radiation shield, D: access for probe laser, E: frame for magnetic field and gradient coils and water cooling, F: sample heater, and G: ferrite magnetic shield. The magnetic sample to be characterized is inserted in the upper quartz tube. From [34].

of the polarized vapour atoms precess around it at the Larmor frequency $\omega_0 = \gamma B$, where γ is the gyromagnetic ratio of the atom. To obtain the highest sensitivity to variations of B , it is crucial that atoms precess in phase, maximizing the polarization of the gas. But the polarization induced in the vapour reduces due to relaxation, when atoms return to their initial state thus decreasing the sensitivity to changes in B . The main contribution to relaxation is spin-exchange. To maintain a high sensitivity state, OPMs work in the Spin Exchange Relaxation Free (SERF) regime. This is achieved at low magnetic flux density and high vapour density, so smaller glass cells are used. Theoretical noise level of $10 \text{ fT/Hz}^{-1/2}$ above 1 Hz were reported for a complete OPM device of $14 \times 21 \times 80 \text{ mm}^3$ volume working at room temperature [30]. With a 1 cm^3 sample, by eliminating ambient magnetic noise and using a gradiometer configuration, $160 \text{ aT/Hz}^{-1/2}$ detectivity value at 40 Hz was reported and measurements up to $420 \text{ }^\circ\text{C}$ temperature were conducted [34]. With a proper field bias and lock-in technique, $0.8 \text{ pT/Hz}^{-1/2}$ above 20 Hz detectivity was reported with a three-axis OPM [35].

Although OPMs achieve very low detectivity performance working at a temperature compatible to the human body, the more complex mounting, increased size or need for magnetic shielding, they must be discarded as possible sensors for the ByAxon project.

1.2.5 GMR sensor

In 1988, two independent research teams led by Albert Fert [36] and Peter Grünberg [37, 38] verified an unexpectedly large resistance variation in magnetically coupled Fe-Cr multilayers with the application of magnetic field. Baibich *et al* showed that for a Cr layer thin enough between Fe layers, an antiferromagnetic coupling arises. So at zero magnetic field, iron layers present antiparallel magnetization directions. When an external field is applied, magnetization in both layers starts to align. It was verified that sample's electrical resistance gradually decreases with increasing field, until sample reaches magnetization saturation and resistance is at a minimum. This is shown in Fig. 1.9. The mechanism proposed to explain such phenomenon is the occurrence of an asymmetric spin-dependent scattering of electrons. If the magnetic layers present parallel magnetization, the channel corresponding to one of spin states will short the current, while electrons with the opposite spin state will be strongly scattered. This leads to a low resistance state. But when magnetization directions are antiparallel, both spin channels will alternate between weak and strong scattering, resulting in a state of high resistance [39]. The discovery of this

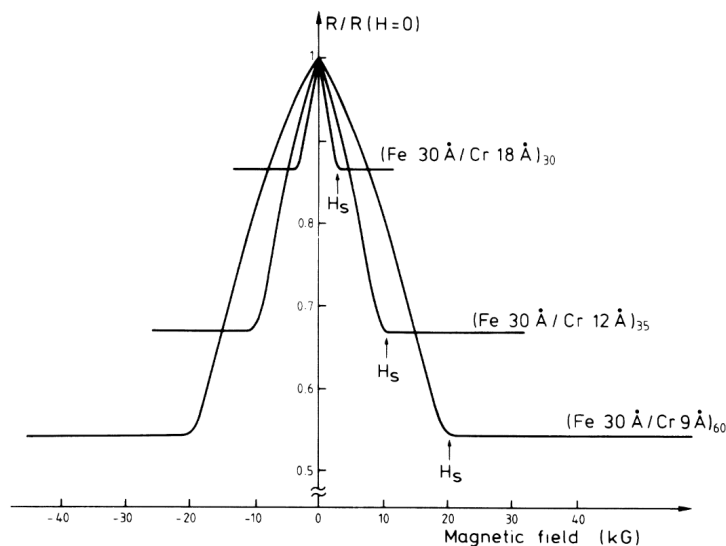


Figure 1.9: Relative resistance of Fe-Cr multilayers as a function of applied field, for current and field along the same direction in sample plane. Resistance is maximum for antiparallel magnetization and minimum for parallel magnetization. From [36].

effect, now dubbed giant magnetoresistance (GMR), awarded both team leaders the 2007 Nobel prize in Physics and led to the development of a whole new era of consumer electronics. Nowadays, GMR devices are stacked multilayers of magnetic and non-magnetic materials known as spin valves [40]. For a better control of sample resistance and achieve operation at lower applied fields, one magnetic layer, known as *pinned layer*, will have its magnetization direction fixed along a specific direction with a strong coercive field. The second magnetic layer, the *free layer*, will have a small coercive field with a magnetization free to rotate in the direction of an applied magnetic field. This free layer will also present a preferential easy axis direction for magnetization when no field is present, in general perpendicular to the pinned layer to have a linear operation around zero applied field. The most common magnetic active materials used in GMR are NiFe and CoFe, thanks to a very soft ferromagnetic behavior and high spin polarisation.

Current can flow either parallel or perpendicular to the stack. Those two configurations are named Current In Plane (CIP) and Current Perpendicular to Plane (CPP), respectively. In the majority of cases, the pinned layer has its magnetization fixed due to an exchange coupling to an adjacent antiferromagnetic layer. The effect of this coupling can be reduced by a spacer layer between both ferromagnetic layers, thus the use of a conductive non-magnetic material. Therefore, the simplest spin valve will require the stacking of at least

four different layers. Figure 1.10 shows the working principle of a spin valve, its output and an actual example of the stacking of different layers to produce one device. The

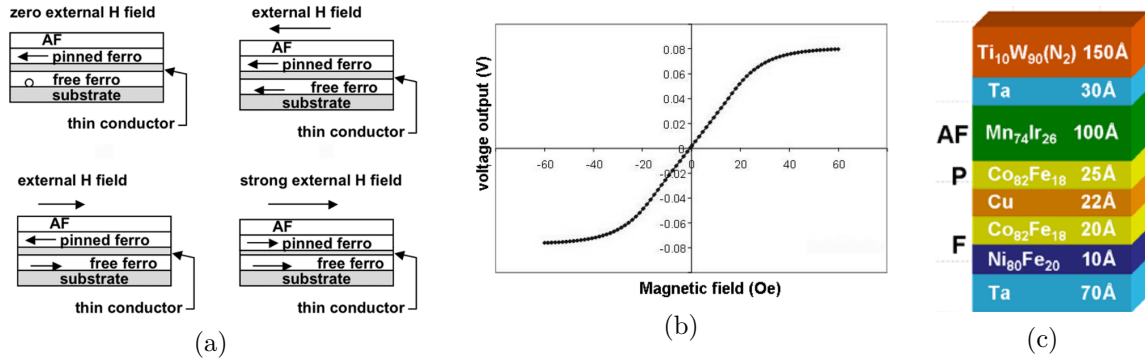


Figure 1.10: Examples of CIP GMR sensor. a) Variation of magnetization direction in a typical spin valve. b) Output signal of a GMR sensor based on spin valve. c) Example of actual spin valve with Cu spacer and Ta buffer layers. Antiferromagnetic (AF), pinned (P) and free (F) layers are indicated. Adapted from [41, 39].

variation of free layer magnetization according to external field is presented in Fig. 1.10(a). At zero external field, free layer magnetization is perpendicular to pinned layer. It rotates following the applied magnetic field, that may also change the pinned layer magnetization if too strong. The output signal of such spin valve sensor is shown in Fig. 1.10(b), linear around zero field. An actual stacking of layers to obtain one spin valve is exemplified in Fig. 1.10(c). Instead of relying only on exchange-based coupling for the magnetic layers, that occurs only when the spacer layer is very thin, one can also make use of magnetostatic coupling. The latter is influenced by the roughness of the interface and grain size [42]. So *buffer layers* were introduced to control the crystalline orientation in multilayers. Even if such layers do not correspond to the active region of the device, they do affect sensor performance [43, 44]. Another factor that might alter GMR performance is a contraction of hysteresis loops with increasing magnetization cycles. This is attributed to fluctuations in exchange bias coupling [45]. For sufficiently high applied field, magnetization in the pinned layer will also change its direction. This in turn degrades the GMR effect. Also, if the free layer magnetization is parallel or antiparallel to the pinned layer at zero applied field, the device would require a bias DC field to operate in the linear range, as can be seen in Fig. 1.9. To obtain a linear response around zero applied field, the free layer must present a magnetization direction perpendicular to that of the pinned layer. This is achievable by designing a specific geometry for shape anisotropy, by weakly pinning the free layer or by external field bias [46].

GMR sensors can be employed in implantable biomedical applications as required for ByAxon. Caruso *et al* showed the *in vivo* detection of biological magnetic signal at the brain of a cat and originating from light stimulation, averaging the signal of a sensor composed of 9 layers GMR as one arm of a balanced Wheatstone bridge [11].

1.2.6 TMR sensor

Tunneling magnetoresistance [47, 48] devices make use of the quantum tunneling effect, the electron's property to pass through a physical barrier composed of a non-conducting material thanks to its wave-like nature. These devices are made up of several magnetic tunnel junctions (MTJ), which are stacks similar to spin valves found in GMR devices, but the spacer layer is replaced by an insulator material. The probability of an electron to tunnel through this insulator depends on the relative direction between magnetization of upper and lower layers. As it is based on tunneling effect, current can only flow perpendicular to the stack, in CPP configuration. As for GMR devices, one ferromagnetic layer will present a magnetization free to rotate while the other will be pinned, usually by

exchange coupling with an antiferromagnetic layer. The fabrication of TMR devices require the deposition of at least four layers, that must be compatible. Historically, amorphous A_2O_3 was used as the insulator layer. Nowadays, it is replaced by crystalline MgO which provides a higher MR ratio and leads to a lower intrinsic noise [49].

The MR ratio obtained in TMR are the highest among magnetoresistance devices and can reach up to 600% at room temperature [50], but this technology also present the highest noise. Nevertheless, it has the lowest values for detectivity among MR sensors [51]. Besides increasing the quality of each stack, reduction of the intrinsic noise can be achieved by connecting several MTJs in series or in parallel [52, 53]. It is also possible to interconnect individual MTJs in a Wheatstone bridge configuration [54], although a more complex fabrication process is required to obtain a full bridge over the same die [55]. A more in-depth explanation of the Wheatstone bridge configuration is presented later in this work. To achieve the highest sensitivities yet, several buffer layers are present, in order to get more reproducible junction properties. Not only the magnetic and spacer layers are of great importance, the performance of TMR devices are also affected by the thickness and composition of such buffer layers [56, 57]. Thus high precision and complex systems are required for a proper fabrication and for achieving peak performance.

The commercial sensor TMR9112 by MultiDimension Technologies presents near $150 \text{ pT Hz}^{-1/2}$ detectivity at 1 Hz. Four dies, each presenting a series of MTJ elements surrounded by magnetic flux concentrators (MFCs), are interconnected in a Wheatstone bridge configuration. A schematic of a die is presented in Fig. 1.11. Another feature of

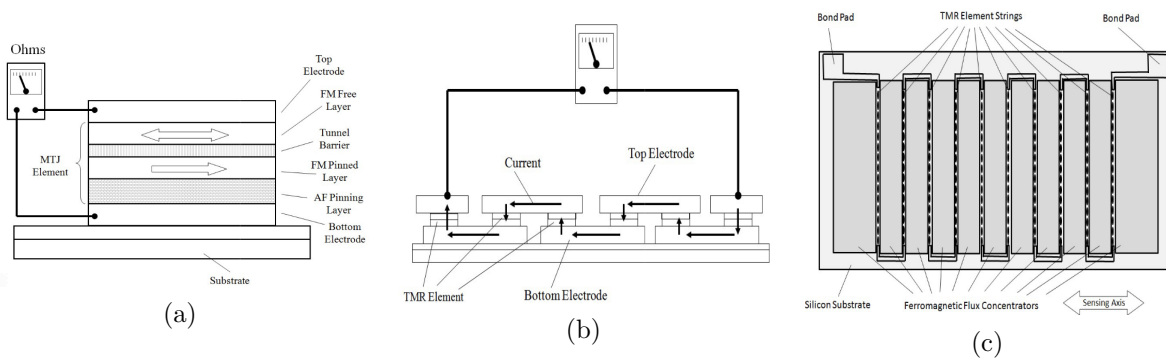


Figure 1.11: a) Representation of a MTJ. b) Series connection of MTJs. c) MTJs surrounded by MFCs to increase sensitivity. From [58].

the commercial sensor is a built-in initialization coil to set the magnetic domains in MTJs and MFCs elements. The layout of a TMR900x device is presented in Fig. 1.12(a). Four

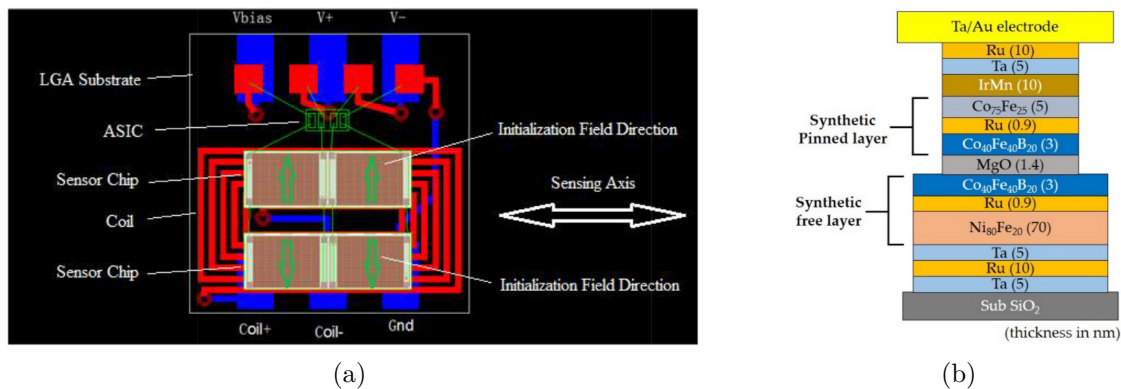


Figure 1.12: a) Layout view of MultiDimension's TMR900x. From [58]. b) A total of 13 layers to obtain a MTJ, plus substrate and metallic contact. Adapted from [54].

interconnected dies, each with several MTJs surrounded by MFCs, form a Wheatstone

bridge structure. Model TMR9001 is assembled in a 6 mm x 5 mm x 1.5 mm package. Finally, an actual example of a current MTJ structure is presented in Fig. 1.12(b).

1.2.7 AMR sensor

As previously mentioned, the change of electrical resistance on a conductor with the presence of a magnetic field was already observed in the XIX century. Nowadays, even if TMR and GMR dominate the market in magnetoresistance sensors due to their higher sensitivities, AMR devices are becoming increasingly attractive. This is due to their lower intrinsic noise in lower frequency regions, likely due to their much less complex multilayer structure [59]. This makes AMR sensors viable competitors for applications in that frequency range, such as for biosensor applications. Instead of relying on magnetization directions between two separate layers, the change of resistance in an AMR device is related to the relative angle between magnetization and current density in the same layer [60]. In a ferromagnetic thin film, magnetization will lie in-plane thanks to the demagnetizing factor. The electrical resistance of a material presenting anisotropic magnetoresistance will have minimum or maximum values when the magnetization direction is perpendicular or parallel to current density. This anisotropy is due to different electron scattering ratios, which can have a crystalline structure origin but is also present in cubic materials. Spin-orbit interactions and band splitting are responsible for introducing differences in scattering rates. As in the free layer of spin valves and MTJs, the in-plane magnetization will rotate based on the direction and amplitude of the external magnetic field and on any present magnetic anisotropy contribution that sets a preferential direction. If at zero applied field magnetization is parallel or perpendicular to current density, magnetoresistance will present roughly a cosine square dependence on the angle between magnetization and current density. For a linear operation around zero applied field, current density direction must be at 45° with respect to magnetization. This is obtained with the use of barber poles, metallic shorting strips deposited over the ferromagnetic material at a 45° angle. Another possibility to obtain a linear operation around zero field is to have the magnetic easy axis at a 45° angle from current density direction.

The most used material in such sensors is permalloy, a metallic alloy consisting roughly of 80% nickel and 20% iron. It presents a relatively large magnetoresistance and is compatible with fabrication techniques for silicon integrated circuits. In permalloys, electric resistance is at its highest when current density and magnetization are parallel, decreasing as magnetization rotates away and becomes perpendicular to current density. Whereas there is effort in increasing the MR ratio of permalloy, it remains much lower than in spin valves and MTJs, barely reaching 4% [61]. Still, low detectivity values can be reached thanks to a lower intrinsic noise in AMR devices. In the present work, the use of LSMO thin films is motivated by its very low intrinsic noise in the low frequency region, as will be discussed further on. Another advantage of AMR devices is that the ferromagnetic thin film can be directly etched in a Wheatstone bridge structure.

One example of a commercially available AMR sensor is Honeywell's HMC1001. It consists of permalloy thin film deposited over silicon substrate and etched in resistive strip elements, forming a Wheatstone bridge structure. A linear operation around zero external field is achieved with the use of barber poles, as presented in Fig. 1.13. The metallic strips force current to flow in a 45° angle with respect to the easy magnetization axis. This product also presents two built-in coils. The first is called offset strap to provide a DC bias magnetic field for calibration or offset correction. The second is a set/reset strap to generate strong pulses of magnetic field and set the domains of the ferromagnetic materials, enabling the sensor to operate in the high sensitivity region, improving linearity and reducing temperature effects. A detectivity of $0.18 \text{ nT Hz}^{-1/2}$ is achieved at 1 Hz. Its 8-pin package has approximate dimensions of 10.5 mm x 3.9 mm x 1.5 mm.

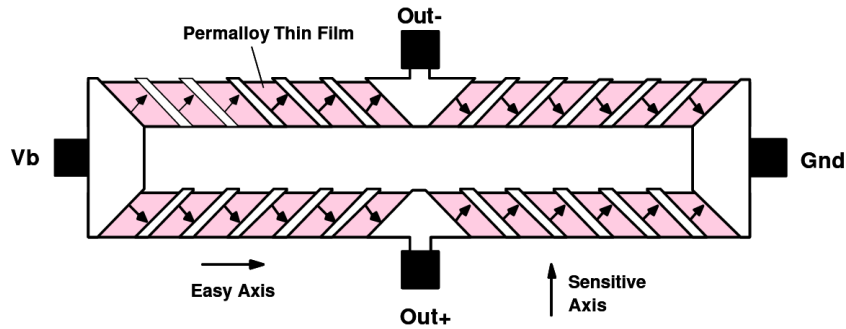


Figure 1.13: Four permalloy resistive strips form a Wheatstone bridge structure. Inner black arrows represent current density direction thanks to the use of barber poles. From [62].

1.3 Conclusion

The motivation behind the development of a new magnetic field sensor was presented, along with different technologies. An outlook of the presented technologies related to the range of target magnetic field is presented in Fig. 1.14. Although Hall effect sensors still

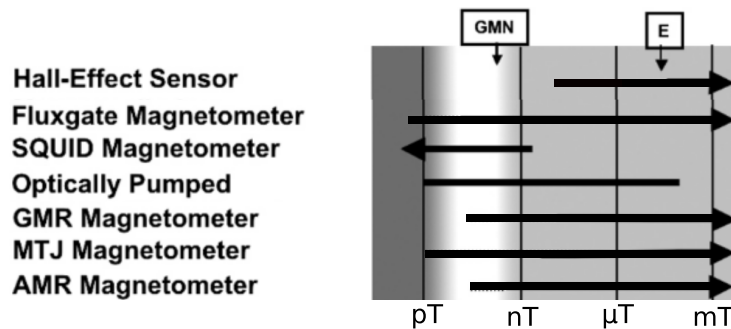


Figure 1.14: Different sensor technologies and their respective range of magnetic field. Amplitude of Earth's magnetic field is indicated by the letter E, whereas GMN stands for geomagnetic noise. Adapted from [41] with more up-to-date performance values.

dominate the market and SQUIDs present the lowest detectivity values, magnetoresistive technologies are the most adapted to the constraints imposed by the target application of ByAxon project. GMR, TMR and AMR sensors achieve low detectivity values in the low frequency region. Thanks to the low cost of AMR devices and the high sensitivity and low power consumption of TMR, MR devices show growth in market share [63]. Numbers of new patents by sensor technology and publications for each MR device are presented in Fig. 1.15. Over the years, magnetoresistive technologies hold more than half the number of new patents for magnetic field sensors. The increase in the number of publications follows the discovery of GMR and TMR. Due to increased performance over Hall effect sensors and an ever reducing fabrication cost thanks to higher production volume, magnetoresistive sensors are to be a driving force for the concept of smart living. The low power consumption of MR devices and small physical dimensions allows them to be configured as networked sensors, gathering data and information for IoT. An overview of the presence of magnetoresistive sensors in smart living is presented in Fig. 1.16. Considering biomedical applications alone, the roadmap prepared by Zheng *et al* [6] sets a detectivity milestone of $10 \text{ fT Hz}^{-1/2}$ to be reached around 2032. With such performance, molecular diagnosis and MR-based magnetoencephalography shall be possible (see Fig. 1.17). To reach such values, the identified technological challenges were:

- increase of sensitivity with MR ratio above 1000% and saturation field below 0.1 mT
- reduction of detectivity with the development of magnetic flux concentrators with gain

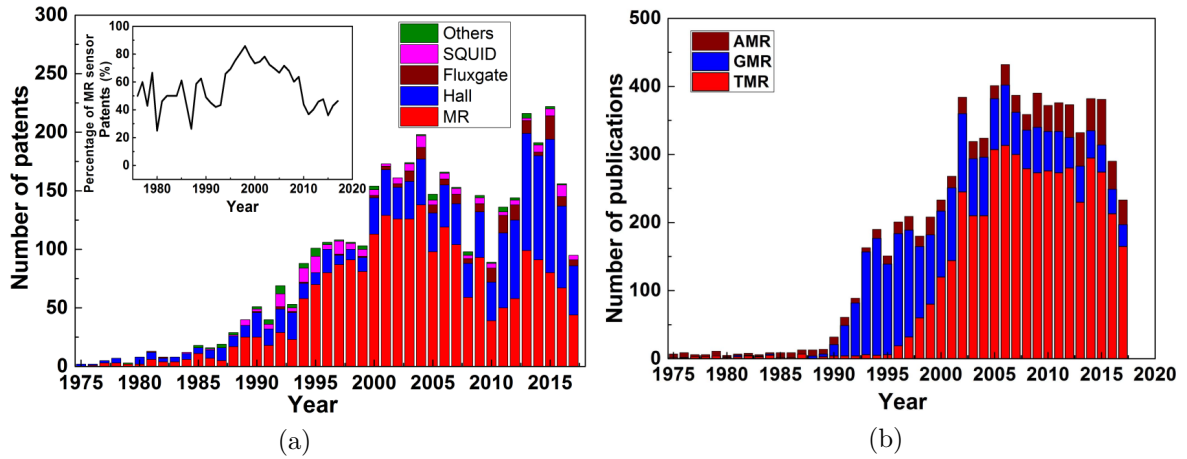


Figure 1.15: a) Number of yearly patents per technology, inset shows the percentage of MR sensors. b) Year by year publications of MR devices. From [6].

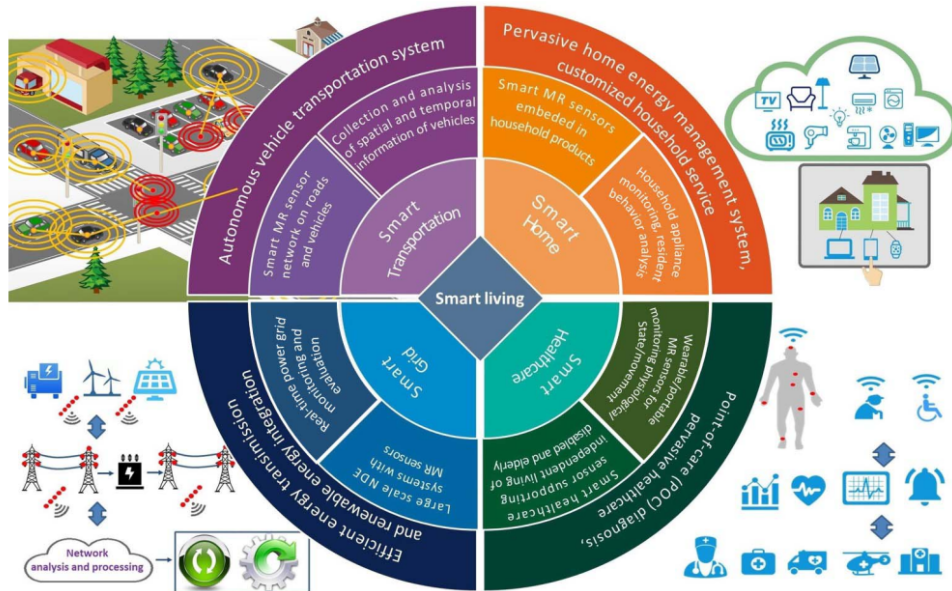


Figure 1.16: The concept of smart living encompasses smart grid, smart transportation, smart home and smart health. All are driven by the Internet of Things. From [6].

above 1000 and reduction of noise normalized by the voltage bias below 10^{-14} Hz^{-1} (under 100 Hz)

The next chapters of this thesis are dedicated to introduce the reader to LSMO manganite oxide and its properties, how this material can be used to obtain high performance AMR sensors with an easy fabrication process, how to optimize the intrinsic properties, design and configuration so as to use it as a proper magnetic field sensor.

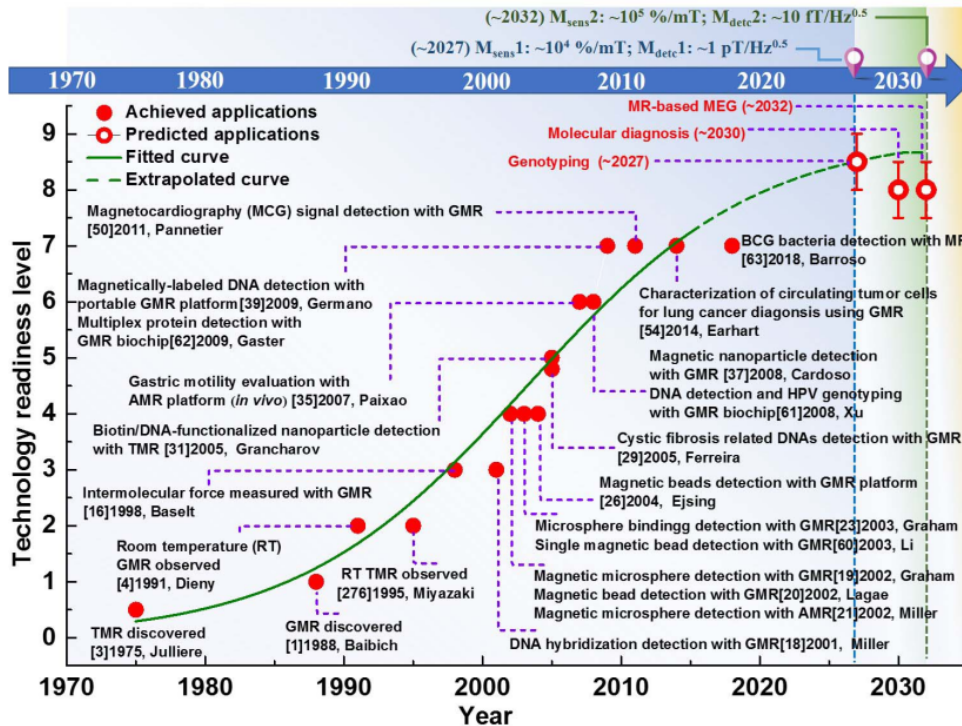


Figure 1.17: Technology readiness level prediction for biomedical applications based on the logistic growth curve. From [6].

Bibliography

- [1] J. M. D. Coey. *Magnetism and Magnetic Materials*. Cambridge University Press, Mar. 2010. ISBN: 9780521816144.
- [2] Merriam-Webster. *Lodestone*. URL: <https://www.merriam-webster.com/dictionary/lodestone> (visited on 02/15/2021).
- [3] Grand View Research. *Permanent Magnets Market Size, Share & Trends Analysis Report By Material (Ferrite, NdFeB, Alnico, SmCo), By Application (Medical, Consumer Goods & Electronics), By Region, And Segment Forecasts, 2020 - 2027*. 2020. URL: <https://www.grandviewresearch.com/industry-analysis/permanent-magnets-industry> (visited on 01/29/2021).
- [4] Global Market Insights. *Magnetic Sensor Market Size By Technology (Hall Effect, Anisotropic Magneto-Resistive (AMR), Giant Magnetoresistance (GMR), Tunnel Magnetoresistance (TMR)), By Application (Speed Sensing, Position Sensing, Detection/Non-Destructive Testing (NDT), Navigation & Electronic Compass), By End-use (Aerospace, Automotive, Consumer Electronics, Industrial), Industry Analysis Report, Regional Outlook, Application Potential, Competitive Market Share & Forecast, 2020 - 2026*. 2020. URL: <https://www.gminsights.com/industry-analysis/magnetic-sensor-market> (visited on 01/29/2021).
- [5] W. Thomson. "XIX. On the electro-dynamic qualities of metals:-Effects of magnetization on the electric conductivity of nickel and of iron". In: *Proceedings of the Royal Society of London* 8 (1857), pp. 546–550. DOI: 10.1098/rsp1.1856.0144. eprint: <https://royalsocietypublishing.org/doi/pdf/10.1098/rsp1.1856.0144>. URL: <https://royalsocietypublishing.org/doi/abs/10.1098/rsp1.1856.0144>.

- [6] C. Zheng, K. Zhu, S. Cardoso de Freitas, J. Chang, J. E. Davies, P. Eames, P. P. Freitas, O. Kazakova, C. Kim, C. Leung, S. Liou, A. Ognev, S. N. Piramanayagam, P. Ripka, A. Samardak, K. Shin, S. Tong, M. Tung, S. X. Wang, S. Xue, X. Yin, and P. W. T. Pong. “Magnetoresistive Sensor Development Roadmap (Non-Recording Applications)”. In: *IEEE Transactions on Magnetics* 55.4 (2019), pp. 1–30. DOI: 10.1109/TMAG.2019.2896036.
- [7] X. Liu, K. H. Lam, K. Zhu, C. Zheng, X. Li, Y. Du, C. Liu, and P. W. T. Pong. “Overview of Spintronic Sensors With Internet of Things for Smart Living”. In: *IEEE Transactions on Magnetics* 55.11 (2019), pp. 1–22. DOI: 10.1109/TMAG.2019.2927457.
- [8] B. Dieny, I. L. Prejbeanu, K. Garello, P. Gambardella, P. Freitas, R. Lehndorff, W. Raberg, U. Ebels, S. O. Demokritov, J. Akerman, A. Deac, P. Pirro, C. Adelman, A. Anane, A. V. Chumak, A. Hirohata, S. Mangin, Sergio O. Valenzuela, M. Cengiz Onbaşı, M. d’Aquino, G. Prenat, G. Finocchio, L. Lopez-Diaz, R. Chantrell, O. Chubykalo-Fesenko, and P. Bortolotti. “Opportunities and challenges for spintronics in the microelectronics industry”. In: *Nature Electronics* 3.8 (2020), pp. 446–459. ISSN: 2520-1131. DOI: 10.1038/s41928-020-0461-5. URL: <https://doi.org/10.1038/s41928-020-0461-5>.
- [9] ByAxon. *ByAxon*. URL: <http://www.byaxon-project.eu/> (visited on 06/07/2021).
- [10] B. J. Roth and J. P. Wikswo Jr. “The magnetic field of a single axon. A comparison of theory and experiment”. In: *Biophys. J.* 48.1 (1985), pp. 93–109. DOI: 10.1016/S0006-3495(85)83763-2.
- [11] L. Caruso, T. Wunderle, C. M. Lewis, J. Valadeiro, V. Trauchessec, J. Trejo Rosillo, J. P. Amaral, J. Ni, P. Jendritza, C. Fermon, S. Cardoso, P. P. Freitas, P. Fries, and M. Pannetier-Lecœur. “In Vivo Magnetic Recording of Neuronal Activity”. In: *Neuron* 95.6 (2017), pp. 1283–1291. ISSN: 0896-6273. DOI: 10.1016/j.neuron.2017.08.012.
- [12] Y. Adachi, D. Oyama, J. Kawai, S. Kawabata, and G. Uehara. “Spinal cord evoked magnetic field measurement using a magnetospinography system equipped with a cryocooler”. In: (2013), pp. 4426–4429. DOI: 10.1109/EMBC.2013.6610528.
- [13] S. Tumanski. “Induction coil sensors — a review”. In: *Measurement Science and Technology* 18.3 (2007), R31. DOI: 10.1088/0957-0233/18/3/R01. URL: <https://iopscience.iop.org/article/10.1088/0957-0233/18/3/R01>.
- [14] R. J. Prance, T. D. Clark, and H. Prance. “Ultra low noise induction magnetometer for variable temperature operation”. In: *Sensors and Actuators A: Physical* 85.1 (2000), pp. 361–364. ISSN: 0924-4247. DOI: [https://doi.org/10.1016/S0924-4247\(00\)00375-7](https://doi.org/10.1016/S0924-4247(00)00375-7). URL: <https://www.sciencedirect.com/science/article/pii/S0924424700003757>.
- [15] J. Vyhnanek and P. Ripka. “Experimental Comparison of the Low-Frequency Noise of Small-Size Magnetic Sensors”. In: *IEEE Transactions on Magnetics* 53.4 (2017), pp. 1–4. DOI: 10.1109/TMAG.2016.2633398.
- [16] J. Tomek. “Inductive Contactless Distance Measurement Intended for a Gastric Electrical Implant”. In: *Acta Polytech.* 47.4-5 (2007).
- [17] M. Djamal and Yulkifli. “Fluxgate magnetic sensor”. In: *International Conference on Instrumentation, Communication, Information Technology, and Biomedical Engineering 2009*. 2009, pp. 1–6. DOI: 10.1109/ICICI-BME.2009.5417227.
- [18] D. Collomb, P. Li, and S. Bending. “Frontiers of graphene-based Hall-effect sensors”. In: *Journal of Physics: Condensed Matter* 33.24 (May 2021), p. 243002. DOI: 10.1088/1361-648x/abf7e2. URL: <https://doi.org/10.1088/1361-648x/abf7e2>.
- [19] J. Heremans. “Solid state magnetic field sensors and applications”. In: *Journal of Physics D: Applied Physics* 26.8 (Aug. 1993), pp. 1149–1168. DOI: 10.1088/0022-3727/26/8/001. URL: <https://doi.org/10.1088/0022-3727/26/8/001>.

-
- [20] J. Clarke. “SQUID Fundamentals”. In: *SQUID Sensors: Fundamentals, Fabrication and Applications*. Ed. by H. Weinstock. NATO ASI Series E: Applied Sciences. Kluwer Academic Publishers, 1996. Chap. 1, pp. 1–62.
- [21] H. K. Onnes. In: *Akad. van Wetenschappen* 14.113 (1911), p. 818.
- [22] J. Bardeen, L. N. Cooper, and J. R. Schrieffer. “Theory of Superconductivity”. In: *Phys. Rev.* 108 (5 Dec. 1957), pp. 1175–1204. DOI: [10.1103/PhysRev.108.1175](https://doi.org/10.1103/PhysRev.108.1175). URL: <https://link.aps.org/doi/10.1103/PhysRev.108.1175>.
- [23] R. L. Fagaly. “Superconducting quantum interference device instruments and applications”. In: *Review of Scientific Instruments* 77.10 (2006), p. 101101. DOI: [10.1063/1.2354545](https://doi.org/10.1063/1.2354545). eprint: <https://doi.org/10.1063/1.2354545>. URL: <https://doi.org/10.1063/1.2354545>.
- [24] B. D. Josephson. “Possible new effects in superconductive tunnelling”. In: *Physics Letters* 1.7 (1962), pp. 251–253. ISSN: 0031-9163. DOI: [https://doi.org/10.1016/0031-9163\(62\)91369-0](https://doi.org/10.1016/0031-9163(62)91369-0). URL: <https://www.sciencedirect.com/science/article/pii/0031916362913690>.
- [25] F. London. *Superfluids*. Wiley, 1950. ISBN: 0486600440.
- [26] J. Clarke. *The SQUID Handbook*. Ed. by J. Clarke and A. I. Braginski. WILEY-VCH Verlag GmbH & Co. KGaA, 2004. ISBN: 3527402292.
- [27] Quantum Design GmbH. *MPMS3*. URL: <https://qd-europe.com/fr/en/product/mpms3-squid-magnetometer/> (visited on 03/05/2021).
- [28] D. Cohen. “Magnetoencephalography: Detection of the Brain’s Electrical Activity with a Superconducting Magnetometer”. In: *Science* 175.4022 (1972), pp. 664–666. ISSN: 0036-8075. DOI: [10.1126/science.175.4022.664](https://doi.org/10.1126/science.175.4022.664). eprint: <https://science.sciencemag.org/content/175/4022/664.full.pdf>. URL: <https://science.sciencemag.org/content/175/4022/664>.
- [29] S. Baillet. “Magnetoencephalography for brain electrophysiology and imaging”. In: *Nature Neuroscience* 20.3 (Mar. 2017), pp. 327–339. ISSN: 1546-1726. DOI: [10.1038/nn.4504](https://doi.org/10.1038/nn.4504). URL: <https://doi.org/10.1038/nn.4504>.
- [30] E. Boto, S. S. Meyer, V. Shah, O. Alem, S. Knappe, P. Kruger, T. M. Fromhold, M. Lim, P. M. Glover, P. G. Morris, R. Bowtell, G. R. Barnes, and M. J. Brookes. “A new generation of magnetoencephalography: Room temperature measurements using optically-pumped magnetometers”. In: *NeuroImage* 149 (2017), pp. 404–414. ISSN: 1053-8119. DOI: <https://doi.org/10.1016/j.neuroimage.2017.01.034>. URL: <https://www.sciencedirect.com/science/article/pii/S1053811917300411>.
- [31] C. Cohen-Tannoudji and A. Kastler. “I Optical Pumping”. In: ed. by E. Wolf. Vol. 5. *Progress in Optics*. Elsevier, 1966, pp. 1–81. DOI: [https://doi.org/10.1016/S0079-6638\(08\)70450-5](https://doi.org/10.1016/S0079-6638(08)70450-5). URL: <https://www.sciencedirect.com/science/article/pii/S0079663808704505>.
- [32] P. Zeeman. “VII. Doublets and triplets in the spectrum produced by external magnetic forces”. In: *The London, Edinburgh, and Dublin Philosophical Magazine and Journal of Science* 44.266 (1897), pp. 55–60. DOI: [10.1080/14786449708621028](https://doi.org/10.1080/14786449708621028). eprint: <https://doi.org/10.1080/14786449708621028>. URL: <https://doi.org/10.1080/14786449708621028>.
- [33] T. N. Tierney, N. Holmes, S. Mellor, J. D. López, G. Roberts, R. M. Hill, E. Boto, J. Leggett, V. Shah, M. J. Brookes, R. Bowtell, and G. R. Barnes. “Optically pumped magnetometers: From quantum origins to multi-channel magnetoencephalography”. In: *NeuroImage* 199 (2019), pp. 598–608. ISSN: 1053-8119. DOI: <https://doi.org/10.1016/j.neuroimage.2019.05.063>. URL: <https://www.sciencedirect.com/science/article/pii/S1053811919304550>.
-

- [34] H. B. Dang, A. C. Maloof, and M. V. Romalis. “Ultrahigh sensitivity magnetic field and magnetization measurements with an atomic magnetometer”. In: *Applied Physics Letters* 97.15 (2010), p. 151110. DOI: 10.1063/1.3491215. eprint: <https://doi.org/10.1063/1.3491215>. URL: <https://doi.org/10.1063/1.3491215>.
- [35] H. C. Huang, H. F. Dong, X. Y. Hu, L. Chen, and Y. Gao. “Three-axis atomic magnetometer based on spin precession modulation”. In: *Applied Physics Letters* 107.18 (2015), p. 182403. DOI: 10.1063/1.4935096. eprint: <https://doi.org/10.1063/1.4935096>. URL: <https://doi.org/10.1063/1.4935096>.
- [36] M. N. Baibich, J. M. Broto, A. Fert, F. Nguyen Van Dau, F. Petroff, P. Etienne, G. Creuzet, A. Friederich, and J. Chazelas. “Giant Magnetoresistance of (001)Fe/(001)Cr Magnetic Superlattices”. In: *Phys. Rev. Lett.* 61 (21 Nov. 1988), pp. 2472–2475. DOI: 10.1103/PhysRevLett.61.2472. URL: <https://link.aps.org/doi/10.1103/PhysRevLett.61.2472>.
- [37] P. Grünberg, R. Schreiber, Y. Pang, M. B. Brodsky, and H. Sowers. “Layered Magnetic Structures: Evidence for Antiferromagnetic Coupling of Fe Layers across Cr Interlayers”. In: *Phys. Rev. Lett.* 57 (19 Nov. 1986), pp. 2442–2445. DOI: 10.1103/PhysRevLett.57.2442. URL: <https://link.aps.org/doi/10.1103/PhysRevLett.57.2442>.
- [38] F. Saurenbach, U. Walz, L. Hinchey, P. Grünberg, and W. Zinn. “Static and dynamic magnetic properties of Fe-Cr-layered structures with antiferromagnetic interlayer exchange”. In: *Journal of Applied Physics* 63.8 (1988), pp. 3473–3475. DOI: 10.1063/1.340770. eprint: <https://doi.org/10.1063/1.340770>. URL: <https://doi.org/10.1063/1.340770>.
- [39] P. P. Freitas, R. Ferreira, S. Cardoso, and F. Cardoso. “Magnetoresistive sensors”. In: *Journal of Physics: Condensed Matter* 19.16 (Apr. 2007), p. 165221. DOI: 10.1088/0953-8984/19/16/165221. URL: <https://doi.org/10.1088/0953-8984/19/16/165221>.
- [40] B. Dieny, V. S. Speriosu, S. S. P. Parkin, B. A. Gurney, D. R. Wilhoit, and D. Mauri. “Giant magnetoresistive in soft ferromagnetic multilayers”. In: *Phys. Rev. B* 43 (1 Jan. 1991), pp. 1297–1300. DOI: 10.1103/PhysRevB.43.1297. URL: <https://link.aps.org/doi/10.1103/PhysRevB.43.1297>.
- [41] J. Lenz and S. Edelstein. “Magnetic sensors and their applications”. In: *IEEE Sensors Journal* 6.3 (2006), pp. 631–649. DOI: 10.1109/JSEN.2006.874493.
- [42] Z. J. Yang and M. R. Scheinfein. “Interfacial-roughness effects on giant magnetoresistance and interlayer coupling in Co/Cu superlattices”. In: *Phys. Rev. B* 52 (6 Aug. 1995), pp. 4263–4274. DOI: 10.1103/PhysRevB.52.4263. URL: <https://link.aps.org/doi/10.1103/PhysRevB.52.4263>.
- [43] G. Li, H. Shen, Q. Shen, T. Li, and S. Zou. “Influence of Si buffer layer on the giant magnetoresistance effect in Co/Cu/Co sandwiches”. In: *Sci. China Ser. E-Technol. Sci.* 43.4 (2000), pp. 225–231. DOI: 10.1007/BF02916826.
- [44] T. Li, H. L. Shen, Q. W. Shen, S. C. Zou, K. Tsukamoto, and M. Okutomi. “Effects of Ni buffer layer on giant magnetoresistance in Co/Cu/Co sandwich”. In: *J. Magn. Magn. Mater* 224.1 (2001), pp. 55–60. ISSN: 0304-8853. DOI: [https://doi.org/10.1016/S0304-8853\(00\)01356-1](https://doi.org/10.1016/S0304-8853(00)01356-1). URL: <https://www.sciencedirect.com/science/article/pii/S0304885300013561>.
- [45] D. Paccard, C. Schlenker, O. Massenet, R. Montmory, and A. Yelon. “A New Property of Ferromagnetic-Antiferromagnetic Coupling”. In: *physica status solidi (b)* 16.1 (1966), pp. 301–311. DOI: <https://doi.org/10.1002/pssb.19660160131>. eprint: <https://onlinelibrary.wiley.com/doi/pdf/10.1002/pssb.19660160131>. URL: <https://onlinelibrary.wiley.com/doi/abs/10.1002/pssb.19660160131>.

-
- [46] A. V. Silva, D. C. Leitao, J. Valadeiro, J. Amaral, P. P. Freitas, and S. Cardoso. “Linearization strategies for high sensitivity magnetoresistive sensors”. In: *Eur. Phys. J. Appl. Phys.* 72.1 (2015), p. 10601. DOI: [10.1051/epjap/2015150214](https://doi.org/10.1051/epjap/2015150214). URL: <https://doi.org/10.1051/epjap/2015150214>.
- [47] M. Julliere. “Tunneling between ferromagnetic films”. In: *Physics Letters A* 54.3 (1975), pp. 225–226. ISSN: 0375-9601. DOI: [https://doi.org/10.1016/0375-9601\(75\)90174-7](https://doi.org/10.1016/0375-9601(75)90174-7). URL: <https://www.sciencedirect.com/science/article/pii/0375960175901747>.
- [48] T. Miyazaki and N. Tezuka. “Giant magnetic tunneling effect in Fe/Al₂O₃/Fe junction”. In: *Journal of Magnetism and Magnetic Materials* 139.3 (1995), pp. 231–234. ISSN: 0304-8853. DOI: [https://doi.org/10.1016/0304-8853\(95\)90001-2](https://doi.org/10.1016/0304-8853(95)90001-2). URL: <http://www.sciencedirect.com/science/article/pii/0304885395900012>.
- [49] S. S. P. Parkin, C. Kaiser, A. Panchula, P. M. Rice, B. Hughes, M. Samant, and S. H. Yang. “Giant tunnelling magnetoresistance at room temperature with MgO (100) tunnel barriers”. In: *Nature Materials* 3.12 (Dec. 2004), pp. 862–867. ISSN: 1476-4660. DOI: [10.1038/nmat1256](https://doi.org/10.1038/nmat1256). URL: <https://doi.org/10.1038/nmat1256>.
- [50] S. Ikeda, J. Hayakawa, Y. Ashizawa, Y. M. Lee, K. Miura, H. Hasegawa, M. Tsunoda, F. Matsukura, and H. Ohno. “Tunnel magnetoresistance of 604% at 300K by suppression of Ta diffusion in CoFeB/MgO/CoFeB pseudo-spin-valves annealed at high temperature”. In: *Applied Physics Letters* 93.8 (2008), p. 082508. DOI: [10.1063/1.2976435](https://doi.org/10.1063/1.2976435). eprint: <https://doi.org/10.1063/1.2976435>. URL: <https://doi.org/10.1063/1.2976435>.
- [51] J. G. Deak, Z. Zhou, and W. Shen. “Tunneling magnetoresistance sensor with pT level 1/f magnetic noise”. In: *AIP Advances* 7 (2017), p. 056676. DOI: [10.1063/1.3701277](https://doi.org/10.1063/1.3701277). URL: <http://dx.doi.org/10.1063/1.3701277>.
- [52] R. Guerrero, M. Pannetier-Lecœur, C. Fermon, S. Cardoso, R. Ferreira, and P. P. Freitas. “Low frequency noise in arrays of magnetic tunnel junctions connected in series and parallel”. In: *Journal of Applied Physics* 105.11 (2009), p. 113922. DOI: [10.1063/1.3139284](https://doi.org/10.1063/1.3139284). eprint: <https://doi.org/10.1063/1.3139284>. URL: <https://doi.org/10.1063/1.3139284>.
- [53] Z. Jin, Y. Wang, K. Fujiwara, M. Oogane, and Y. Ando. “Detection of Small Magnetic Fields Using Serial Magnetic Tunnel Junctions with Various Geometrical Characteristics”. In: *Sensors* 20.19 (2020). ISSN: 1424-8220. DOI: [10.3390/s20195704](https://doi.org/10.3390/s20195704). URL: <https://www.mdpi.com/1424-8220/20/19/5704>.
- [54] Z. Jin, M. A. I. Mohd Noor Sam, M. Oogane, and Y. Ando. “Serial MTJ-Based TMR Sensors in Bridge Configuration for Detection of Fractured Steel Bar in Magnetic Flux Leakage Testing”. In: *Sensors* 21.2 (2021). ISSN: 1424-8220. DOI: [10.3390/s21020668](https://doi.org/10.3390/s21020668). URL: <https://www.mdpi.com/1424-8220/21/2/668>.
- [55] R. Ferreira, E. Paz, P. P. Freitas, J. Ribeiro, J. Germano, and L. Sousa. “2-Axis Magnetometers Based on Full Wheatstone Bridges Incorporating Magnetic Tunnel Junctions Connected in Series”. In: *IEEE Transactions on Magnetics* 48.11 (2012), pp. 4107–4110. DOI: [10.1109/TMAG.2012.2202381](https://doi.org/10.1109/TMAG.2012.2202381).
- [56] M. Sun, T. Kubota, S. Takahashi, Y. Kawato, Y. Sonobe, and K. Takanashi. “Buffer layer dependence of magnetoresistance effects in Co₂Fe_{0.4}Mn_{0.6}Si/MgO/Co₅₀Fe₅₀ tunnel junctions”. In: *AIP Adv.* 8 (2018), p. 055902. DOI: [10.1063/1.5007766](https://doi.org/10.1063/1.5007766). URL: <https://doi.org/10.1063/1.5007766>.
- [57] M. Sun, T. Kubota, Y. Kawato, S. Takahashi, A. Tsukamoto, Y. Sonobe, and K. Takanashi. “Buffer-Layer Dependence of Interface Magnetic Anisotropy in Co₂Fe_{0.4}Mn_{0.6}Si Heusler Alloy Ultrathin Films”. In: *IEEE Trans. Magn.* 53.11 (2017), pp. 1–4. DOI: [10.1109/TMAG.2017.2728627](https://doi.org/10.1109/TMAG.2017.2728627).
-

- [58] MultiDimension. *Application Note TMR91xx*.
- [59] N. A. Stutzke, S. E. Russek, D. P. Pappas, and M. Tondra. “Low-frequency noise measurements on commercial magnetoresistive magnetic field sensors”. In: *Journal of Applied Physics* 97.10 (2005), 10Q107. DOI: 10.1063/1.1861375. eprint: <https://doi.org/10.1063/1.1861375>. URL: <https://doi.org/10.1063/1.1861375>.
- [60] T. McGuire and R. Potter. “Anisotropic magnetoresistance in ferromagnetic 3d alloys”. In: *IEEE Transactions on Magnetism* 11.4 (1975), pp. 1018–1038. DOI: 10.1109/TMAG.1975.1058782.
- [61] W.Y. Lee, M.F. Toney, and D. Mauri. “High magnetoresistance in sputtered Permalloy thin films through growth on seed layers of $(\text{Ni}_{0.81}\text{Fe}_{0.19})_{1-x}\text{Cr}_x$ ”. In: *IEEE Transactions on Magnetism* 36.1 (2000), pp. 381–385. DOI: 10.1109/20.822551.
- [62] Honeywell. *1- and 2-Axis Magnetic Sensors HMC1001/1002/1021/1022*. 2008.
- [63] Yole Développement. *Magnetic sensor market: the increasing adoption of the xMR technologies*. 2017. URL: http://www.yole.fr/Magnetic_Sensor_TechnologyOverview.aspx#.YQdGozqxXZ4 (visited on 08/02/2021).

Chapter II

AMR LSMO Sensor

This chapter will elucidate why $\text{La}_{1-x}\text{Sr}_x\text{MnO}_3$ (LSMO) was the chosen material for developing low noise AMR sensors, with a target biomedical application. As previously introduced, biological signal can be in low frequency range, below 1 kHz, and of very small amplitude. Therefore low values for detectivity are needed. LSMO not only presents magnetoresistive properties (thus can be exploited for sensor design), but also a very low intrinsic noise. Although the underlying phenomena found in LSMO are introduced, deeper explanations can be found in an extensive review of mixed-valence manganites by Coey *et al* [1]. The terms resistivity and electrical resistivity are interchangeable throughout this work.

The chapter starts by presenting material properties and crystalline structure, along with an explanation of the double-exchange conduction mechanism. It is followed by an introduction to uniaxial magnetic anisotropy and magnetic energy according to Stoner-Wohlfarth model, and an explanation on how such anisotropy can be induced in LSMO thin films by using vicinal substrates. Then, equations for anisotropic magnetoresistance are developed based on different geometries for LSMO stripes, and experimental data are presented that meet the expected behavior. The next section is focused on electrical noise: how to properly measure such low voltage values using an preamplifier circuit adapted to the device and noise sources in LSMO. The Wheatstone bridge configuration is evoked thanks to its capability of rejecting common-mode signals. Finally, all the supporting work is used to validate the operation of LSMO Wheatstone bridges as AMR sensors, showing magnetization loops and sensor output with numerical modeling based on presented equations. After a brief comment on the equivalent noise of a Wheatstone bridge, this chapter concludes by introducing the equation for the detectivity of the device, which leads to a chapter focused on performance optimization.

2.1 $\text{La}_{2/3}\text{Sr}_{1/3}\text{MnO}_3$

Mixed-valence manganese oxides attracted the attention of the research community thanks to its rich electronic and magnetic phases, leading to concepts such as the double-exchange mechanism and Jahn-Teller polarons. Those unusual properties are due to the metal-oxygen bonds and strong electron correlations. Such interactions can result in the ordering of spins, an essential property for spintronics devices. Plus, parameters such as temperature, pressure and strain affect material's properties, turning them useful for sensing applications, as they can be made into transducers. Particularly, the research community was drawn to perovskites since the discovery of high-temperature superconductors. A perovskite general formula is ABO_3 , where cations A and B occupy simple cubic and body centered cubic while oxygen occupies face-centered cubic crystalline structures. The 6 oxygen atoms surrounding cation B form an octahedral network, and in an ideal perovskite all the bonds B - O are equal and bond angle B - O - B is 180° . But depending on the radius of a dopant cation, the perovskite will present only a pseudo-cubic structure, which

can be orthorhombic, rhombohedral, triclinic, etc.

The concentration and radius of a dopant cation will affect the physical and structural properties of a manganite perovskite [2, 3]. The material used in this work, $\text{La}_{1-x}\text{Sr}_x\text{MnO}_3$ (LSMO), present a variation of crystalline structure, electric and magnetic properties depending on strontium dopant concentration [4], as it can be seen in its phase diagram Fig. C.3(a). With a similar structure to $\text{La}_{1-x}\text{Ca}_x\text{MnO}_3$, LSMO is a half-metal with only spin-up electrons above the Fermi energy and an insulating bandgap for spin-down states [5]. This fully spin-polarised conduction band makes LSMO an interesting case of study for transport mechanisms and spintronics. The bulk of this work was carried using LSMO with a dopant concentration of $x = 1/3$, due to ferromagnetic behaviour with highest Curie temperature. Such behaviour is explained by the double-exchange mechanism. With Sr dopant concentration of $x = 1/3$, the rhombohedral perovskite structure can be seen as a pseudocubic crystal, as in the case of BiFeO_3 presented in Fig. 2.1(b).

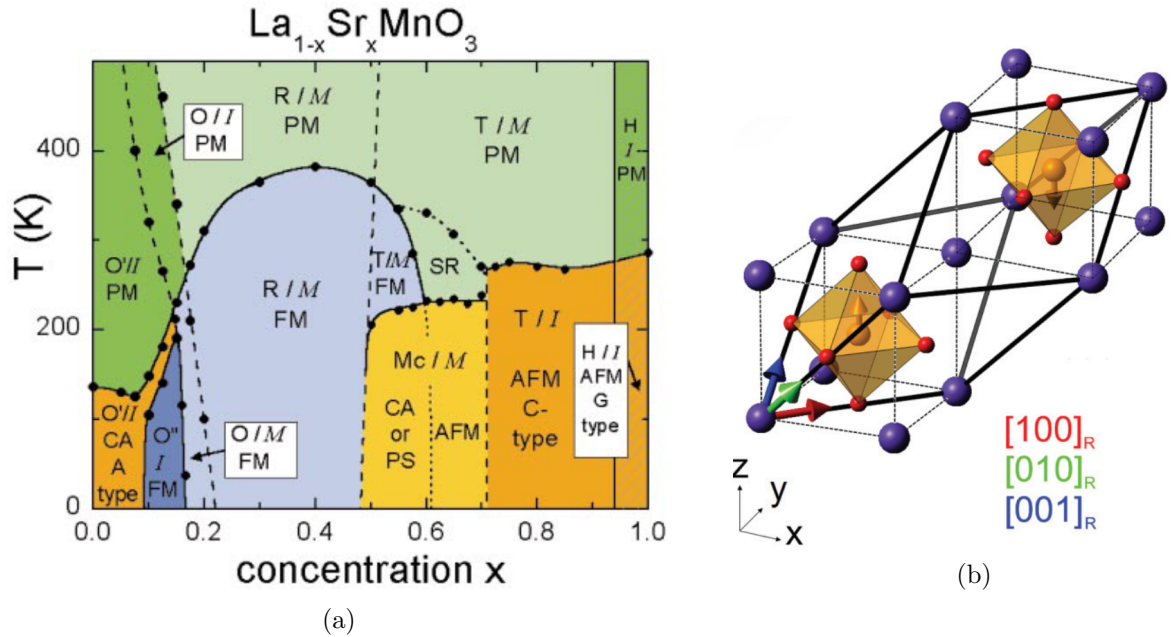


Figure 2.1: a) LSMO phase diagram according to dopant concentration. The crystal structures are orthorhombic O , Jahn-Teller distorted orthorhombic O' , orbital-ordered orthorhombic O'' , rhombohedral R , tetragonal T , monoclinic Mc and hexagonal H . The magnetic structures are paramagnetic PM , short-range order SR , canted CA , A -type antiferromagnetic AFM , ferromagnetic FM , phase-separated PS and AFM C -type. The electronic states are insulating I and metallic M . LSMO is ferromagnetic and presents rhombohedral structure with $x = 1/3$. From [4]. b) Transformation from rhombohedral unit cell (thick lines) to pseudocubic structure (thin lines). From [6].

2.1.1 Double-exchange mechanism and epitaxial strain

Electrical conductivity and ferromagnetic behavior in $\text{La}_{0.7}\text{Sr}_{0.3}\text{MnO}_3$ are highly tied and can be explained thanks to the *double-exchange* (DE) mechanism proposed by Zener [7]. In manganites with $\text{La}_{1-x}\text{A}_x\text{MnO}_3$ composition, where A represents Ca, Sr or Ba, materials were not good conductors neither ferromagnetic with zero or complete doping, $x = 0, 1$. Ferromagnetism was verified only when $0.2 < x < 0.4$ [8]. Also, oxygen atoms presented always a $2-$ charge regardless of atom A and x value. So if $x = 0$, the obtained manganite composition is $\text{La}^{3+}\text{Mn}^{3+}\text{O}_3^{2-}$. When La atoms are substituted by Sr dopants that present only two electrons in the outer shell, the same number of Mn atoms must present a $4+$ charge. This ensures the proper charge balance of the composition. Pure LaMnO_3 is a semiconductor, and what gives rise to the electrical conductivity in doped

composition is a Mn^{4+} ion capturing an electron from a neighboring Mn^{3+} . Charge is carried by holes, but the same development can be made for electrons. Considering localized atomic orbitals, there is no appreciable overlapping between Mn atoms as they are far apart, separated by an oxygen atom. The underlying mechanism is an indirect coupling through O^{2-} ion. One electron from Mn^{3+} cation is transferred to oxygen while simultaneously the Mn^{4+} receives an electron from the same anion, as shown in Fig. 2.2. Also, thanks to the presence of two Mn ions, the system would be degenerate. There

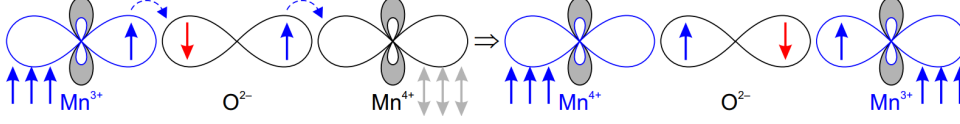


Figure 2.2: Simultaneous transfer between two manganese and one oxygen atoms. This interaction is favored with alignment of spins, causing a ferromagnetic behavior. From [9].

are two electronic configurations that present the same energy level: when one ion has spin up and the other spin down. Thanks to a large Hund's rule coupling [10], the lowest energy level of the system is achieved when the spins of both Mn d -shells are aligned. Therefore DE mechanism provokes a ferromagnetic alignment, and lining up the spins of Mn outer shells increase the probability of electron transfer. Thus, with aligned spins there is an increase in electrical conductivity. Finally, an expression to link ferromagnetism and electrical conductivity was proposed by Zener and is presented in Eq. (2.1) as

$$\sigma \approx (xe^2/ah)(T_C/T) \quad (2.1)$$

in which σ is the electrical conductivity, e is the electron charge, x the fraction of Mn^{4+} ions, a the lattice parameter, h is Planck's constant, T_C is the Curie temperature and T is the temperature of the material. As the DE mechanism is responsible for electrical transport and ferromagnetism behavior, both are linked. Indeed, LSMO presents metal-to-insulator temperature T_{MI} close to T_C . Near the temperature that causes a sudden increase in electrical resistivity, this manganite loses its ferromagnetic properties. The increase of thermal energy wins over alignment of spins and double-exchange is nullified. Variations in the probability that an electron will hop from one Mn atom to another affect both properties. The Mn-O-Mn bond and electron hopping probabilities will not only vary with Sr dopant concentration x , but also by strain present in the perovskite crystalline structure. Electrical transport and magnetic properties are thus highly dependent of strain in manganite thin films, and one method of selecting the biaxial strain is by performing epitaxial deposition over compatible substrates with a lattice mismatch [11, 12, 13]. Bulk LSMO is a perovskite lattice that can be described as a pseudocubic with little deformation, presenting lattice parameter $a_{bulk} = 0.3876$ nm and with cell angle of 90.26° . The substrate used in this work, SrTiO_3 (STO), presents a cubic structure with $a = 0.3905$ nm, so the lattice misfit is of $+0.75\%$ and induces biaxial tensile strain in LSMO thin film [14]. Milis *et al* [15] proposed a T_C dependence on strain for manganites. The origin of such dependence is a bulk compression ε_B , which tends to increase the electron hopping probability, and a biaxial distortion ε_{JT} , related to the Jahn-Teller splitting [10]. The interaction between the charge carrier and the crystalline lattice is manifested as polarons that tends to localize the electrons by deforming the geometry of the system, in order to reduce its symmetry and energy [16]. For a cubic symmetry, the strain parameters can be written as

$$\begin{aligned} \varepsilon_B &= \frac{1}{3} (2\varepsilon_{\parallel} + \varepsilon_{\perp}) \\ \varepsilon_{JT} &= \frac{1}{2} (\varepsilon_{\perp} - \varepsilon_{\parallel}) \end{aligned} \quad (2.2)$$

where ε_{\parallel} and ε_{\perp} are the in-plane and out-of-plane strains, respectively. Both are coupled through Poisson's ratio $\nu = 1/(1 - 2\varepsilon_{\parallel}/\varepsilon_{\perp})$, with an estimated value of $\nu = 0.37$ for

LSMO [17, 18, 19]. So the dependence of T_C on strain for LSMO thin films is, from [18],

$$T_C(\varepsilon_B, \varepsilon_{JT}) = T_C^0 \left(1 - \alpha \varepsilon_B - 0.5 \Delta \varepsilon_{JT}^2 \right)$$

where

$$\alpha = \frac{1}{T_C^0} \frac{dT_C}{d\varepsilon_B} \tag{2.3}$$

$$\Delta = \frac{1}{T_C^0} \frac{d^2T_C}{d\varepsilon_B^2}$$

The effect of strain on electrical transport and magnetic properties in LSMO has been studied, with published experimental results already available [17, 18, 20]. A decrease in T_C and T_{MI} is observed in LSMO thin films over STO when compared to bulk values when increasing biaxial in-plane strain. Plus, a relaxation of LSMO film over STO is observed only above critical thickness $t_c = 100$ nm, and a dependence of t_c on biaxial strain can be presented as $t_c[\text{nm}] = 86/\varepsilon_{\parallel}[\%]$ [19].

2.2 Uniaxial magnetic anisotropy in LSMO

In the previous section, the origin of electrical conductivity and ferromagnetism in half-metallic oxide LSMO thin films was highlighted, and how those properties are affected by biaxial strain in the thin film. Now, we shall see how magnetic anisotropy and magnetization behavior can be exploited to achieve a linear response with the applied magnetic field. Such linear variation is desired for sensing applications. Should we be interested in effects of a local magnetic field amplitude regardless of its direction, a linear and isotropic magnetization satisfies. But several factors are responsible for inducing a preferential direction for magnetization alignment. This break of symmetry can have its origins in magnetocrystalline, magneto-elastic, exchange interaction, and shape contributions. A material with a single preferential direction is referred to as *uniaxial*, and with two preferential directions as *biaxial*. A model to predict the magnetization behavior of a material presenting uniaxial magnetic anisotropy was proposed by Stoner and Wohlfarth. As we will see, a linear dependence of magnetization is obtained when the magnetic field is applied perpendicular to such preferential direction.

When in bulk, LSMO has a biaxial anisotropy due to magnetocrystalline effect. As previously mentioned, the material is a pseudocubic crystal. Therefore, the anisotropy is cubic, with three orthogonal preferential directions. This preferential direction for magnetization alignment is known as magnetic *easy axis* (e.a.). There are several ways to induce such anisotropy in ferromagnetic materials for MR devices: it can be created by exchange-bias with a secondary layer and magnetic field during deposition [21], induced by shape [22] thanks to exchange and demagnetizing energies or by interaction with the substrate. As previously mentioned, the break of symmetry can also be induced by strain in the crystalline structure of the film, when performing epitaxial deposition over a substrate with a different lattice parameter. This affects the angle and distance of interatomic bonds in the thin film, thus changing orbitals occupation. In fact, it is possible to completely break or remove some bonds, by performing epitaxial deposition over a substrate with terraces and steps in its crystalline structure [23]. This was the alternative exploited in the present work. The theory for magnetization reversal in a single domain magnetic particle with uniaxial anisotropy will now be presented, and then how such anisotropy can be induced in LSMO thin films by using vicinal substrates.

2.2.1 Stoner-Wohlfarth model

The simplest model for hysteresis in a magnetic material consists in considering a magnetic particle that presents a single magnetization easy axis. Its magnetic energy

density can be written as [24]

$$E = K_u \sin^2 \theta - \mu_0 H M_S \cos(\theta - \gamma) \quad (2.4)$$

where θ is the angle between magnetization M and easy axis, K_u is the effective uniaxial anisotropy constant of whatever origin and γ is the angle between applied field H and easy axis. The term M_S is the magnetization saturation. For a given γ , minimizing Eq. (2.4) yields one or two energy minima, and magnetic hysteresis is present when there are two minima in the energy configuration. The jump from one state of minimum energy to another is irreversible and occurs at $d^2 E/d\theta^2 = 0$. The shape of the hysteresis curve depends on the angle γ , and extremes are a perfect square when field is parallel to easy axis or a linear dependence when $\gamma = 90^\circ$. In the latter case, the energy density expression is

$$E = K_u \sin^2 \theta - \mu_0 H M_S \sin \theta \quad (2.5)$$

and an analytical dependence for angle θ can be obtained when minimizing energy. By doing $\frac{\partial E}{\partial \theta} = 0$, it yields

$$\theta = \arcsin\left(\frac{\mu_0 H M_S}{2K_u}\right) \quad (2.6)$$

and here the term *anisotropy field* H_a is defined as

$$H_a = \frac{2K_u}{\mu_0 M_S} \quad (2.7)$$

which is the necessary field to apply perpendicular to easy axis so sample reaches magnetization saturation. This direction perpendicular to easy axis is also known as hard axis. Experimentally, it can be obtained by measuring $M(H)$ curves and verifying at which applied field the magnetization saturates. The presented analytical approach is limited to $|H| \leq H_a$. Using the expression for H_a , Eq. (2.4) can be rewritten to obtain an equation for the dimensionless magnetic energy:

$$\frac{E}{2K_u} = \frac{1}{2} \sin^2 \theta - \frac{H}{H_a} \cos(\theta - \gamma) \quad (2.8)$$

which can be used to minimize energy considering only the ratio of applied field over anisotropy field, applied field direction and magnetization direction. This will be specially useful for numerical solutions. In practice, it is impossible to dissociate magnetization direction θ and H/H_a ratio. Let's consider the case when the applied magnetic field H is not perfectly perpendicular to sample easy axis. This is expressed as a deviation δ in H direction as $\gamma = 90^\circ + \delta$. A small deviation of few degrees gives rise to a weak field component parallel to easy axis. Because of this component along easy axis, the magnetic energy landscape of the system is affected. Also, it is no longer possible to use the analytical expression of Eq. (2.6) to estimate angle θ , and we must resort to a numerical solution by minimizing the dimensionless magnetic energy. Figure 2.3 shows the evolution of magnetic energy curves for the case $\delta = 0^\circ$ and $\delta = 3^\circ$. Considering an initial saturated state with $\theta = -90^\circ$, the right-hand side of Eq. (2.8) is plotted as a function of θ for increasing positive and arbitrary values of H/H_a ratio. When there is no deviation, two minima of equal values are symmetrically apart from $\theta = 90^\circ$, with an energy barrier between both points. As H increases, θ rotates to higher positive angle and the equilibrium point is the first minimum that is reached. As applied field approaches H_a , the energy barrier decreases and the minima meet at $\theta = 90^\circ$ when H reaches anisotropy field value. But if a deviation of few degrees is present, the two minima no longer present the same energy level. For small values of applied field, the energy barrier is still present, and equilibrium point is obtained for $\theta < 90^\circ$. But when H reaches a critical value, the energy barrier disappears and a single minimum is present in the energy curve. The

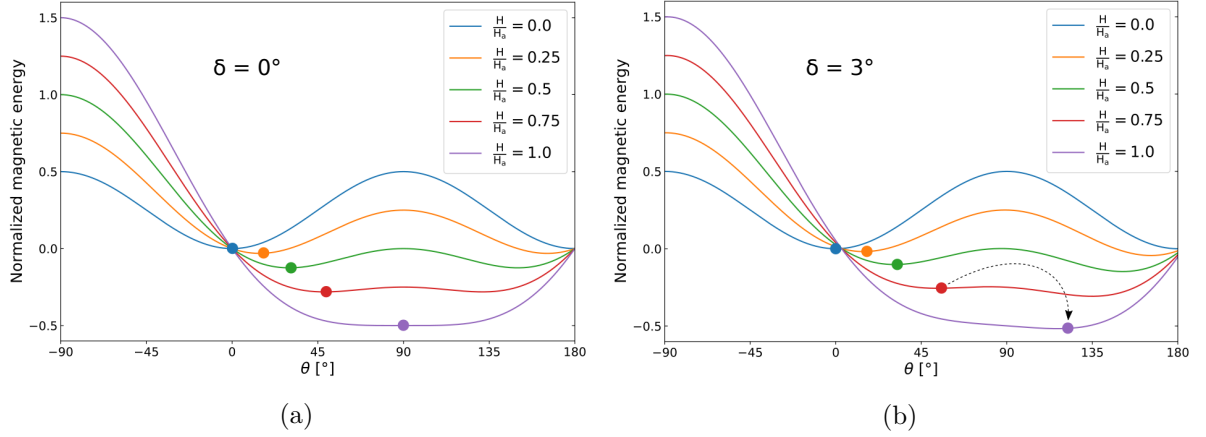


Figure 2.3: Evolution of dimensionless magnetic energy for increasing positive field, with $\gamma = 90^\circ$. Dots indicate the energy equilibrium point. a) Applied field perpendicular to easy axis. b) Small deviation of $\delta = 3^\circ$, provoking a sudden jump in magnetization direction.

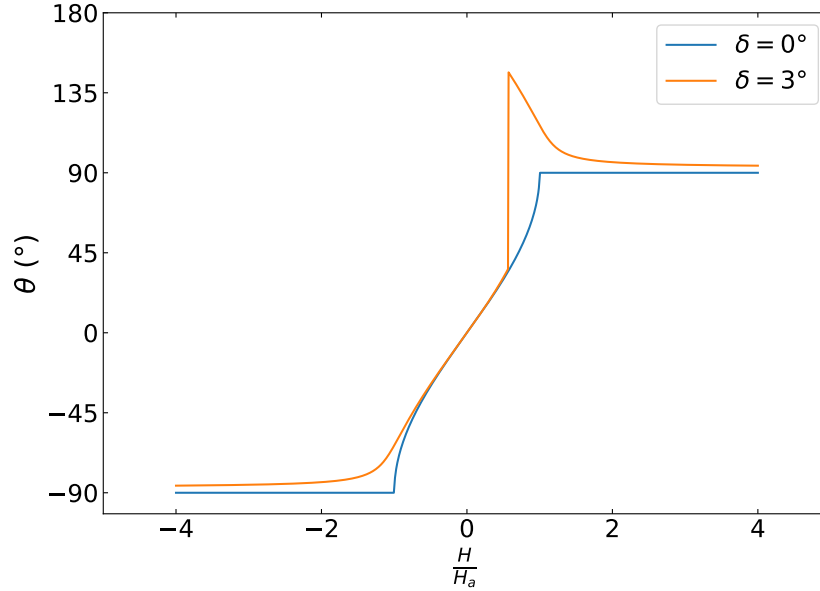


Figure 2.4: θ values obtained by numerical minimization of dimensionless magnetic energy. Jump in magnetization direction when $\delta = 3^\circ$ as a single minimum is present in the energy curve.

equilibrium point of the system is suddenly at $\theta > 90^\circ$, and magnetization direction undergoes a fast switch. Figure 2.4 shows with a numerical minimization of Eq. (2.8) the obtained values for θ for different H/H_a ratios. To obtain the presented θ value, the dimensionless magnetic energy was numerically minimized for each H/H_a value of an evenly distributed set using Brent's algorithm [25]. This method combines the bisection method, secant method and inverse quadratic interpolation to find the root of a function. Limits for θ are added to bound the converged result. Corresponding γ values are kept fixed for the whole curve. Such change in θ will be reflected in the output signal of the anisotropic magnetoresistance device, as the resistance value depends on magnetization direction. Later in this chapter, this method will be used to fit a numerical model of the expected output of AMR LSMO devices to the experimental measurements. A good agreement between the fit and experimental data shall validate the assumption of a single domain magnetic particle and the use of the Stoner-Wohlfarth model. Sections of the model implemented in Python language are available in Appendix Characterization.

2.2.2 Uniaxial anisotropy with vicinal substrate

The Stoner-Wohlfarth model considers a single magnetic anisotropy axis, known as easy axis. As previously mentioned, uniaxial anisotropy is required to have a linear response of magnetization with applied field amplitude, when the latter is in the hard axis direction. A linear behavior for magnetization translates to a linear output of the AMR sensor. Thus, it is essential to correctly induce this easy axis in the magnetic active material. The most common methods are by etching the film in a specific geometry to induce shape anisotropy, by applying a magnetic field during film deposition or by exchange bias interaction with an antiferromagnet layer. An established method for obtaining uniaxial magnetic anisotropy in LSMO thin films is by performing thin film deposition over substrates that present terraces separated by steps [26, 27]. A possible mean to obtain such structure is to perform a miscut at substrate surface. Such substrates are referred to as vicinal substrates. Terraces and steps are formed by performing surface polishing at a miscut angle, known as vicinal angle. The step density, related to the distance between adjacent steps, increases with the vicinal angle. The rise of anisotropy can be explained by a modified Néel model of surface anisotropy [28], which presents an additional term in anisotropy energy that arises due to broken or missing bonds at the step edges and strain in the remaining bonds [29]. Chuang *et al* presented a simple relation of the magnetic energy of a system composed of thin films over vicinal substrates as

$$E_{film} = E_{bulk} - 2 \cdot \frac{E_{surface}}{t} - 2 \cdot \frac{E_{edge} + E_{corner}}{t \cdot d} \quad (2.9)$$

where t is thin film thickness and d is the terrace width, the distance between steps. This so-called step-induced anisotropy can cause an easy axis either parallel or perpendicular to step edges, depending on the elements that make up the system. The dominance of this effect can be verified if the anisotropy is affected or not by thin film thickness [30]. According to Eq. (2.9), a reduction in uniaxial anisotropy with increased film thickness is not directly linked to strain relaxation over film growth. Some published experimental results show that thickness of LSMO layer does influence the magnetic properties of the sample [31, 23], therefore uniaxial anisotropy is dominated by surface anisotropy in vicinal substrate and not by film strain. As already mentioned, strain relaxation of LSMO film over STO starts above 100 nm thickness. Also, substrates with higher vicinal angles shall result in a stronger anisotropy, thanks to lower d [32, 33]. For the case of LSMO, it was shown that the use of vicinal substrates also affects magnetoresistance ratio, which increases when compared to a flat STO substrate [34]. XRD scans were performed on LSMO/STO for different vicinal angles and smaller terrace width was measured for increased angle [35], with no dependence on thin film thickness.

By performing $\theta - 2\theta$ scans with X-Ray Diffraction (XRD) technique, it is possible to verify if the thin film presents the same offset as the substrate due to the vicinal cut. Then, the rocking curve for LSMO indicates the quality of the film. To do so, a ω scan was first performed using the (200) STO peak of $2\theta = 46.5^\circ$. With the adjustment of the offset, a full 2θ scan is performed, and peaks for STO and LSMO are found. The position of LSMO peak is affected by the in-plane strain imposed by the substrate, as the lattice parameter changes. Then a second ω scan is performed around the obtained 2θ for LSMO, and a gaussian fit is performed over the measured rocking curve. The Full Width at Half Maximum (FWHM) of the fit indicates crystalline quality. In Fig. 2.5 XRD curves from a 30 nm thick LSMO sample deposited over 4° vicinal substrate are presented. The obtained offset for scan was of 4.7° , within acceptable deviation according to substrate datasheet ($\pm 0.5^\circ$) and manually placing sample over sample holder. This result confirms that our fabricated LSMO samples undergo epitaxial deposition over vicinal STO. Images obtained with Atomic Force Microscopy (AFM) also indicate a surface presenting step and terraces, as showed in Fig. 2.6 with a profile scan along the LSMO surface. Therefore, uniaxial magnetic anisotropy induced by substrate steps is expected in the samples fabricated during this work.

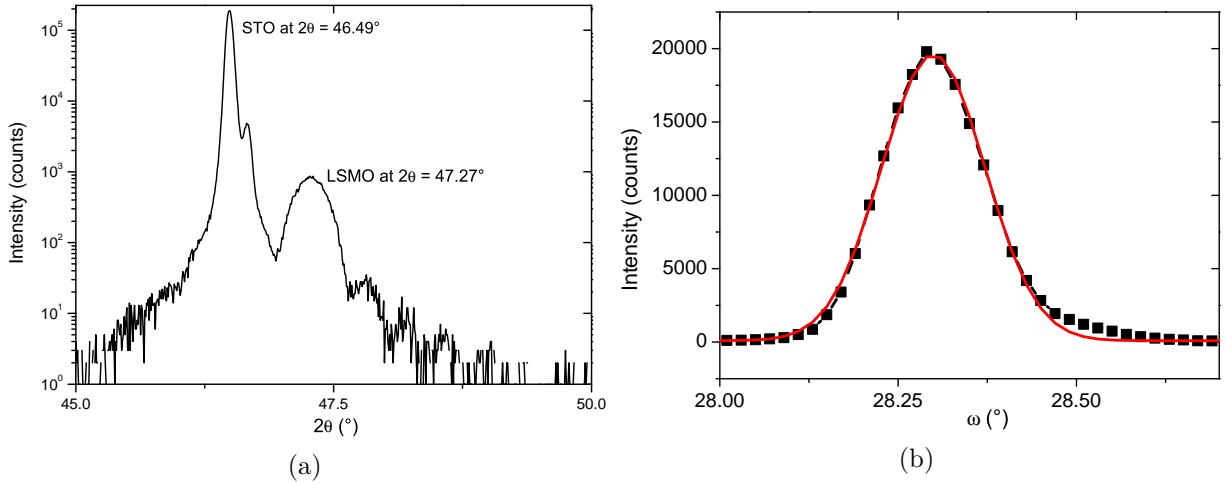


Figure 2.5: Structural analysis of LSMO thin film over vicinal STO. (a) 2θ scan and (b) LSMO rocking curve. FWHM of 0.17° indicates high crystalline quality. [Sample BA143]

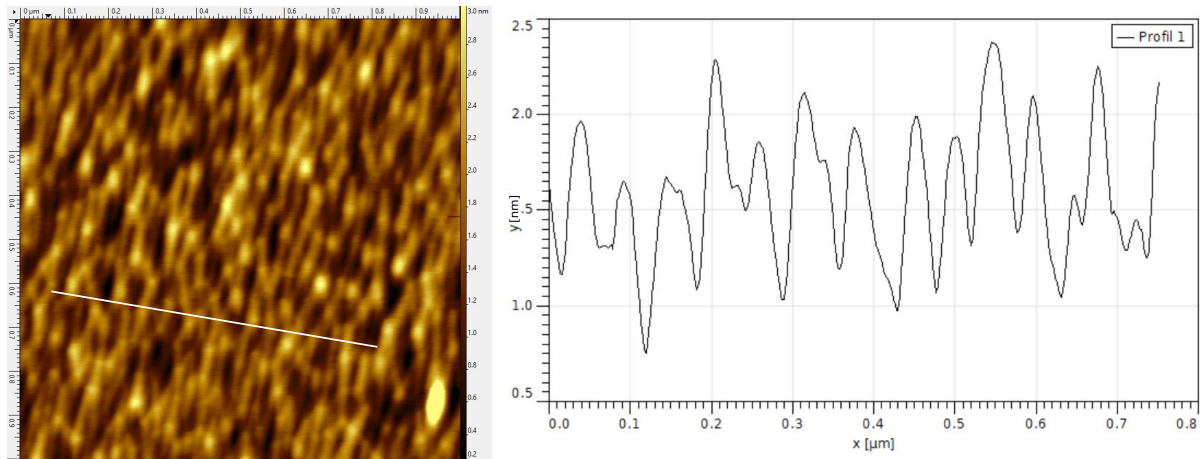


Figure 2.6: AFM image obtained in tapping mode, 45 nm LSMO deposited over 4° vicinal STO. White line indicates the zone of the profile scan. [Sample BA068]

The magnetization loops of a single 60 nm LSMO thin film stripe on 8° vicinal STO can be seen in Fig. 2.7. Such curves were obtained with a Magneto-optical Kerr Effect (MOKE) imaging system built at GREYC. The system is configured in the longitudinal mode of operation, providing the component of the in-plane magnetization along the direction of the applied magnetic field. The system is more thoroughly described in Appendix Characterization. Magnetization loops are obtained from the images, using a differential technique. First image is obtained at negative magnetization saturation and acts as a background value to be subtracted from coming images. Images are in gray levels, and as magnetization rotates away from initial state, magnetic active area becomes darker. The darkest image is obtained at positive magnetization saturation. When applied field is swept back to negative values, magnetic material once again presents a lighter gray level. By averaging the gray level over a magnetic area and dividing it by the average gray level of a non-magnetic area, we obtain the magnetization ratio. Then after proper normalization, a $M/M_S(\mu_0 H)$ curve is obtained.

When magnetic field is applied parallel to substrate step edges, a typical square hysteresis magnetization loop is obtained. This indicates the direction of the easy axis, with nucleation and propagation of magnetic domains demonstrated by the fast surge of dark areas in MOKE images. When sample is rotated by 90° , a gradual darkening of magnetic area on MOKE images is obtained. This corresponds to a magnetization with linear dependence on applied field and hysteresis-free curve, indicating a coherent

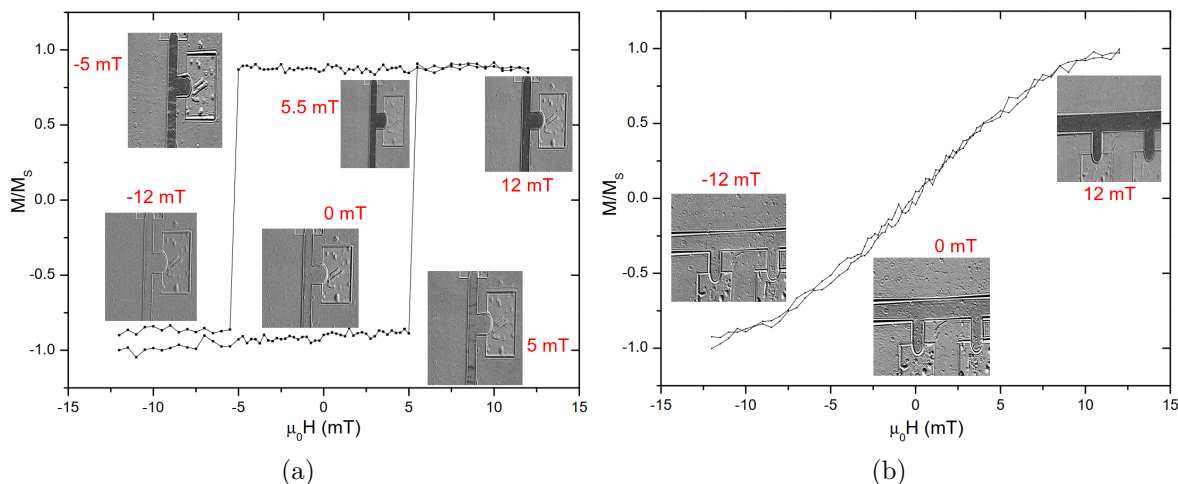


Figure 2.7: Magnetization loops obtained from MOKE images. Selected images surround the curves, with the indication of field value. a) Easy axis direction, showing nucleation of magnetic domains. b) Field applied along hard axis, causing a rotation of magnetization. [Sample BA137]

magnetization reversal. The hard axis direction is then perpendicular to the step edges of the vicinal substrate. Therefore, this shows that we obtain high quality epitaxial thin films on top of vicinal substrates. To measure the presence of a steps and terraces structure on the LSMO surface is at the limit of the available AFM system. Now, discussion will move to the anisotropic magnetoresistance effect itself and how it is measured.

2.3 Anisotropic Magnetoresistance

As mentioned in the introductory chapter, magnetoresistance is the property of a material when its electrical resistivity changes with the presence of a magnetic field. When the measured resistivity variations depend on the direction of applied field or current density direction, the material is said to present anisotropic magnetoresistance.

Thanks to double-exchange mechanism, electrical transport and magnetization state are directly linked in LSMO. The AMR effect is the resistivity dependence on magnetization and current density directions on the same material, and it is explained by a spin-orbit interaction on the $s - d$ orbitals. An in-depth analysis on the origin of AMR for metals and half-metal ferromagnets was performed by Kokado *et al* [36]. LSMO as a half-metallic ferromagnet presents an AMR ratio with inverted behavior when compared to permalloy, another material widely used for AMR sensors. This ratio is defined as the difference between electrical resistance when current density and magnetization are parallel and when they are perpendicular. LSMO sample resistance is higher when magnetization and current density directions are perpendicular than when they are parallel [37]. By comparing the effects of dopant concentration and the modulation of charge density by electric field, it was shown that carrier concentration alone does not explain the changes in AMR by changing doping levels. The AMR effect for LSMO films seems to be dominated by lattice distortion [38]. Although a proper theory for AMR in manganites is not yet fully developed, direct observation of magnetization reversal and magnetoresistance at room temperature show this effect in LSMO thin films [39].

2.3.1 Resistance of single stripes

Consider an in-plane single domain ferromagnetic material that presents anisotropic magnetoresistance with a single easy axis of magnetization. The passage of a vector current density J will create a vector electric field E through the resistivity tensor ρ , following the

expression $E = [\rho]J$. Let θ be the angle between the magnetization vector M and the easy axis. The resistivity tensor is given by

$$\rho = \begin{bmatrix} \rho_{\perp} - \Delta\rho \cdot \cos^2 \theta & -\frac{1}{2}\Delta\rho' \cdot \sin(2\theta) \\ -\frac{1}{2}\Delta\rho' \cdot \sin(2\theta) & \rho_{\perp} - \Delta\rho \cdot \sin^2 \theta \end{bmatrix} \quad (2.10)$$

where $\Delta\rho = \rho_{\perp} - \rho_{\parallel}$, ρ_{\perp} is the resistivity when magnetization is perpendicular to the easy axis and ρ_{\parallel} is the resistivity when magnetization is parallel to said axis. We consider the X-axis to be the easy magnetization axis of the domain. In the present work $\Delta\rho$ was defined as such to have a positive value. We also define ρ_0 as the mean resistivity value, $\rho_0 = (\rho_{\parallel} + \rho_{\perp})/2$. The main diagonal terms are coined as the usual AMR effect and the antidiagonal terms are coined as *planar Hall effect* (PHE) [40, 41]. The latter causes a voltage difference transversal to the passing current, similar to the usual Hall effect when a magnetic field is applied perpendicular to the sample plane. The use of $\Delta\rho'$ is to account for possible differences in resistivity variations between AMR and PHE. Resistivity and its variation can present different values depending on the direction of applied current, according to the crystalline structure of the material. Differences in the distribution of atoms, electrons and the occupation of energy levels gives rise to such anisotropy in electrical conductivity. First, consider a ferromagnetic material with AMR effect and cubic crystalline structure. For a current density applied along the [001] crystalline direction, the resulting variation in the electric field $E = \rho J$ would be the same along said direction and orthogonal to it. Even though the LSMO structure is generally considered pseudo-cubic and epitaxial deposition can be performed on cubic STO, some deformations are indeed present. Such deformations could result in different values for resistivity variations between AMR and PHE terms. Although the term ‘‘planar Hall effect’’ is widely used, and it will be so in this work, its origin is entirely driven by anisotropic magnetoresistance [42]. Let α be the angle between the easy magnetization axis and the current density direction, as shown in Fig. 2.8. The scalar resistivity along the said direction is obtained by projecting the tensor on the unit vector $e_{\alpha} = (\cos \alpha, \sin \alpha)$, $(\rho \cdot e_{\alpha})e_{\alpha}$, and can be written as

$$\begin{aligned} \rho_{\alpha}(\theta, \alpha) &= (\rho_{\perp} - \Delta\rho \cdot \cos^2 \theta) \cdot \cos^2 \alpha \\ &+ (\rho_{\perp} - \Delta\rho \cdot \sin^2 \theta) \cdot \sin^2 \alpha \\ &- \frac{1}{2}\Delta\rho' \cdot \sin(2\theta) \cdot \sin(2\alpha) \end{aligned} \quad (2.11)$$

Therefore, for a given LSMO thin film with a established easy axis of magnetization, the

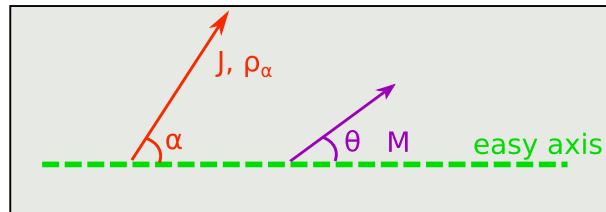


Figure 2.8: Schematic of arbitrary directions for magnetization and current density in an uniaxial anisotropy ferromagnetic material.

direction of current density affects how resistivity along the same direction will behave as a function of θ . When such thin film with thickness t is etched forming resistive stripes with length l and width w , the angle α is fixed. A substitution for sample electrical resistance can be done by $R(\theta, \alpha) = \rho_{\alpha}(\theta, \alpha)l(wt)^{-1}$. This work is focused on resistive stripes along 0° , 45° , 90° and 135° values for α .

First, by making $\alpha = 45^\circ$ and $\alpha = 135^\circ$ we obtain

$$\begin{aligned} R(\theta, 45^\circ) &= R_0 - \frac{1}{2}\Delta R' \sin(2\theta) \\ R(\theta, 135^\circ) &= R_0 + \frac{1}{2}\Delta R' \sin(2\theta) \end{aligned} \quad (2.12)$$

Maximum and minimum values for electrical resistance will be reached when magnetization is at a 45° or 135° from easy axis, depending on α .

$$\begin{aligned} R(45^\circ, 45^\circ) &= R_0 - \frac{1}{2}\Delta R' & R(135^\circ, 45^\circ) &= R_0 + \frac{1}{2}\Delta R' \\ R(45^\circ, 135^\circ) &= R_0 + \frac{1}{2}\Delta R' & R(135^\circ, 135^\circ) &= R_0 - \frac{1}{2}\Delta R' \end{aligned} \quad (2.13)$$

The variation ΔR^{45} of electrical resistance according to magnetization direction θ for such stripes is

$$\Delta R^{45} = \frac{1}{2}\Delta R' \sin 2\theta \quad (2.14)$$

and considering the Stoner-Wohlfarth model and the ideal case when $\gamma = 90^\circ$, θ can be substituted using Eq. (2.6). Then the obtained expression is

$$\Delta R^{45} = \Delta R' \frac{H}{H_a} \sqrt{1 - \left(\frac{H}{H_a}\right)^2} \quad (2.15)$$

and the maximum and minimum values are obtained for $H = \pm H_a/\sqrt{2}$.

The electrical resistance for stripes with $\alpha = 0^\circ$ and $\alpha = 90^\circ$ is

$$\begin{aligned} R(\theta, 0^\circ) &= R_\perp - \Delta R \cos^2 \theta \\ R(\theta, 90^\circ) &= R_\perp - \Delta R \sin^2 \theta \end{aligned} \quad (2.16)$$

In this case, maximum and minimum values for resistance are reached when magnetization is either perpendicular or parallel to easy axis, with $\theta = 0^\circ$ or $\theta = 90^\circ$

$$\begin{aligned} R(0^\circ, 0^\circ) &= R_\parallel & R(90^\circ, 0^\circ) &= R_\perp \\ R(0^\circ, 90^\circ) &= R_\perp & R(90^\circ, 90^\circ) &= R_\parallel \end{aligned} \quad (2.17)$$

and the change ΔR^{90} in resistance by variations of θ for these stripes is

$$\Delta R^{90} = \frac{1}{2}\Delta R \cos 2\theta \quad (2.18)$$

that in the ideal case, writing as a function of H_a becomes

$$\Delta R^{90} = \frac{1}{2}\Delta R - \Delta R \left(\frac{H}{H_a}\right)^2 \quad (2.19)$$

therefore maximum and minimum values are obtained for $H = 0$ and $|H| = H_a$. The interest of writing in terms of resistance and not resistivity is that the former is easily measured with a $V(I)$ curve thanks to Ohm's law $V = RI$. If the LSMO stripe is biased with a fixed current, the variation in resistance is reflected in the measured voltage curve. The general magnetoresistance ratio of a material is generally given by

$$\text{MR} = \frac{\Delta R}{R_0} \times 100 \quad (2.20)$$

but it can also be obtained by calculating the total variation of output signal with a proper normalization. Figure 2.9 presents the AMR curves for LSMO stripes in the same sample, with magnetic uniaxial anisotropy obtained by epitaxial deposition on top of a vicinal substrate. Stripes were etched with $\alpha = 45^\circ$ and $\alpha = 0^\circ$ values. Magnetic field H is applied as perpendicular as possible to sample easy axis. Based on the Stoner-Wohlfarth model for magnetization reversal, the corresponding dependencies on applied field H and therefore magnetization direction θ are obtained. The scale of the axis of ordinates was

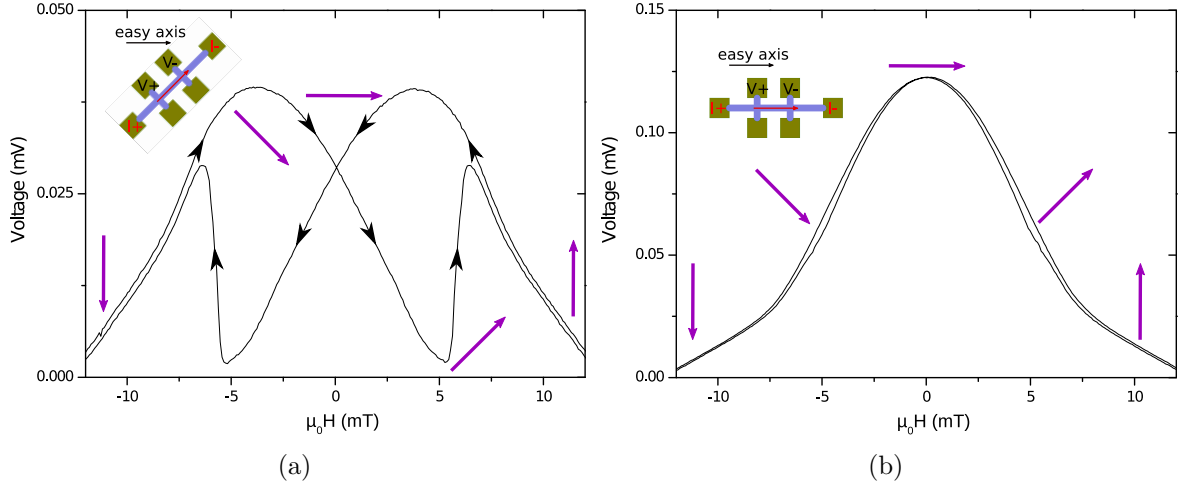


Figure 2.9: Variation of measured voltage as a function of applied field, with a $25 \mu\text{A}$ current and at 310 K temperature. LSMO stripes with $300 \mu\text{m}$ length and $100 \mu\text{m}$ width. a) $\alpha = 45^\circ$, with black arrows indicating the evolution of voltage signal according to field sweep, and b) $\alpha = 0^\circ$. In both curves the offset was suppressed, and schematic shows the direction of current density and how voltage is measured. Purple arrows indicate magnetization direction in the negative to positive field sweep. [Sample BA097]

intentionally changed to easily see the shape of the curves. LSMO stripes do present the expected $\sin 2\theta$ and $\cos^2 \theta$ behavior. In this sample, an AMR (ΔR) three times greater than PHE ($\Delta R'$) was observed. The sudden variation in signal for $\alpha = 45^\circ$ after crossing zero field is linked to the jump in magnetization direction θ . As explained in Section 2.2.1, this fast magnetization switch occurs when a small deviation δ is present in applied field direction. In the ideal case considering Stoner-Wohlfarth model, when $\alpha = 45^\circ$ conditions for maximum and minimum resistance are satisfied when $H = H_a/\sqrt{2}$. For $\alpha = 0^\circ$, such conditions are met at zero applied field (as magnetization aligns with easy axis) and for $H \geq H_a$, respectively. Obtained with a different sample, Fig. 2.10 shows the variation of output signal in a LSMO stripe with $\alpha = 0^\circ$ but voltage is measured transverse to the direction of passing current. This is a direct measure of the planar Hall effect, and the obtained curve should present the same shape as when the current is applied at a 45° angle of the easy axis. The measured voltage output curve does present the $\sin 2\theta$ dependence for small applied field, with the abrupt variation due to the sudden jump in magnetization direction. The total voltage output variation should not be directly compared to previous curves as it is a different sample, although the variation is clearly weaker than for standard AMR.

A higher signal variation was systematically observed for stripes with $\alpha = 0^\circ$ than when $\alpha = 45^\circ$. The transverse voltage also presents a lower peak-to-peak signal compared to measurements along stripe length. This smaller signal variation ($\Delta R' < \Delta R$) suggests that the off-diagonal terms of the resistivity tensor present smaller variation than the main diagonal terms. Etching the stripes with a 45° rotation in respect to easy axis allows obtaining a linear response around zero applied field. But this will affect negatively the sensitivity of the device, as measured voltage presents a lower amplitude variation as a function of magnetization direction θ . Previous work on LSMO thin film etched in a

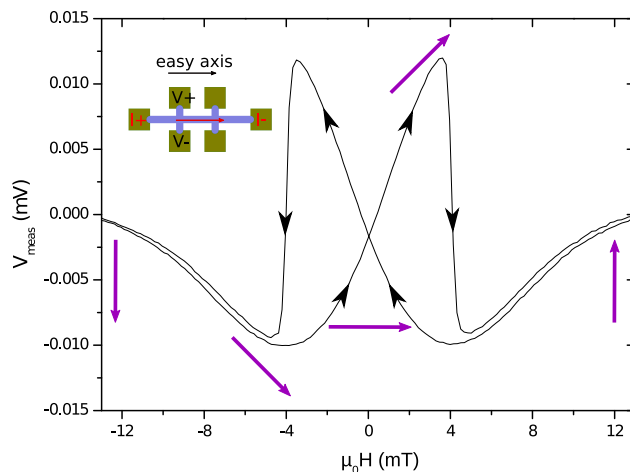


Figure 2.10: Transverse measure of voltage at $25\mu\text{A}$ bias and 310 K temperature. Schematic of a visual representation on how measurement was performed is included. Purple arrows indicate the magnetization direction in the negative to positive field sweep, and black arrows show the evolution of voltage signal. [Sample BA138]

Hall bar already reported a $\cos^2\theta$ and $\sin 2\theta$ dependence on longitudinal and transverse resistance values, with a difference in magnitude for resistance variation [43]. Although values are sample dependent and a different dopant ratio was used by Bason *et al*, a lower variation of the planar Hall contribution than linear AMR was presented which corresponds to the results obtained in this work.

The presented equations are valid for an uniaxial magnetic particle, with defined current density direction and coherent magnetization rotation. In this work, the uniaxial anisotropy is induced by the use of vicinal substrates. Perfect uniaxial anisotropy is not always obtained or can be reduced when film thickness gets too large, for instance. Besides from magnetization loops, the loss of uniaxial anisotropy can be deduced from the shape of magnetoresistance curves, specifically when $\alpha = 0^\circ$ or $\alpha = 90^\circ$. If there is any other contribution to magnetic energy not aligned to the step-induced anisotropy and that can't be neglected, magnetization and current density won't be parallel or perpendicular at zero applied field. A small applied field will be required to reach such configuration. In other words, there won't be a complete superposition of the curve when the applied magnetic field is swept from negative to positive and back. Two separated peaks will be present, as shown in Fig. 2.11.

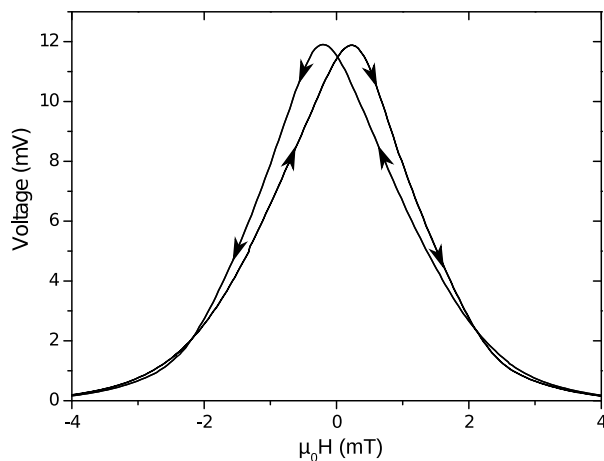


Figure 2.11: Small loss of complete step-induced anisotropy evidenced by the presence of two peaks in the signal of a $\alpha = 0^\circ$ structure. Black arrows indicate the signal according to field sweep. [Sample BA076]

2.4 Considerations on Electrical Noise

Random fluctuations of a signal is known as *noise* [44]. Noise can be of acoustic, optical or electric nature, among others. The same way we can't identify a single LED lit up in front of a strong light source or distinguish a particular voice when everyone in the stadium is singing Bohemian Rhapsody, an electric signal won't be detected if its amplitude is lower than the electric noise. The limit of detection is when the signal to be detected and the noise of the system are of equal amplitude, when the signal to noise ratio (SNR) equals one. So to detect even weaker signals, noise must be lowered. There are several techniques to reduce the noise in electronic circuits such as guarding cables, proper shielding and opting for devices with low intrinsic noise. Unfortunately, one can never get totally rid of electric noise. The lowest noise level of a system is referred as the *noise floor*. The intensity of noise power by frequency is known as Power Spectral Density (PSD), expressed in V^2/Hz . It can be of many origins and it presents different naming convention depending on the frequency region it is present or the physics behind it. A constant noise level for all frequencies is known as *white noise*, for which broadband *thermal noise* is an excellent example. A noise level that increases as frequency reduces is called excess low frequency noise, sometimes *flicker noise*. Other noise contributions in electronic devices can be *shot noise* and *random telegraph noise*. The present work is focused on LSMO thin films, which present two main noise sources that are intrinsic to it due to the physics of such material. Electric noise can also be expressed by voltage levels as Voltage Spectrum Density (VSD) in $V/\text{Hz}^{1/2}$, and its amplitude is obtained by calculating the square root of PSD. When there are uncorrelated noise sources, the sum must be performed in terms of power. So the total VSD is the square root of each VSD contribution squared.

2.4.1 Measuring noise

No system is free of noise. That includes any voltage or current supply for the system and even the equipment used to perform measurements. The voltage signal at the input of the measuring equipment will be added to the noise of the equipment itself. As the total noise is the sum of each term squared, a difference of one order of magnitude in a voltage signal will actually translate to a 100 times difference before taking the square root. If two noise sources present equal noise, but only one is multiplied by a gain factor of 10 the result is

$$\sqrt{1^2 + (10 \times 1)^2} \approx 10.05$$

which is a 0.5% difference from 10. We say that the noise source that was amplified **dominates** the total noise. Increasing the gain factor reduces the difference between the total noise and the dominant noise value. Therefore to correctly measure a small signal of interest, a proper amplification is required so that signal amplitude is above the noise floor of the measuring equipment itself. With an amplification factor high enough, further sources of noise can be ignored. Knowing the gain value applied, it is possible to trace back to the original noise level before amplification. Such gain value may change according to the frequency of the incoming signal, and the gain as a function of frequency is known as the transfer function of the amplifier system.

To amplify electric signals, instrumentation amplifiers integrated circuits (ICs) have a widespread use. At its simplest representation, this IC has two input ports and one output port. The output signal follows the difference between the two inputs, amplified by a gain factor G . Based on transistor technology, amplifiers have an intrinsic noise at its inputs associated to the internal components, that will also be amplified by the gain factor. Amplifier noise can be split in voltage noise e_n and current noise i_n . Independent of input load, e_n is always sensed and amplified. Meanwhile, i_n generates a voltage noise when circulating through a load resistance at the inputs of the IC. So the total noise of the amplifier is a function of resistance value at its inputs. Figure 2.12 shows the schematic

of a simple operational amplifier noise model, with a load R and an optional source to provoke a passage of current. The total VSD at the output of the amplifier is

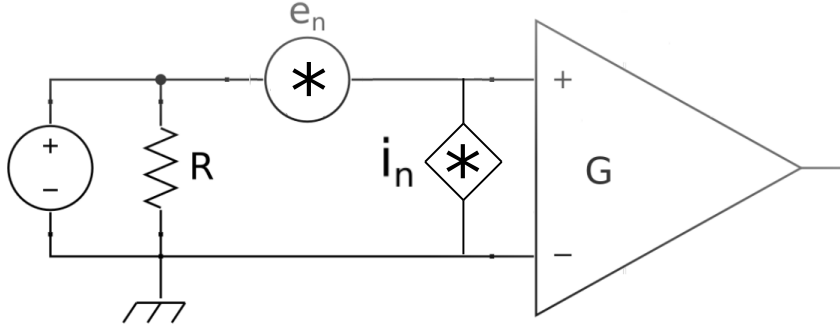


Figure 2.12: Current and voltage noise of an instrumentation amplifier. Source and load noise were intentionally omitted.

$$e_{out} = \sqrt{(G \cdot e_n)^2 + (G \cdot R \cdot i_n)^2 + G^2 \cdot 4k_B T R + G^2 \cdot S_V} \quad (2.21)$$

where S_V represents an excess noise in the low frequency region. The third term in the right-hand side of the equation represents the thermal noise, that will be further explained later on. An additional term corresponding to noise from the source may also be present, thus it will be amplified and added to total noise. The amplifier's e_n can be directly measured when grounding both inputs, as resistance R drops to zero. Performing measurements at a high enough resistance load allows estimating i_n , as only the second and third terms in the right-hand side of Eq. (2.21) will dominate, and thermal noise can be easily calculated and subtracted from the experimental values. In the case of an amplification chain, the noise from the first stage will be amplified by each gain factor, thus dominating the total noise. For a two-stages amplifier with a gain of 10 for each stage, the output noise is

$$\begin{aligned} e_{out} &= \sqrt{G_1^2 \cdot G_2^2 \cdot e_{1st}^2 + G_2^2 \cdot e_{2nd}^2} \\ &= \sqrt{10^4 \cdot e_{1st}^2 + 10^2 \cdot e_{2nd}^2} \end{aligned} \quad (2.22)$$

The amplifier IC must be correctly chosen according to the load resistance and frequency range of operation. If the load has a high electrical resistance value, one should opt for an amplifier with low current noise even though it might present a voltage noise above other ICs. The lower e_n and i_n the better, but a compromise must be respected due to limitations in manufacturing technology and design.

2.4.2 Preamplifier Circuit Design

At the start of this thesis, the available reading electronics was based on amplifier AD743, that was designed to perform noise measurements on sample with high values of electrical resistance. While it does present a very low current noise i_n , its voltage noise e_n at low frequencies is so high that it dominated the total noise of the system. Thus, the first step to improve the setup and obtain correct measurements was to choose a more appropriate preamplifier well suited to the fabricated LSMO samples. Several different commercial amplifier ICs were acquired, based on datasheet information and target resistance values of manufactured LSMO samples. Noise measurements at grounded inputs and with different loads were performed, which allowed to estimate the current and voltage noise of each IC. With these values, it is possible to estimate the total amplifier noise as a function of the load resistance with Eq. (2.21), ignoring the excess low frequency

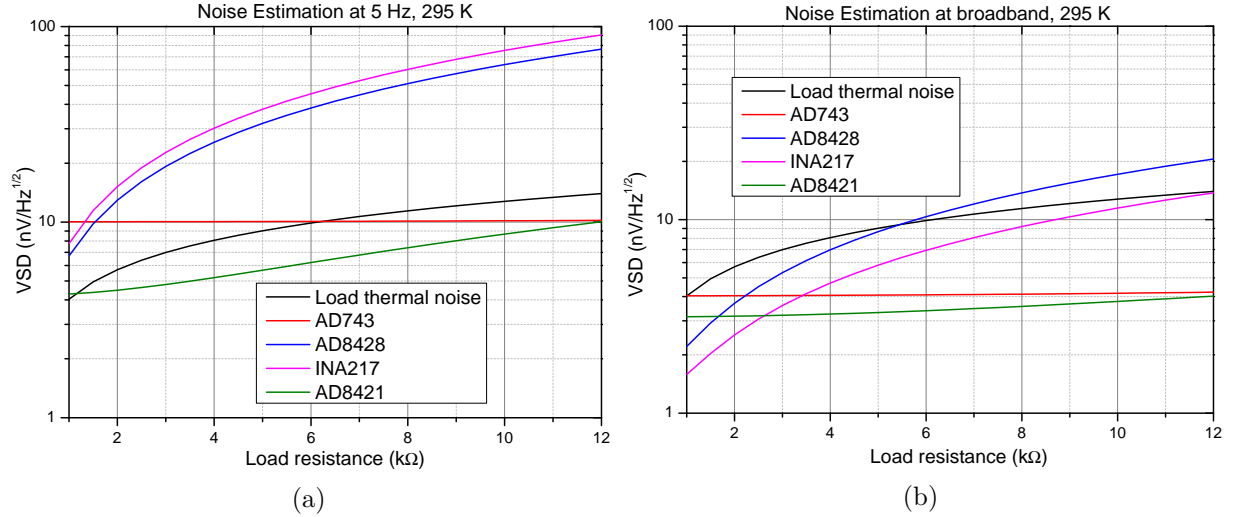


Figure 2.13: Estimated total noise of different amplifier models at 295 K temperature, without adding the thermal noise of the load. a) Values at 5 Hz. b) Values in white noise region.

noise S_V . This dependence is exhibited in Fig. 2.13. The thermal noise of the load is added as comparison but is not included in each amplifier noise curves. For correct measurements, noise from amplifier must be lower than sample noise. An increase in total noise with load resistance indicates a higher current noise, while a higher starting value translates to an increased voltage noise. Presenting the lowest total noise overall, we opted to build an amplifier circuit for LSMO noise measurements using AD8421 from Analog Devices. As shown in Fig. 2.14 with experimental input equivalent noise values, previous amplifier based on AD743 is not well adapted to the resistance range we aim for. It does present a lower current noise, but its voltage noise completely dominates the low frequency region. As we are interested in measuring both DC (MR ratio) and AC (noise) voltages from

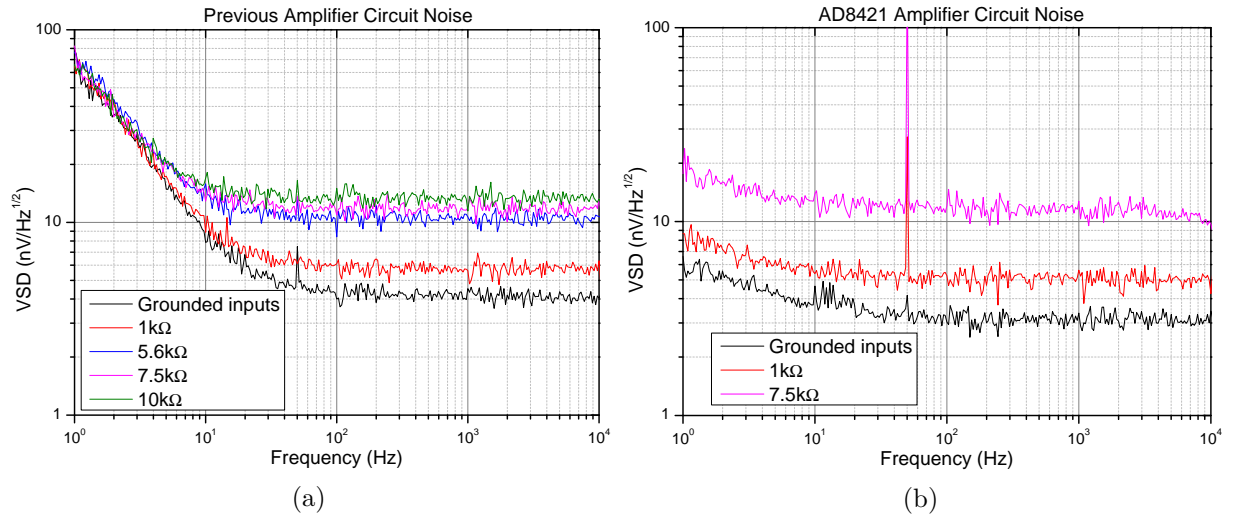


Figure 2.14: Input noise values for different loads, at room temperature. (a) Amplifier with AD743. (b) Amplifier with AD8421.

our LSMO device, we designed a two stages amplifier chain in which $G_1 = 40$ dB and $G_2 = 26$ dB. A high-pass filter with a cut-off frequency of 0.16 Hz after the first stage decouples the AC component for higher amplification, therefore $G^{AC} = 66$ dB. Gain values were chosen so as to minimize e_n contribution while avoiding amplifier saturation and ensuring that the output signal is above the noise floor of the reading equipment. Circuit was prepared with two identical channels and a gradiometer output, providing

the difference of AC signals. The advantage of a gradiometer configuration is to reject the non-random noise present at both channels, such as the 50 Hz signal from power grid. The final circuit is capable of measuring two samples at once and presents a total of five output ports. Noise and gain measurements, along with performance simulation via SPICE, are exhibited in Fig. 2.15. A low-pass filter with a cut-off frequency at 16 kHz was added at the output after experimentally noticing unexpected high amplitude spikes in high frequencies. Although already beyond the target frequency of operation for LSMO sensors, these high spikes would cause a rejection of the measured signal at the spectrum analyzer. Noise values in Fig. 2.15(b) are presented in raw PSD, not divided by each channel's transfer function, to directly compare the sum and the measured raw PSD of gradiometer. For a single channel, total voltage noise e_n was measured and current noise

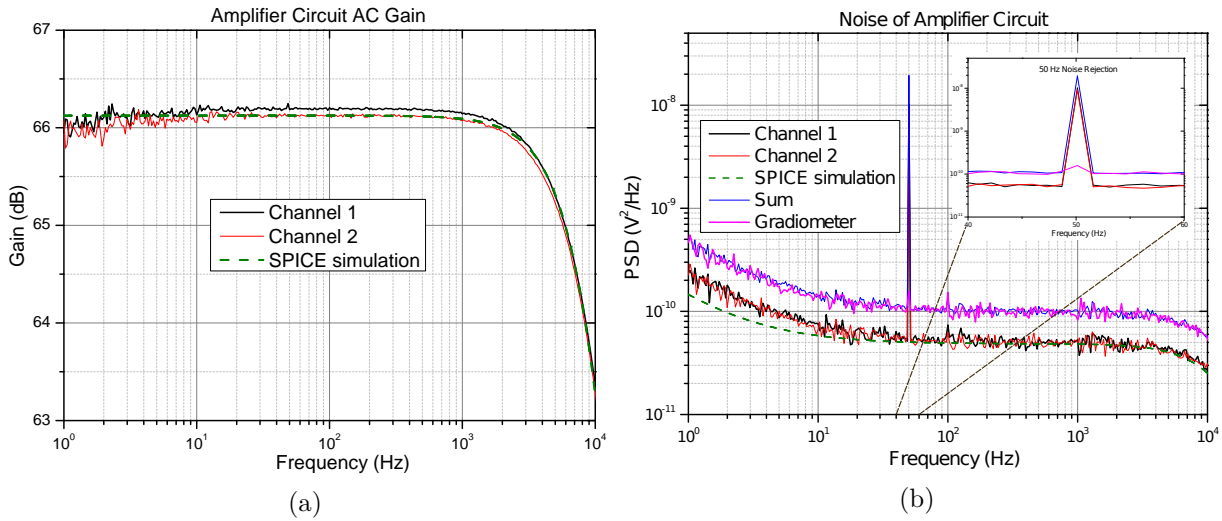


Figure 2.15: Characterization and SPICE simulation of amplifier chain based on AD8421. (a) Transfer function with a projected gain of 66 dB for each channel. (b) Measured and estimated noise for each channel. Measured gradiometer noise matches the quadratic sum of each channel, inset shows the 50 Hz rejection.

i_n was estimated using a high resistance load at 22 °C. Results are compatible to datasheet values and presented in Fig. 2.16. As estimation of total noise, with sample at 310 K and zero bias, is presented in Fig. 2.17 for frequencies of 1 Hz, 100 Hz and 1 kHz. The voltage and current noise values used for calculations are displayed in Table 2.1. This progress towards better noise measurements resulted in a contribution not limited to this particular thesis and that can be employed for any other sample, respecting the target resistance and frequency values. At lower frequencies, amplifier current noise i_n dominates above 3 k Ω resistance. It does reduces for increasing frequency, and has to be considered up to 10 Hz for higher resistance loads. At 1 kHz and beyond, contribution from amplifier current noise is negligible. The voltage noise e_n from the amplifier also reduces with frequency. Independent of load resistance value, e_n dominates only for low frequency and small loads. At 10 Hz for middle resistance values and above 1 kHz, the total noise follows the thermal noise from the load. Considering a simple $A/f + B$ expression for noise where f is the

	1 Hz	10 Hz	1 kHz
e_n [nV Hz ^{-1/2}]	7.9	5.5	3.5
i_n [pA Hz ^{-1/2}]	2.8	0.9	0.3

Table 2.1: Measured voltage noise and current noise.

frequency, a fit can be performed on voltage and current noise curves from amplifier. The

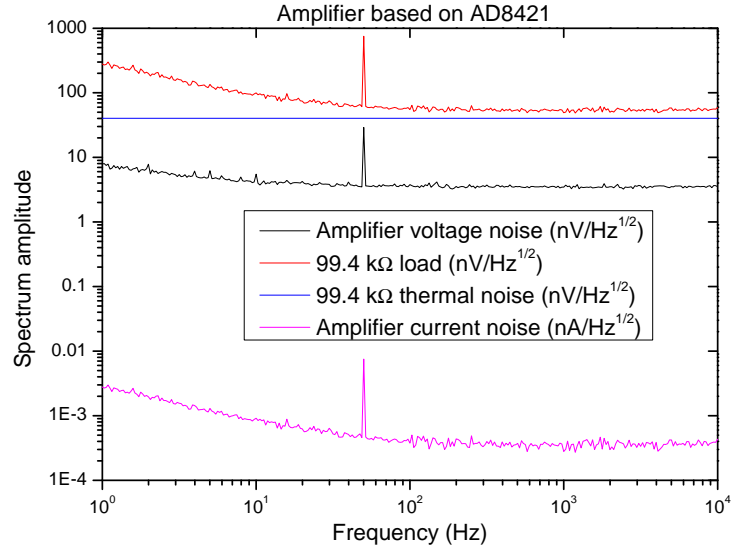


Figure 2.16: Noise characterization of two-stages amplifier.

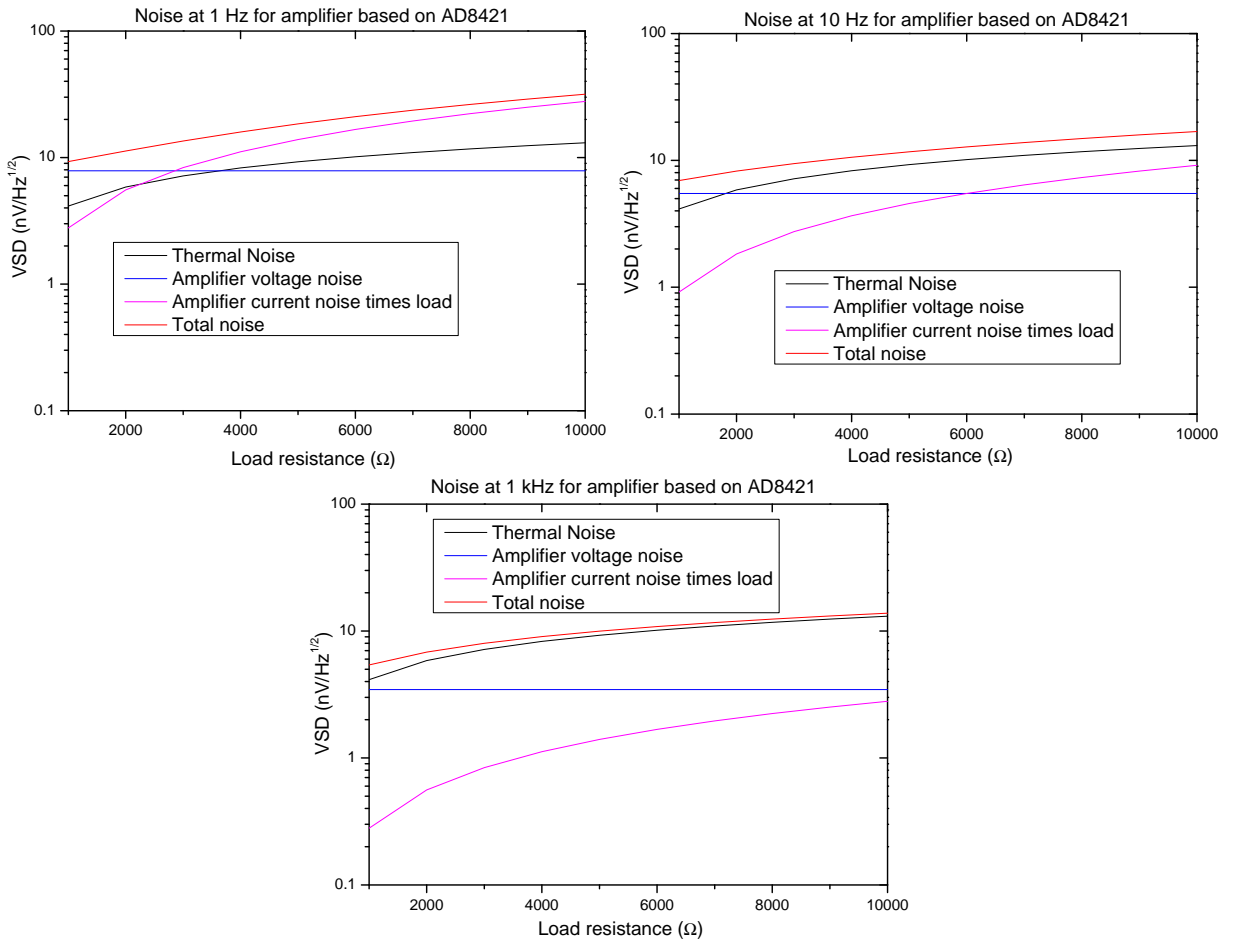


Figure 2.17: Dominant noise source at for a) 1 Hz, b) 10 Hz and c) 1 kHz. Contribution from amplifier current noise and thermal noise scale with sample resistance. Beyond 10 Hz and 2 kΩ, at 310 K temperature the load thermal noise is the dominant factor.

resulting adjusted expression with fitted parameters for total noise due to the amplifier can be written as

$$S_V^{amp} = \frac{(7.1 \times 10^{-9})^2}{f} + (3.5 \times 10^{-9})^2 + R^2 \left(\frac{(2.7 \times 10^{-12})^2}{f} + (3.3 \times 10^{-13})^2 \right) \quad (2.23)$$

where the first two terms represent the voltage noise e_n and the last two represent the current noise i_n , with R the resistance of the load. Excess low frequency and constant noise contributions are verified.

Finally, if a source is connected to bias the device under test, we must add the noise contribution of the source itself. Two sources were mainly used in this work: a very low noise current source developed at GREYC and presented in a PhD thesis by Dr. Sheng Wu [45], and a commercial voltage/current source Yokogawa GS200 model that presents a much higher noise. For measurements when samples are biased with a fixed current, the home-made low noise current source was used. Batteries are another type of low noise voltage source, although with a fixed bias. The noise contribution from the source can be discarded if somehow the sample itself rejects it. The reduction of common-mode noise is the main strength of what is known as Wheatstone bridge configuration. Experimental data using Yokogawa is shown in Fig. 2.18, where a balanced bridge greatly reduces the noise from the source.

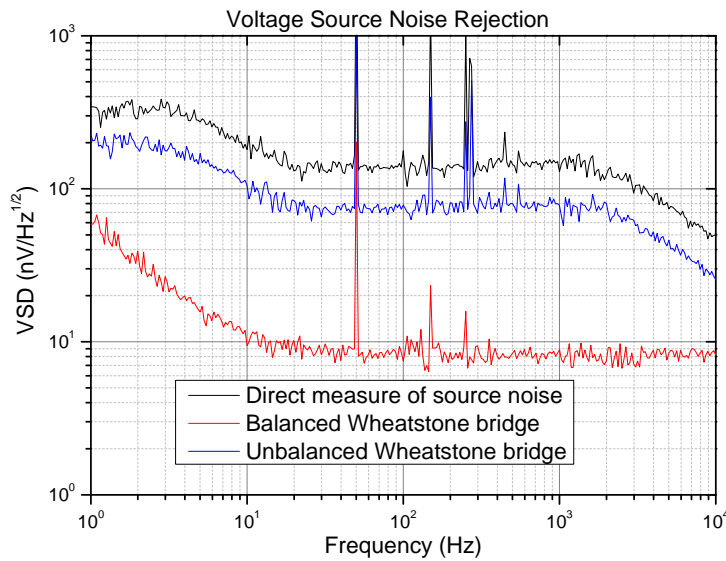


Figure 2.18: A well balanced Wheatstone bridge will greatly reduce common signals, such as the noise from the voltage supply.

2.4.3 LSMO noise sources

Thermally excited vibrations of charge carriers in conductors is a source of electric noise known as Johnson-Nyquist noise or thermal noise [46, 47]. Its distribution of noise power over frequency is written as

$$e_T = 4k_B T R \quad (2.24)$$

with k_B the Boltzmann constant, T the device temperature and R its electrical resistance. Note that there is no dependence on frequency f . Therefore it presents an equal power over all frequency spectrum. That's why it is also known as white noise. To dispose of it one must keep the material at absolute zero temperature, which is not feasible. Other sources of intrinsic noise in common materials used in Electronics are shot noise and excess low-frequency noise, that appear when there is a current flowing through the device. The latter presents an increasing spectral density with decreasing frequency f , which gives its $1/f$ name. It is limited only by the start time of the system [44]. It is also referenced in literature as flicker noise, and no electronic amplifier so far has been found to be free of it. Quite common [48, 49], this noise is not exclusive to transistors and resistors but also found in thermistors, thin films, light sources and membrane potential in biological

system. It follows a $1/f^\gamma$ power with typically $\gamma = 1$. Fluctuations of Earth's rotation frequency presents $\gamma = 2$ and galactic radiation has $\gamma = 2.7$.

It was observed that LSMO thin films present a $1/f$ noise that can be modeled by Hooge's empirical relation [50], written as

$$S_V = \frac{\alpha_H}{n} \frac{1}{\Omega f} V_{bias}^2 \quad (2.25)$$

where α_H is the Hooge parameter, n is the charge carrier concentration, Ω is the thin film volume and V_{bias} is the voltage difference across the device and related to the flowing current. To obtain the total VSD in $V \text{ Hz}^{-1/2}$ of a LSMO resistance element, we sum PSD values in Eqs. (2.24) and (2.25) then obtain its square root:

$$\text{VSD} = \sqrt{\frac{\alpha_H}{n} \frac{1}{\Omega f} V_{bias}^2 + 4k_B T R} \quad (2.26)$$

A squared sum must be performed as noise sources are completely uncorrelated. Commonly, noise values are of very low amplitude. A resistance of $1 \text{ k}\Omega$ at $20 \text{ }^\circ\text{C}$ presents $4 \text{ nV Hz}^{-1/2}$ white noise. Therefore correctly measuring noise is an art on its own, as even the system used to perform measurements is not free of it. Figure 2.19 presents noise curves for a LSMO stripe, next to a magnetoresistance curve obtained at fixed $25 \text{ }\mu\text{A}$. The straight

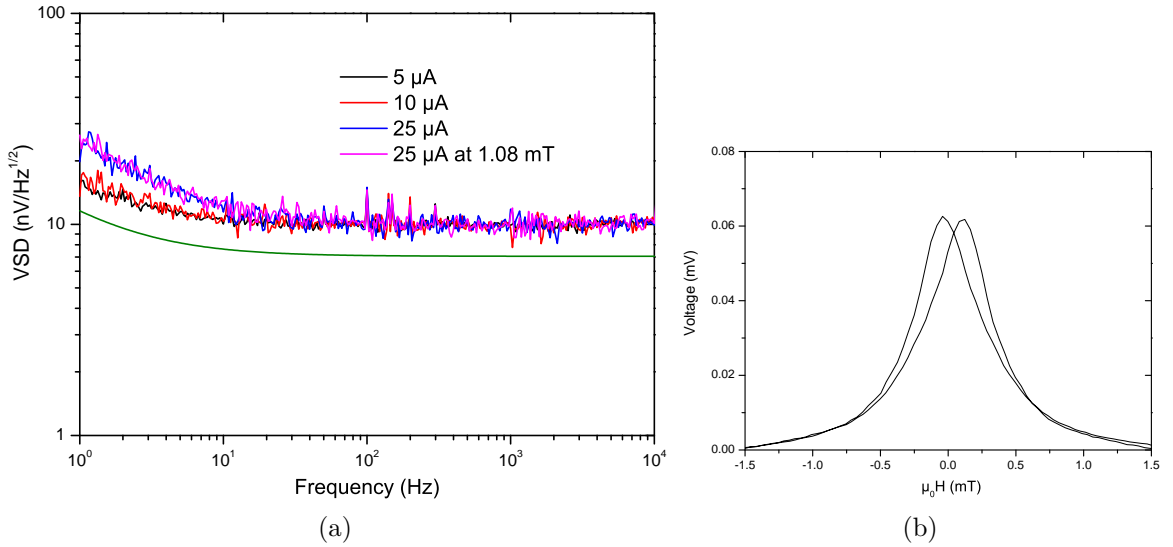


Figure 2.19: Measurements with LSMO stripe at 310 K, sample has $2.2 \text{ k}\Omega$ resistance value measured in 4-probes configuration. a) Experimental noise curves at different current bias. Green line is the calculated noise considering sample thermal noise and contribution from preamplifier. b) Typical magnetoresistance curve, with LSMO stripe etched parallel to easy axis. [Sample BA106]

green line in the noise graph represents the sum of sample thermal noise and noise from reading electronics. The difference from experimental data can be due to extra current noise from current source, not considered in the calculation. Using the experimental data at the lowest bias, this current noise from the current source is estimated to be of $5 \text{ pA Hz}^{-1/2}$ at 1 Hz and $3 \text{ pA Hz}^{-1/2}$ in white noise region. For $5 \text{ }\mu\text{A}$ and $10 \text{ }\mu\text{A}$ current bias, measured noise is at same level. But when bias is increased to $25 \text{ }\mu\text{A}$, the behavior according to Eq. (2.26) is obtained. This means that for lower bias, contribution from the sample itself to total noise in low frequency region is negligible. Should an even higher current be applied, $1/f$ noise will increase. To mitigate noise from the home-made current source, the maximum current that can be provided is limited by design. No change in noise spectrum was observed when a controlled magnetic field was applied, compared to

ambient field. Therefore we conclude that there is no contribution from magnetic noise. The presence of two shifted peaks in the MR curve for this stripe etched perpendicular to easy axis (therefore $\alpha = 90^\circ$) can be explained by a slightly loss of uniaxial anisotropy. This does not affect the conclusions related to noise performance.

Following Eq. (2.26), a squared increase of low frequency noise is expected for increasing voltage bias of the sample. This squared dependence can be verified by performing noise measurements at different values for voltage bias, and then performing a linear fit in log-log scale with a fixed slope of 2 for noise times frequency values, averaged in the region where sample S_V is dominant. In Fig. 2.20 an example of noise curves from an AMR LSMO device obtained at different voltage bias values is presented, along with a numerical fit over the experimental data. For now, let us focus on the noise curves themselves, as a proper explanation of the device will be presented further in this work. As expected from the VSD equation, low frequency noise increases with voltage bias while

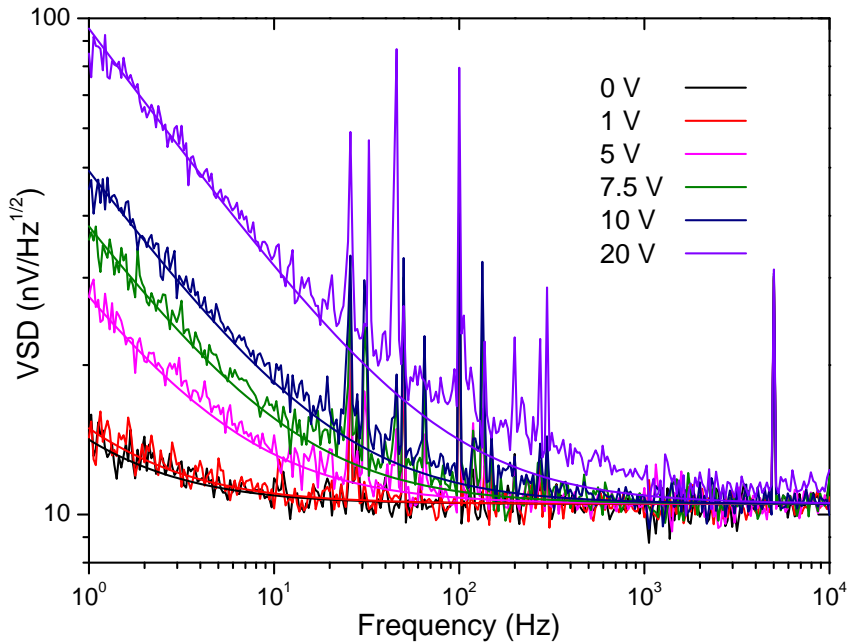


Figure 2.20: Measured voltage noise dependency on bias voltage at 310 K, with calculated noise compared to experimental data. The resistance of the sample is 5.5 k Ω . [Sample BA114]

white noise remains constant. Using Eq. (2.26), a numerical fit can be performed over the experimental noise data. Using the known values for volume $\Omega = 1.35 \times 10^{-15} \text{ m}^3$ and the measurement temperature $T = 310 \text{ K}$, the fit over measured noise was obtained with $\alpha_H/n = 1.2 \times 10^{-31} \text{ m}^3$ and $R = 5.5 \text{ k}\Omega$. Such a low α_H/n value of 10^{-31} m^3 is typical for high quality epitaxial LSMO films [51]. The mentioned linear fit to verify the squared dependence is presented in Figure 2.21 for two samples of different LSMO thickness, from 1 V to 20 V bias voltage. To remove the contribution from electronics noise, the obtained voltage spectrum at zero bias voltage is subtracted from subsequent measurements. Each point is the resulting noise multiplied by measured frequency and then averaged from 1 Hz to 10 Hz. The squared dependence is thus verified. The intercept value of such fit also allows to obtain the slope of S_V/V^2 versus f , and this dimensionless value can be used as a comparison parameter between sensors for low frequency noise. The value of such slope already takes into account the geometry of the sensor, and the lower this value, the better. For the presented fit of the 60 nm thick sample, this value is of 4.3×10^{-17} . Other sensor technologies such as magnetic tunnel junctions present values few orders of magnitude higher [52, 53]. Considering the same geometry for vortex-state magnetization for TMR and GMR devices, the former presented a Hooge parameter 300 times higher than the latter, and a 2 μm diameter GMR sensor presented a dimensionless Hooge parameter around 4.3×10^{-13} [54]. This shows that LSMO can indeed be used to fabricate low noise

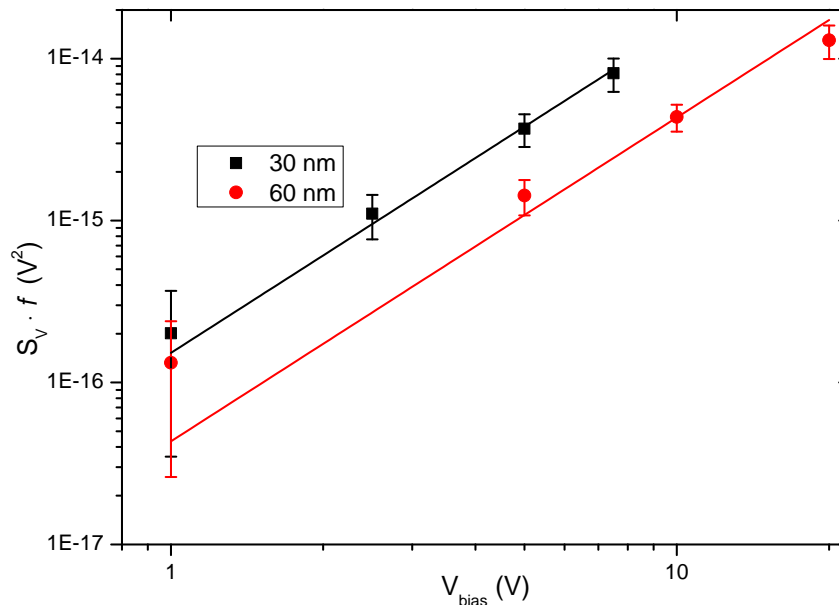


Figure 2.21: Average values for $S_v \times f$, and error bars correspond to two times the standard deviation. [Samples BA098, BA104]

magneto-resistive sensors. The MTJ presented by Fujiwara *et al* has a value of 1.5×10^{-10} , so an array of 100 by 100 MTJs was built to increase the total volume and reduce the intrinsic $1/f$ noise of the device [55].

2.5 Wheatstone Bridge working principle and device validation

A Wheatstone bridge is a common configuration for transducers based on resistance variation, generating an electric signal ideally proportional to the physical quantity of interest. It is made of four resistance elements connected in a loop, forming two branches connected in parallel, each branch consisting of two elements connected in series. It is a four terminal device, with one node at each connection. Two opposing nodes are used to feed the bridge with a given bias, now referenced as excitation terminals, and the remaining two are used for signal reading, now referenced as signal terminals. If all four resistances are equal, what is called a balanced Wheatstone bridge, current density spreads equally through both branches. So both signal terminals are at same potential, thus no voltage difference is measured and bridge output is zero. If all four resistive elements present the same variation in resistance, the output remains at zero. So a Wheatstone bridge configuration is immune to noise that is common to the whole device itself, such as temperature drifts. That is without a doubt the main advantage of such configuration. The output of a Wheatstone bridge as shown in Figure 2.22, considering a unity gain, can be written as

$$V_{meas} = V_{bias} \left(\frac{R_2}{R_1 + R_2} - \frac{R_3}{R_3 + R_4} \right) \quad (2.27)$$

and with it one can easily verify how output remains at zero when all elements undergo same resistance variation, for a balanced bridge. But if the resistance variation is not equal in all four elements, the distribution of current will be affected, and signal terminals will be at different potentials. A voltage difference arises, and a non-zero output is read. If even without any perturbation the bridge is imbalanced (when resistive elements that make up the bridge do not have same nominal values for resistance), there will be a constant voltage difference between signal terminals, known as *bridge offset*. For a Wheatstone bridge to be used as a sensing device, it suffices that only one element is sensitive of the physical

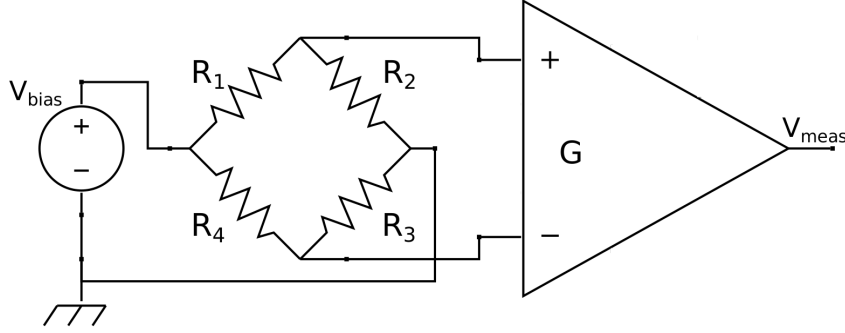


Figure 2.22: Basic schematic of a Wheatstone bridge.

quantity of interest. The bridge will give an output signal that follows the resistance variation. Common uses for Wheatstone bridge configuration besides magnetic sensors are for strain gauges and temperature measurements. When resistive elements suffer elastic deformations or temperature variations not equal to whole bridge, an electric signal related to strain or heat transfer is obtained. One possibility is to build a bridge in which all elements have same nominal resistance but only one is sensitive to strain, temperature or magnetic field variations. Another option is letting only one element under the influence of the physical quantity of interest while the rest of the bridge remains isolated.

A third possibility, which was employed in this work, is building the Wheatstone bridge in such a manner that adjacent elements will present opposite sign variations in resistance. Such configuration is known as a *full bridge*. The voltage difference of such configuration can be written as

$$\Delta V_{meas} = V_{bias} \left(\frac{R_2 + \Delta R_2}{R_1 - \Delta R_1 + R_2 + \Delta R_2} - \frac{R_3 - \Delta R_3}{R_3 - \Delta R_3 + R_4 + \Delta R_4} \right) \quad (2.28)$$

and if the bridge is balanced with all arms presenting same nominal resistance and variation, it simplifies to

$$\Delta V_{meas} = V_{bias} \cdot \frac{\Delta R}{R} \quad (2.29)$$

The strong reduction of voltage supply noise can be seen when we break down the V_{bias} in a DC contribution plus a e_n^{supply} voltage noise, orders of magnitude lower than the constant voltage. Both are multiplied by the ΔR factor, which is itself small. Therefore the noise from the supply is masked in the well balanced LSMO Wheatstone bridge. For magnetic field sensing, the relative position between each element can be designed in such a way that ensures resistance variations at adjacent arms will have opposite signals even if the whole bridge is under the influence of a homogeneous magnetic field. The resistance variation as function of magnetization direction θ and current density direction α in LSMO stripes was presented in the previous section. Such stripes can be interconnected in order to build a Wheatstone bridge, performing the correct substitutions in Equation 2.27. The two bridge geometries built in this work are presented in Figure 2.23, along with a schematic to recall the reader of directions and angles of interest. An AMR sensor presenting a Wheatstone bridge geometry is also known as Planar Hall Effect Bride (PHEB) [56]. The design presenting LSMO stripes with $\alpha = 45^\circ$ and $\alpha = 135^\circ$ is named 45° Wheatstone bridge (45WB), while the design with $\alpha = 0^\circ$ and $\alpha = 90^\circ$ is named 90° Wheatstone bridge (90WB). Expressions for electrical resistance of each stripe as a function of angle θ were presented in Eqs. (2.12) and (2.16). In literature, 45WB is also referenced as diamond shaped bridges. It was already verified that this geometry presents a higher sensitivity than ring-shaped sensors for equal size [57, 58]. The standard lithography mask design used to fabricate the majority of LSMO samples is shown in Fig. 2.24, next to a photograph of a sample after fabrication process (explained in Appendix Fabrication). In general, for each STO substrate, there are two 45WB and two 90WB bridges, with three single LSMO lines prepared for 4-probes measurements.

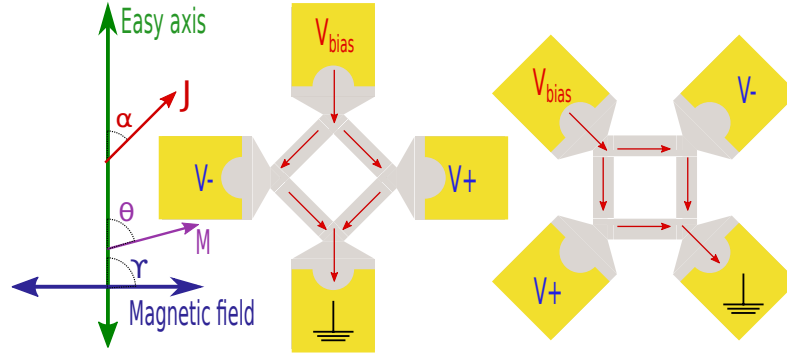


Figure 2.23: A recall to important directions and angles, next to two bridge geometries. Red arrows indicate current direction between excitation terminals, while $V+$ and $V-$ indicate signal terminals.

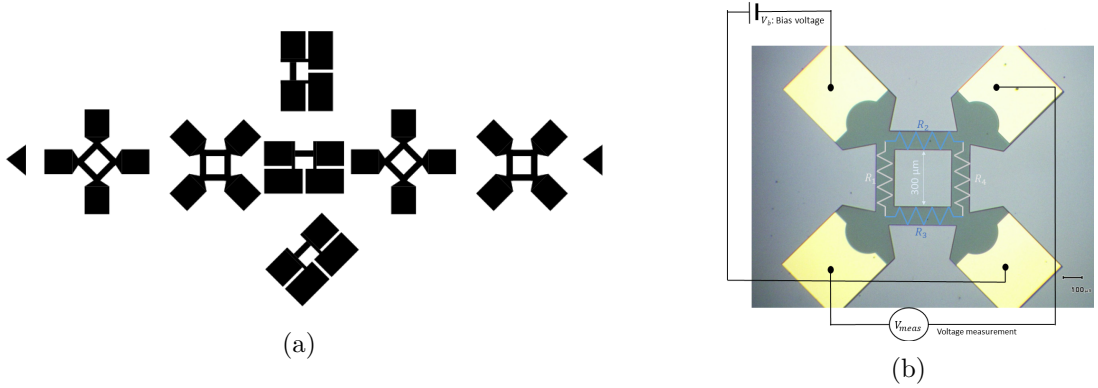


Figure 2.24: Standard design of LSMO samples. Single lines and Wheatstone bridge arms present $100 \mu\text{m}$ length and $300 \mu\text{m}$ width. a) Physical mask layout for MJB3. b) Photograph of a fabricated 90WB, indicating excitation and signal terminals.

2.5.1 45° Wheatstone Bridge

In this design, two opposing arms present $\alpha = 45^\circ$ while the other two have $\alpha = 135^\circ$. So we can write

$$R_2 = R_4 = R(\theta, 45^\circ) = R_0 + \frac{1}{2} \Delta R' \cdot \sin 2\theta \quad (2.30)$$

$$R_1 = R_3 = R(\theta, 135^\circ) = R_0 - \frac{1}{2} \Delta R' \cdot \sin 2\theta$$

that when substituting in Eq. (2.27) yields

$$V_{meas} = \frac{V_{bias}}{2} \frac{\Delta R'}{R_0} \sin 2\theta \quad (2.31)$$

By applying the expression for θ obtained when minimizing the uniaxial anisotropy energy with Stoner-Wohlfarth model, $\theta = \arcsin(H/H_a)$, the dependence on applied field is obtained as

$$V_{meas} = V_{bias} \frac{\Delta R'}{R_0} \frac{H}{H_a} \sqrt{1 - \left(\frac{H}{H_a}\right)^2} \quad (2.32)$$

so for small applied fields the 45° WB design presents a linear response. The obtained expression checks with published work on AMR sensors presenting a Wheatstone bridge design. The variation of output signal with changes of applied field is the sensor's

sensitivity S :

$$S^{45WB} = \frac{\partial V_{meas}}{\mu_0 \partial H} = \frac{1}{\mu_0} V_{bias} \frac{\Delta R'}{R_0} \frac{H_a^2 - 2H^2}{H_a^3 \sqrt{1 - \left(\frac{H}{H_a}\right)^2}} \quad (2.33)$$

in which μ_0 was added to have in units of volt per tesla. A constant sensitivity is observed near zero applied field, and around $H = 0$ we have

$$S = V_{bias} \frac{\Delta R'}{R_0} \frac{1}{\mu_0 H_a} \quad (2.34)$$

Therefore this design does not require a magnetic field bias to remain at its working point of linear operation.

2.5.2 90° Wheatstone Bridge

With a 45° shift from 45WB, the 90WB presents arms with $\alpha = 0^\circ$ and $\alpha = 90^\circ$. That is, LSMO stripes are either parallel or perpendicular to magnetic easy axis.

$$\begin{aligned} R_2 = R_4 = R(\theta, 90^\circ) &= R_\perp - \Delta R \cdot \sin^2 \theta \\ R_1 = R_3 = R(\theta, 0^\circ) &= R_\perp - \Delta R \cdot \cos^2 \theta \end{aligned} \quad (2.35)$$

That when putting on Wheatstone bridge output

$$V_{meas} = V_{bias} \frac{\Delta R}{R_\perp + R_\parallel} (1 - 2 \sin^2 \theta) \quad (2.36)$$

and again by using the expression for θ and $2R_0 = R_\perp + R_\parallel$

$$V_{meas} = V_{bias} \frac{\Delta R}{2R_0} - V_{bias} \frac{\Delta R}{R_0} \left(\frac{H}{H_a}\right)^2 \quad (2.37)$$

There is an offset in output voltage independent of anisotropy field H_a and applied field H . For a fixed setup this offset may prevent from biasing the bridge with higher voltage when compared to 45WB, due to amplifier saturation. From Eq. (2.37) we can also verify that the middle value of V_{meas} will be reached when $H = H_a/\sqrt{2}$. Therefore we can estimate H_a by obtaining the Full Width at Half Maximum (FWHM) of the curve, which will correspond to $\sqrt{2}H_a$. The obtained expression for sensitivity is

$$S^{90WB} = \frac{1}{\mu_0} V_{bias} \frac{\Delta R}{R_0} \frac{2H}{H_a^2} \quad (2.38)$$

where a zero sensitivity is obtained at zero applied field. So this design requires a DC bias magnetic field to present a linear operation [59]. The majority of detectivity curves presented in this work will be calculated using the sensitivity as the derivative of V_{meas} curve in the linear operation range. Using a pair of Helmholtz coils to keep the sensor at the correct working point, such design was already used to detect magnetic nanoparticles [60]. In fact, at applied field $H = H_a/2$, the obtained sensitivity presents the same expression as for the 45WB around zero field, Eq. (2.34). Therefore, if both geometries present same MR ratio ($\Delta R' = \Delta R$) and anisotropy field, they should obtain similar sensitivity values for $H = 0$ in 45WB and $H = H_a/2$ in 90WB. Besides $V T^{-1}$, sensitivity is also commonly presented in $\% T^{-1}$, independent of voltage bias.

2.5.3 Device validation

Now that the basic theory was presented, it is time to validate the fabricated LSMO Wheatstone bridges as AMR sensors. Magnetic characterization was performed using a lab-made Magneto-optical Kerr Effect (MOKE) imaging setup in longitudinal configuration. By using the longitudinal configuration, it provides the component of the in-plane magnetization along the direction of the applied magnetic field. The magnetization loops of a 60 nm thick LSMO deposited over 8° vicinal STO, along with selected MOKE images, are shown in Figs. 2.25 and 2.26. Specific points of the curves are linked using colors to the corresponding images. Black arrows are an indication of field sweep direction. For both Wheatstone bridge designs, nucleation and propagation of magnetic domains is observed when applied field is along easy axis direction (parallel to step edges), while coherent reversal is obtained when field is perpendicular to said axis. The value of anisotropy field H_a

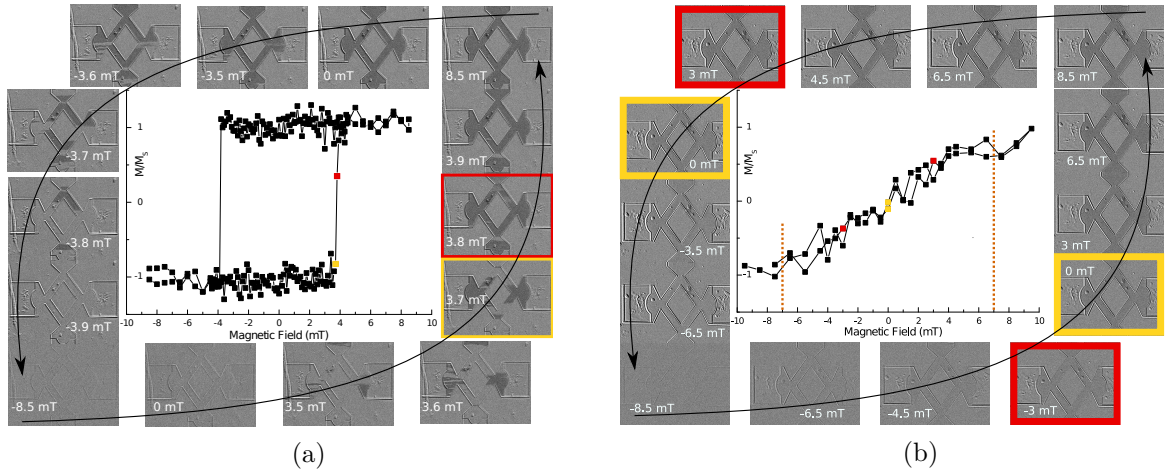


Figure 2.25: Magnetization cycles for (a) easy and (b) hard axis in 45WB. [Sample BA097]

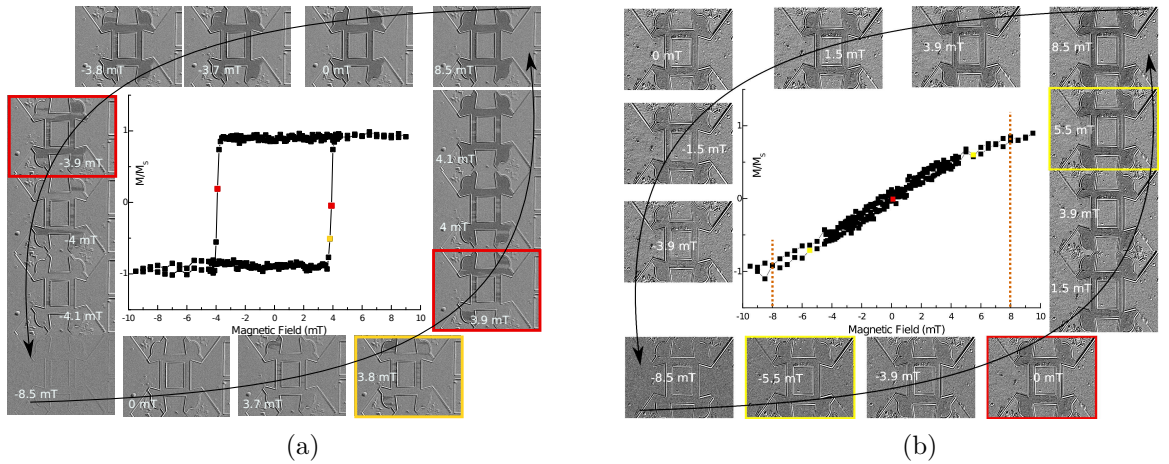


Figure 2.26: Magnetization cycles for (a) easy and (b) hard axis in 90WB. [Sample BA097]

can be deduced from the magnetization curve perpendicular to easy axis. This direction is also known as hard axis. The anisotropy field value is obtained when magnetization reaches saturation, no longer increasing with higher applied field. Deduced values are around 7 mT and 8 mT from Fig. 2.25(b) and Fig. 2.26(b), respectively. While this technique allows verifying a coherent magnetization reversal or domain nucleation and propagation, it does not indicate the exact direction of the magnetization vector, only if it is away from initial saturated state. If one resistor arm in the Wheatstone bridge presents a magnetization that rotates clockwise while in another arm it rotates counter-clockwise, the image will

present the same gray level. In the case that does happen, bridge output will be affected, as arms don't present the expected resistance variation. Nevertheless, MOKE imaging is a very useful technique to study and validate the magnetic behavior of LSMO sensors. Although magnetization reversal in LSMO over vicinal substrates was previously shown [61], and MOKE imaging has been reported [31], during the development of this thesis it was a first for magnetization imaging of this half-metallic oxide etched in Wheatstone bridge structure. Magnetic uniaxial anisotropy is indeed induced, thanks to the use of vicinal substrate, over the whole thin film. So we can consider the Stoner-Wohlfarth model for a coherent magnetization reversal in LSMO Wheatstone bridges.

To obtain a magnetization rotation direction that is equal in all arms of the Wheatstone bridge, we can slightly deviate the direction of applied field H . An independent rotation is more critical for 45WB geometry, as the minimum as maximum values of V_{meas} will be reached when magnetization is at $\pm 45^\circ$ from easy axis. In the ideal case this is reached for an applied field $H = H_a/\sqrt{2}$. For 90WB structure, those values are reached when M is perpendicular or parallel to easy axis. In other words, at $H \geq H_a$ and zero applied field. The effect of this small deviation δ creates a small field component parallel to easy axis, and its effect on the magnetic energy was discussed in Section 2.2.1. As expressed in Eqs. (2.31) and (2.36), the output signal of the Wheatstone bridges depend on magnetization direction θ . So V_{meas} curves will reflect the change from the ideal case when applied field is perfectly perpendicular to easy axis. In practice, a perfect alignment is difficult to achieve, as in this work sample positioning is performed manually and alignment is verified by eye. Fig. 2.27 presents a comparison of V_{meas} for a 45WB structure when field is applied with the smallest deviation δ as possible and when a 6° rotation is added. This small deviation led to an

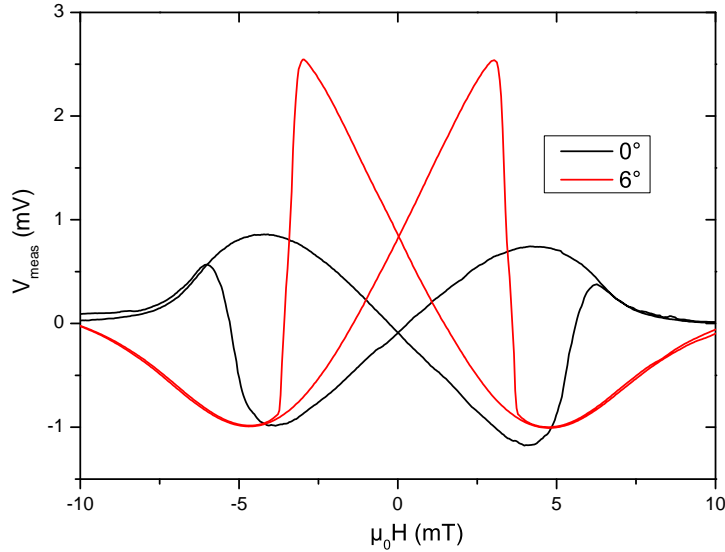


Figure 2.27: For a fixed V_{bias} , higher MR ratio in 45WB with $\delta = 6^\circ$. [Sample BA097]

increased total variation of output signal for a fixed V_{bias} , H_a and operation temperature. Thus, a higher MR ratio and sensitivity was obtained. Plus, the expected symmetry is achieved and sample presents a linear behavior around zero applied field as expected from Eq. (2.32). This higher MR ratio and symmetric curve is linked to an equal magnetization rotation direction over the whole Wheatstone bridge structure. The sudden change in voltage level is linked to the θ jump to a higher angle value, which then slowly returns to 90° as mentioned in Section 2.2.1. Another consequence of this small deviation δ in the V_{meas} curve are the curved extremities. Theoretically, the device would present a flat response for $|H| > H_a$ with $\gamma = 90^\circ$. Although for even higher applied field there is the contribution of colossal magnetoresistance, such effect can be neglected in the scope of the present work. For an initial saturated state with negative applied field, this sudden jump in magnetization occurs only at a given positive value for increasing $\mu_0 H$. Figure 2.28

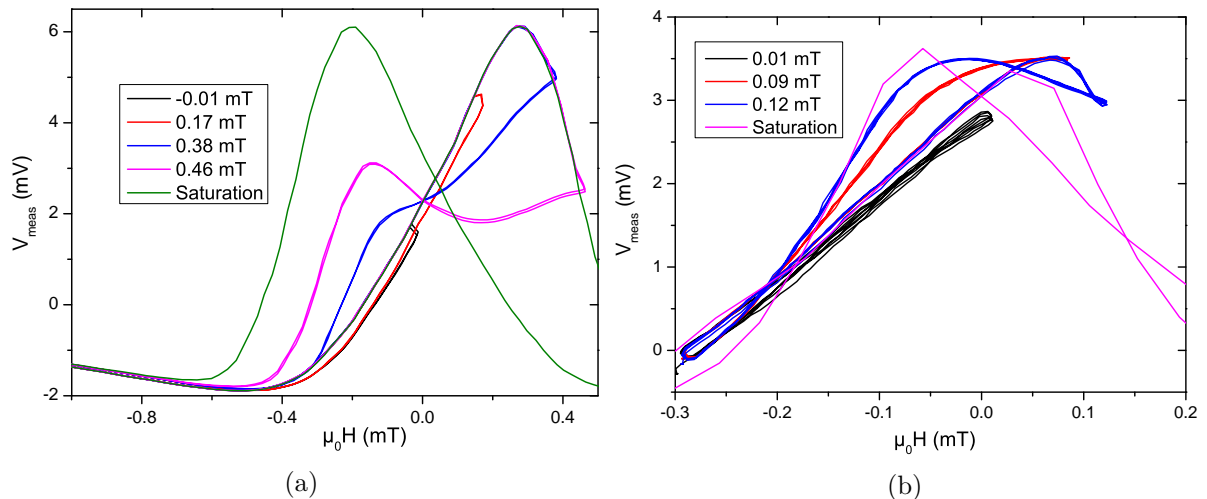


Figure 2.28: Stability of sensor output. Legend indicates the maximum value of applied field. a) Example of a 45WB structure and b) of 90WB structure. [Samples BA104, BA068]

shows repeatability tests of V_{meas} for 45WB and 90WB structures. Those were obtained with different LSMO samples, so MR ratio and saturation field are not to be compared. The interest is to show that before the jump in magnetization direction, V_{meas} curve is stable. Therefore it is possible to use the sensitivity value obtained from the derivative of V_{meas} in this region.

As the LSMO structure can be considered as a single-domain magnetic particle with uniaxial anisotropy, a numerical model can be developed to fit a simulated curve with optimized parameters to experimental magnetoresistance measurements. The fit is performed by estimating θ from numerical minimization of Eq. (2.8), and then comparing the calculated output with Eq. (2.31) or Eq. (2.36), depending on the bridge geometry. While V_{bias} is a known fixed parameter for each measure, MR ratio, anisotropy field H_a and magnetic field direction γ can be left as optimization parameters. Such real physical values can then be extracted from the optimization results. With measured V_{meas} and $\mu_0 H$ data, only the negative to positive field sweep is considered. This is done to limit the problem with the boundary condition of $-90^\circ \leq \theta \leq 180^\circ$. The first step is to remove any offset from experimental data, forcing a zero volt output at zero applied field. This is done by subtracting from V_{meas} curve the voltage value at the lowest absolute measured field. The term independent of magnetic field in Eq. (2.36) is ignored, which poses no problem for the extraction of physical parameters. Initial values for parameters are estimated using the *differential evolution* algorithm, a stochastic method to find the minimum of a multivariate function [62]. Then, a bounded non-linear least squares problem solved by trust region reflective function (see [63]) varies the adjustable parameters to reduce the total error between the experimental data and calculations, while minimizing energy and obtaining θ for all sets of values for such parameters. Minimization of the energy expression is done using Brent's method [25]. The range of values for each parameter can be limited based on previously known information. For example, if the voltage output curve of a bridge saturates at $H = 2$ mT, anisotropy field can be limited from 0.5 mT to 3 mT. Total variation in bridge output informs range for MR ratio limits. The code implemented to perform such curve fit is available in Appendix Characterization. Figure 2.29 presents an example of obtained results, for 45WB and 90WB bridge geometries on 60 nm thick LSMO over 8° vicinal STO. Measurements were obtained with a small deviation δ in applied magnetic field direction, with sample at 310 K temperature and 10 V bias. The green line is the experimental data and the fitted curve is shown in dashed red. Below each V_{meas} curve, the corresponding θ values obtained from the numerical minimization of the uniaxial magnetic energy are shown. At zero applied field magnetization is parallel to easy axis. The sudden switch in magnetization direction due to the deviation in applied

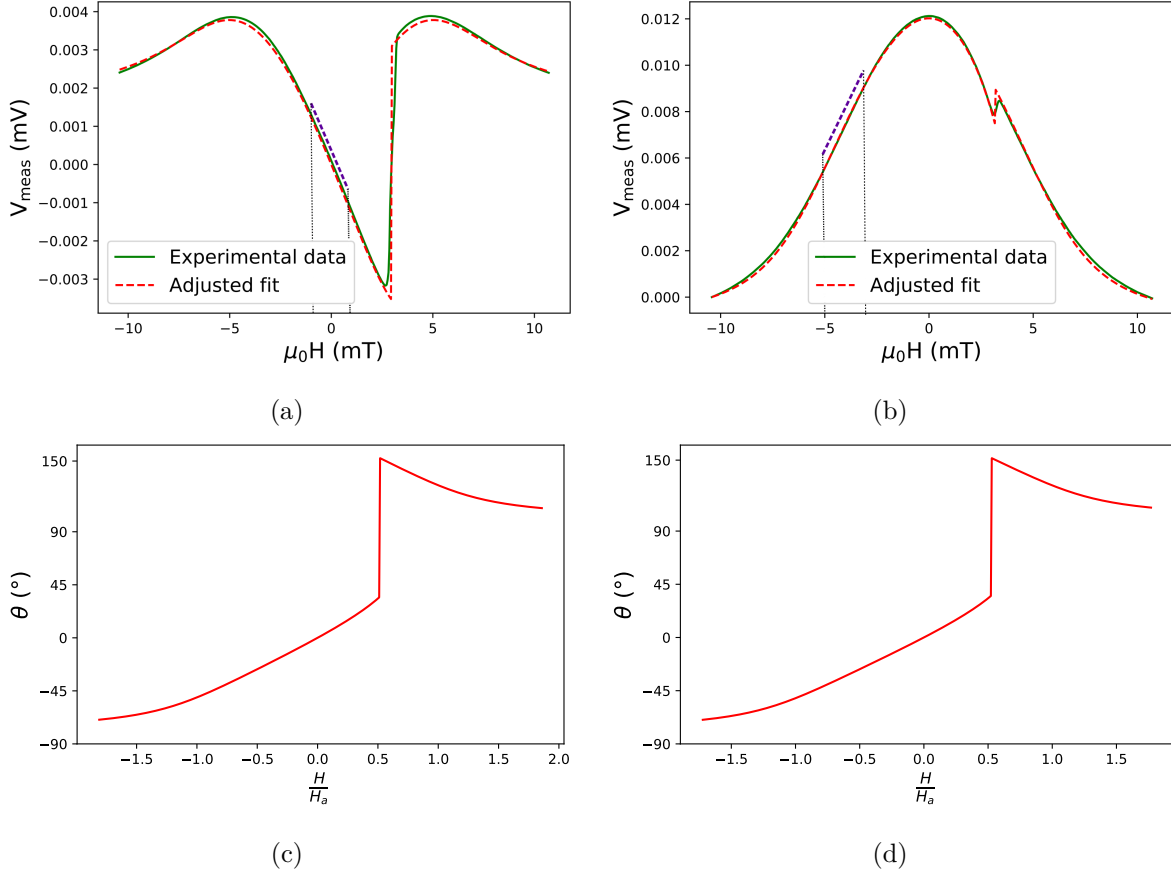


Figure 2.29: Fit over experimental data using a) Eq. (2.31) and b) adapted Eq. (2.36). Linear operation range is indicated with purple dashed line. Respective values for θ in c,d) are obtained by minimizing right-hand side of Eq. (2.8). [Sample BA097]

field direction is correctly predicted. This can be seen in the V_{meas} curve after crossing zero applied field, and clearly shown in the curves of θ by H/H_a ratio. The value for anisotropy field is extracted from the adjustment process itself. For the presented sample, the corresponding values are of 5.8 mT and 6.0 mT for 45WB and 90WB geometries, respectively. Slightly above $H = 0.5H_a$, magnetization direction jumps close to 150° , then starts to reduce towards 90° with increasing applied field. This smooth rotation is also responsible for the curved extremities in the V_{meas} curves, instead of a flat response for $H > H_a$. In fact, this deviation can be another parameter to be optimized in the fit, which minimizes the global error between the experimental and adjusted curves. The good agreement between experimental data and fit shows that all the presented assumptions so far can be accepted, and device behaves as intended. As already mentioned, another consequence of the fit is the extraction of physical parameters such as anisotropy field H_a value. With H_a and MR ratio, it is possible to calculate the sensitivity using Eq. (2.34). While the anisotropy field is a parameter more homogeneous to the thin film itself, the total MR ratio can be affected by the geometry and magnetization rotation direction. To achieve the maximum value for bridge output in Eq. (2.27), magnetization have to be perpendicular to R_2 and R_4 while parallel to R_1 and R_3 . The opposite configuration results in the minimum output value. This is why adjacent arms have to be at 90° to each other. It is also necessary that all four arms of the Wheatstone bridge present a magnetization that rotates in the same direction. Therefore a small deviation in the direction of the applied field is necessary, to have a component along the easy axis responsible for forcing a direction of magnetization rotation.

It was verified that for the same die, 45WB did not reach same MR ratios as 90WB. This is reflected in the device sensitivity, that won't be the same for a fixed voltage bias.

This difference in MR ratio between both geometries may be due to a different magnitude in standard AMR and PHE terms in the resistivity tensor, as discussed in Section 2.3.1. In single stripes and Wheatstone bridge structure alike, the total signal variation is greater when current density is perpendicular or parallel to easy axis than when it is at an 45° angle.

2.5.4 Noise in Wheatstone Bridge

Sources of electrical noise in LSMO Wheatstone bridge devices are the same presented for a single LSMO stripe: Johnson-Nyquist noise and excess $1/f$ noise modeled by Hooge's empirical equation. But as stripes are interconnected and each element has a independent and uncorrelated noise source, an equivalent noise expression must be obtained. By considering each arm of the bridge as a resistor in series with a voltage noise source, it suffices to apply the superposition theorem and the voltage divider rule. The noise from a single resistor is considered at a time, then a square sum is calculated as sources are uncorrelated. The idea is to consider that one signal terminal is grounded and the other presents a voltage V . This simplifies the voltage difference between both terminals. Using the bridge schematic presented in Fig. 2.22, the contribution V_i of each resistor R_i is

$$\begin{aligned} V_{1,4} &= \frac{R_2 + R_3}{R_1 + R_2 + R_3 + R_4} \cdot e_{n1,4} \\ V_{2,3} &= \frac{R_1 + R_4}{R_1 + R_2 + R_3 + R_4} \cdot e_{n2,3} \end{aligned} \quad (2.39)$$

where e_{ni} is the thermal or $1/f$ noise of the i -th resistor. For thermal noise, it's simply $\sqrt{4k_B T R_i}$. For low-frequency noise, consider that a voltage bias V_{bias} that gives origin to a current I_{bias} flowing strictly between excitation terminals. For a balanced bridge this current is split equally between each segment, so the current through one resistor is $I_{bias}/2$. Fluctuations in resistor conductivity than give rise to the voltage noise e_n expressed by Hooge's relation. And in this case, the expression is $\sqrt{\alpha_H/n \cdot 1/\Omega_i f \cdot R_i^2 (I_{bias}/2)^2}$. Considering an uniform LSMO thin film deposition and etching, the four stripes forming the Wheatstone bridge will present same volume Ω_i and resistance R_i . Substituting e_n expressions in Eq. (2.39) and adding all four contributions, the total noise of a PHEB [64] can be written as

$$S_V = \sqrt{4k_B T R_0 + \frac{\alpha_H}{n} \frac{1}{\Omega f} \frac{V_{bias}^2}{4}} \quad (2.40)$$

which only slightly differs from the noise of a single LSMO resistor stripe.

2.5.5 Detectivity

Finally, the general expression for a sensor's detectivity is recalled: the ratio of total noise by its sensitivity. Using Eqs. (2.34) and (2.40) we obtain the detectivity D in T/ $\sqrt{\text{Hz}}$ for 45WB as

$$D = \mu_0 H_a \frac{R_0}{\Delta R'} \sqrt{\frac{\alpha_H}{n} \frac{1}{4\Omega f} + \frac{4k_B T R_0}{V_{bias}^2}} \quad (2.41)$$

whereas for the 90WB design will be the same expression using ΔR and considering a bias field of $H = H_a/2$. These expressions are the pillars equations of this work. At the end, the goal is to reduce D as much as possible, within the constraints imposed by material choice, target applications and available equipment and instruments.

2.6 Conclusion

After introducing the reader to physical characteristics of the manganite oxide LSMO and how its electric and magnetic properties are entwined due to double-exchange, it was shown how step-induced uniaxial magnetic anisotropy can be achieved by epitaxial deposition on vicinal substrates. Magnetization loops typical of easy and hard axis directions were presented for LSMO single stripe, obtained with MOKE imaging technique. Then, magnetoresistance measurements showed that stripes do present the expected behavior according to the equations developed, both for a current density direction parallel to easy magnetic axis or at a 45° angle. It was also shown that the voltage output of a stripe at 45° has the same shape that when measuring the transverse voltage of a stripe along the easy axis. Both measurements are dependent of the off-diagonal terms of the resistivity tensor, the terms related to the planar Hall effect. For LSMO, the total resistance variation is greater for standard AMR than for PHE.

A preamplifier circuit was built based on commercially available AD8421. This new preamplifier, much more adapted to LSMO samples characteristics, presents two independent channels and a gradiometer output. Experimental values for voltage and current noise were extracted and can be used to fit over noise measurements. The total noise from the LSMO device can be written by the sum of thermal noise and excess $1/f$ noise. The latter is modeled by Hooge's empirical relation, and the squared dependence of voltage bias is indeed obtained. The very low Hooge parameter values found in LSMO, orders of magnitude smaller than GMR and TMR devices, is what makes this material a suitable candidate for high performance magnetic field sensors in low frequency regions.

Lastly, LSMO Wheatstone bridges were fabricated and their principle of operation as AMR sensors was validated. MOKE imaging over the whole structure and obtained magnetization loops show that there is nucleation and propagation of magnetic domains when field is applied parallel to step edges of the vicinal substrate. A coherent magnetization rotation is presented with a 90° sample rotation, with field perpendicular to easy axis. As the information of magnetization direction θ is not obtainable for each arm of the Wheatstone bridge with MOKE imaging, a small deviation δ is performed on purpose to force the direction of magnetization rotation for magnetoresistance measurements. This increases the total output signal variation of 45WB structures and causes a sudden jump in magnetization direction θ , due to a global energy minimum in the magnetic energy curve. As showed in repeatability measurements, this jump poses no problem as it happens outside the working range of the device. With a numerical minimization of uniaxial magnetic energy, the equation of sensor output can be fitted to experimental data, thus showing that the device behaves following the presented equations and allowing the extraction of parameters such as H_a . Lastly, an expression for detectivity is obtained. This expression acts as a guide on how to achieve increased sensor performance.

Bibliography

- [1] J. M. D. Coey, M. Viret, and S. von Molnár. "Mixed-valence manganites". In: *Advances in Physics* 48.2 (1999), pp. 167–293. DOI: [10.1080/000187399243455](https://doi.org/10.1080/000187399243455). eprint: <https://doi.org/10.1080/000187399243455>. URL: <https://doi.org/10.1080/000187399243455>.
- [2] I. Yasuda and M. Hishinuma. "Electrical Conductivity and Chemical Diffusion Coefficient of Strontium-Doped Lanthanum Manganites". In: *Journal of Solid State Chemistry* 123.2 (1996), pp. 382–390. ISSN: 0022-4596. DOI: <https://doi.org/10.1006/jssc.1996.0193>. URL: <https://www.sciencedirect.com/science/article/pii/S0022459696901930>.

- [3] J. Wolfman, Ch. Simon, M. Hervieu, A. Maignan, and B. Raveau. “Increase of T_N up to 190 K in the Type II CMR Manganite $\text{Pr}_{1/2}\text{Sr}_{1/2}\text{MnO}_3$ ”. In: *Journal of Solid State Chemistry* 123.2 (1996), pp. 413–416. ISSN: 0022-4596. DOI: <https://doi.org/10.1006/jssc.1996.0197>. URL: <https://www.sciencedirect.com/science/article/pii/S0022459696901978>.
- [4] J. Hemberger, A. Krimmel, T. Kurz, H.-A. Krug von Nidda, V. Yu. Ivanov, A. A. Mukhin, A. M. Balbashov, and A. Loidl. “Structural, magnetic, and electrical properties of single-crystalline $\text{La}_{1-x}\text{Sr}_x\text{MnO}_3$ ($0.4 < x < 0.85$)”. In: *Phys. Rev. B* 66 (9 July 2002), p. 094410. DOI: 10.1103/PhysRevB.66.094410. URL: <https://link.aps.org/doi/10.1103/PhysRevB.66.094410>.
- [5] W. E. Pickett and D. J. Singh. “Electronic structure and half-metallic transport in the $\text{La}_{1-x}\text{Ca}_x\text{MnO}_3$ system”. In: *Phys. Rev. B* 53 (3 Jan. 1996), pp. 1146–1160. DOI: 10.1103/PhysRevB.53.1146. URL: <https://link.aps.org/doi/10.1103/PhysRevB.53.1146>.
- [6] K. I. Doig, F. Aguesse, A. K. Axelsson, N. M. Alford, S. Nawaz, V. R. Palkar, S. P. P. Jones, R. D. Johnson, R. A. Synowicki, and J. Lloyd-Hughes. “Coherent magnon and acoustic phonon dynamics in tetragonal and rare-earth-doped BiFeO_3 multiferroic thin films”. In: *Phys. Rev. B* 88 (9 Sept. 2013), p. 094425. DOI: 10.1103/PhysRevB.88.094425. URL: <https://link.aps.org/doi/10.1103/PhysRevB.88.094425>.
- [7] C. Zener. “Interaction between the d -Shells in the Transition Metals. II. Ferromagnetic Compounds of Manganese with Perovskite Structure”. In: *Phys. Rev.* 82 (3 May 1951), pp. 403–405. DOI: 10.1103/PhysRev.82.403. URL: <https://link.aps.org/doi/10.1103/PhysRev.82.403>.
- [8] G. H. Jonker and J. H. Van Santen. “Ferromagnetic compounds of manganese with perovskite structure”. In: *Physica* 16.3 (Mar. 1950), pp. 337–349. DOI: 10.1016/0031-8914(50)90033-4.
- [9] Matthias Opel. “Spintronic oxides grown by laser-MBE”. In: *Journal of Physics D: Applied Physics* 45.3 (Dec. 2011), p. 033001. DOI: 10.1088/0022-3727/45/3/033001. URL: <https://doi.org/10.1088/0022-3727/45/3/033001>.
- [10] A. J. Millis, B. I. Shraiman, and R. Mueller. “Dynamic Jahn-Teller Effect and Colossal Magnetoresistance in $\text{La}_{1-x}\text{Sr}_x\text{MnO}_3$ ”. In: *Phys. Rev. Lett.* 77 (1 July 1996), pp. 175–178. DOI: 10.1103/PhysRevLett.77.175. URL: <https://link.aps.org/doi/10.1103/PhysRevLett.77.175>.
- [11] M. Izumi, Y. Ogimoto, Y. Konishi, T. Manako, M. Kawasaki, and Y. Tokura. “Perovskite superlattices as tailored materials of correlated electrons”. In: *Materials Science and Engineering: B* 84.1 (2001), pp. 53–57. ISSN: 0921-5107. DOI: [https://doi.org/10.1016/S0921-5107\(01\)00569-4](https://doi.org/10.1016/S0921-5107(01)00569-4). URL: <https://www.sciencedirect.com/science/article/pii/S0921510701005694>.
- [12] W. Prellier, A. Biswas, M. Rajeswari, T. Venkatesan, and R. L. Greene. “Effect of substrate-induced strain on the charge-ordering transition in $\text{Nd}_{0.5}\text{Sr}_{0.5}\text{MnO}_3$ thin films”. In: *Applied Physics Letters* 75.3 (1999), pp. 397–399. DOI: 10.1063/1.124387. eprint: <https://doi.org/10.1063/1.124387>. URL: <https://doi.org/10.1063/1.124387>.
- [13] W. Prellier, M. Rajeswari, T. Venkatesan, and R. L. Greene. “Effects of annealing and strain on $\text{La}_{1-x}\text{Ca}_x\text{MnO}_3$ thin films: A phase diagram in the ferromagnetic region”. In: *Applied Physics Letters* 75.10 (1999), pp. 1446–1448. DOI: 10.1063/1.124720. eprint: <https://doi.org/10.1063/1.124720>. URL: <https://doi.org/10.1063/1.124720>.

-
- [14] M. Španková, V. Štrbík, Š. Chromik, D. Zheng, J. Li, D. Machajdík, A. Kobzev, T. Plecenik, and M. Sojková. “Characterization of Epitaxial LSMO Films Grown on STO Substrates”. In: *Acta Physica Polonica A* 131.4 (Apr. 2017), pp. 848–850. ISSN: 0587-4246.
- [15] A. J. Millis, T. Darling, and A. Migliori. “Quantifying strain dependence in “colossal” magnetoresistance manganites”. In: *Journal of Applied Physics* 83.3 (1998), pp. 1588–1591. DOI: 10.1063/1.367310. eprint: <https://doi.org/10.1063/1.367310>. URL: <https://doi.org/10.1063/1.367310>.
- [16] O. F. Schirmer. “Jahn-Teller Polarons in Oxide Perovskites”. In: *Ferroelectrics* 303.1 (2004), pp. 131–135. DOI: 10.1080/00150190490452947. eprint: <https://doi.org/10.1080/00150190490452947>. URL: <https://doi.org/10.1080/00150190490452947>.
- [17] C. Adamo, X. Ke, H. Q. Wang, H. L. Xin, T. Heeg, M. E. Hawley, W. Zander, J. Schubert, P. Schiffer, D. A. Muller, L. Maritato, and D. G. Schlom. “Effect of biaxial strain on the electrical and magnetic properties of (001) $\text{La}_{0.7}\text{Sr}_{0.3}\text{MnO}_3$ thin films”. In: *Applied Physics Letters* 95.11 (2009), p. 112504. DOI: 10.1063/1.3213346. eprint: <https://doi.org/10.1063/1.3213346>. URL: <https://doi.org/10.1063/1.3213346>.
- [18] M. Španková, V. Štrbík, E. Dobročka, Š. Chromik, M. Sojková, M. Zheng, and J. Li. “Characterization of epitaxial LSMO thin films with high Curie temperature prepared on different substrates”. In: *Vacuum* 126 (2016), pp. 24–28. ISSN: 0042-207X. DOI: <https://doi.org/10.1016/j.vacuum.2016.01.009>. URL: <https://www.sciencedirect.com/science/article/pii/S0042207X16300094>.
- [19] L. Ranno, A. Llobet, R. Tiron, and E. Favre-Nicolin. “Strain-induced magnetic anisotropy in epitaxial manganite films”. In: *Applied Surface Science* 188.1 (2002), pp. 170–175. ISSN: 0169-4332. DOI: [https://doi.org/10.1016/S0169-4332\(01\)00730-9](https://doi.org/10.1016/S0169-4332(01)00730-9). URL: <https://www.sciencedirect.com/science/article/pii/S0169433201007309>.
- [20] B. Wang, L. You, P. Ren, X. Yin, Y. Peng, B. Xia, L. Wang, X. Yu, S. Mui Poh, P. Yang, G. Yuan, L. Chen, A. Rusydi, and J. Wang. “Oxygen-driven anisotropic transport in ultra-thin manganite films”. In: *Nature Communications* 4.2778 (2013). DOI: 10.1038/ncomms3778. URL: <https://doi.org/10.1038/ncomms3778>.
- [21] C. D. Damsgaard, S. C. Freitas, P. P. Freitas, and M. F. Hansen. “Exchange-biased planar Hall effect sensor optimized for biosensor applications”. In: *Journal of Applied Physics* 103.7 (2008), 07A302. DOI: 10.1063/1.2830008. eprint: <https://doi.org/10.1063/1.2830008>. URL: <https://doi.org/10.1063/1.2830008>.
- [22] V. Mor, M. Schultz, O. Sinwani, A. Grosz, E. Paperno, and L. Klein. “Planar Hall effect sensors with shape-induced effective single domain behavior”. In: *Journal of Applied Physics* 111.7 (2012), 07E519. DOI: 10.1063/1.3680084. eprint: <https://doi.org/10.1063/1.3680084>. URL: <https://doi.org/10.1063/1.3680084>.
- [23] P. Perna, C. Rodrigo, E. Jiménez, F. J. Teran, N. Mikuszeit, L. Méchin, J. Camarero, and R. Miranda. “Tailoring magnetic anisotropy in epitaxial half metallic $\text{La}_{0.7}\text{Sr}_{0.3}\text{MnO}_3$ thin films”. In: *Journal of Applied Physics* 110.1 (July 2011), p. 013919. ISSN: 1089-7550. DOI: 10.1063/1.3605542. URL: <http://dx.doi.org/10.1063/1.3605542>.
- [24] C. Tannous and J. Gieraltowski. “The Stoner-Wohlfarth model of ferromagnetism”. In: *European Journal of Physics* 29.3 (Mar. 2008), pp. 475–487. DOI: 10.1088/0143-0807/29/3/008. URL: <https://doi.org/10.1088/0143-0807/29/3/008>.
-

- [25] R. P. Brent. “An algorithm with guaranteed convergence for finding a zero of a function”. In: *The Computer Journal* 14.4 (Jan. 1971), pp. 422–425. ISSN: 0010-4620. DOI: 10.1093/comjnl/14.4.422. eprint: <https://academic.oup.com/comjnl/article-pdf/14/4/422/927778/140422.pdf>. URL: <https://doi.org/10.1093/comjnl/14.4.422>.
- [26] M. Mathews, F. M. Postma, J. C. Lodder, R. Jansen, G. Rijnders, and D. H. A. Blank. “Step-induced uniaxial magnetic anisotropy of $\text{La}_{0.67}\text{Sr}_{0.33}\text{MnO}_3$ thin films”. In: *Applied Physics Letters* 87.24 (2005), p. 242507. DOI: 10.1063/1.2143136. eprint: <https://doi.org/10.1063/1.2143136>. URL: <https://doi.org/10.1063/1.2143136>.
- [27] Z. H. Wang, G. Cristiani, and H. U. Habermeier. “Uniaxial magnetic anisotropy and magnetic switching in $\text{La}_{0.67}\text{Sr}_{0.33}\text{MnO}_3$ thin films grown on vicinal $\text{SrTiO}_3(100)$ ”. In: *Applied Physics Letters* 82.21 (2003), pp. 3731–3733. DOI: 10.1063/1.1578711. eprint: <https://doi.org/10.1063/1.1578711>. URL: <https://doi.org/10.1063/1.1578711>.
- [28] L. Néel. “Anisotropie magnétique superficielle et surstructures d’orientation”. In: *J. Phys. Radium* 15.4 (1954), pp. 225–239. DOI: 10.1051/jphysrad:01954001504022500. URL: <https://doi.org/10.1051/jphysrad:01954001504022500>.
- [29] D. S. Chuang, C. A. Ballentine, and R. C. O’Handley. “Surface and step magnetic anisotropy”. In: *Phys. Rev. B* 49 (21 June 1994), pp. 15084–15095. DOI: 10.1103/PhysRevB.49.15084. URL: <https://link.aps.org/doi/10.1103/PhysRevB.49.15084>.
- [30] Y. Z. Wu, C. Won, and Z. Q. Qiu. “Magnetic uniaxial anisotropy of Fe films grown on vicinal $\text{Ag}(001)$ ”. In: *Phys. Rev. B* 65 (18 Apr. 2002), p. 184419. DOI: 10.1103/PhysRevB.65.184419. URL: <https://link.aps.org/doi/10.1103/PhysRevB.65.184419>.
- [31] P. Perna, L. Méchin, M. Saïb, J. Camarero, and S. Flament. “Imaging the magnetization reversal of step-induced uniaxial magnetic anisotropy in vicinal epitaxial $\text{La}_{0.7}\text{Sr}_{0.3}\text{MnO}_3$ films”. In: *New Journal of Physics* 12.10 (Oct. 2010), p. 103033. DOI: 10.1088/1367-2630/12/10/103033. URL: <https://doi.org/10.1088/1367-2630/12/10/103033>.
- [32] R. K. Kawakami, E. J. Escorcia-Aparicio, and Z. Q. Qiu. “Symmetry-Induced Magnetic Anisotropy in Fe Films Grown on Stepped $\text{Ag}(001)$ ”. In: *Phys. Rev. Lett.* 77 (12 Sept. 1996), pp. 2570–2573. DOI: 10.1103/PhysRevLett.77.2570. URL: <https://link.aps.org/doi/10.1103/PhysRevLett.77.2570>.
- [33] P. Perna, C. Rodrigo, E. Jiménez, N. Mikuszeit, F. J. Teran, L. Méchin, J. Camarero, and R. Miranda. “Magnetization reversal in half metallic $\text{La}_{0.7}\text{Sr}_{0.3}\text{MnO}_3$ films grown onto vicinal surfaces”. In: *Journal of Applied Physics* 109.7 (2011), 07B107. DOI: 10.1063/1.3560893. eprint: <https://doi.org/10.1063/1.3560893>. URL: <https://doi.org/10.1063/1.3560893>.
- [34] P. Perna, D. Maccariello, F. Ajejas, R. Guerrero, L. Méchin, S. Flament, J. Santamaria, R. Miranda, and J. Camarero. “Engineering Large Anisotropic Magnetoresistance in $\text{La}_{0.7}\text{Sr}_{0.3}\text{MnO}_3$ Films at Room Temperature”. In: *Advanced Functional Materials* 27.26 (2017), p. 1700664. DOI: <https://doi.org/10.1002/adfm.201700664>. eprint: <https://onlinelibrary.wiley.com/doi/pdf/10.1002/adfm.201700664>. URL: <https://onlinelibrary.wiley.com/doi/abs/10.1002/adfm.201700664>.
- [35] L. Méchin, P. Perna, M. Saïb, M. Belmeguenai, S. Flament, C. Barone, J. Routoure, and Ch. Simon. “Structural, $1/f$ Noise and MOKE Characterization of Vicinal $\text{La}_{0.7}\text{Sr}_{0.3}\text{MnO}_3$ Thin Films”. In: *Acta Physica Polonica A* 111.1 (Jan. 2007), pp. 63–70. ISSN: 0587-4246.

- [36] S. Kokado, M. Tsunoda, K. Harigaya, and A. Sakuma. “Anisotropic Magnetoresistance Effects in Fe, Co, Ni, Fe₄N, and Half-Metallic Ferromagnet: A Systematic Analysis”. In: *Journal of the Physical Society of Japan* 81.2 (2012), p. 024705. DOI: 10.1143/JPSJ.81.024705. eprint: <https://doi.org/10.1143/JPSJ.81.024705>. URL: <https://doi.org/10.1143/JPSJ.81.024705>.
- [37] J. B. Yau, X. Hong, A. Posadas, C. H. Ahn, W. Gao, E. Altman, Y. Bason, L. Klein, M. Sidorov, and Z. Krivokapic. “Anisotropic magnetoresistance in colossal magnetoresistive La_{1-x}Sr_xMnO₃ thin films”. In: *Journal of Applied Physics* 102.10 (2007), p. 103901. DOI: 10.1063/1.2811919. eprint: <https://doi.org/10.1063/1.2811919>. URL: <https://doi.org/10.1063/1.2811919>.
- [38] X. Hong, J. B. Yau, J. D. Hoffman, C. H. Ahn, Y. Bason, and L. Klein. “Effect of electric field doping on the anisotropic magnetoresistance in doped manganites”. In: *Phys. Rev. B* 74 (17 Nov. 2006), p. 174406. DOI: 10.1103/PhysRevB.74.174406. URL: <https://link.aps.org/doi/10.1103/PhysRevB.74.174406>.
- [39] D. Fadil, S. Wu, P. Perna, B. Renault, M. Saïb, S. Lebargy, J. Gasnier, B. Guillet, J. M. Routoure, S. Flament, and L. Méchin. “Direct observation of magnetization reversal and low field magnetoresistance of epitaxial La_{0.7}Sr_{0.3}MnO₃/SrTiO₃ (001) thin films at room temperature”. In: *Journal of Applied Physics* 112.1 (2012), p. 013906. DOI: 10.1063/1.4730966. eprint: <https://doi.org/10.1063/1.4730966>. URL: <https://doi.org/10.1063/1.4730966>.
- [40] C. Goldberg and R. E. Davis. “New Galvanomagnetic Effect”. In: *Phys. Rev.* 94 (5 June 1954), pp. 1121–1125. DOI: 10.1103/PhysRev.94.1121. URL: <https://link.aps.org/doi/10.1103/PhysRev.94.1121>.
- [41] F. G. West. “Rotating-Field Technique for Galvanomagnetic Measurements”. In: *Journal of Applied Physics* 34.4 (1963), pp. 1171–1173. DOI: 10.1063/1.1729418. eprint: <https://doi.org/10.1063/1.1729418>. URL: <https://doi.org/10.1063/1.1729418>.
- [42] K. M. Seemann, F. Freimuth, H. Zhang, S. Blügel, Y. Mokrousov, D. E. Bürgler, and C. M. Schneider. “Origin of the Planar Hall Effect in Nanocrystalline Co₆₀Fe₂₀B₂₀”. In: *Phys. Rev. Lett.* 107 (8 Aug. 2011), p. 086603. DOI: 10.1103/PhysRevLett.107.086603. URL: <https://link.aps.org/doi/10.1103/PhysRevLett.107.086603>.
- [43] Y. Bason, L. Klein, J. B. Yau, X. Hong, and C. H. Ahn. “Giant planar Hall effect in colossal magnetoresistive La_{0.84}Sr_{0.16}MnO₃ thin films”. In: *Applied Physics Letters* 84.14 (2004), pp. 2593–2595. DOI: 10.1063/1.1695197. eprint: <https://doi.org/10.1063/1.1695197>. URL: <https://doi.org/10.1063/1.1695197>.
- [44] C.D Motchenbacher and J. A. Connelly. *Low-Noise Electronic System Design*. Wiley, 1993. ISBN: 978-0-471-57742-3.
- [45] S. Wu. “Bruit basse fréquence dans des couches minces de La_{0.7}Sr_{0.3}MnO₃ gravées : vers la réalisation de micro-capteurs performants”. Theses. Université de Caen, July 2012. URL: <https://hal.archives-ouvertes.fr/tel-01077315>.
- [46] J. B. Johnson. “Thermal Agitation of Electricity in Conductors”. In: *Phys. Rev.* 32 (1 1928), pp. 97–109. DOI: 10.1103/PhysRev.32.97. URL: <https://link.aps.org/doi/10.1103/PhysRev.32.97>.
- [47] H. Nyquist. “Thermal Agitation of Electric Charge in Conductors”. In: *Phys. Rev.* 32 (1 1928), pp. 110–113. DOI: 10.1103/PhysRev.32.110. URL: <https://link.aps.org/doi/10.1103/PhysRev.32.110>.
- [48] D. Halford. “A general mechanical model for $|f|^\alpha$ spectral density random noise with special reference to flicker noise $1/|f|$ ”. In: *Proceedings of the IEEE* 56.3 (1968), pp. 251–258. DOI: 10.1109/PROC.1968.6269.

- [49] M. S. Keshner. “1/f noise”. In: *Proceedings of the IEEE* 70.3 (1982), pp. 212–218. DOI: 10.1109/PROC.1982.12282.
- [50] F. N. Hooge. “1/f noise is no surface effect”. In: *Physics Letters A* 29.3 (1969), pp. 139–140. ISSN: 0375-9601. DOI: [https://doi.org/10.1016/0375-9601\(69\)90076-0](https://doi.org/10.1016/0375-9601(69)90076-0).
- [51] L. Méchin, S. Wu, B. Guillet, P. Perna, C. Fur, S. Lebargy, C. Adamo, D.G. Schlom, and J. M. Routoure. “Experimental evidence of correlation between 1/f noise level and metal-to-insulator transition temperature in epitaxial $\text{La}_{0.7}\text{Sr}_{0.3}\text{MnO}_3$ thin films”. In: *J. Phys. D: Appl. Phys. - Fast Track Communication* 46 (2013), p. 202001. URL: <https://hal.archives-ouvertes.fr/hal-00977721>.
- [52] J. Y. Chen, J. F. Feng, and J. M. D. Coey. “Tunable linear magnetoresistance in MgO magnetic tunnel junction sensors using two pinned CoFeB electrodes”. In: *Appl. Phys. Lett.* 100 (2012), p. 142407. DOI: 10.1063/1.4978465. URL: <https://doi.org/10.1063/1.4978465>.
- [53] J. Scola, H. Polovy, C. Fermon, M. Pannetier-Lecœur, G. Feng, K. Fahy, and J. M. D. Coey. “Noise in MgO barrier magnetic tunnel junctions with CoFeB electrodes: Influence of annealing temperature”. In: *Applied Physics Letters* 90.25 (2007), p. 252501. DOI: 10.1063/1.2749433. eprint: <https://doi.org/10.1063/1.2749433>. URL: <https://doi.org/10.1063/1.2749433>.
- [54] H. Weitensfelder, H. Brueckl, A. Satz, K. Pruegl, J. Zimmer, S. Luber, W. Raberg, C. Abert, F. Bruckner, A. Bachleitner-Hofmann, R Windl, and D. Suess. “Comparison of Sensitivity and Low-Frequency Noise Contributions in Giant-Magnetoresistive and Tunneling-Magnetoresistive Spin-Valve Sensors with a Vortex-State Free Layer”. In: *Physical Review Applied* 10.5 (Nov. 2018). ISSN: 2331-7019. DOI: 10.1103/physrevapplied.10.054056. URL: <http://dx.doi.org/10.1103/PhysRevApplied.10.054056>.
- [55] K. Fujiwara, M. Oogane, D. Kato, T. Nishikawa, H. Naganuma, and Y. Ando. “Fabrication of Integrated Magnetic Tunnel Junctions for Detection of Bio-magnetic Field”. In: *Transactions of Japanese Society for Medical and Biological Engineering* 52.Supplement (2014), O-505-O-506. DOI: 10.11239/jsmbe.52.0-505.
- [56] A. D. Henriksen, B. T. Dalslet, D. H. Skieller, K. H. Lee, F. Okkels, and M. F. Hansen. “Planar Hall effect bridge magnetic field sensors”. In: *Applied Physics Letters* 97.1 (2010), p. 013507. DOI: 10.1063/1.3460290. eprint: <https://doi.org/10.1063/1.3460290>. URL: <https://doi.org/10.1063/1.3460290>.
- [57] A. D. Henriksen, G. Rizzi, and M. F. Hansen. “Experimental comparison of ring and diamond shaped planar Hall effect bridge magnetic field sensors”. In: *Journal of Applied Physics* 118.10 (2015), p. 103901. DOI: 10.1063/1.4930068. eprint: <https://doi.org/10.1063/1.4930068>. URL: <https://doi.org/10.1063/1.4930068>.
- [58] F. W. Østerberg, A. D. Henriksen, G. Rizzi, and M. F. Hansen. “Comment on “Planar Hall resistance ring sensor based on NiFe/Cu/IrMn trilayer structure” [J. Appl. Phys. 113, 063903 (2013)]”. In: *Journal of Applied Physics* 114.10 (2013), p. 106101. DOI: 10.1063/1.4820925. eprint: <https://doi.org/10.1063/1.4820925>. URL: <https://doi.org/10.1063/1.4820925>.
- [59] M. J. Haji-Sheikh and Y. Yoo. “An accurate model of highly ordered 81/19 Permalloy AMR Wheatstone bridge sensor against a 48 pole pair ring-magnet”. In: *International Journal of Intelligent Systems Technologies and Applications* 3.1/2 (2007), pp. 95–105. DOI: 10.1504/IJISTA.2007.014129.

-
- [60] L. K. Quynh, B. D. Tu, D. X. Dang, D. Q. Viet, L. T. Hien, D. T. Huong Giang, and N. H. Duc. “Detection of magnetic nanoparticles using simple AMR sensors in Wheatstone bridge”. In: *Journal of Science: Advanced Materials and Devices* 1.1 (2016), pp. 98–102. ISSN: 2468-2179. DOI: <https://doi.org/10.1016/j.jsamd.2016.04.006>. URL: <https://www.sciencedirect.com/science/article/pii/S2468217916300168>.
- [61] P. Perna, C. Rodrigo, E. Jiménez, N. Mikuszeit, F. J. Teran, L. Méchin, J. Camarero, and R. Miranda. “Magnetization reversal in half metallic $\text{La}_{0.7}\text{Sr}_{0.3}\text{MnO}_3$ films grown onto vicinal surfaces”. In: *Journal of Applied Physics* 109.7 (2011), 07B107. DOI: 10.1063/1.3560893. eprint: <https://doi.org/10.1063/1.3560893>. URL: <https://doi.org/10.1063/1.3560893>.
- [62] R. Storn and K. Price. “Differential Evolution – A Simple and Efficient Heuristic for global Optimization over Continuous Spaces”. In: *Journal of Global Optimization* 11.4 (Dec. 1997), pp. 341–359. ISSN: 1573-2916. DOI: 10.1023/A:1008202821328. URL: <https://doi.org/10.1023/A:1008202821328>.
- [63] M. A. Branch, T. F. Coleman, and Y. Li. “A Subspace, Interior, and Conjugate Gradient Method for Large-Scale Bound-Constrained Minimization Problems”. In: *SIAM Journal on Scientific Computing* 21.1 (1999), pp. 1–23. DOI: 10.1137/S1064827595289108. eprint: <https://doi.org/10.1137/S1064827595289108>. URL: <https://doi.org/10.1137/S1064827595289108>.
- [64] A. Persson, R.S. Bejhed, H. Nguyen, K. Gunnarsson, B.T. Dalslet, F.W. Østerberg, M.F. Hansen, and P. Svedlindh. “Low-frequency noise in planar Hall effect bridge sensors”. In: *Sensors and Actuators A: Physical* 171.2 (2011), pp. 212–218. ISSN: 0924-4247. DOI: <https://doi.org/10.1016/j.sna.2011.09.014>. URL: <https://www.sciencedirect.com/science/article/pii/S0924424711005280>.

Chapter III

Sensor Optimization

Now that the operation of the device is validated, the focus can be shifted towards sensor optimization by following the detectivity expression obtained at the end of the previous chapter and by tweaking fabrication parameters. First, operation at different voltage bias and temperature was investigated. This can be easily done without changing the sample loaded in the probe station. Then the effects of different fabrication parameters on sensor performance were analyzed: thin film thickness, vicinal angle of substrate, substrate temperature during PLD deposition and design of lithography masks. Regarding the different lithography mask designs, the distribution of current density and effect of size were also investigated.

Due to the nature of this device, with magnetic and electrical properties linked by the double-exchange mechanism and uniaxial magnetic anisotropy induced by epitaxial deposition on a vicinal substrate, there is not a complete expression that estimates all the effects when a single fabrication parameter is changed. Experimental data obtained with a hands-on approach is crucial to sensor optimization, as some unexpected effects may arise. This chapter also presents some characterization results obtained at IMDEA Nanociencia, a partner laboratory in the ByAxon European project. For an explanation of sample fabrication, please refer to Appendix Fabrication, and further information on characterization equipment is available in Appendix Characterization.

3.1 Effect of bias voltage and operation temperature

Following the equation for detectivity

$$D = \mu_0 H_a \frac{R_0}{\Delta R} \sqrt{\frac{\alpha_H}{n} \frac{1}{4\Omega f} + \frac{4k_B T R_0}{V_{bias}^2}} \quad (3.1)$$

first presented at the end of the previous chapter, the easiest effect to be investigated is that of the bias voltage V_{bias} . Provided that contribution from the LSMO sample itself dominates total noise, its increase should affect the performance of the sensor only in the white noise region. Therefore having a low noise preamplifier properly adapted to the characteristics of the sample is crucial. Let's take as an example sample BA055, with nominal 30 nm thick LSMO deposited over 4° vicinal STO. Curves for V_{meas} are shown in Fig. 3.1. It is from the derivative of V_{meas} curves, in the linear operation region, that sensitivity values are obtained to calculate the detectivity of the sensor. Noise curves at increasing V_{bias} for a 90WB structure were measured both with the previously available preamplifier and the one developed during this thesis, and are presented in Fig. 3.2. This bridge has a 5.5 kΩ equivalent resistance measured in 2-probes configuration. Comparing noise curves at 0 V, 1 V and 5 V between the two amplifiers, one can see that with AD743 there is a greater contribution from preamplifier noise in the low frequency region. This becomes easier to see in detectivity curves, presented in Fig. 3.3. With noise measured

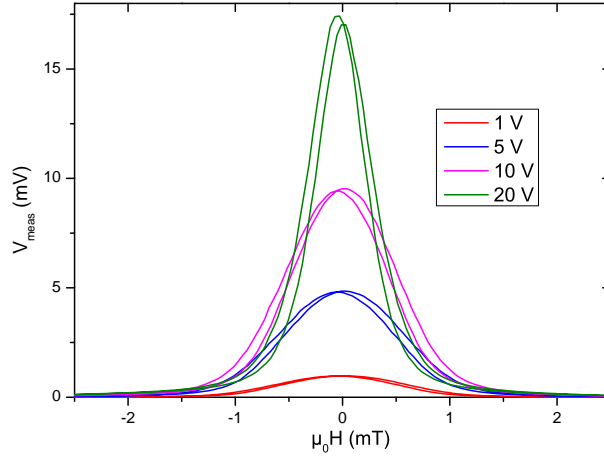


Figure 3.1: Output of a 90WB structure at 310 K, with offset suppression. [Sample BA055]

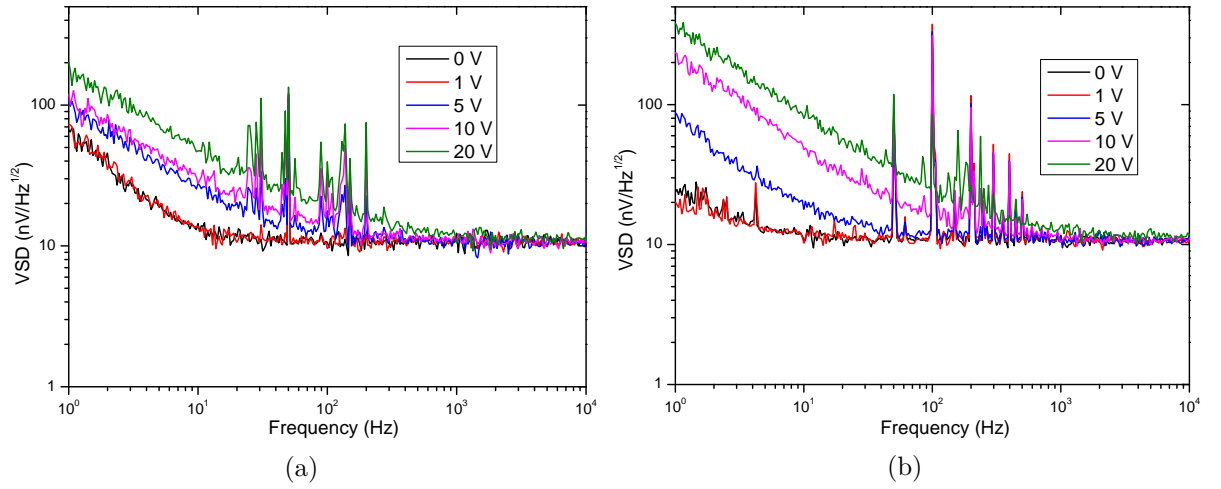


Figure 3.2: Noise curves obtained with different preamplifiers. a) Previously available preamplifier based on AD743. b) New preamplifier based on AD8421. [Sample BA055]

with AD743, detectivity decreases with higher V_{bias} even in low frequency region, different from what expected in Eq. (3.1). With noise measured using the new amplifier, curves follow the expected behavior when sample noise is the dominant contribution. The same value of sensitivity was used in both cases. The increased low frequency noise above 5 V bias when using AD8421 might be due to a different contact noise contribution, as sample was manipulated and metallic probes for measurements were moved. The two sets of measurements were performed several weeks apart.

In Fig. 3.4, curves of V_{meas} , noise and detectivity at increasing voltage bias for a 45WB structure are presented. Sample is BA114, with nominal 45 nm LSMO thickness over 4° vicinal STO. In this case, the step for V_{bias} was smaller, and we see that sample noise starts to dominate at 2.5 V. Sensitivity is obtained around zero applied field, thanks to linear behavior of the 45WB structure. The correct setup for noise measurement results in detectivity curves that follow the expected behavior: similar performance in $1/f$ noise region and increased performance in white noise region.

The power provided to the sample has a quadratic increase with bias, which can also lead to self heating due to the Joule effect. Theoretically, it seems of best interest to use the highest voltage bias as possible. It would ensure that the sample itself dominates the total noise and improve performance in the thermal noise region. But voltage bias is limited experimentally by several factors. At the device level, an increase in current density through the material not only causes a self heating effect, but a too high current may create defects in the crystalline structure due to electromigration [1]. Experiments with high

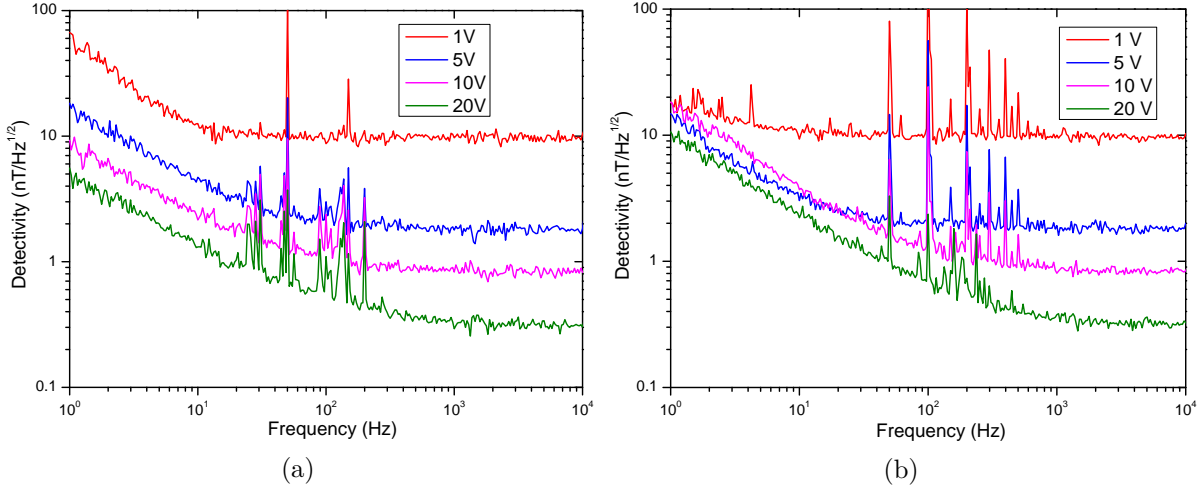


Figure 3.3: Obtained detectivity curves. a) Apparent overall decrease of detectivity due to the preamplifier with AD743. b) Performance in low frequency region independent of voltage bias using AD8421. [Sample BA055]

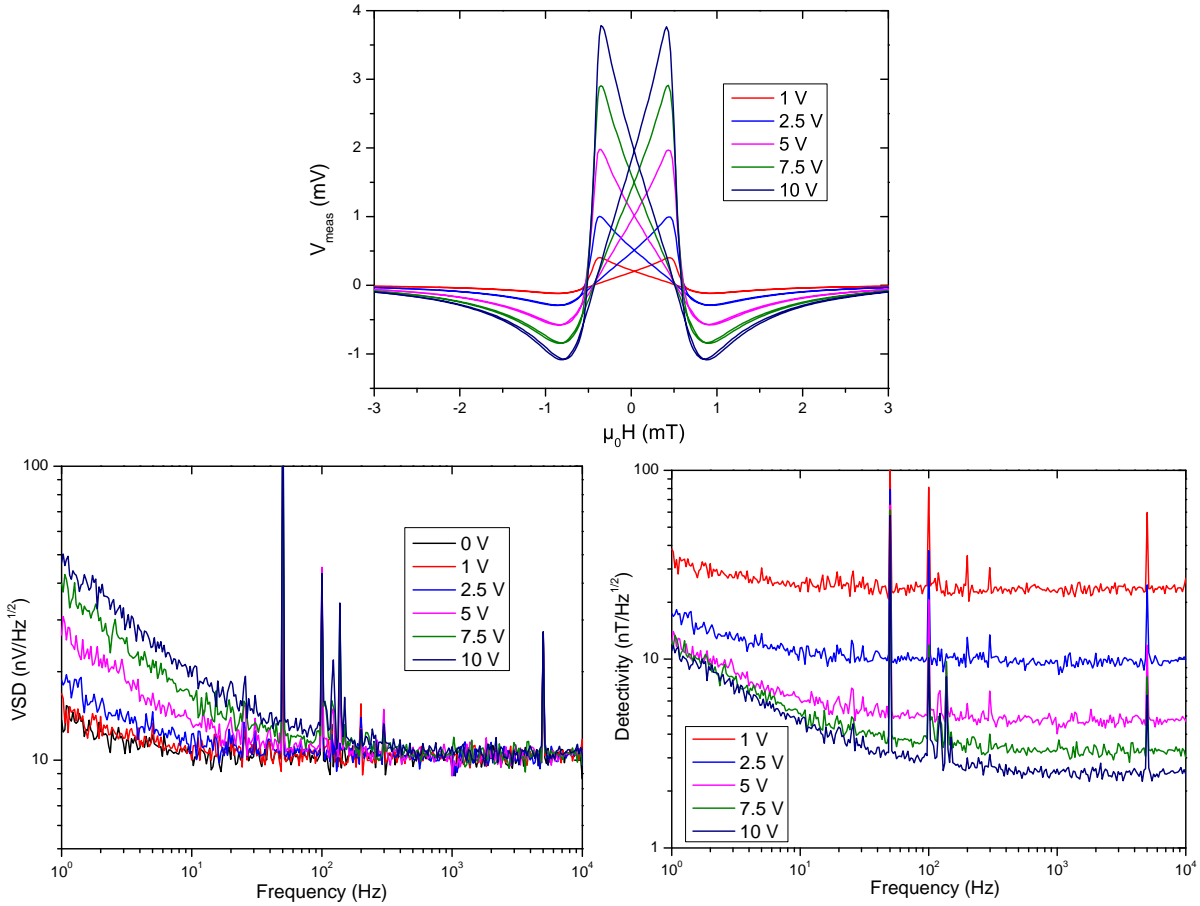


Figure 3.4: Evolution of 45WB structure performance with increasing V_{bias} . a) Sensor output, c) noise and d) detectivity. [Sample BA114]

tunnel current showed the displacement of oxygen atoms at the surface of manganites [2]. In this work, possible effects of electromigration were not investigated. At the reading electronics level, the instrumentation preamplifier must work within its common-mode voltage and saturation ranges, both influenced by its voltage supply. When a higher gain in the first stage is used to reduce electronics noise, preamplifier saturation is reached for lower input signal. In other words, for lower voltage bias of the sensor. Everything must

be taken into consideration to achieve a satisfactory balance. As the V_{meas} equation for the 90WB structure has a constant component independent of applied and anisotropy fields, at preamplifier inputs there is a higher DC offset that adds to bridge imbalance. This will lead to saturation of the first stage at much lower voltage biases than those for 45WB structures. To avoid this problem, we could supply the preamplifier with uneven voltage values, such as +24 V and -6 V instead of ± 15 V for example. This will also deform the common-mode voltage region of the preamplifier. Care must then be taken to always supply the Wheatstone bridges with positive voltage values and to have a higher voltage at the positive input of the preamplifier than at the negative input. This solution was tested and it works, but it was decided to keep an even supply and connect the signal terminals of the Wheatstone bridge in any order.

3.1.1 Operating temperature

Another investigation that can be made using the same sample, without comparing effects of fabrication parameters, is by changing the working temperature. When sample is heated above 310 K, it approaches its Curie temperature T_C . Closer to T_C , magnetization saturation M_S reduces. This affects the anisotropy field H_a , previously defined as

$$H_a = \frac{2K_u}{\mu_0 M_S} \quad (3.2)$$

But anisotropy constant K_u is also affected by M_S . Ultimately, anisotropy field can be written to be proportional to M_S^p (magnetization saturation to power p), with p being strictly positive [3, 4]. Therefore, a reduction in M_S leads to a reduction in H_a , increasing sensitivity and decreasing detectivity. In Fig. 3.5, V_{meas} curves at different operating temperatures and fixed 5 V bias are shown, along with fits at selected temperatures to extract values for H_a . Sample is a 45WB structure from BA104, a 60 nm thick LSMO film deposited on 4° vicinal STO at 730 °C. This bridge has a 2.3 k Ω equivalent resistance in 2-probes configuration at 310 K. At 330 K, sample practically lost its ferromagnetic behavior and the corresponding V_{meas} curve is barely visible. Only the sweep from negative to positive field saturation was considered for the fits, performed for 310 K, 315 K and 320 K. The model considers a perfectly uniaxial device, which may not be exactly the case for a 60 nm thick LSMO on top of 4° vicinal STO as will be shown later in thin film thickness comparison. Plus, the jump in the calculated V_{meas} is abrupt, while in the experimental data this jump is a bit smoother. This adds to the total error between measurement and numerical model. Nevertheless, values for anisotropy field can be extracted and a clear reduction with increasing temperature is obtained. Table 3.1 presents the comparison of sensitivity values obtained from the derivative of V_{meas} curves around zero applied field and calculated using the expression

$$S = V_{bias} \frac{\Delta R}{R_0} \frac{1}{\mu_0 H_a} \quad (3.3)$$

In the latter case, the MR ratio $\Delta R/R_0$ can be obtained by $(V_{meas}^{max} - V_{meas}^{min})/V_{bias}$. In fact, the MR ratio decreased with higher operating temperature, but the effect on H_a is dominant. Sensitivity does increase with operating temperature up to the point where sample starts to lose its magnetic properties. Another source of difference between sensitivity values from Eq. (3.3) and derivative of V_{meas} is that the analytical expression considers an applied field perfectly perpendicular to sample easy axis, whereas the experimental V_{meas} curves were obtained with a deviation of $\delta = 12^\circ$. As discussed in the previous chapter, this deviation is done to provoke a homogeneous magnetization rotation in all arms of the 45WB structure. Sample performance can be estimated with Eq. (3.1) using extracted values for MR ratio and H_a and a normalized Hooge parameter α_H/n obtained from a linear fit of average $1/f$ noise at 310 K. A value of $\alpha_H/n = 3 \times 10^{-31} \text{ m}^3$ is obtained as

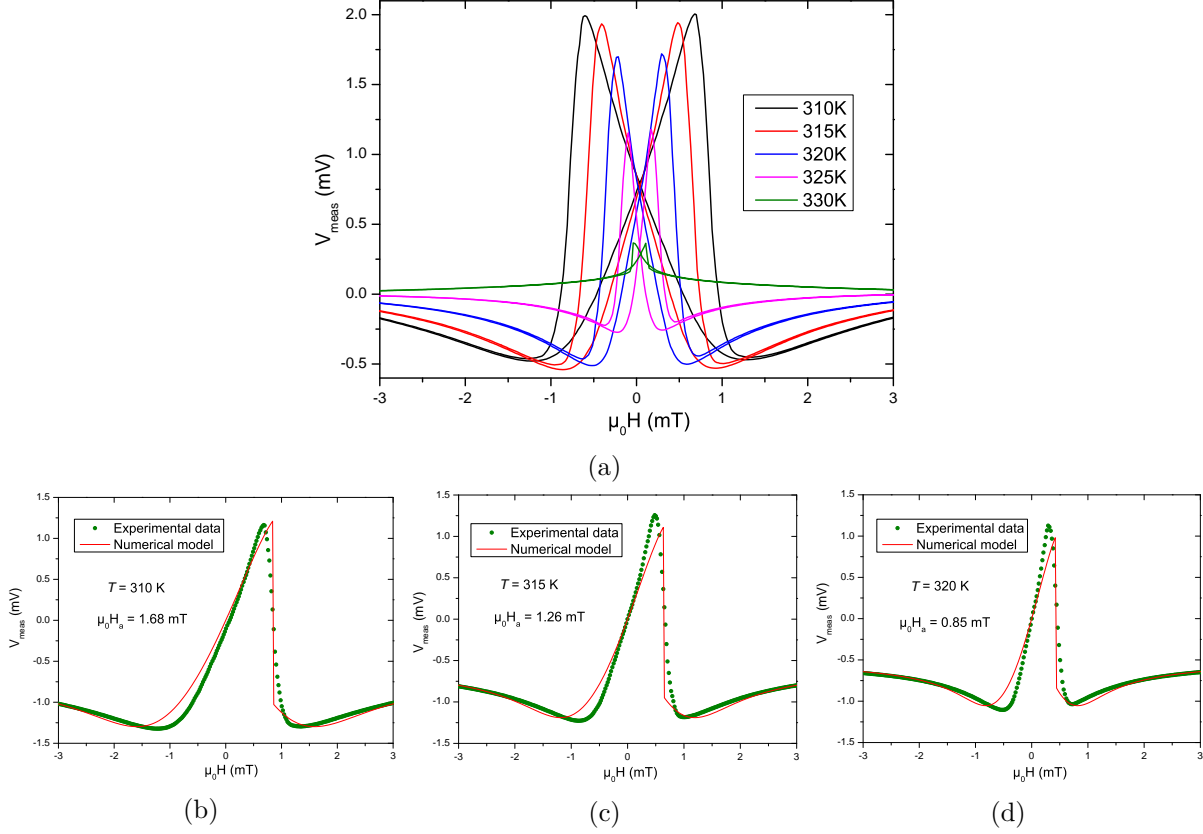


Figure 3.5: Effect of sample temperature on sensor output, at a fixed 5 V bias. a) V_{meas} curves show reduction of both H_a and MR ratio. b, c, d) Fits to sensor output using the previously presented model, allowing the extraction of H_a . Offset is adjusted to have 0 mV output at zero applied field. [Sample BA104]

Working temperature (K)	310	315	320
S from derivative of V_{meas} (V/T)	1.67	2.23	3.37
$\mu_0 H_a$ extracted from model (mT)	1.68	1.26	0.85
S calculated with Eq. (3.3) (V/T)	1.54	1.97	2.64

Table 3.1: Summary of sensitivity and extracted anisotropy field values for increasing working temperature.

shown in Fig. 3.6, along with fits to experimental noise. Sample volume is $7.2 \times 10^{-15} \text{ m}^3$. Noise from preamplifier is considered in the fit, and matching is better for increased bias where sample noise dominates. Considering a fixed α_H/n , $2.3 \text{ k}\Omega$ resistance from 310 K to 320 K and 5 V bias, estimated detectivity curves are presented in Fig. 3.7. A detectivity slightly above $20 \text{ nT Hz}^{-1/2}$ at 1 Hz is obtained at 310 K. This value drops to $13 \text{ nT Hz}^{-1/2}$ at 320 K. In white noise region, detectivity drops from $4.7 \text{ nT Hz}^{-1/2}$ to $2.8 \text{ nT Hz}^{-1/2}$. The fact that sample sensitivity changes with sample temperature was explored more in depth by fellow researchers at IMDEA Nanociencia. All LSMO samples sent were scanned in terms of operating temperature to find the best working point. Figure 3.8 gives an example of the measurements performed. In this case, sample is BA055, 30 nm LSMO on 4° vicinal STO. This 90WB structure sensor presented the highest sensitivity at 41°C , reaching up to $400 \% \text{ T}^{-1}$. Even if MR ratio only decreases with higher temperature, it is for a middle value that the highest sensitivity is reached. This only shows that the effect on anisotropy field reduction dominates. At even higher temperature, sample loses its ferromagnetic properties and sensitivity drops fast. With further studies on different operating temperatures, its effect on H_a and MR ratio could be made more explicit in the detectivity equation.

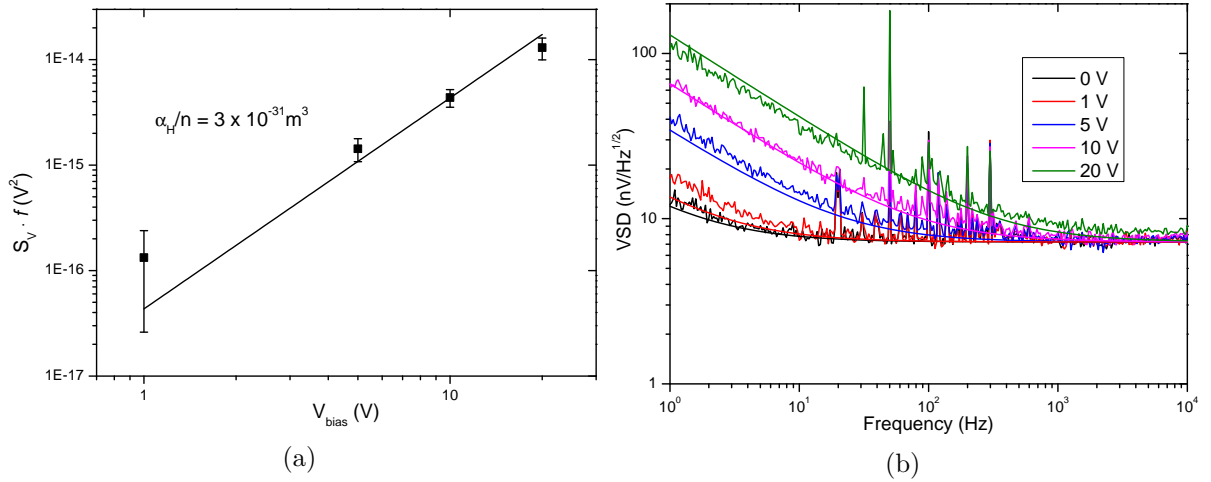


Figure 3.6: Noise characterization at fixed 310 K. a) Extraction of Hooge parameter. b) Straight lines are fits to experimental data using total noise equation and sample parameters. [Sample BA104]

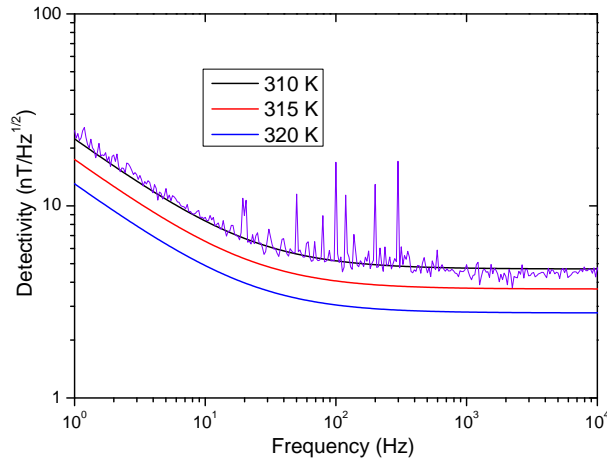


Figure 3.7: Estimated detectivity at 5 V bias for increasing temperature, calculated with extracted $\mu_0 H_a$ and α_H/n . Curve at 310 K is compared to experimental noise divided by sensitivity from the derivative of V_{meas} . [Sample BA104]

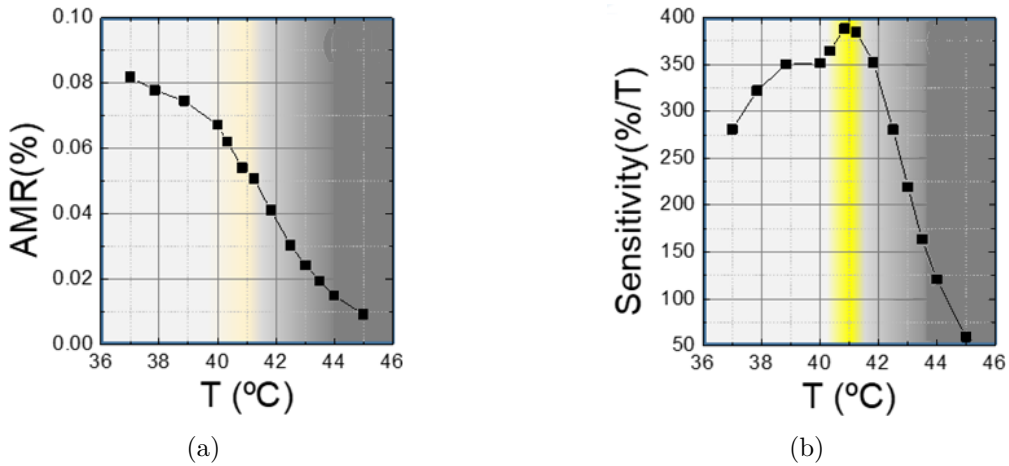


Figure 3.8: Effect of sample temperature as investigated at IMDEA Nanociencia. a) AMR steadily decreases with increasing temperature. b) Highest sensitivity is achieved for 41 °C working temperature. [Sample BA055]

3.2 Effect of thin film thickness

The detectivity of PHEBs based on permalloy and exchange bias interaction can be improved by tuning its geometry, increasing the width w and length l of Wheatstone bridge arms or ferromagnetic thin film thickness t [5]. Persson *et al* showed that while single-domain configuration is maintained, increasing bridge arms length l increases sensor's sensitivity, thus obtaining a lower detectivity for a fixed current bias. As LSMO presents a much higher resistivity than NiFe, an increase in arms length without keeping the same aspect ratio would result in a much higher thermal noise in the manganite oxide samples. Therefore, it was decided to keep unchanged the bridge size while increasing thin film thickness. If the thickness of the thin film is increased while using the same lithography masks for etching the Wheatstone bridge structures, device volume is increased and its resistance is reduced. This ought to reduce noise both in $1/f$ and thermal regions. The first investigation then consisted of a series of samples fabricated with LSMO thicknesses ranging from 30 nm to 90 nm over 4° vicinal STO. Substrate temperature was kept at 730°C during PLD deposition. Due to the miscut angle in the vicinal substrate surface, it was not possible to obtain a RHEED signal during PLD to follow film growth in real time. A calibration of laser shots per LSMO monolayer growth was obtained using flat STO, and that calibration was followed when using vicinal substrates.

While an increased thickness directly increases sample volume and reduces its resistance, unwanted secondary effects may also appear. According to the step-induced anisotropy theory [6], an increase in film thickness t on a substrate with fixed terrace width d reduces the uniaxial anisotropy energy. For a given vicinal angle of the STO substrate, sample will lose a clear uniaxial anisotropy as thickness increases. When that happens, the model for AMR LSMO Wheatstone bridge previously presented will no longer be valid. The behavior of V_{meas} curves with applied field H will change, as magnetization direction θ will not follow the expected coherent rotation. Figure 3.9 shows the results from magnetoresistance measurements of samples with increasing LSMO thickness on 4° vicinal STO, obtained at a fixed 5 V bias for a 90WB structure. In every case, magnetic field was applied perpendicular to step edges of the vicinal substrate. That is, perpendicular to the expected easy axis. According to the previously developed model, output signal of the bridge should follow a $(H/H_a)^2$ behavior in such conditions, as explicit in Equation (2.35). It can be

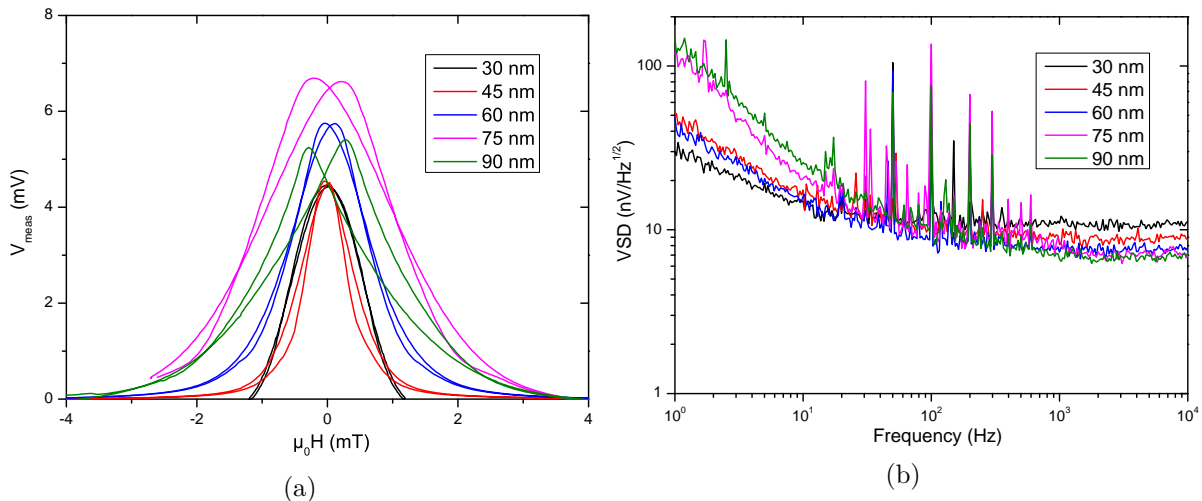


Figure 3.9: 90WB design MR at 310 K temperature and 5 V bias. [Samples BA055, BA068, BA070, BA072, BA076]

seen that as thickness increases, the field value at which V_{meas} reaches its maximum is shifted. This shift is similar in amplitude for both directions of field sweep, and the two peaks present a near symmetric distance from $\mu_0 H = 0$ mT. This shift is attributed to the loss of uniaxial anisotropy with increased film thickness t for a fixed substrate terrace

width d . The width and slope of the MR curve also change, which affects the sensitivity and DC field bias working point of the sample. For higher thicknesses, a loss of uniaxial magnetic anisotropy is evidenced by the now clearly separated peaks of V_{meas} . A single peak should be present when field is swept from negative to positive and back. As a clear uniaxial anisotropy is lost, the sensitivity of the sample also drops. When thickness is increased, a fixed 5 V bias results in higher current. The increase of sensitivity thanks to the increase of the current is not enough to avoid this reduction. This loss of uniaxial anisotropy with increased thickness shows that indeed in the LSMO over vicinal STO system what we obtain is a dominating step-induced anisotropy, and not an anisotropy due to strain in the thin film. As presented by Chuang *et al*, Equation (2.9) shows a reduction in step induced anisotropy with increasing film thickness. And even the thicker film does not reach the critical thickness of 100 nm for stress relaxation of LSMO over STO [7]. If the uniaxial magnetic anisotropy induced by epitaxial deposition on vicinal STO is no longer the clear dominating contribution to magnetic energy, the device model developed so far is no longer valid. A reduction in thermal noise, as expected from reduced resistance with increasing thickness, is indeed obtained. If the increase in thickness does not affect any other parameter, noise in low frequency region modeled by Hooge's expression should also reduce thanks to a increase in volume. But an unexpected increase in $1/f$ noise was measured for the thicker samples, at the same voltage bias for the Wheatstone bridges. This may be due a degraded crystalline quality of the film. If crystal structure changes, so does the electrical transport. A film with a heterogeneous resistivity along its thickness is prone to higher random fluctuations of its effective conductivity. This will be reflected in a higher normalized Hooge's parameter α_H/n , and the $1/f$ noise may increase instead of reducing. The resulting detectivity values for nominal LSMO thickness of 30 nm, 45 nm and 60 nm are shown in Fig. 3.10. Curves from 75 nm and 90 nm are not displayed as films are not uniaxial and present higher noise in the low frequency region. Samples with higher sensitivity and lower noise present better performance. The thinnest LSMO sample

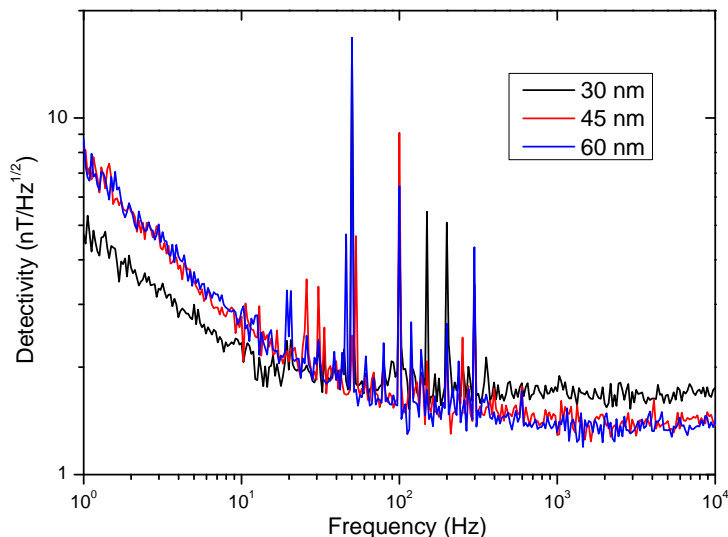


Figure 3.10: Measured noise divided by corresponding sensitivity, at 5 V bias and 310 K temperature. [Samples BA055, BA068, BA070]

presents the best performance of this set in frequencies below 10 Hz, thanks to its higher sensitivity and lower noise in the $1/f$ region.

3.2.1 Characterization at IMDEA Nanociencia

This set of samples was then sent to IMDEA Nanociencia, our partner in ByAxon project, for further investigation. Magnetic characterization with vectorial MOKE was performed by Jose Manuel Díez Toledano, along with another run of magnetoresistance

experiments by Arturo Vera and Dr. Isidoro Martínez. Magnetization curves from MOKE are shown in Fig. 3.11 for a 90WB structure in each LSMO sample. A square magnetization

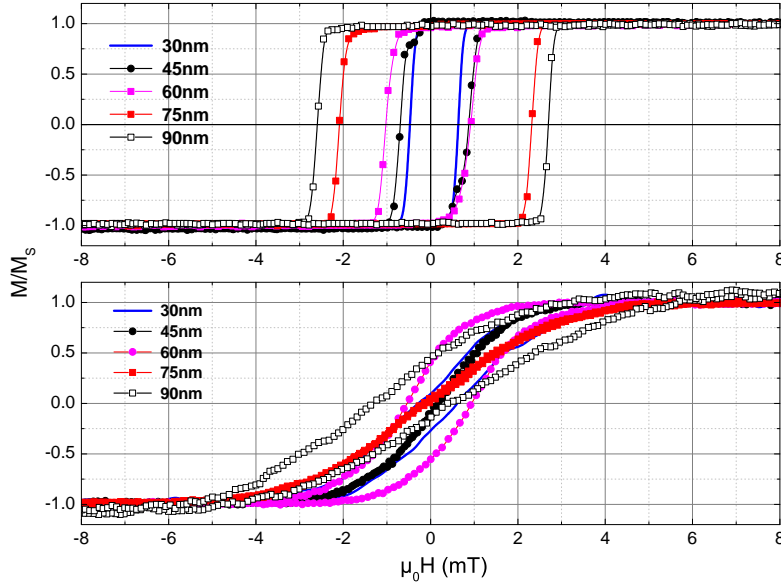


Figure 3.11: MOKE performed at IMDEA, with magnetization loops parallel (easy axis) and perpendicular (hard axis) to substrate step edges. Measurements at room temperature. [Samples BA055, BA068, BA070, BA072, BA076]

loop typical of easy axis direction is verified when magnetic field is applied parallel to step edges, while a linear dependence is obtained in the perpendicular direction. The loss of clear uniaxial anisotropy is again verified with increasing thickness. A stronger magnetic field is required to switch magnetization direction when field is along easy axis, and samples with increased thickness start to present hysteresis when field is along hard axis direction. We decided to keep the anisotropy field H_a definition even if sample is not perfectly uniaxial for the sake of comparison. Values for anisotropy field can be estimated from the hard axis magnetization loops, and Fig. 3.12 shows the evolution of H_a with thickness. Values for H_a were estimated by obtaining the intersection point between a line parallel to the flat saturated region and a line parallel to magnetization curve around zero applied field. Up to 60 nm thickness, samples present similar anisotropy field values. It increases for 75 nm and even more for 90 nm, indicating the presence of another contribution to magnetic energy besides the uniaxial anisotropy induced by the vicinal substrate. This result agrees with the V_{meas} curves shown in Fig. 3.9, measured at GREYC. For MR measurements at IMDEA, instead of sweeping a magnetic field to obtain sensitivity from the derivative of the obtained curve, an AC field with well defined 2 Hz frequency and 8.6 μT amplitude was applied. The voltage spectrum of the output signal was analyzed, and sensitivity is calculated with the voltage peak at the applied field frequency and using the known field amplitude. The MR ratio of each bridge was calculated by the difference between the maximum and minimum values of V_{meas} divided by V_{bias} . Values presented in Fig. 3.13 were obtained at each sample's working point, that is, at the temperature and DC field bias for highest sensitivity. To obtain such working point, a continuous component is added to the alternating magnetic field, and the value of such DC field is swept. Once the proper DC field bias is found, sample is placed over a heating plate, and temperature slowly increases to find the highest sensitivity. Samples with increased LSMO thickness presented higher MR ratio, although lower sensitivity. An increase in MR ratio with film thickness was also verified in permalloy PHEBs, given that single domain is maintained [8, 9]. Sample with 30 nm LSMO had the highest sensitivity of the set. This is due to a reduced anisotropy field H_a when compared to thicker films, even with smaller MR ratio. At its working point, the 90WB structure in the thinnest sample presented a 400 % T^{-1} sensitivity. Sample was heated to 314 K.

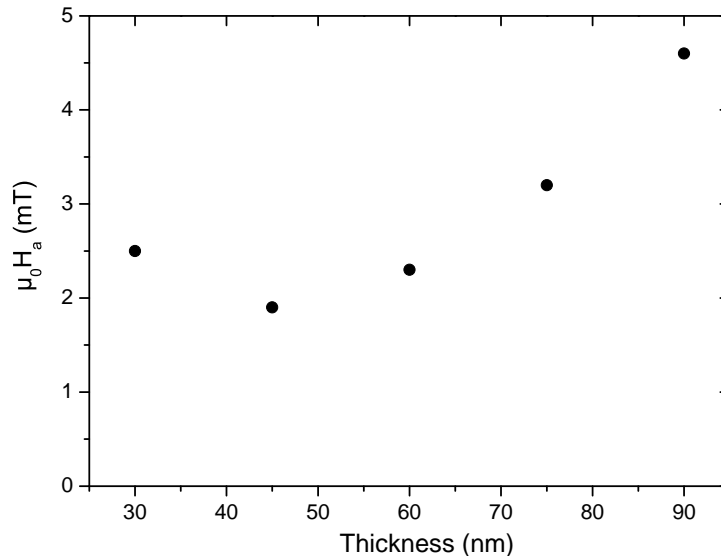


Figure 3.12: Anisotropy field at room temperature, estimated from hard axis magnetization curves in Fig. 3.11. [Samples BA055, BA068, BA070, BA072, BA076]

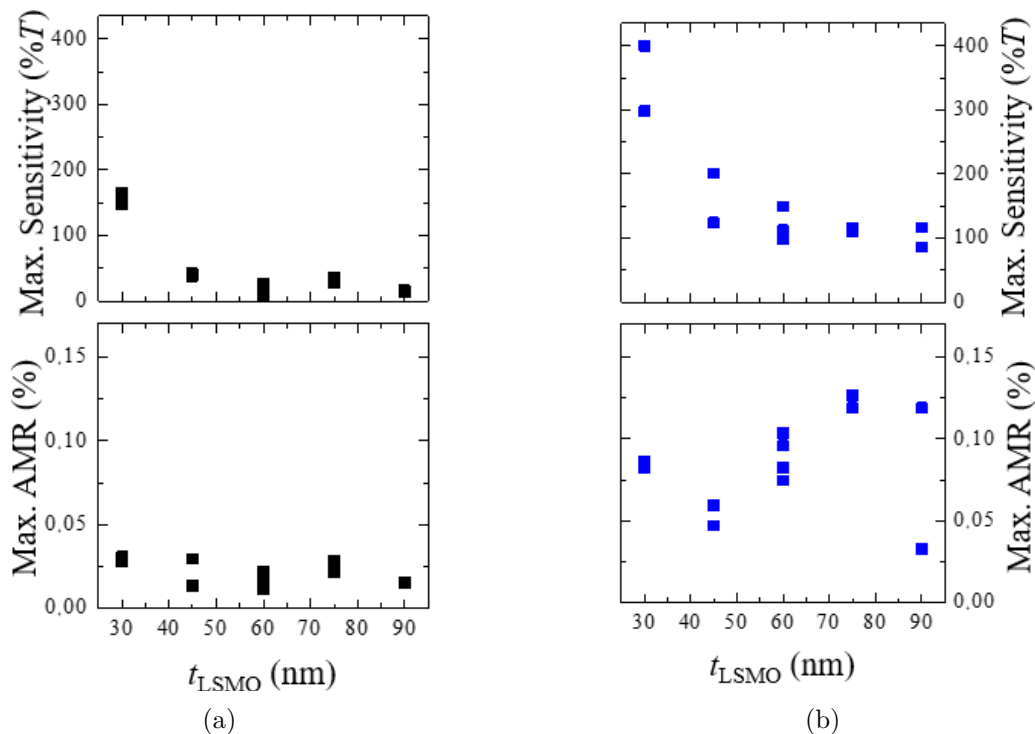


Figure 3.13: IMDEA Nanociencia measurements of AMR and sensitivity obtained at corresponding work point for each sample. a) Values for 45WB design and b) 90WB design. [Samples BA055, BA068, BA070, BA072, BA076]

3.2.2 Second batch of samples

A second series of samples with increasing thickness was prepared and further investigated at GREYC. The same 4° vicinal substrate was used, but as uniaxial anisotropy was clearly lost for thicker films, this new series presents only 30 nm, 45 nm and 60 nm LSMO thickness values. Electrical characterization of this second set, at fixed 5 V bias, is presented in Fig. 3.14. An increase in MR ratio is observed for thicker films, which agrees with previous results. Whereas the 60 nm sample had the largest H_a , the lowest value of anisotropy field was obtained for the middle value of 45 nm. Therefore this sample

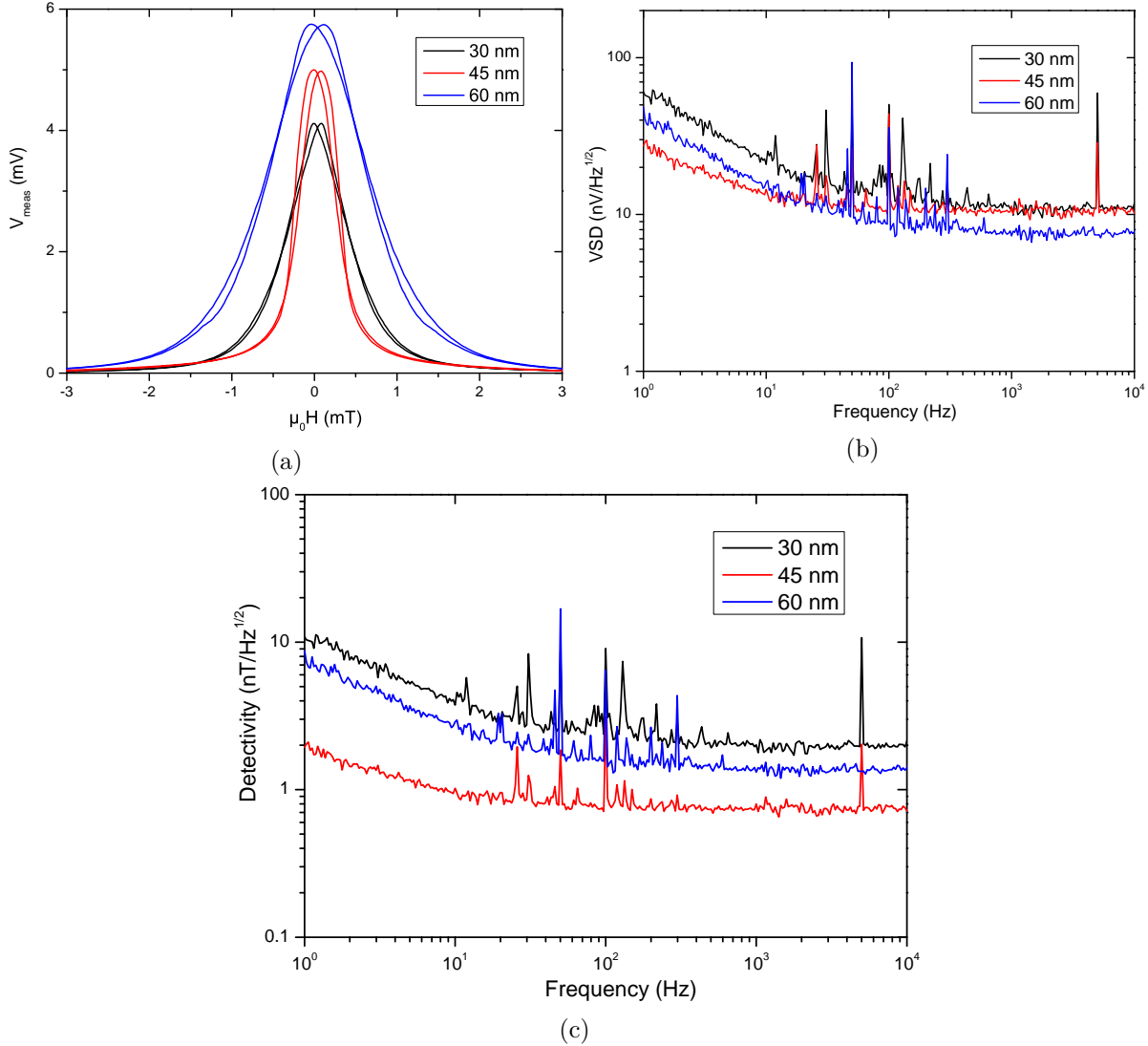


Figure 3.14: Results from electrical characterization of second set of samples, at 5 V bias and 310 K temperature. a) AMR curves of 90WB design. b) Corresponding measured noise. c) Obtained detectivity. [Samples BA098, BA114, BA104]

presents the highest sensitivity between the three. And although thermal noise does scale down as expected with increased thickness, it is the 45 nm LSMO sample that presents the lowest noise below 10 Hz. Therefore, it has the best performance overall in the whole range of frequencies. It is unknown exactly why this middle value for LSMO thickness presented the lowest $1/f$ noise. Measured resistance does reduce with increased thickness, so with 45 nm LSMO sample has a middle value for volume Ω . Possibly, it is related to film growth and fabrication itself, affecting the normalized Hooge parameter α_H/n .

For a STO substrate with 4° vicinal angle, thickness must be kept low to avoid losing uniaxial anisotropy. A middle value for LSMO thickness among the investigated samples presents the best performance, indicating an optimal thin film thickness on 4° vicinal STO substrate. Uniaxial anisotropy was lost for thicker LSMO films, but keeping it can be done by using a substrate with a higher vicinal angle. Such substrate will present a reduced terrace width d , therefore increasing the step-induced magnetic anisotropy energy contribution. An appropriate thickness value for LSMO thin films should achieve a good balance between uniaxial anisotropy, anisotropy field and noise.

3.3 Vicinal Angle

Apart from most magnetic sensors commercially available, LSMO devices in this work present step-induced anisotropy thanks to the use of vicinal substrates. The vicinal angle (miscut angle on substrate surface) in SrTiO₃ sets the terrace width d , which in turn affects the uniaxial anisotropy energy as presented by Chuang *et al.* Therefore, variations in vicinal angle ought to result in different magnetic behavior of the thin film. It is expected that a lower d increases the step-induced uniaxial energy. So a higher vicinal angle will be able to keep uniaxial anisotropy even for thicker films. A higher uniaxial energy corresponds to a higher uniaxial anisotropy constant K_u and thus a higher anisotropy field H_a . To verify such claims, a 60 nm LSMO film was deposited on a 8° vicinal STO, and its magnetic behavior was compared to that of the sample presenting the same thickness but on 4° vicinal substrate. Figure 3.15 presents V_{meas} and magnetization loops from MOKE imaging for both vicinal substrates. The 4° sample is from the second fabrication batch presented on the previous section. As expected, an increase in H_a is obtained, with a

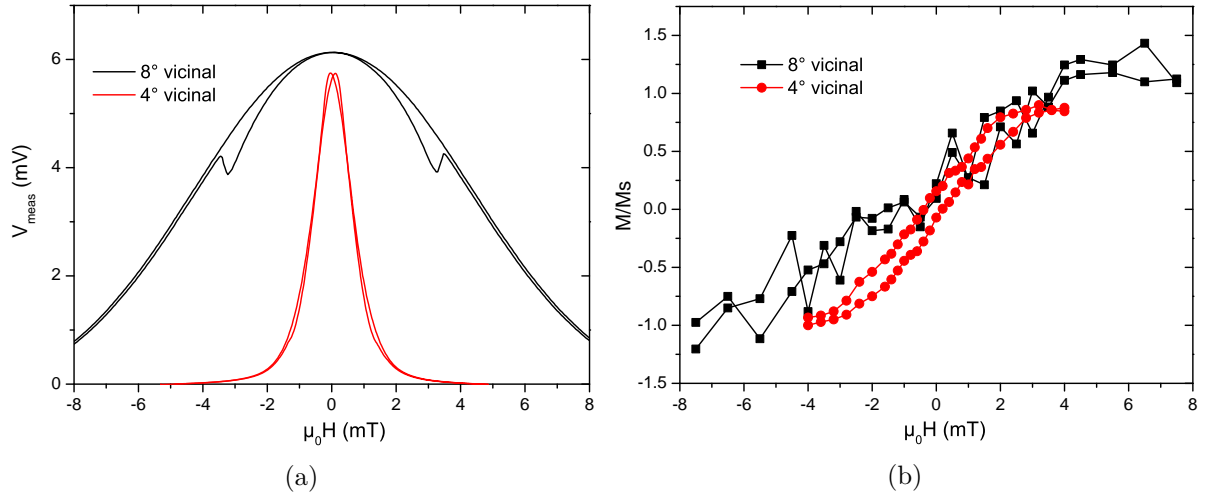


Figure 3.15: 60 nm LSMO deposited on 4° and 8° vicinal substrates. a) V_{meas} curves of 90WB structures measured at 5 V bias and 310 K. b) Magnetization loop obtained from MOKE imaging at room temperature, with magnetic field perpendicular to easy axis. [Samples BA097, BA104]

significant drop in sensitivity from 111.2 % T⁻¹ to 20.6 % T⁻¹ when increasing the vicinal angle. Another visual cue to a stronger uniaxial anisotropy besides the need for a higher applied field to saturate the sample is the coinciding peaks of V_{meas} in the 90WB structure.

Also, as terraces get closer, the in-plane strain in LSMO may alter. Changes in strain result in variations of thin film resistivity ρ and Curie temperature T_C , by affecting the electron-hopping probability in the double-exchange mechanism [10, 11, 7, 12]. To study the effect on how different vicinal angles affect LSMO thin films, 30 nm LSMO samples over increasing vicinal angle were fabricated, with a fixed 730 °C substrate temperature during deposition. One sample for each of the following vicinal angles was fabricated: 2°, 4°, 6° and 10°. MR curves from this set at fixed 310 K temperature and 5 V bias for a 90WB Wheatstone bridge are presented in Fig. 3.16. All samples present a uniaxial anisotropy behavior, with V_{meas} curve presenting the expected $(H/H_a)^2$ dependence. But a direct relation between MR ratio and anisotropy field with substrate vicinal angle is not observed. A higher angle corresponds to a smaller terrace width d . As sample thickness is kept the same, this should be presented as a higher anisotropy field, since contribution from step-induced anisotropy to magnetic energy increases. The value for H_a is related to the necessary field to saturate V_{meas} curve, and a wider curve means a higher anisotropy field. Curiously, studied samples presented an alternating H_a evolution. Surprisingly, the highest vicinal angle of 10° presents the lowest saturation field, leading to the highest

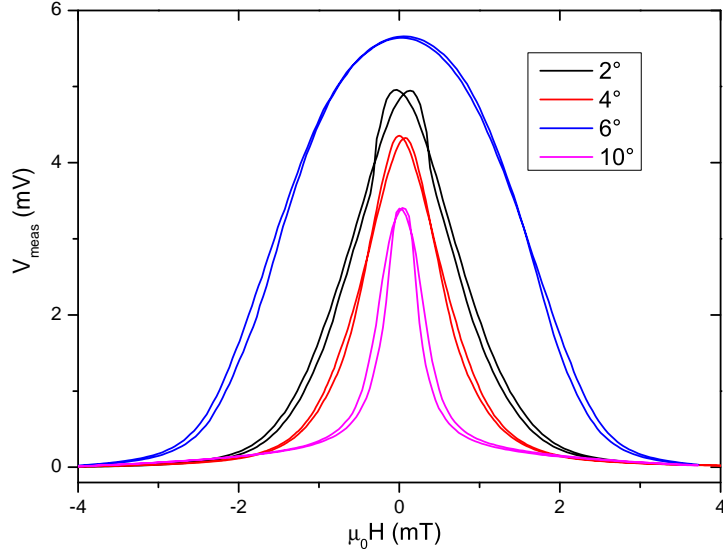


Figure 3.16: V_{meas} of 30 nm thin film over increasing vicinal angle. Samples were kept at 310 K and 5 V bias. [Samples BA054, BA098, BA062, BA064]

sensitivity even if MR ratio is reduced. Meanwhile, 6° presents the highest H_a and MR ratio, and has the lowest sensitivity. The 2° vicinal angle sample has an H_a larger than the 4° one, while the opposite would be expected with the expression for step-induced anisotropy. Most likely, there are extra effects influencing the properties of the LSMO thin film. The physics phenomena of this manganite oxide are more intricate, with several factors influencing one another. The electrical noise for each sample was also measured, at 0 V bias and 5 V bias for Wheatstone bridge structure. Such noise curves are presented in Fig. 3.17. This time, a direct relation can be verified in thermal noise region. As

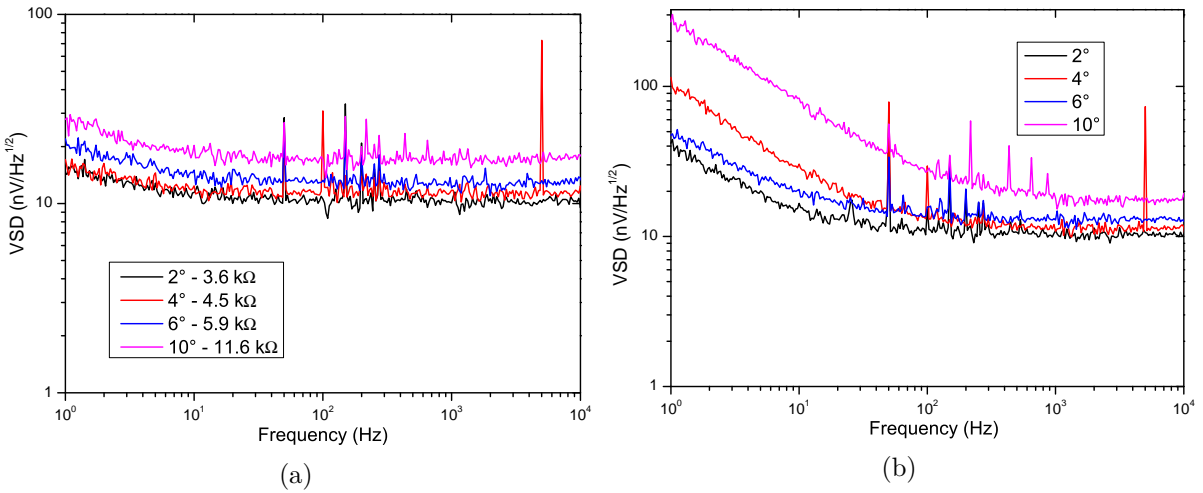


Figure 3.17: Electrical noise measured at 310 K for a) 0 V bias and b) 5 V bias. [Samples BA054, BA098, BA062, BA064]

vicinal angle increases, so does the thermal noise, indicating higher electrical resistance value. The presented resistance values along with the noise curve were obtained from an I-V curve, and indicate the resistance of a single LSMO stripe measured in four probes configuration. This stripe has the same dimensions as one arm of the Wheatstone bridge. The increase in resistance is then confirmed. The noise behavior was different in the $1/f$ region for 5 V bias: while the highest and lowest values are respectively presented by 10° and 2° vicinal substrates, the 4° sample presented a noise above the 6° one. This behavior may be explained by the difference of the in-plane strain in the LSMO thin film, and

how it evolves with substrate vicinal angle. As the electric and magnetic properties of LSMO manganite are linked and governed by the double-exchange mechanism, a reduction in electron-hopping probability affects electrical conductivity and ferromagnetism. It has been shown that as strain increases the electron-hopping probability reduces due to deformation of Mn octahedra, so film resistivity increases while its T_C decreases. The increase in electrical resistance and thermal noise is easily explained. As the electrical characterization was performed at fixed 310 K, a lower Curie temperature leads to a reduced magnetization saturation M_S . This affects the anisotropy field, as was explained in Section 3.1.1. Concerning the low frequency noise, the normalized Hooge's parameter α_H/n can also be affected by strain. With a higher α_H/n , the empirical relation for $1/f$ noise predicts an increased noise for a fixed voltage bias. As T_C and T_{MI} are directly linked thanks to the double-exchange mechanism, they reduced together. A study showing the increase in normalized Hooge parameter α_H/n with reduced T_{MI} in LSMO thin films has already been published [13]. The results here presented, with 2° and 6° showing higher anisotropy fields and lower noise, indicate that there might be a preferable vicinal angle for LSMO thin film growth depending on terrace width and step height. The resulting detectivity curves are presented in Fig. 3.18. Sample with 2° vicinal angle presents the

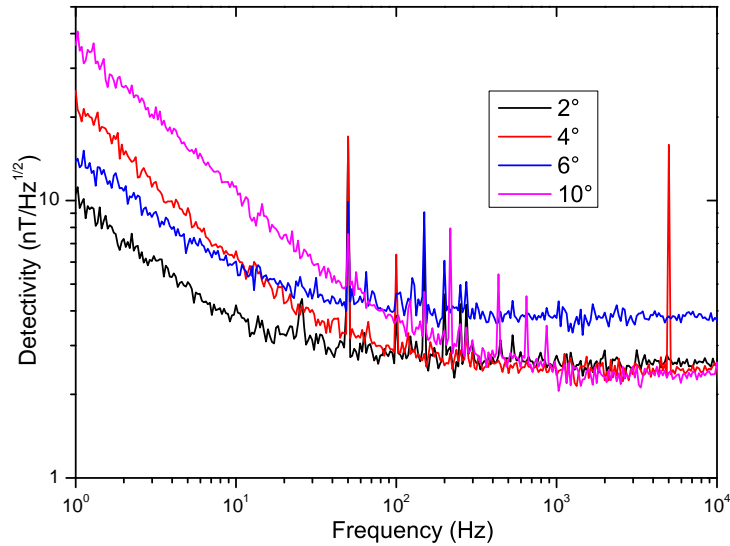


Figure 3.18: Detectivity curves obtained using the measured noise and best sensitivity as the derivative of V_{meas} , at 5 V bias and 310 K temperature. [Samples BA054, BA098, BA062, BA064]

best performance in the low frequency region. A similar detectivity value is reached at white noise region, except for 6° vicinal sample. Although the sample with 10° vicinal angle presented the highest noise, it also has the highest sensitivity. From V_{meas} curves only, we might get tempted to choose the 10° vicinal STO sample thanks to its reduced H_a and therefore high sensitivity. But in reality it presents the worse performance in the low frequency region.

3.3.1 Electron Microscopy

The first step to verify the hypothesis of the effect of strain is to investigate if all films actually present the same LSMO thickness value. Such verification was done with Scanning Electron Microscopy (SEM) technique, obtaining an image of a cross-section of the samples using the Helios Nanolab 660 system by FEI company available at CRISMAT UMR 6508, ENSICAEN. The cross-section was opened using the focused ion beam (FIB) of the microscope. Figure 3.19 shows the substrates positions over sample holder and where the cross-section was obtained, perpendicular to step edges of the vicinal substrate. Although the expected thin film thickness of 30 nm is near the limit of resolution for the

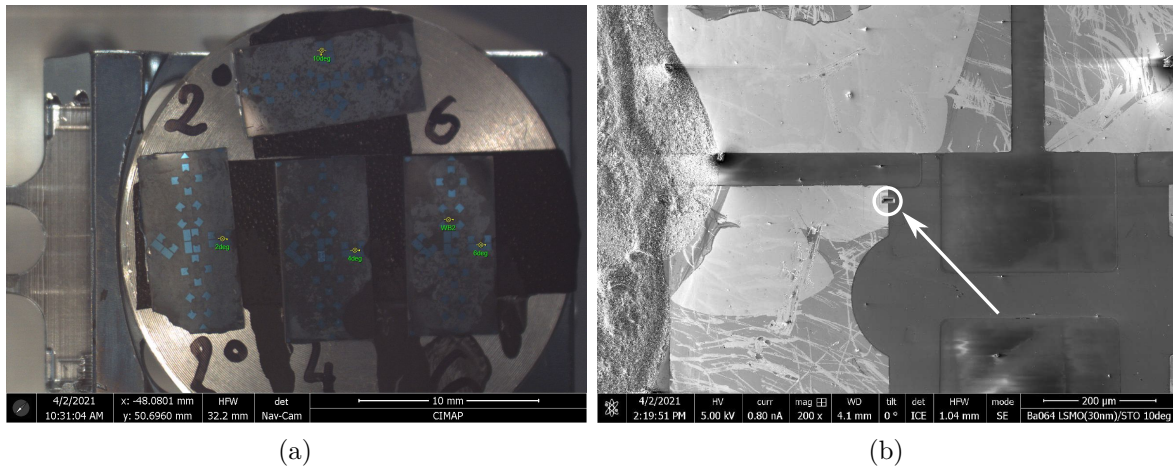


Figure 3.19: a) Samples on SEM sample holder and b) magnified image with a white circle indicating where the cross-section is obtained, perpendicular to vicinal substrate step edges.

equipment, a difference in thickness leading from $3.6 \text{ k}\Omega$ to $11.6 \text{ k}\Omega$ values of resistance (2° vicinal and 10° vicinal, as showed in Fig. C.24(a)) should be detected. SEM images of this set of samples, obtained using a back-scattered electrons detector, are presented in Fig. 3.20. By employing this type of detector, a higher resolution by atomic number of the studied specimen is obtained. Thanks to its higher atomic number, the gold layer for electrical contact is easily identified as it appears the brightest. The exact interface

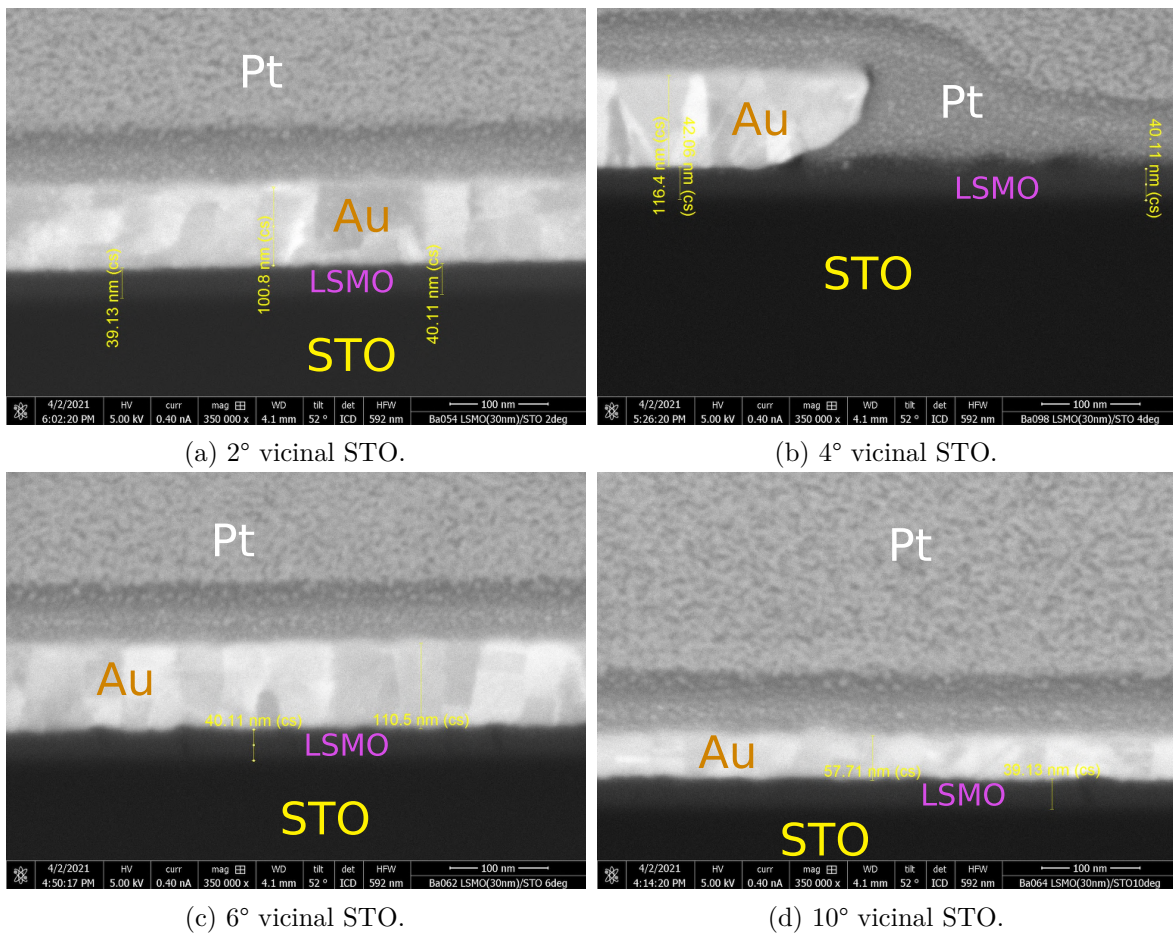


Figure 3.20: Cross-section SEM images for nominal 30 nm samples over increasing vicinal angle substrate. A similar thickness for all samples was estimated. Platinum top layer is used to protect sample during FIB. [Samples BA054, BA098, BA062, BA064]

between LSMO and STO is difficult to be determined, but independent of vicinal angle value a LSMO thickness of around 40 nm was estimated. These first results corroborate with the hypothesis that differences in electrical resistance and anisotropy field values are due to varying in-plane strain.

To obtain a better image of the crystalline structure for achieving a better estimation of LSMO thickness and verify if film is strained, a very thin slice of the 10° vicinal sample was prepared for Transmission Electron Microscopy (TEM) analysis, at the same sample region indicated in Fig. 3.19. This technique presents a higher spatial resolution when compared to SEM. High-angle angular dark-field (HAADF) images from scanning TEM (STEM) are presented in Fig. 3.21. Sensitive to scattered electrons, brightness increases with atomic number Z of the specimen. This is why the gold layer appears as saturated white and LSMO is brighter than STO. The interface between STO, LSMO and gold is much more

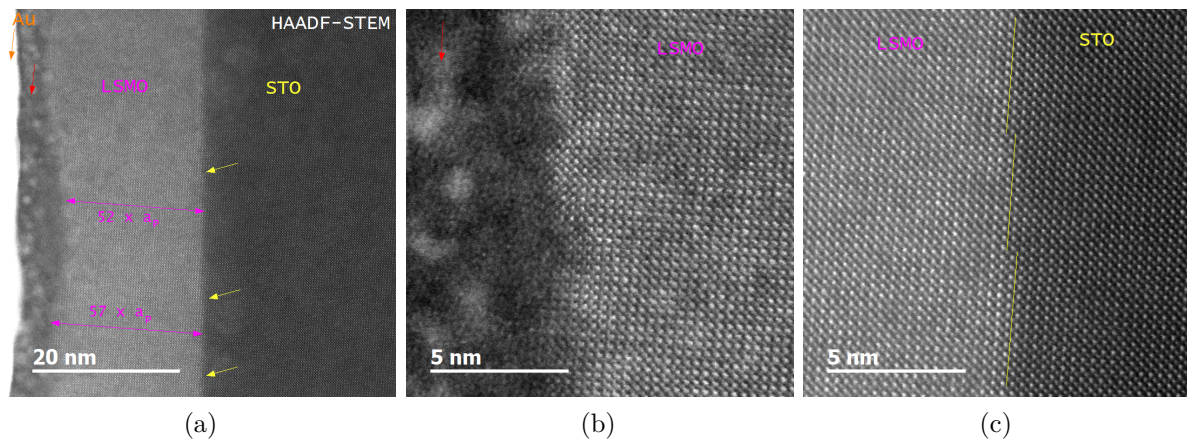


Figure 3.21: STEM images of nominal 30 nm thick LSMO over 10° STO. a) The effective LSMO layer thickness is reduced to around 22 nm due to amorphization near the surface. b) Magnification close to LSMO surface, showing the transition from crystalline to an amorphous structure. c) Zoomed view of the interface between LSMO and STO substrate, with well ordered atoms. [Samples BA064]

visible. LSMO grows following the substrate matrix, up to a point where an amorphous layer is seen at the surface of the manganite oxide, even under the gold. This reduces the effective thickness of the crystalline layer to around 22 nm, which explains the increased electrical resistance of the 10° vicinal sample. To confirm that the amorphous layer is indeed LSMO, an intensity profile using energy-dispersive x-ray spectroscopy (EDX) was traced, and the result is shown in Fig. 3.22. The same analysis was performed for the nominal 30 nm film on top of 4° vicinal STO. Figure 3.23 shows a bright-field STEM image, HAADF-STEM and the corresponding EDX profile. Whereas the amorphous layer is still present, its thickness is much smaller than for the 10° vicinal substrate. In this case, the effective LSMO layer has a thickness of around 28 nm. This corroborates with the previous results of electrical resistance and MR measurements. In the study presented in Section 3.2, it was shown that MR ratio and H_a follow the increase in LSMO thickness, and the same relation was observed between 4° and 10° vicinal substrate. Investigations with the 2° and 4° vicinal STO samples are planned, to verify the evolution of such amorphous LSMO layer with vicinal angle. TEM slices were obtained close to the border of the gold pad, so the metallic layer may not completely protect the oxide layer underneath during the fabrication process. One hypothesis is that a higher vicinal angle renders the crystalline structure of LSMO more fragile, and the amorphization occurs during the gold etching process with KI (see Appendix Fabrication). To verify this hypothesis, another slice of the 10° vicinal STO sample was prepared, obtained in the middle of the gold pad. Results were not yet obtained previous to the writing of this manuscript. I would like to thank Dr. Bernadette Domenges for operating SEM and TEM at CRISMAT, UNICAEN. Her help in analysis of the results and enthusiasm made this investigation possible.

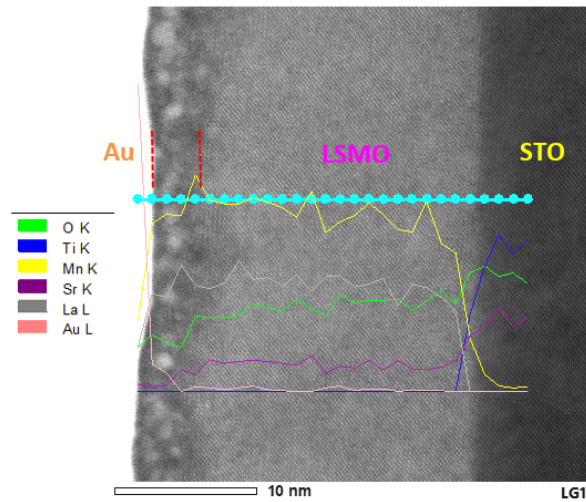


Figure 3.22: Presence of La, Sr, Mn and O in the amorphous layer. Legend indicates color code for each element and the energy band analyzed, and blue line indicates the scan direction. [Sample BA064]

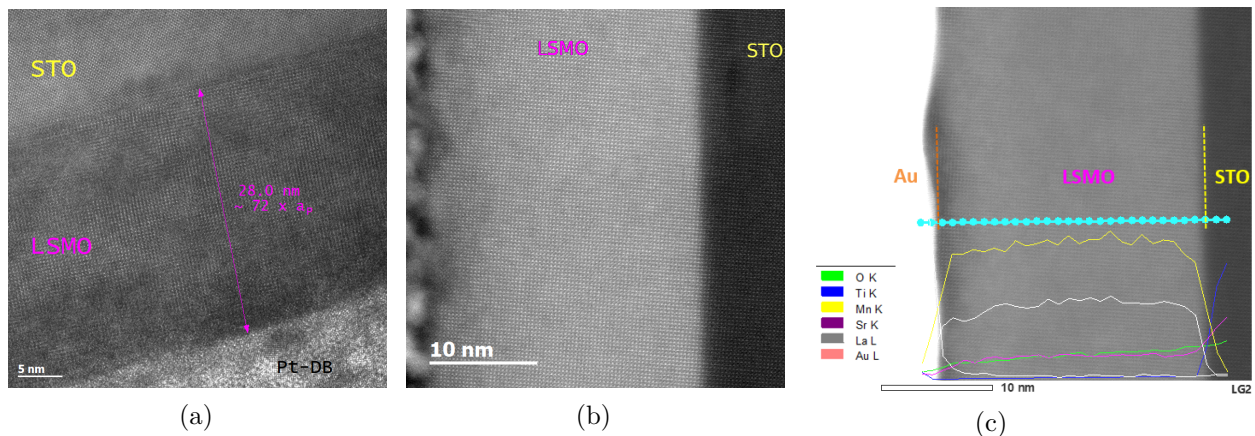


Figure 3.23: Investigation of nominal 30 nm LSMO on 4° vicinal STO. a) Bright-field STEM indicates a crystalline LSMO layer with 28 nm thickness. b) HAADF-STEM shows a well ordered LSMO structure, following the STO matrix. c) EDX profile confirms the presence of elements. [Samples BA098]

It was also planned to perform analysis of strain and Curie temperature in LSMO thin films using XRD and SQUID techniques, respectively. With the structural map obtained with XRD, it will be possible to obtain the crystalline parameters of substrate and film, and strain can be calculated. The estimation of T_C consists of measuring the total magnetization of the ferromagnetic film for increasing sample temperature. At Curie temperature, sample loses its ferromagnetic properties and magnetization drops to zero. XRD and SQUID measurements are better if more material is available. The presented set of 30 nm samples already had LSMO film etched in Wheatstone bridge and single stripes structures, so there is way less manganite material available. Therefore, a new set of samples with increasing vicinal angle was fabricated. This time, 45 nm thick LSMO film was deposited and the oxide was not covered by the gold layer for electrical contact. The first verification after deposition was to obtain $\rho(T)$ curves. With four inline probes to apply current and measure voltage over LSMO itself, sample is first heated up to 450 K. Voltage is measured keeping a constant current of 50 μA while temperature drops down to room temperature. This technique can be used to estimate the metal to insulator transition temperature T_{MI} of the film, directly linked to T_C . Also, this technique would indicate if any film is not of good quality, by a great difference in resistivity value or a different shape

of the $\rho(T)$ curve. Results for the 45 nm samples are shown in Fig. 3.24. Even though

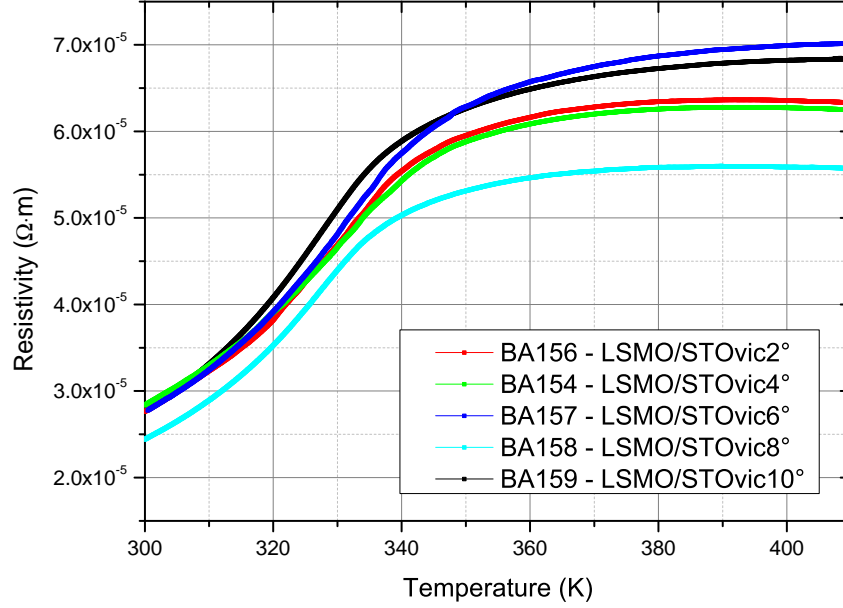


Figure 3.24: Resistivity versus temperature curves for second batch of vicinal substrates.

minor differences are seen, all samples present the expected curve. This corroborates a good quality PLD deposition. Before sending samples for XRD and SQUID measurements, trials with AFM scans were performed to check terrace width. Unfortunately, the available AFM equipment does not present a spatial resolution low enough to obtain clear measurements. The more in-depth XRD and SQUID measurements are not performed at GREYC, and unfortunately the results were not obtained until the completion of this thesis. A second sample consisting of 30 nm LSMO over 10° vicinal STO presented a Wheatstone bridge equivalent resistance of 11.7 k Ω , again higher than its lower vicinal angle counterparts. So this is indeed a topic to be further investigated.

3.3.2 Substrate temperature during deposition

Additional samples were fabricated to study the effect of different substrate temperature during PLD deposition, with two values for vicinal angle of the substrate. For 60 nm thick LSMO film, we used 8° and 4° vicinal substrates, at deposition temperatures of 730 °C, 680 °C and 630 °C. Deposition temperature of 730 °C was previously verified to be the optimal for high quality epitaxial films. The idea behind performing deposition at reduced temperature is to slightly degrade film quality, in order to reduce its Curie temperature. As was discussed earlier, a lower T_C represents a lower anisotropy field when samples are kept at constant 310 K temperature. Still with a focus on 90WB structures, the effect on anisotropy field was verified by the values extracted from the fit to the model presented in Chapter 2 and by the Full Width at Half Maximum (FWHM) of the experimental V_{meas} curves. For the latter, the expression for 90WB sensor output is recalled:

$$V_{meas} = V_{bias} \frac{\Delta R}{R_0} \left(\frac{1}{2} - \frac{H^2}{H_a^2} \right)$$

With it, we deduce that the FWHM of the curve corresponds to $\sqrt{2}H_a$. This expression is only valid for an applied magnetic field H perpendicular to easy axis and $|H| \leq H_a$. Still, it can be used to compare values for anisotropy field. In Fig. 3.25 the V_{meas} and resulting detectivity curves for the mentioned samples are presented, at 5 V bias and 310 K temperature. The fit for V_{meas} is added over the experimental data. The fits to

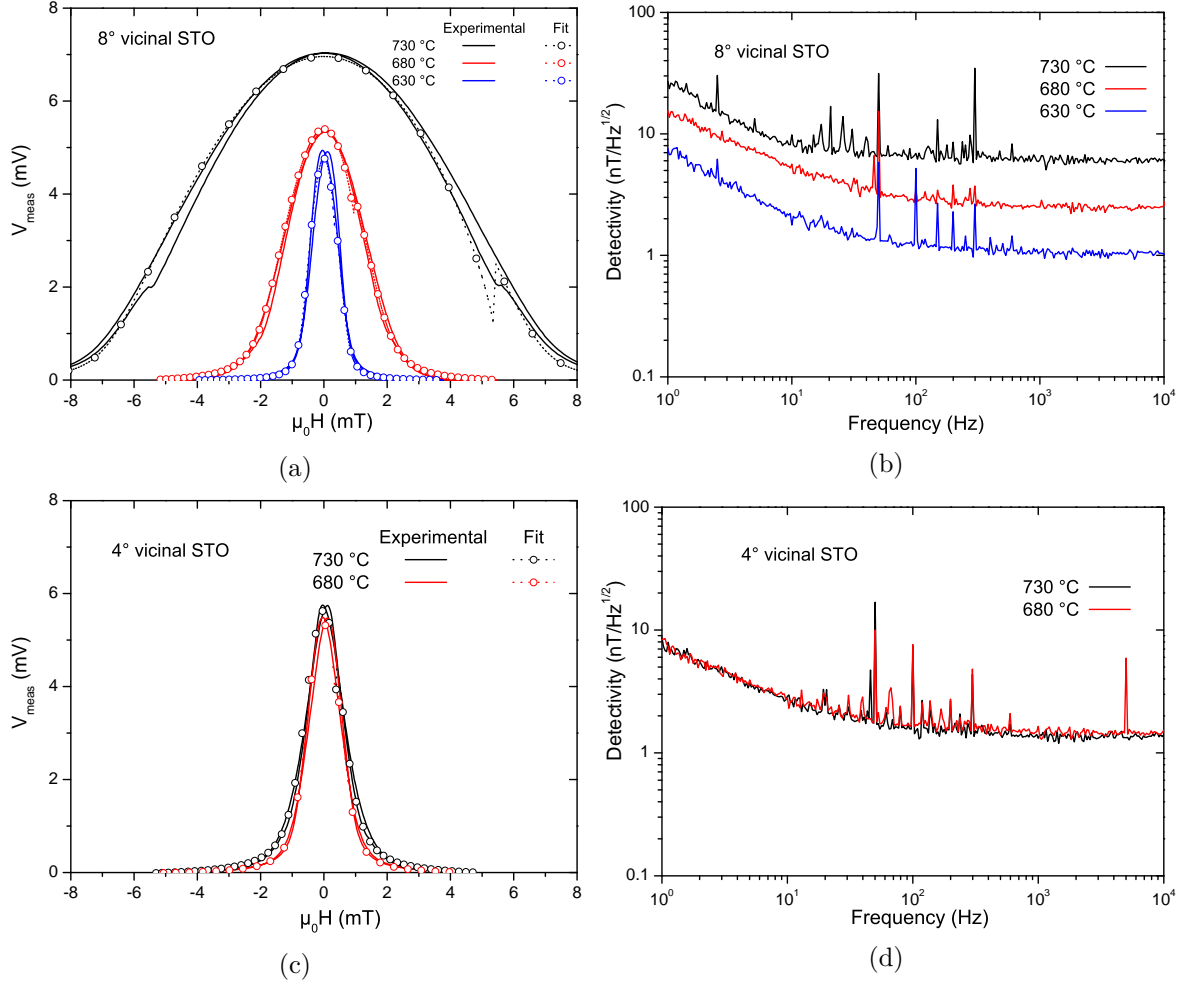


Figure 3.25: Effects of substrate vicinal angle and deposition temperature in 60 nm films. Experimental shifted $V_{meas}(H)$ curves and numerical fit derived from energy minimization for a) 8° and c) 4° vicinal substrates. Detectivity deduced from measured noise and sensitivity at 5 V bias for b) 8° and d) 4° vicinal substrates. [Samples BA097, BA103, BA104, BA105, BA106]

V_{meas} were performed using only the negative to positive field sweep. A clear reduction in H_a is observed when reducing deposition temperature for 8° vicinal substrate, and also when changing from 8° to 4° vicinal angle and keeping 730 °C deposition temperature. No significant change was observed when reducing temperature for the smaller vicinal angle, either in V_{meas} or noise. The effect on anisotropy field can also be verified with the hard axis magnetization loops presented in Fig. 3.26, obtained with the MOKE imaging system. Why no variation was obtained with 4° vicinal substrate is unknown. Table 3.2 summarizes values for anisotropy field, sensitivity and detectivity for the presented samples. A similar

Substrate	8° vicinal			4° vicinal	
	730 °C	680 °C	630 °C	730 °C	680 °C
Deposition temperature					
$\mu_0 H_a$ (mT) from FWHM	6.6	2.0	0.6	0.9	0.8
$\mu_0 H_a$ (mT) from $V_{meas}(H)$ fit	6.4	1.8	0.7	0.8	0.8
S (% T ⁻¹)	26	62	155	111	113
D (nT Hz ^{-1/2}) at 1 Hz	27	15	7.6	8.7	8.4
D (nT Hz ^{-1/2}) at 1 kHz	6.1	2.5	1.1	1.3	1.6

Table 3.2: Evolution of anisotropy field and performance of the Wheatstone bridge LSMO sensor.

performance was obtained when using a 8° vicinal STO at 630 °C deposition temperature

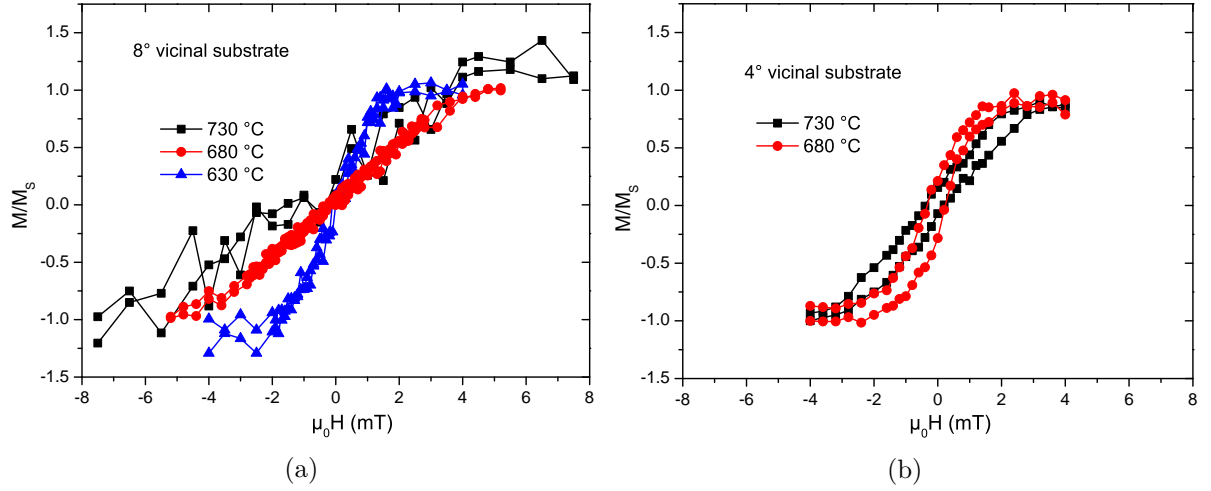


Figure 3.26: Hard axis magnetization loops obtained from MOKE imaging at room temperature. a) 8° vicinal STO, with three different deposition temperatures. b) No significant change for 4° substrate. [Samples BA097, BA103, BA104, BA105, BA106]

and using a 4° vicinal substrate. As the deposition temperature of 730 °C had already been verified to yield high quality films, it is preferable for reproducibility to use the 4° vicinal substrate rather than reduce the deposition temperature with the 8° one.

3.4 Optimized sample

Tweaking the fabrication parameters as previous presented, the sample presenting the best performance below 1 kHz consists of 45 nm LSMO thin film deposited on top of 4° STO substrate at 730 °C. To verify if this sample follows the V_{bias} dependence in detectivity expression of the model, MR and noise measurements were performed at different V_{bias} values on a 90WB geometry and results are presented in Fig. 3.27. For noise and detectivity curves, a fit using the corresponding expressions was added, with an extracted α_H/n , estimated sample volume, measured electrical resistance and operation temperature. In this case, some self heating due to Joule effect can be identified in the slightly higher thermal noise at 20 V bias. The good agreement between the fitted curves and experimental data show that indeed sample noise is composed of Hooge's $1/f$ and Johnson-Nyquist contributions. Values used in calculations are $R = 5.5 \text{ k}\Omega$, $T = 310 \text{ K}$, $\Omega = 5.4 \times 10^{-15} \text{ m}^3$ and $\alpha_H/n = 1.2 \times 10^{-31} \text{ m}^3$. Current noise from preamplifier was also considered, and detectivity was calculated using sensitivity obtained from the derivative of the V_{meas} curves considering a DC bias field for linear range of operation. The increase of voltage bias above 1 V almost does not affect detectivity in low frequency region as expected, with a gain in performance at thermal noise region. Values as low as $1.4 \text{ nT Hz}^{-1/2}$ at 1 Hz and $240 \text{ pT Hz}^{-1/2}$ at 1 kHz were achieved.

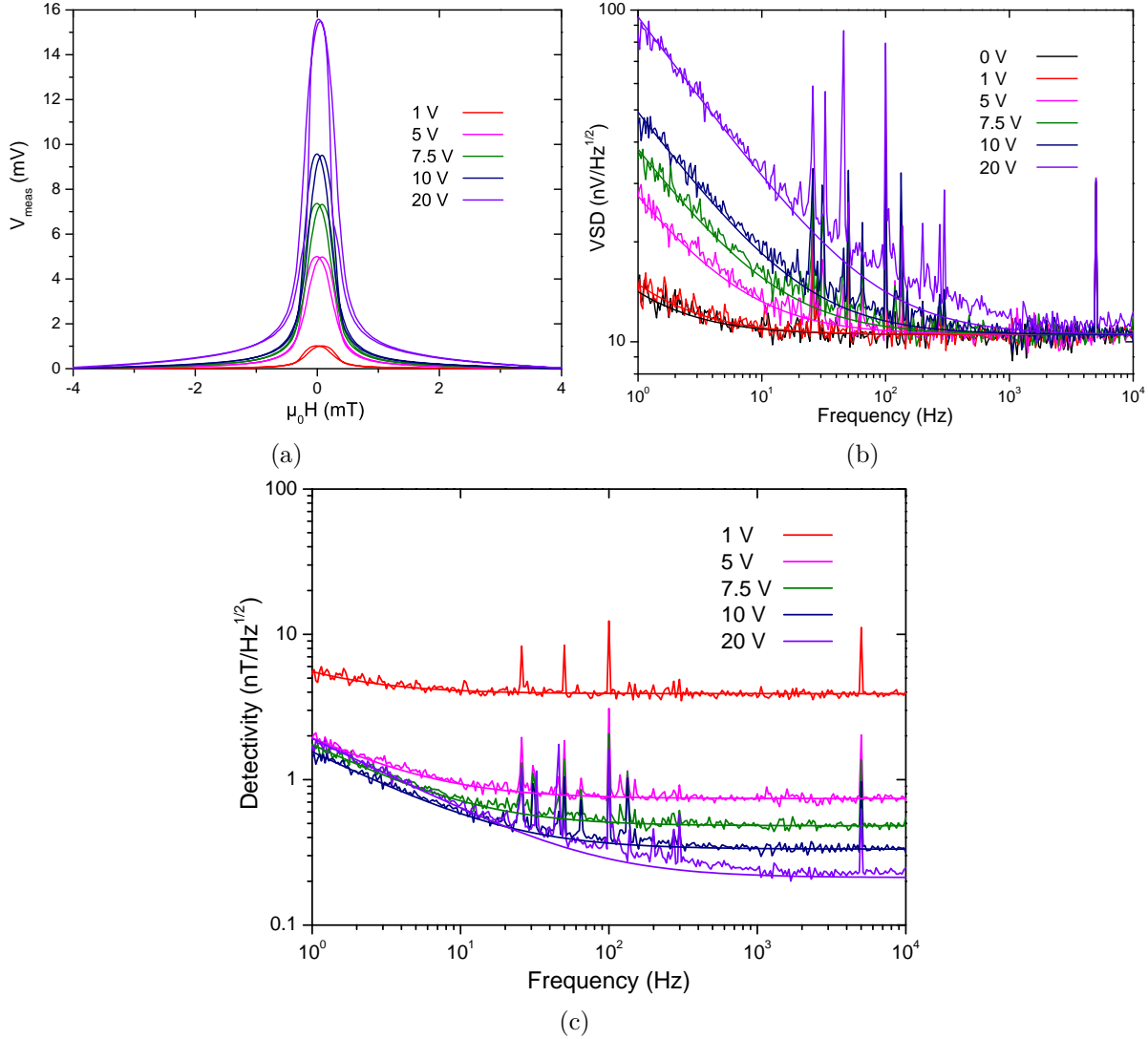


Figure 3.27: Characterization of a 90WB bridge on sample BA114 at 310 K. a) V_{meas} curves to obtain sensitivity. b) Measured noise with fit according to the total noise expression. c) Resulting curves for detectivity. [Sample BA114]

3.5 Masks geometry

The AMR effect is based on the relative angle between current density and magnetization directions. While ring shaped AMR Wheatstone bridges have already been proposed, the squared geometry (also referenced as diamond shaped) as presented in this work has a higher sensitivity [14]. The ideal case considers that both current density and magnetization are homogeneous along a LSMO stripe. Should at least one present a non-uniform distribution over the magnetic film, the effective AMR is degraded as contributions from each segment of the stripe won't add up. The angles α and θ (as defined in Chapter 2) won't be equal in the resistive stripe, so maximum and minimum values for electrical resistance won't be reached. Also, when verifying the expression for $1/f$ modeled by Hooge's empirical equation, we see that it depends on the square of the voltage bias. This dependence can be substituted to obtain an equation as a function of electrical resistance R of the element and current bias I :

$$S_V \propto \frac{1}{\Omega} R^2 I^2 \quad (3.4)$$

This excess noise is related to conductivity fluctuations in the material presenting a volume Ω . While the Hooge parameter is intrinsic to the material itself, the distribution of current

can affect the low frequency noise. If current is not uniform, in reality we will have an effective volume Ω_{eff} which will be lower than the total device volume. When current concentrates in smaller areas, low frequency noise is increased. This was well explained in cross-shaped Hall devices REF. So it is of best interest to optimize the design to obtain a current density distribution as uniform as possible. To perform such investigation, different lithography masks to use in MicroWriter 3 equipment were designed. Changes in Wheatstone bridge designs include geometry of gold contacts, width and length of bridge arms, total bridge size and the addition of a magnetic active region around the bridge separated by a small gap. While the magnetic behavior can be studied with the MR measurements and MOKE imaging, for current distribution the PHEMOS-1000 equipment by Hamamatsu was used to obtain Optical Beam Induced Resistance Change (OBIRCH) data. This measurement allows detecting in which zones the device's electrical resistance is more sensitive to local heating. An amplifier supplies a constant voltage between two terminals while a laser scans the sample. To keep a fixed voltage which value is chosen by the user, the supplied current follows variations of device's electrical resistance due to heating by the laser. The spatial information (position of the laser in the plane of the sample) and the electrical information (current amplitude supplied by amplifier) are linked, and the result is a gray scale image of the sample in which gray levels reflect the local variation in current. This gray scale image can be superimposed to a pattern image of the sample, and the effect of heating can be seen directly over the sample. Three images for two LSMO stripes are presented in Fig. 3.28: pattern, OBIRCH and superimposed. In superimposed image, the display can be chosen between a fixed color with varying brightness and a color map. The limits of the histogram of the OBIRCH image can be adjusted to show a range of current variation from the OBIRCH amplifier. In the superimposed image, increasing current variation is displayed from red (lowest

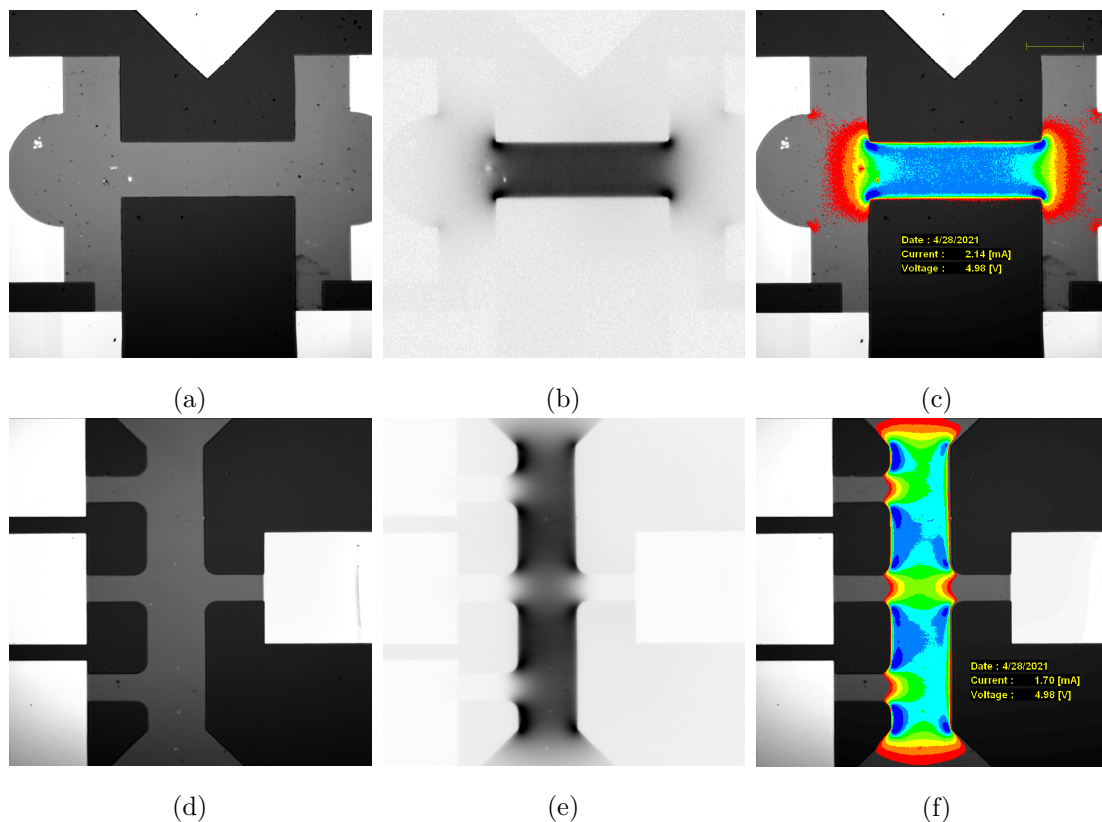


Figure 3.28: Example of images obtained with PHEMOS-1000. a, d) Pattern image of sample. b, e) OBIRCH gray scale image informing current variation. c, f) Given range of current variation superimposed over pattern image. [Sample BA146]

current variation) to orange, yellow, light green, dark green, light blue and finally blue

(highest current variation), if the color map option is chosen. This corresponds to lower signal amplitude in OBIRCH image histogram, therefore darker gray levels. A darker pixel corresponds to reduced current from OBIRCH amplifier, indicating an increase in resistance as expected when a semi-metallic material is heated. An increase in current, thus lower electrical resistance, would be seen as lighter spots. It is possible to limit the gray level histogram of the image to select only a region of interest for OBIRCH signal variations, but the resulting image will also be normalized to such limits. In Fig. 3.28(c) it is possible to verify that current leaves gold pads at the extremities and concentrates at the LSMO corners, taking the shortest path. An analysis of Fig. 3.28(f) indicates a lower sensitivity to laser heating around LSMO paths leading to gold contacts added to perform voltage measurements. This means that current density “spreads” when compared to a straight LSMO stripe. But it also shows a convex form, meaning that at the same time it avoids going towards such directions, as a longer path leads to higher resistance. Current density presents an equilibrium behavior so as to obtain the lowest total electrical resistance possible.

For each measure, the laser scan is performed at a fixed speed and power, so the provided thermal energy is the same anywhere in the sample. A higher OBIRCH signal (greater variation in current supplied by amplifier) in a given region can be linked to two possibilities:

- Lower diffusion of thermal energy, so effective local heating is higher
- Higher current concentration, so the effective resistance change is higher

Considering that all LSMO structures are on top of STO substrate, thermal diffusion should not be affected. In the case of a suspended LSMO stripe, with no material underneath it, thermal diffusion is considerably lower. In fact, in studies conducted aside this thesis, suspended LSMO bridges were completely burnt when using even weaker laser power than the one in the present work. But for the AMR LSMO devices such problem was never encountered. The thermal contact conductance between LSMO and STO was estimated to be of $0.28 \times 10^6 \text{ W K}^{-1} \text{ m}^{-2}$ [15]. Therefore, variations in OBIRCH signal will be considered only as variations of current concentration.

3.5.1 Gold pad geometry

The analysis of superimposed figures show current density behavior on top of sample image. In this section, I’ll present superimposed images with a green coloring to have a cleaner figure. Brighter green is related to higher negative current variation (so a greater increase in resistance) while darker green relates to lower signal variation. The superimposed image obtained from regular gold contact geometry using the physical lithography mask for MJB3 system is shown in Fig. 3.29(a). The sample consists of 45 nm LSMO thin film on top of 4° vicinal substrate. A first analysis is performed for 45WB design. Notice how current leaves gold pads at the corners closer to the remaining LSMO structure and not in a uniform way. It completely ignores the circular shape to reach the electrical contact with much higher conductivity as soon as possible. It also avoids the inner corners where it doesn’t need to go around while concentrating in the corners around which passage is mandatory. In other words, it avoids corners that it approaches perpendicularly and concentrates around corners approached in a parallel fashion. It also spreads a little at paths leading to signal terminals, as a higher volume relates to lower resistance. With this information, a new mask was designed in order to obtain better current density uniformity. Thanks to the MicroWriter ML3 Pro system acquired mid-2020, the process of testing new masks geometries is easily achievable as only the digital files for the mask is needed. Without the need to actually manufacture a physical mask, prototyping is much faster. New gold pads geometries were tested in 45 nm thick LSMO deposited over 8° vicinal STO. The first modification was for gold contacts, with

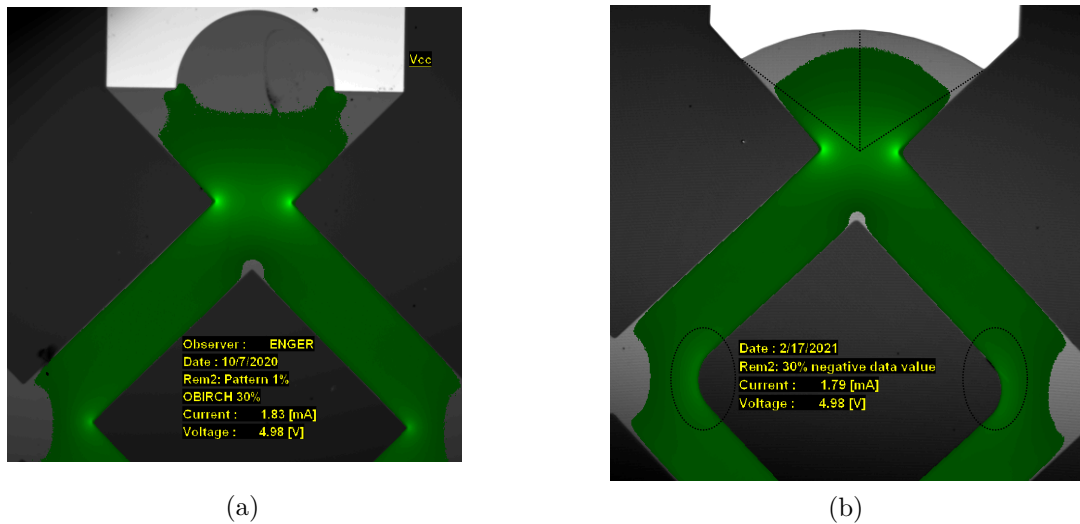


Figure 3.29: Superimposed images of gold pads geometries. a) Design on physical mask used in MJB3. b) First design using MicroWriter ML3 Pro, referenced as Pad A geometry. [Samples BA136, BA147]

the goal of obtaining a current density that leaves the metal homogeneously. Each point of the interface between gold and LSMO is equidistant to the center of the LSMO path leading to the Wheatstone bridge. Inner corners of the bridge where current makes a turn were also rounded to reduce concentration. A resulting superimposed image is presented in Fig. 3.29(b). This geometry will from now on be referenced as Pad A. A more homogeneous current density leaving the contact pad is indeed achieved. Point of current concentration at inner LSMO corners (represented in light green in Fig. 3.29(a)) is also avoided.

Two additional gold pads geometries for excitation terminals were studied, still with the goal of reaching a homogeneous current density distribution in the LSMO Wheatstone bridge. Results from OBIRCH analysis are presented in Fig. 3.30. The rounded inner corners were maintained. In the geometry referenced as Pad B, the LSMO path leading to contact was excluded by moving gold layer towards bridge and making a straight line interface. With Pad B geometry, current once again leaves gold pads at the extremities,

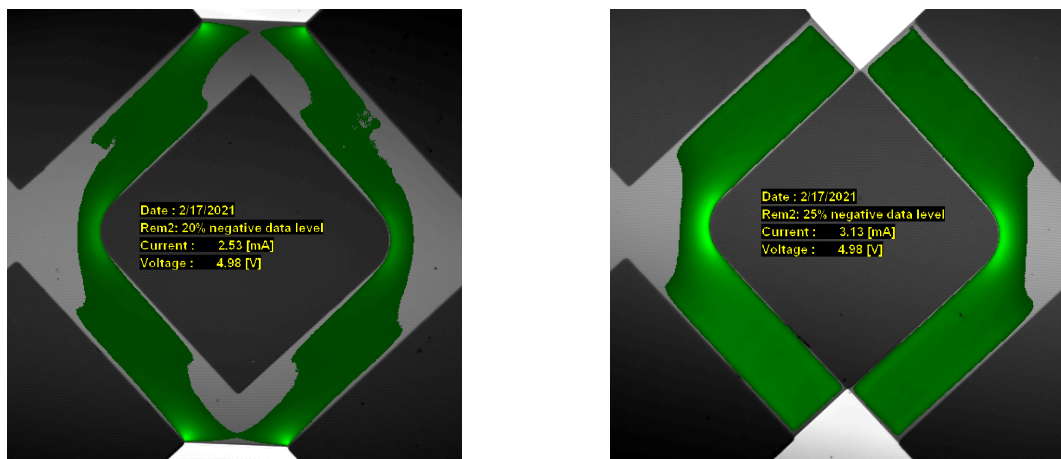


Figure 3.30: Superimposed images of a) Pad B and b) Pad C geometries. [Sample BA147]

following the shortest path. For the geometry called Pad C, gold pad was further increased to inject current directly along arms of the bridge. While all the presented samples have a nominal thickness of 45 nm and measurements were performed with a fixed 5 V bias, electrical resistance between the excitation terminals is lower for the last two gold pad

designs due to a reduced LSMO path. Thus a higher current flows through LSMO bridge with a increased gold layer. As it is not possible to obtain the exact corresponding current provided by the OBIRCH amplifier at each position of the laser scan, a quantitative analysis is not possible. In fact, such technique is mostly used for qualitative studies, to detect faults and defects in electronic circuits and devices. As a more homogeneous current distribution is clearly seen in geometries prepared with ML3, the first mask geometry will be excluded from coming discussions.

The effects of such geometry changes can be studied with MR and noise measurements, as previously mentioned. The MR curves for each ML3 geometry are presented in Fig. 3.31 for a fixed current bias of 1 mA (Fig. C.26(a)) and a fixed voltage bias of 5 V (Fig. C.26(b)) between excitation terminals. A fixed voltage bias corresponds to higher current in geometries with reduced electrical resistance. Sensitivity values at zero field are also shown, both in $V T^{-1}$ and $\% T^{-1}$ related to bias voltage. The bias voltage for a fixed current was calculated using the electrical resistance measured between the excitation terminals, in 2-probes configuration. Values at 310 K are 3.37 k Ω for Pad A, 2.30 k Ω for Pad B and 1.88 k Ω for Pad C. For fixed current, V_{meas} curves do not show a considerable difference

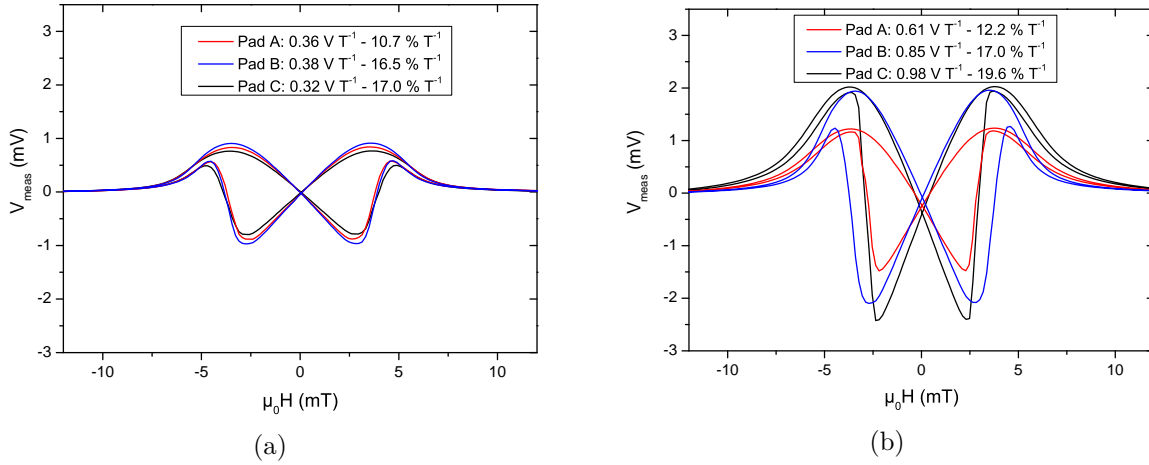


Figure 3.31: MR curves at 310 K for different gold pads geometry. a) Fixed 1 mA current bias. b) Fixed 5 V voltage bias. [Sample BA147]

and sensitivity values in $V T^{-1}$ are quite close to each other. But when calculating the corresponding voltage bias with the measured 2-probes resistance value, we see that Pad B and Pad C present higher sensitivity ratios. For a fixed voltage, current is inversely proportional to resistance. The highest sensitivity ratio is once again obtained for Pad C. The structures present the same anisotropy field as they are etched on the same sample. Therefore the difference in sensitivity is related to a difference in MR ratio only. To compare actual sensing performance, noise measurements were performed to obtain detectivity curves. As the noise from Yokogawa source is even higher when operating in current mode and considering the $1/f$ noise dependence on voltage bias independent of sample resistance, noise measurements were performed at fixed 0 V and 5 V bias only instead of supplying a fixed current. Results along with detectivity values are presented in Fig. 3.32. The presented variations in gold pad geometry were applied only for the excitation terminals of the Wheatstone bridge, while the signal terminals present the same Pad A geometry. Therefore, all three designs have the same equivalent resistance between the signal terminals were V_{meas} and noise measurements are performed. With same resistance value, the same thermal noise level is obtained. Pad C geometry presented the highest noise in the low frequency region at 0 V and 5 V bias. The increased $1/f$ noise can be linked to the passage of current between LSMO and gold layers. Each time current moves between LSMO and gold, it adds to noise. Pad A and Pad B geometries present only two interfaces between LSMO and gold, each at the extremities of the Wheatstone bridge, that can be modeled as a resistance in series with the whole structure. Whereas

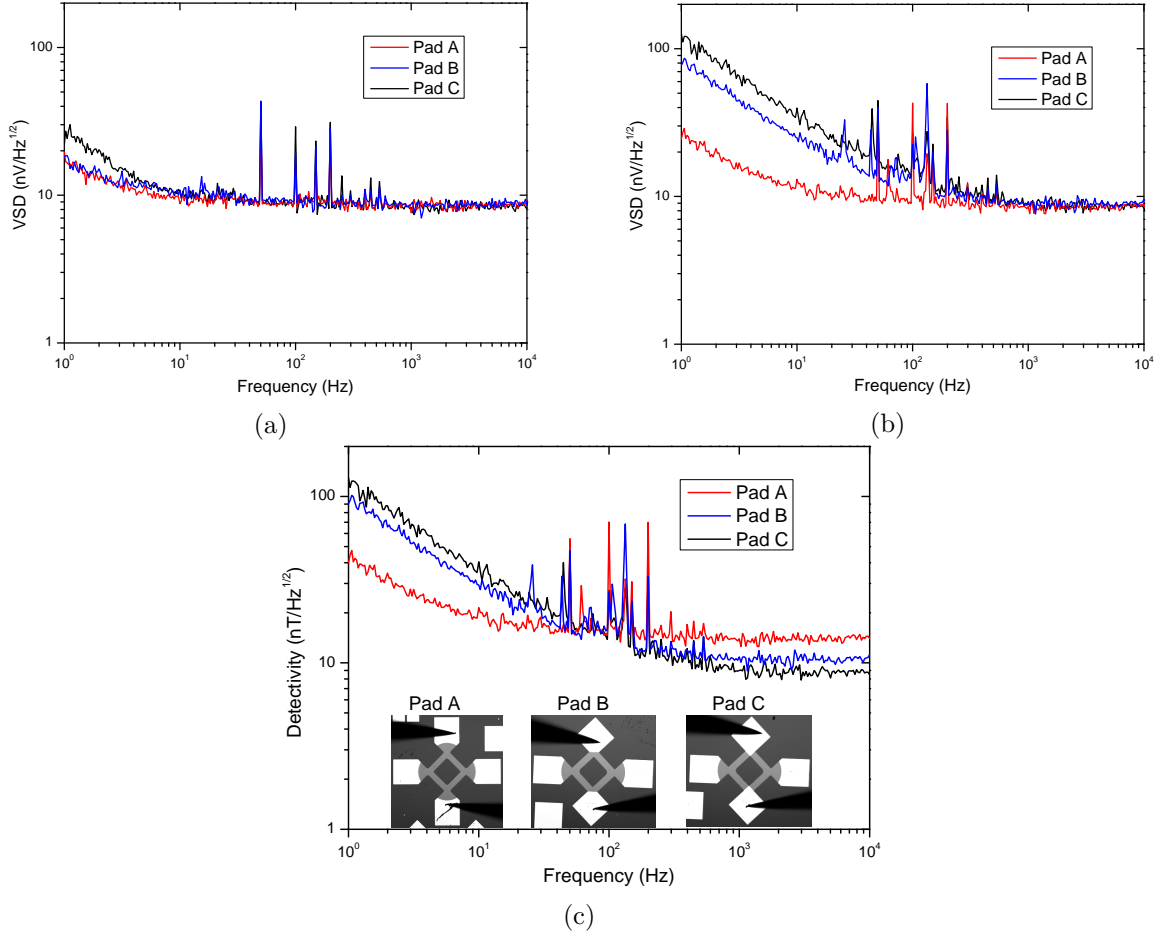


Figure 3.32: 45WB structure performance for different pads geometries at 310 K temperature. a) Noise at 0 V. b) Noise at 5 V. c) Obtained detectivity at 5 V bias, with OBIRCH pattern images. [Sample BA147]

Pad C has two interfaces for each branch of the bridge, and each single interface has a smaller area when compared to Pad A and Pad B. This can be seen as two series contact resistance for each branch of the bridge, both with an increased resistance when compared to the LSMO/Au interface in the other two designs, which adds to noise. With contact pads moved forward, current will seek the metal layer as it presents a much lower electrical resistance. Due to this extra $1/f$ noise, it is Pad A geometry that presents the best performance below 10 Hz frequency. Above 1 kHz, Pad C has lower detectivity thanks to higher sensitivity. This higher sensitivity can be originated from the fact that the now excluded LSMO path had a small negative contribution to bridge output signal. The zone of LSMO now covered by gold no longer contributes to AMR.

The same study on gold pad geometries for excitation terminals was conducted for 90WB bridge design. MR curves were measured for a fixed 1 mA current and fixed 5 V voltage bias and are presented in Fig. 3.33. Samples also present the reduction in 2-probes resistance between excitation terminals, with Pad A presenting 3.57 k Ω , Pad B with 2.12 k Ω and Pad C having 1.90 k Ω . Therefore for a fixed voltage, current increases from Pad A to Pad C. This design was etched over same die with 45WB bridges, so it remains a 45 nm LSMO thin film on top of 8 $^\circ$ vicinal STO. Again, the MR ratio did not change much for fixed current bias. And estimating the voltage corresponding to 1 mA, it is Pad C that presents the highest percentage sensitivity. It is unclear why the same bridge presented such degradation when measuring V_{meas} with a fixed voltage bias, as observed in Fig. 3.33(b). Supplying 5 V to Pad C geometry corresponds to a current bias of around 2.6 mA. Further studies would be necessary to obtain a better understanding, but unfortunately those were not conducted in this work. Noise measurements and detectivity

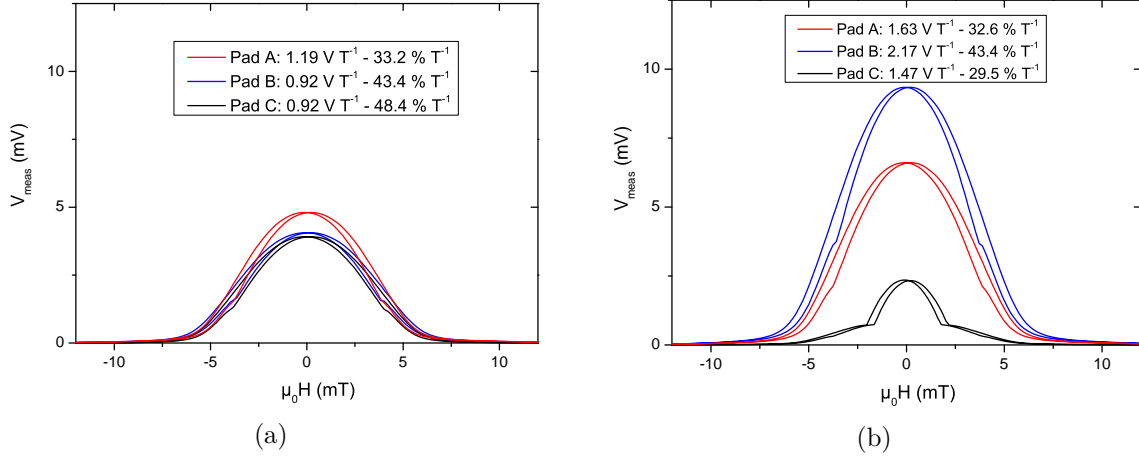


Figure 3.33: Magnetoresistance curves for 90WB design at 310 K with different gold pad geometries. a) Bridges biased with fixed 1 mA current. b) Measurement with 5 V bias. [Sample BA147]

calculations for the 90WB geometry are presented in Fig. 3.34, again only with voltage bias. The same white noise level is reached as measurements are performed between signal

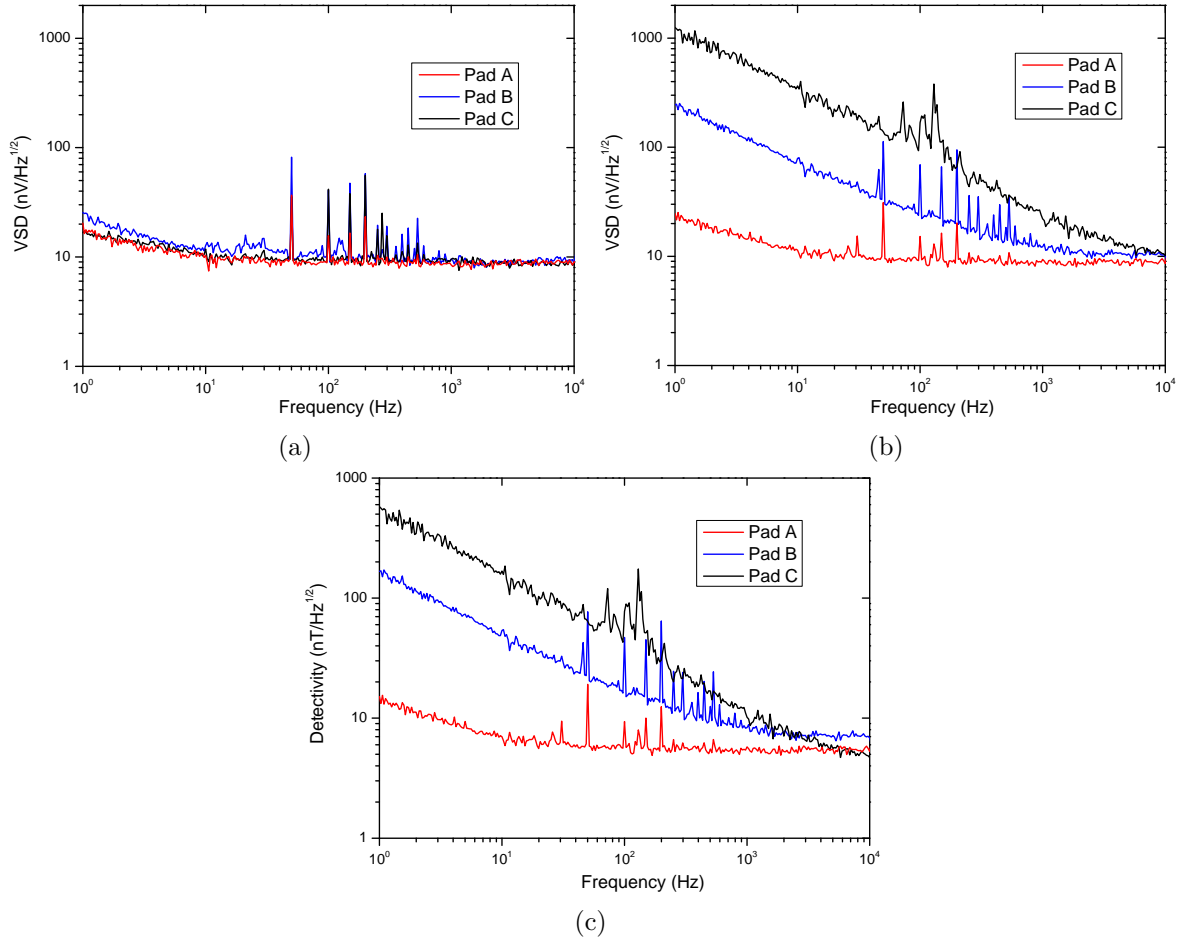


Figure 3.34: 90WB performance comparison for different gold pad geometries, at 310 K. a) Noise at 0 V bias. b) Noise at 5 V bias. c) Obtained detectivity at 5 V bias. [Sample BA147]

terminals of the Wheatstone bridges, that present the same gold pad geometry (Pad A geometry in all structures). When bias is applied, the same behavior as in 45WB was verified. A greatly increased low frequency noise was observed, specially for Pad C sample.

As mentioned, this increased noise may be due to the current transition from gold layer to LSMO, as each geometry has a different zone of current injection. With lowest noise, Pad A sample has the lowest detectivity, so best performance. Pad A was the geometry chosen for the upcoming samples after this study.

3.5.2 Effect of demagnetizing energy

When the in-plane magnetization of an etched thin film is perpendicular to interface, a stray field arises. Maintaining a stray field represents a high cost in energy, therefore the system will try to reduce it as much as possible. To achieve zero stray field, magnetization has to be in-plane and parallel to thin film interface. So irrespective of magnetization direction in the middle of magnetic thin film body, magnetization rotates near the interface to avoid being perpendicular to it. How magnetization rotates depends on a balance of stray field and exchange energies, so it is a function of demagnetizing factor and magnetic stiffness of the material. This can be exploited to obtain magnetic particles with an uniaxial anisotropy based on the shape of the thin film only. Notably, ellipsoids are well studied as they present a magnetic easy axis that is along the longest length of the structure. It is possible to obtain magnetic sensors using ellipsoidal particles only, without the need of an exchange bias with a pinned magnetic layer or the use of vicinal substrates [16]. But when another method is used to achieve an uniaxial magnetic behavior, effects due to shape may hinder the expected performance.

Considering a LSMO stripe etched in a rectangular shape, magnetization will try to align itself along the interface near the borders. Therefore, it will contribute to reach $\theta = \alpha$, when stripe has its lowest resistance R_{\parallel} . For a stripe etched with $\alpha = 0^\circ$, magnetization will have a greater contribution to align itself parallel to easy axis around zero applied field. If the stripe is perpendicular to such axis, demagnetizing energy will contribute to align magnetization along hard axis at magnetization saturation. As for $\alpha = 45^\circ$, such magnetization direction is only reached at a given applied field value as it is a middle point between easy and hard axes. Regions that have a “fixed” magnetization direction due to shape anisotropy won’t contribute to total AMR signal. So if LSMO stripes present a significant contribution to magnetic energy originating from stripe shape, changing bridge design will affect magnetoresistance values. To study the possible influence of such effect, two new Wheatstone bridge designs were prepared. Digital masks were drawn with CleWin 5 and samples were prepared using ML3. The typical design used so far will be referenced as Shape A. Design Shape B presents Wheatstone bridges with arms divided in two segments, as if a trench was dug in the center of each arm. Mask design is shown in Fig. 3.35. This should reinforce the effect of demagnetizing energy while keeping same total bridge size, keeping LSMO arms with $300 \mu\text{m}$ length. The bridge will also present increased resistance and reduced volume, which in turn increases overall noise. The total

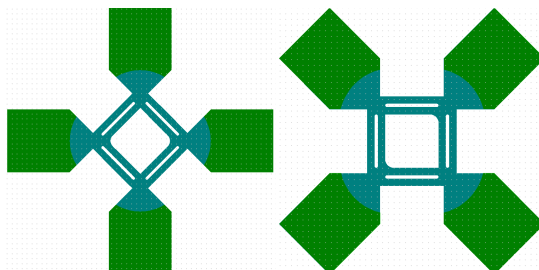


Figure 3.35: Shape B: masks for bridges with trenches 45WB and 90WB

$100 \mu\text{m}$ width was divided in two $40 \mu\text{m}$ segments, with the trench presenting rounded edges to avoid corners of current density concentration. Meanwhile, for a third Shape C, a LSMO body was left around the bridge arms. The idea behind such geometry is to reduce effect of demagnetizing energy by reinforcing an exchange energy contribution. The

magnetic body surrounding the bridge will present same step-induced uniaxial anisotropy, easy axis direction and magnetization rotation, as it is effectively the same thin film. So by leaving just a small gap between Wheatstone bridge and the remaining magnetic layer, magnetization in bridge arms will follow along magnetization of the surrounding body. This geometry was presented by Henriksen *et al* using permalloy film, and a reduction in shape anisotropy was indeed obtained [17]. What is called “diamond shape” by Henriksen corresponds in this thesis to the 45WB design. As an initial guess and respecting the limits of the laser lithography ML3 system, LSMO samples were first prepared with a $5 \mu\text{m}$ gap. In the same mask, 45WB bridge design with a 50% aspect ratio reduction was included. So for Shape C, 45WB structures with $150 \mu\text{m}$ length, $50 \mu\text{m}$ width and $2.5 \mu\text{m}$ gap are also available. Corresponding sections of mask design are presented in Fig. 3.36. To verify

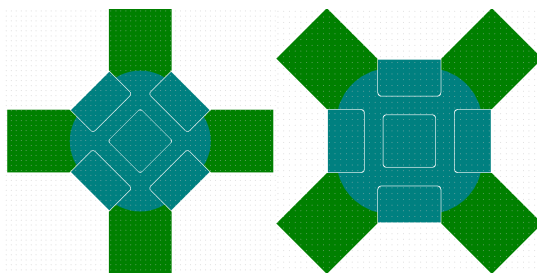


Figure 3.36: Shape C: mask for surrounded bridges

that etching was correctly performed following such geometries, OBIRCH analysis was performed for Shape B and both sizes of Shape C bridges. Resulting superimposed images for both bridge designs in Shape B are presented in Fig. 3.37. In Fig. 3.38, OBIRCH

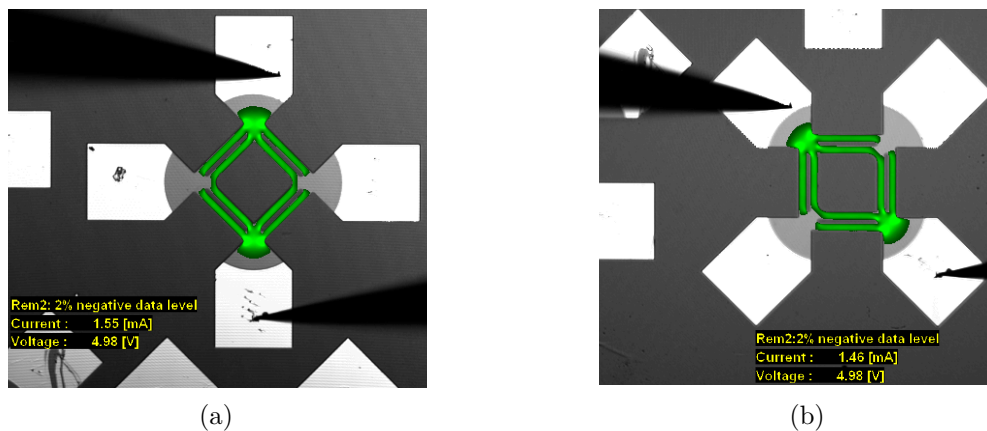


Figure 3.37: In Shape B, current splits between the now divided bridge arms, with two parallel paths. [Sample BA147]

images for the two 45WB sizes in Shape C can be seen, with the magnetic material surrounding the Wheatstone bridge. Even for the smallest resolution of $2.5 \mu\text{m}$, etched was performed correctly with no short paths between LSMO stripes of the Wheatstone bridge the and surrounding body. These images provide a visual confirmation that a well defined LSMO etch was obtained, even with a small gap of $2.5 \mu\text{m}$ in Fig. 3.38(b). Current follows the desired path with no shorts. Also, it is possible to verify how current density does indeed leave gold pads of excitation terminals in a homogeneous fashion, thanks to Pad A geometry. With the confirmation that electrical current follows only the desired paths, magnetoelectrical characterization can be performed. This first test sample did not present a clear uniaxial magnetic anisotropy as verified by MOKE imaging, but OBIRCH measurements are useful to validate the lithography and etching steps. A proper uniaxial magnetic anisotropy is required for correct comparison between the geometries, so a new sample consisting of 30 nm LSMO over 10° STO and deposited

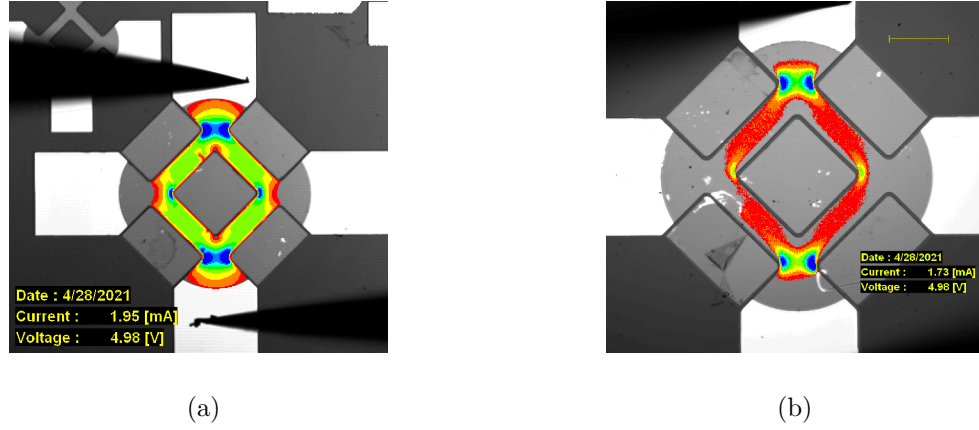


Figure 3.38: Superimposed images for Shape C geometry. a) Usual size bridge, with $300 \mu\text{m}$ length and $100 \mu\text{m}$ width. b) Bridge scaled down by 50%, image obtained at higher magnification. [Sample BA146]

at $680 \text{ }^\circ\text{C}$ was fabricated. Although in this sample the smaller 45WBs structures are not present, a standard 45WB with increased length and width was added and a size comparison will be presented later in this chapter. Figure 3.39 presents the MR curves measured at fixed 5 V bias and 310 K temperature. The MR ratio and anisotropy field

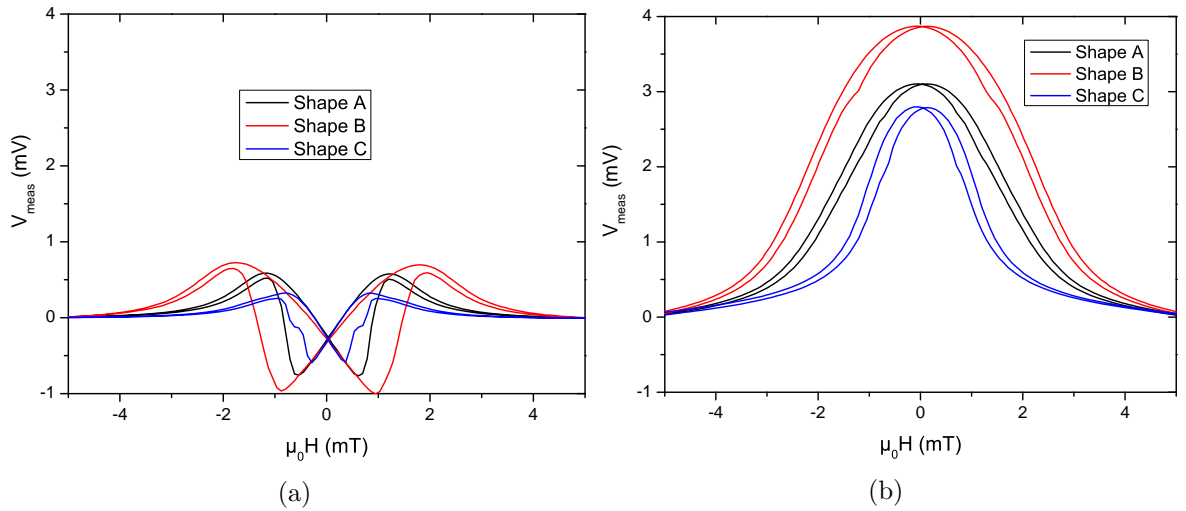


Figure 3.39: Comparison of V_{meas} curves for Shape A, Shape B and Shape C at 5 V bias and 310 K temperature for a) 45WB structure and b) 90WB structure. [Sample BA144]

are both increased in Shape B and reduced in Shape C. The changes on saturation field indicates that there is some shape effect that contributes to the effective H_a . The 45WB structure reaches maximum and minimum values for V_{meas} at different applied fields, and the curves for 90WB structure have different widths. The fact that saturation field increases for Shape B, on bridges with reduced width, seems to indicate that magnetization would rather align itself parallel to thin film interface. So a stronger field is necessary to saturate magnetization in the applied field direction. The opposite is seen for Shape C. As the magnetic body surrounding the LSMO Wheatstone bridge has less boundaries for magnetization rotation regarding its shape, magnetization itself follows more easily the coherent reversal proposed by Stoner-Wohlfarth. Then through exchange interaction due to the small gap, magnetization in etched LSMO arms will follow. This reduces the shape effect on the Wheatstone bridge and sample reaches saturation with reduced applied field. As the MR ratio is also affected, the resulting effect on sensitivity is not direct. Curves obtained from the derivative of V_{meas} are presented in Fig. 3.40. The highest sensitivity is

indeed obtained for the geometry with the smallest H_a . In both structures it is Shape C

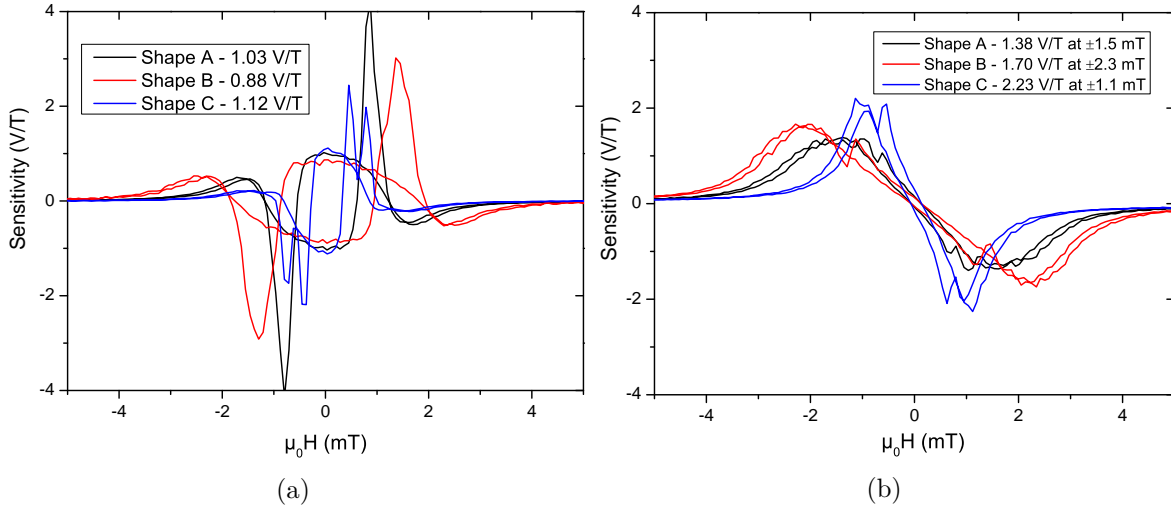


Figure 3.40: Sensitivity curves from the derivative of Fig. 3.39 for Shape A, Shape B and Shape C for a) 45WB structure around zero applied field and b) 90WB structure with the need of a bias DC field. [Sample BA144]

that presents the highest sensitivity, although there is a difference in relative sensitivity values between Shape A and Shape B. Whereas the standard Shape A geometry has the middle value of sensitivity for 45WB structure, it has the lowest value for 90WB. In the latter case, a different value of bias DC field is also required for each geometry. Sensitivity values are very close to each other for 45WB structure, with up to 10% difference. As for 90WB, the value almost doubled from Shape A to Shape C. This shows that there is a stronger shape effect when LSMO stripes are parallel or perpendicular to easy axis. The final comparison of performance is with noise measurements and obtained detectivity values. Figure 3.41 shows the corresponding curves at 5 V bias for both structures

For both 45WB and 90WB structures, the trenches in Shape B resulted in increased thermal noise due to higher electrical resistance. Whereas for Shape A design in 45WB (90WB) structure had 11.9 k Ω (11.7 k Ω) resistance, Shape B presents 14.0 k Ω (13.6 k Ω). The cause of high low frequency noise found in Shape B of 45WB structure is unknown, but might be due to some problem in the fabrication process. The squared dependence of S_V on voltage bias was indeed verified, and a Hooge parameter 20 times greater than for the standard design is calculated. Still considering the 45WB structure, similar noise and sensitivity values are obtained for Shape A and Shape C, resulting in practically same detectivity. As for the studied 90WB structures, there was no big difference in noise measures among the designs. As Shape C presented the highest sensitivity (which was also the case for 45WB structure), it achieves the lowest detectivity values. Therefore the latter design, combined with the Pad A geometry for gold contact, seems interesting for further optimization of AMR LSMO sensors.

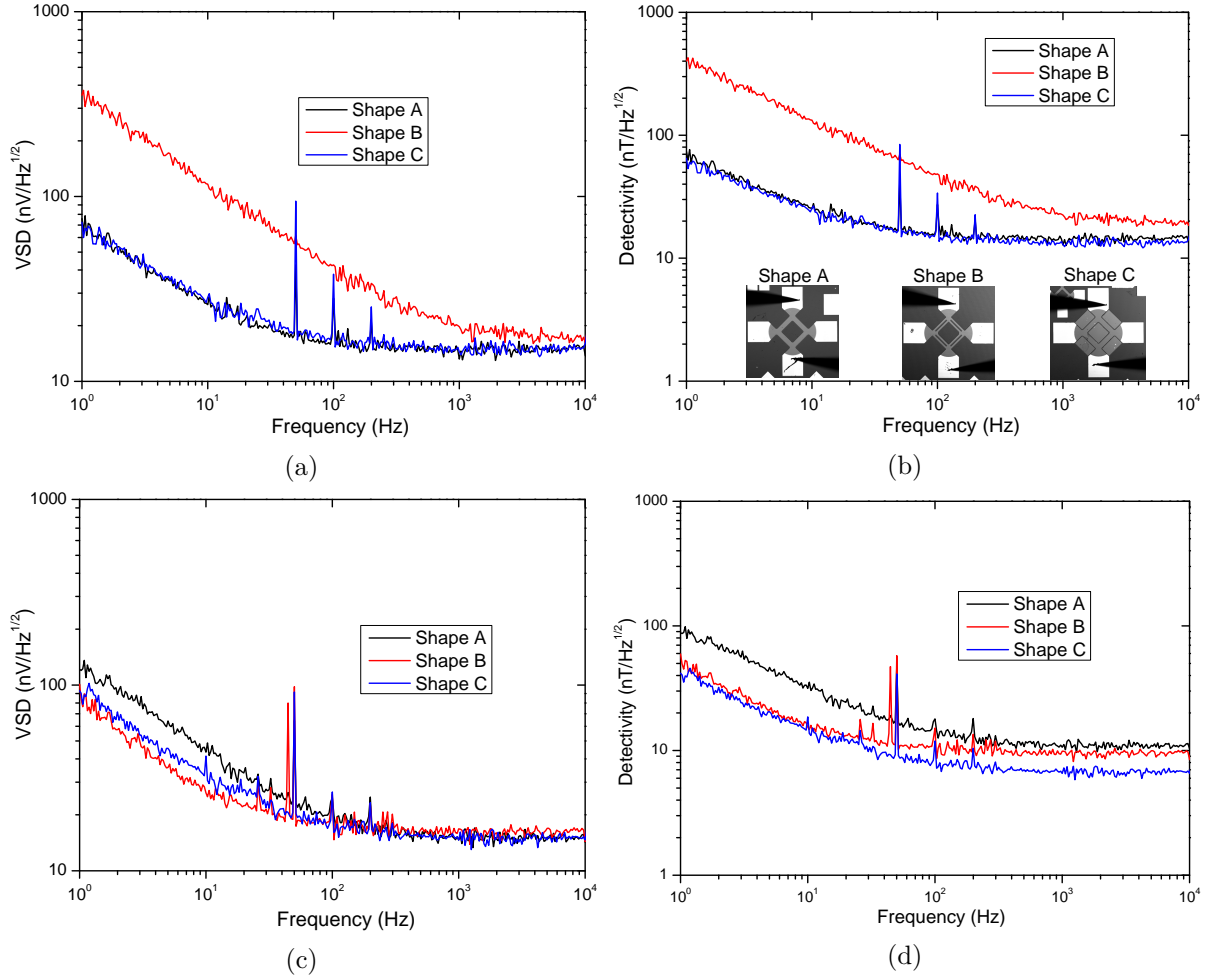


Figure 3.41: Noise measurements and obtained detectivity at 5 V bias and 310 K temperature for a, b) 45WB structure and c, d) for 90WB. OBIRCH pattern images of 45WB structure recall the difference in design. [Sample BA144]

3.5.3 Comparison in size

Another possibility to reduce the intrinsic noise of the Wheatstone bridge is by increasing its volume, with increased lateral dimensions while keeping the same aspect ratio and thin film thickness. In the same sample used for the previous comparison of different shapes, 30 nm LSMO over 10° vicinal STO, a 45WB structure with a 50% size increase was etched. This bridge has the standard Shape A design and Pad A geometry for gold pads, presenting arms with $450 \mu\text{m}$ length and $150 \mu\text{m}$ width and is not surrounded by magnetic material. Both bridge sizes present an equivalent $11.8 \text{ k}\Omega$ resistance, measured in 2-probes configuration. Figure 3.42 presents VSD curves at increasing voltage bias for the standard bridge, next to noise curves for the bridge with increased size. As expected, an increased volume resulted in reduced $1/f$ noise according to the expression by Hooge

$$S_V = \frac{\alpha_H}{n} \frac{1}{\Omega f} V^2$$

With the bigger bridge, sample noise dominates the low frequency noise starting at 5 V only. The comparison can also be made with the slope of the S_V/V^2 by f , as discussed in Chapter 2. This value can be obtained by a linear fit of the average $S_V \times f$ for each bias voltage. The standard size bridge presents a slope of 2×10^{-16} , whereas with increased dimensions a slope of 6×10^{-17} is obtained. This results in a α_H/n of $6.9 \times 10^{-31} \text{ m}^3$ and $4.9 \times 10^{-31} \text{ m}^3$ for the standard and increased size bridges, respectively. But the

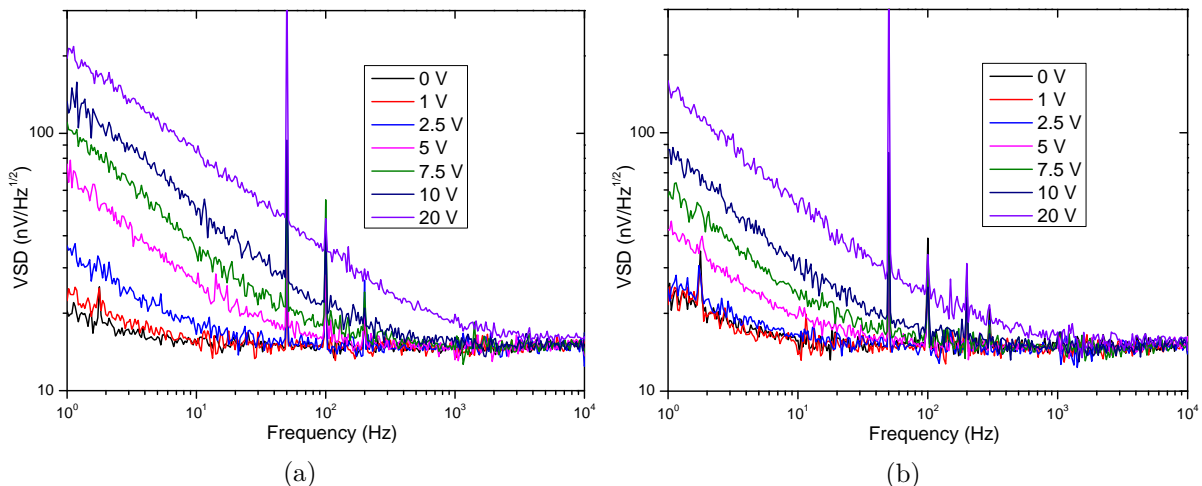


Figure 3.42: Measured noise at increasing voltage bias in 45WB structures. a) Standard size bridge. b) Bridge length and width increased by 50%. [Sample BA144]

actual performance as a sensor also depends on the sensitivity, in this case calculated by the derivative of the V_{meas} curve. The curves for magnetoresistance characterization and corresponding detectivities at 5 V bias are presented in Fig. 3.43. With a reduced MR

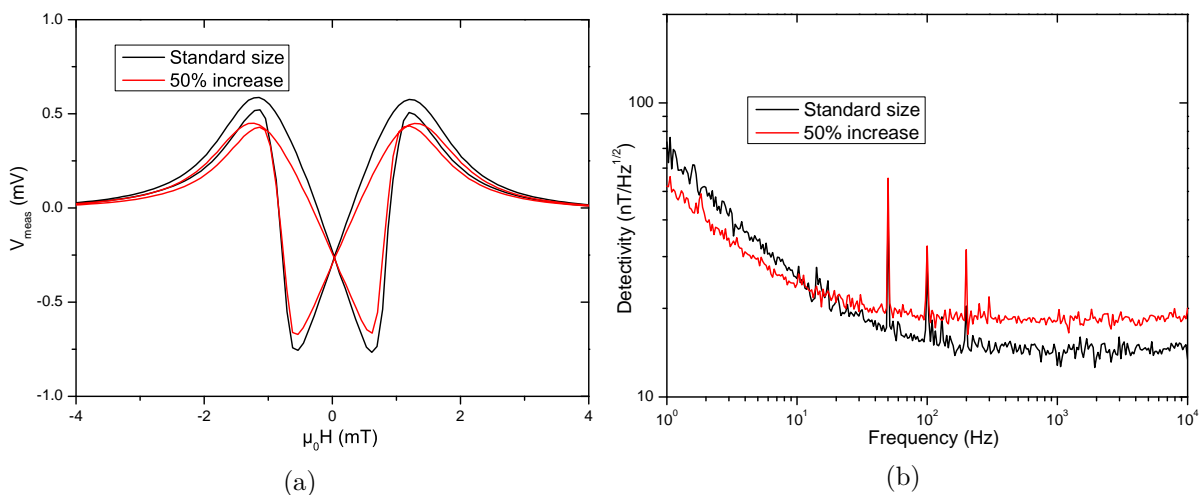


Figure 3.43: Performance comparison for bridge with increased size. a) Slight reduction in MR ratio. b) Lower noise and lower sensitivity results in reduced detectivity in $1/f$ region and higher detectivity in white noise region. [Sample BA144]

ratio, the bigger structure presents a lower sensitivity around zero applied field. Thanks to lower noise due to increased volume, the bigger bridge presents a lower detectivity below 10 Hz even though it has reduced sensitivity. But as both bridges have the same resistance thus same white noise value, the standard size sensor presents a better performance for higher frequencies.

For this particular case, the increase in performance at low frequency does not account for the increase in the occupied area of the bridge, so the smaller geometry is preferable. With a smaller bridge, a higher density can be achieved if a sensor array is to be built, so the standard size is preferred. Further studies on size could be conducted, also investigating smaller size bridges. It is important to point out that the presented results were obtained with an homogeneous magnetic field in the whole sensor area. Different results might be obtained when the Wheatstone bridge is under the influence of a more local, inhomogeneous magnetic field.

3.6 Samples reaching sub-nT

With over 20 fabricated LSMO/STO samples, presenting different manganite film thickness, substrate vicinal angle and/or deposition temperature, Table 3.3 presents those reaching below sub-nT detectivity values at 1 kHz. The informed thickness is the nominal value following a RHEED calibration with flat STO and not results from measurements. Differences in substrate mounting in PLD chamber such as tilts or in effective laser power due to decreased efficiency of the optical window may affect final thickness. Not all fabricated samples were characterized for the whole range of voltage bias. They were all kept at fixed 310 K temperature for MR and noise characterization. With the increase of V_{bias} or working at the optimal temperature, this list could be longer. Depending on the

Sample	LSMO thickness (nm)	Vicinal substrate (°)	Deposition temperature (°C)
BA017	15	4	730
BA054	30	2	730
BA055	30	4	730
BA068	45	4	730
BA072	75	4	730
BA098	30	4	730
BA103	60	8	630
BA104	60	4	730
BA105	60	8	680
BA106	60	4	680
BA114	45	4	730

Table 3.3: Samples that achieve sub-nT performance and their respective fabrication parameters. Samples characterization at 310 K.

set of fabrication parameters, some samples required a higher voltage bias than others. For the minimum V_{bias} among the performed measurements, Table 3.4 shows which structures achieve sub-nT detectivity at 1 kHz. Values for MR ratio and sensitivity obtained from V_{meas} curves are also listed. As verified, 90WB structures present a higher sensitivity than any equivalent 45WB device. Both geometries have similar values of anisotropy field, extracted from the magnetization loops obtained by MOKE imaging or performing the numerical fit over the experimental V_{meas} curves. The difference in sensitivity is then only due to different MR ratios between the standard anisotropic magnetoresistance coefficients and the planar Hall effect. This difference was first observed in single LSMO stripes and confirmed in Wheatstone bridge structures. So for 45WB structures, generally a higher voltage bias is required.

The sample named BA114 reaches sub-nT performance with the lowest necessary voltage bias between all fabricated LSMO sensors. This is due to a high sensitivity thanks to a low anisotropy field. At $V_{bias} = 5$ V, a value of 0.3 mT is extracted from the fit to the presented model and from the FWHM of the V_{meas} curve. In fact, this was the sample presented in Section 3.4, reaching a detectivity of 240 pT Hz^{-1/2} at 1 kHz. One 45WB structure on the same substrate reaches 1 nT Hz^{-1/2} at 1 kHz but with a bias of 20 V. When compared to commercially available sensors, the LSMO devices still do not reach the lowest detectivity values presented by fully developed devices. Whereas available products stack different materials, present built-in coils and magnetic flux concentrators, AMR LSMO sensors are very simple single active layer devices: vicinal STO substrate, ferromagnetic manganite oxide and gold layer for electrical contact. When compared to AMR sensors based on permalloy, LSMO Wheatstone bridge sensors are limited by the much higher resistivity of the manganite oxide, with minimal resistance values around 1.8 kΩ with the dimensions investigated in this work.

Sample & Structure	V_{bias} (V)	MR ratio (%)	Sensitivity ($\% T^{-1}$)	Detectivity ($nT Hz^{-1/2}$)
BA017 90WB	24 (24)	0.06 (0.07)	127 (151)	0.5 (0.5)
BA054 90WB	15 (15)	0.09 (0.10)	87 (107)	0.5 (0.9)
BA055 90WB	10 (10)	0.09 (0.10)	130 (120)	0.8 (0.8)
BA068 90WB	10 (10)	0.07 (0.09)	114 (130)	0.9 (0.6)
BA072 45WB	20	0.04	56	0.7
BA098 45WB	20	0.01	82	0.8
BA103 90WB	10 (10)	0.10 (0.10)	154 (179)	0.7 (0.5)
BA104 45WB	20 (20)	0.04 (0.02)	75 (58)	0.6 (0.8)
BA104 90WB	10 (10)	0.11 (0.11)	122 (97)	0.6 (0.8)
BA105 90WB	20 (20)	0.08 (0.09)	100 (85)	0.5 (0.6)
BA106 90WB	7.5	0.11	173	0.7
BA114 90WB	5 (7.5)	0.10 (0.10)	283 (226)	0.8 (0.6)

Table 3.4: List of Wheatstone bridge structures reaching sub-nT detectivity at 1 kHz for a minimum measured V_{bias} . Sensitivity values are obtained by the derivative of V_{meas} curve. Values in parentheses are for a second structure on the same substrate.

3.7 Comparison with commercially available sensors

Magnetoresistive sensors such as the HMC1001 from Honeywell and TMR9112 from MultiDimension Technologies are fully developed devices that present superior performance than the best individual LSMO Wheatstone bridge fabricated so far. The AMR sensor HMC1001 uses permalloy as the magnetic active material, with a resistivity around $60 \mu\Omega cm$ and an equivalent bridge resistance typically of 850Ω . The permalloy film is deposited over Si and etched in a Wheatstone bridge geometry. It has built-in offset and set/reset straps in order to account for imbalance or external fields and to condition the magnetic domains of the magnetoresistive elements, which also reduces noise. It has barber poles over the permalloy film to achieve a linear operation around zero applied field, with a full scale linear range of 0.4 mT. With a noise of $29 nV Hz^{-1/2}$ at 1 Hz with 5 V bias at room temperature and a sensitivity of $3200 \% T^{-1}$, it reaches $180 pT Hz^{-1/2}$ detectivity value at 1 Hz consuming 29 mW. It is not clear how the easy axis is set in HMC1001 and if magnetic flux concentrators are used. The packaged device, not considering the pins, covers an area of $40.95 mm^2$. Meanwhile, the TMR sensor TMR9112 is a multilayer device, also based on permalloy. A Wheatstone bridge structure is made by interconnecting four individual dies, each consisting of several MTJ elements in series. The magnetization of the pinned layer is fixed by coupling with an antiferromagnetic layer, and easy axis of the free layer is set by shape anisotropy. To improve sensitivity, the MTJs are surrounded by magnetic flux concentrators, and a built-in initialization coil is used to align the magnetic domains. A typical resistance value is $50 k\Omega$. At 1 V bias and room temperature, it has an impressive sensitivity of $100000 \% T^{-1}$ in a 0.2 mT linear range. The product datasheet informs detectivity values of $150 pT Hz^{-1/2}$ at 1 Hz and $4.5 pT Hz^{-1/2}$ at 10 kHz. This shows how TMR devices have an increased $1/f$ noise compared to AMR sensors, as a comparable detectivity at 1 Hz is achieved with a sensitivity 30 times greater. The TMR9112 consumes only 0.02 mW thanks to its high resistance, and the packaged device occupies an area of $36 mm^2$. For comparison, LSMO thin films have a resistivity around $3.2 m\Omega cm$ near 310 K. At this temperature, a 90WB structure on sample BA114 presents $5.5 k\Omega$ equivalent resistance, and at 5 V bias it presents $27 nV Hz^{-1/2}$ noise at 1 Hz, linear range of 0.2 mT, a sensitivity of $280 \% T^{-1}$ and $1.9 nT Hz^{-1/2}$ detectivity at 1 Hz. While there is a difference of one order of magnitude in performance, the AMR LSMO sensor is nothing more than a single layer manganite oxide film etched in a Wheatstone bridge geometry. The LSMO device consumes 4.5 mW and the Wheatstone bridge element occupies a surface area of only $2.25 mm^2$. This area could be further reduced by shrinking down the gold pads for metallic contact.

3.8 Conclusions

The expression for detectivity presented at the end of Chapter 2 acts as a guide on how to improve sensor performance. It is valid when LSMO sample is the dominating contribution to total noise and when the device presents a clear uniaxial magnetic anisotropy. The first requirement can be satisfied with proper reading electronics, while the second relies on fabrication parameters, mainly vicinal angle of the substrate and thin film thickness. Those parameters also affect the MR ratio and anisotropy field, key factors for sensor performance. Lower detectivity values in the whole frequency range are obtained when increasing the MR ratio and/or reducing H_a . It was shown that increasing thin film thickness resulted in a higher MR ratio, but above a given thickness the anisotropy field starts to increase and sample loses its uniaxial anisotropy. Substrates with higher vicinal angle are able to maintain uniaxial behavior for thicker films as they have a reduced terrace width d , while also affecting the MR ratio and H_a . Higher vicinal angles can provoke a surface amorphization of the LSMO layer, which reduces the effective thickness. For a nominal 30 nm LSMO thickness, sample over 10° had an effective crystalline LSMO layer of only 22 nm, while over 4° this value is of 28 nm. Characterization results of these samples agree with the investigation of different thin film thickness over a 4° vicinal STO, with a thinner oxide layer presenting lower MR ratio and anisotropy field. But a reduced film thickness also results in an increased electrical resistance, which increases the noise contribution from the sample, degrading the detectivity. An equilibrium must be achieved between thickness of the LSMO layer and vicinal angle of the STO substrate. In the end, the best compromise to keep uniaxial anisotropy, reasonable values for MR ratio and electrical resistance as well as low anisotropy field is by having thinner films deposited on top of substrates with low vicinal angle. The sample which presented the best performance in the low frequency region consists of 45 nm LSMO over 4° vicinal STO, achieving $1.4 \text{ nT Hz}^{-1/2}$ at 1 Hz and $240 \text{ pT Hz}^{-1/2}$ at 1 kHz while working at 310 K temperature, and a sub-nT resolution already at 5 V bias. This sensor was compared to commercially available devices, and while it does not reach the same detectivity values, it consumes less power than HMC1001 and occupies a very small surface area.

It was also verified that detectivity can have an overall improvement by heating up the device, to an optimal working point. This improvement is due to a reduction of H_a when sample approaches its Curie temperature, up to a point where it starts to lose its ferromagnetic behavior and performance is degraded. A 40% improvement was estimated for sample BA104 with a 10 K increase, from 310 K to 320 K. Another possibility to reduce further the detectivity, although only in the thermal noise region, is by increasing the bias voltage of the LSMO Wheatstone bridge. As the $1/f$ noise also grows with V_{bias} , performance in low frequency range is unchanged, and care must be taken to avoid saturation of the instrumentation preamplifier and self-heating of the LSMO sample. Eventually, this self-heating could be exploited instead of heating up the sample itself, but possible degradation of the oxide layer with high current values during long periods was not investigated. To improve sensor performance in the low frequency region, a study on current density distribution was conducted, in order to reduce $1/f$ noise. Different designs for gold pads were designed and current distribution was analyzed with OBIRCH technique. A more homogeneous current and with less points of concentration was obtained with Pad A design, which also presented the lowest $1/f$ noise. As the 45WB structure always presented a lower MR ratio than its 90WB counterpart, an investigation on the effects of shape anisotropy was conducted. Two additional geometries for Wheatstone bridges were prepared, and the presence of a magnetic body surrounding the bridge reduced the MR ratio and anisotropy field, indicating some contribution of demagnetizing energy. This geometry presented a performance similar to the standard Wheatstone bridge design, and more studies could be conducted for a better comprehension. Although the 45WB still presents lower performance than 90WB structure, due to the reduced MR ratio of the PHE when compared to standard AMR terms in the resistivity tensor. Increasing the size of the standard 45WB design resulted in a bridge with reduced low frequency

noise, similar H_a and reduced MR ratio. With a slightly reduced sensitivity, the enlarged bridge has lower detectivity values below 10 Hz when compared to the standard size, but a poorer performance for higher frequencies. The improvement in $1/f$ region is not relevant compared to the increase in area occupation, but the investigation was conducted only for homogeneous magnetic field over the whole sample. Results might differ for a more localized and inhomogeneous field.

Further improvement of AMR LSMO sensors can be achieved with the implementation of magnetic flux concentrators (MFCs). This will reduce the effective anisotropy field of the device, thus increasing its sensitivity without affecting noise. With proper MFCs design, gains above one order of magnitude can be predicted [18]. This will allow the LSMO sensors to reach sub-nT resolution at 1 Hz. Lastly, it is important to highlight that a limitation in device performance is the intrinsic resistivity of LSMO, resulting in an increased thermal noise when comparing to permalloy. The analysis performed in this work can be extended to other materials. Should a new ferromagnetic oxide with reduced resistivity and that can have uniaxial magnetic anisotropy induced by epitaxial deposition on vicinal substrate be available, AMR devices with lower intrinsic noise can be fabricated. The investigation here presented contributes to push forward the development of electronic devices based on functional oxides. The adoption of oxide based sensors will also benefit from a large scale production, reducing production cost. The deposition of manganite perovskite thin films such as LSMO can be performed via metal-organic chemical vapor deposition [19]. If high quality films are achievable, this technique allows a good control of thickness, composition and strain over large areas, although the need for high temperatures during deposition is a drawback to integrate oxide electronics in the already established semiconductor industry.

Bibliography

- [1] J.R. Black. “Electromigration—A brief survey and some recent results”. In: *IEEE Transactions on Electron Devices* 16.4 (1969), pp. 338–347. DOI: 10.1109/T-ED.1969.16754.
- [2] M. A. Belogolovskii, Y. F. Revenko, A. Y. Gerasimenko, V. M. Svistunov, E. Hatta, G. Plitnik, V. E. Shaternik, and E. M. Rudenko. “Inelastic electron tunneling across magnetically active interfaces in cuprate and manganite heterostructures modified by electromigration processes”. In: *Low Temperature Physics* 28.6 (2002), pp. 391–394. DOI: 10.1063/1.1491178. eprint: <https://doi.org/10.1063/1.1491178>. URL: <https://doi.org/10.1063/1.1491178>.
- [3] J. Wang, H. Duan, X. Lin, V. Aguilar, A. Mosqueda, and G. Zhao. “Temperature dependence of magnetic anisotropy constant in iron chalcogenide Fe_3Se_4 : Excellent agreement with theories”. In: *J. Appl. Phys.* 112.10 (2012), p. 103905. DOI: 10.1063/1.4759352. eprint: <https://doi.org/10.1063/1.4759352>. URL: <https://doi.org/10.1063/1.4759352>.
- [4] M. Belmeguenai, S. Mercone, C. Adamo, L. Mechin, C. Fur, P. Monod, P. Moch, and D. G. Schlom. “Temperature dependence of magnetic properties of $\text{La}_{0.7}\text{Sr}_{0.3}\text{MnO}_3/\text{SrTiO}_3$ thin films on silicon substrates”. In: *Phys. Rev. B* 81 (2010), p. 054410. DOI: 10.1103/PhysRevB.81.054410. URL: <https://doi:10.1103/PhysRevB.81.054410>.
- [5] A. Persson, R.S. Bejhed, H. Nguyen, K. Gunnarsson, B.T. Dalslet, F.W. Østerberg, M.F. Hansen, and P. Svedlindh. “Low-frequency noise in planar Hall effect bridge sensors”. In: *Sensors and Actuators A: Physical* 171.2 (2011), pp. 212–218. ISSN: 0924-4247. DOI: <https://doi.org/10.1016/j.sna.2011.09.014>. URL: <https://www.sciencedirect.com/science/article/pii/S0924424711005280>.

- [6] D. S. Chuang, C. A. Ballentine, and R. C. O’Handley. “Surface and step magnetic anisotropy”. In: *Phys. Rev. B* 49 (21 June 1994), pp. 15084–15095. DOI: 10.1103/PhysRevB.49.15084. URL: <https://link.aps.org/doi/10.1103/PhysRevB.49.15084>.
- [7] L. Ranno, A. Llobet, R. Tiron, and E. Favre-Nicolin. “Strain-induced magnetic anisotropy in epitaxial manganite films”. In: *Applied Surface Science* 188.1 (2002), pp. 170–175. ISSN: 0169-4332. DOI: [https://doi.org/10.1016/S0169-4332\(01\)00730-9](https://doi.org/10.1016/S0169-4332(01)00730-9). URL: <https://www.sciencedirect.com/science/article/pii/S0169433201007309>.
- [8] A. Persson, R.S. Bejhed, F.W. Østerberg, K. Gunnarsson, H. Nguyen, G. Rizzi, M.F. Hansen, and P. Svedlindh. “Modelling and design of planar Hall effect bridge sensors for low-frequency applications”. English. In: *Sensors & Actuators: A. Physical* 189.Complete (2013), pp. 459–465. DOI: 10.1016/j.sna.2012.10.037.
- [9] C. D. Damsgaard, S. C. Freitas, P. P. Freitas, and M. F. Hansen. “Exchange-biased planar Hall effect sensor optimized for biosensor applications”. In: *Journal of Applied Physics* 103.7 (2008), 07A302. DOI: 10.1063/1.2830008. eprint: <https://doi.org/10.1063/1.2830008>. URL: <https://doi.org/10.1063/1.2830008>.
- [10] J. M. D. Coey, M. Viret, L. Ranno, and K. Ounadjela. “Electron Localization in Mixed-Valence Manganites”. In: *Phys. Rev. Lett.* 75 (21 Nov. 1995), pp. 3910–3913. DOI: 10.1103/PhysRevLett.75.3910. URL: <https://link.aps.org/doi/10.1103/PhysRevLett.75.3910>.
- [11] C. Adamo, X. Ke, H. Q. Wang, H. L. Xin, T. Heeg, M. E. Hawley, W. Zander, J. Schubert, P. Schiffer, D. A. Muller, L. Maritato, and D. G. Schlom. “Effect of biaxial strain on the electrical and magnetic properties of (001) $\text{La}_{0.7}\text{Sr}_{0.3}\text{MnO}_3$ thin films”. In: *Applied Physics Letters* 95.11 (2009), p. 112504. DOI: 10.1063/1.3213346. eprint: <https://doi.org/10.1063/1.3213346>. URL: <https://doi.org/10.1063/1.3213346>.
- [12] M. Španková, V. Štrbík, E. Dobročka, Š. Chromik, M. Sojková, M. Zheng, and J. Li. “Characterization of epitaxial LSMO thin films with high Curie temperature prepared on different substrates”. In: *Vacuum* 126 (2016), pp. 24–28. ISSN: 0042-207X. DOI: <https://doi.org/10.1016/j.vacuum.2016.01.009>. URL: <https://www.sciencedirect.com/science/article/pii/S0042207X16300094>.
- [13] L. Méchin, S. Wu, B. Guillet, P. Perna, C. Fur, S. Lebargy, C. Adamo, D.G. Schlom, and J. M. Routoure. “Experimental evidence of correlation between 1/f noise level and metal-to-insulator transition temperature in epitaxial $\text{La}_{0.7}\text{Sr}_{0.3}\text{MnO}_3$ thin films”. In: *J. Phys. D: Appl. Phys. - Fast Track Communication* 46 (2013), p. 202001. URL: <https://hal.archives-ouvertes.fr/hal-00977721>.
- [14] F. W. Østerberg, A. D. Henriksen, G. Rizzi, and M. F. Hansen. “Comment on “Planar Hall resistance ring sensor based on NiFe/Cu/IrMn trilayer structure” [J. Appl. Phys. 113, 063903 (2013)]”. In: *Journal of Applied Physics* 114.10 (2013), p. 106101. DOI: 10.1063/1.4820925. eprint: <https://doi.org/10.1063/1.4820925>. URL: <https://doi.org/10.1063/1.4820925>.
- [15] A. Aryan, B. Guillet, J.M. Routoure, C. Fur, P. Langlois, and L. Méchin. “Measurement of thermal conductance of $\text{La}_{0.7}\text{Sr}_{0.3}\text{MnO}_3$ thin films deposited on SrTiO_3 and MgO substrates”. In: *Applied Surface Science* 326 (2015), pp. 204–210. ISSN: 0169-4332. DOI: <https://doi.org/10.1016/j.apsusc.2014.11.119>. URL: <https://www.sciencedirect.com/science/article/pii/S0169433214026014>.
- [16] V. Mor, M. Schultz, O. Sinwani, A. Grosz, E. Paperno, and L. Klein. “Planar Hall effect sensors with shape-induced effective single domain behavior”. In: *Journal of Applied Physics* 111.7 (2012), 07E519. DOI: 10.1063/1.3680084. eprint: <https://doi.org/10.1063/1.3680084>. URL: <https://doi.org/10.1063/1.3680084>.

- [17] A. D. Henriksen, G. Rizzi, and M. F. Hansen. “Experimental comparison of ring and diamond shaped planar Hall effect bridge magnetic field sensors”. In: *Journal of Applied Physics* 118.10 (2015), p. 103901. DOI: 10.1063/1.4930068. eprint: <https://doi.org/10.1063/1.4930068>. URL: <https://doi.org/10.1063/1.4930068>.
- [18] X. Zhang, Y. Bi, G. Chen, J. Liu, J. Li, K. Feng, C. Lv, and W. Wang. “Influence of size parameters and magnetic field intensity upon the amplification characteristics of magnetic flux concentrators”. In: *AIP Advances* 8.12 (2018), p. 125222. DOI: 10.1063/1.5066271. URL: <https://doi.org/10.1063/1.5066271>.
- [19] D. Pla, C. Jimenez, and M. Burriel. “Engineering of Functional Manganites Grown by MOCVD for Miniaturized Devices”. In: *Advanced Materials Interfaces* 4.8 (2017), p. 1600974. DOI: <https://doi.org/10.1002/admi.201600974>. eprint: <https://onlinelibrary.wiley.com/doi/pdf/10.1002/admi.201600974>. URL: <https://onlinelibrary.wiley.com/doi/abs/10.1002/admi.201600974>.

Chapter IV

Applications in Real Environment

Whereas previous magnetotransport and noise characterization of LSMO sensors were conducted inside a closed station, with electrical contact by metallic probes, controlled temperature and homogeneous magnetic field, this chapter is focused on how the AMR LSMO device can be used as a proper sensor in real world environment. Discussions on possible packaging for protection and portability, the detection of alternating magnetic fields instead of a DC sweep, sensing inhomogeneous fields and connecting sensors in a gradiometer arrangement are carried out. An experiment conducted at SISSA to detect the magnetic field originating from the spontaneous activity of live neuronal cells is also presented.

4.1 Sensor mounting and Packaging

Previous noise, V_{meas} and OBIRCH measurements were conducted using metallic probes to obtain electrical contact with the gold pads of the samples. Once the probes are in contact, sample can no longer be moved. To make the sensor portable and move it as desired, it must be mounted on top of a Printed Circuit Board (PCB). A custom 25 x 16 mm PCB consisting of two layers was prepared by Dr. Laurence Méchin and Julien Gasnier. The first layer serves as the support for the STO substrate, which can be fixed either by silver paste or double-side tape. The second layer goes on top of the first and has a cavity for the STO substrate to pass through. It is in the second layer that copper tracks are present, and thanks to this two-layers mounting they stay roughly at the same level of the gold pads of the device. This facilitates the connection from gold pads of the LSMO structures to the copper tracks of the PCB. Figure 4.1 shows the PCB and a sample mounted on it. In this work, such electrical connections were done by wire bonding technique, although we discussed the possibility to make a direct solder using Wood's metal, a metal alloy with a melting point around 70 °C, or deposit a new layer of gold forming a path from gold pads to copper tracks. The benefit of such connections would be to obtain a thinner final device, as the aluminium wires from wire bonding add some height. Plus, the mentioned flat connections are more robust and allow to place a second device over the PCB, whereas bonding wires can get deformed and break. To perform a direct solder with Wood's metal from gold on LSMO/STO to copper on PCB, gold path must reach sample borders. Another photolithography mask could be used to cover sample in gold and then remove excess material via lift-off technique. If a new mask is drawn already with extended gold pads, there would also be LSMO underneath due to how samples are fabricated. It is unknown if the added LSMO stripes, although covered in gold so that all electrical current will pass through the metal, would affect the magnetic properties of the Wheatstone bridge structure. A similar lift-off process is needed for a direct deposition of gold forming a path from sample gold pads to PCB copper tracks. But in this case, the correct alignment between the sample and PCB during lithography step is crucial. As the STO substrate is fixed to the first PCB layer by hand, and same

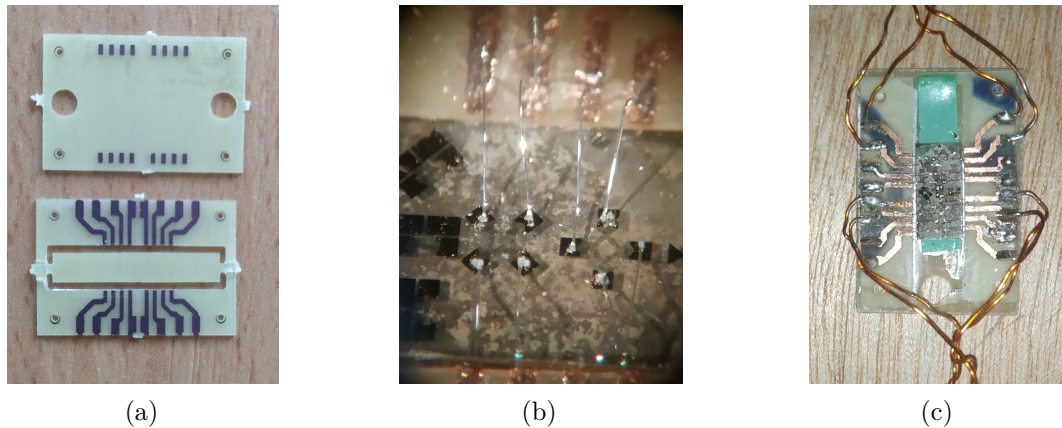


Figure 4.1: a) PCB of 25 x 16 mm consisting of two layers. b) Zoomed view of wire bonding connection from gold pads to copper tracks. c) LSMO sample mounted on PCB, with wire bonding from copper tracks to gold pads and copper wires soldered to PCB. STO substrate is of 10 x 5 mm.

for the placement of the second layer, a correct and repeatable alignment is not an easy task. Another experimental obstacle is to obtain an homogeneous film of photoresist covering the whole sample and PCB. There will always be some gap between the STO substrate and the second PCB layer, where the photoresist will concentrate. Plus, it may not present a good adherence to the PCB material when performing spin coating. For those reasons, it was decided to use wire bonding only, although this is something that should be further discussed and developed to obtain actual sensors with a lower final height. The thinner the final device, the closer the source of a magnetic signal of interest can be placed. Wire bonding is done by a manual wire bonder equipment from West Bond company. Aluminium wires with 50 μm diameter were used.

Once gold pads of LSMO structures are connected to copper tracks of the PCB, standard tin soldering can be done to connect samples to electronics with copper wires. The next step is to completely cover the LSMO sample, protecting it from the environment. As the ByAxon project considers a biomedical application, the sensor can be covered by polydimethylsiloxane (PDMS), a biocompatible polymer widely used in microfluidics as it is chemically inert, thermally stable and permeable to gases [1]. Using FreeCAD software and 3D printer, a mold was prepared in polylactic acid (PLA) to place the PCB already with the sample and cover it with PDMS. The PDMS was prepared at the standard weight ratio of 10:1 curing agent, and left to cure during two days at ambient temperature and pressure before removing it from the mold. While still liquid, it correctly covers LSMO sample and PCB, but bonding wires may be left uncovered if arc from copper track to gold pad is too high. Ideally, wire bonding wires should be as low as possible, but as it is a task done by a hand controlled equipment, it can be difficult to achieve. The mold printed in polylactic acid and a covered LSMO sample are presented in Fig. 4.2. The mold presents a 20 mm radius circular shape so a small Petri dish can be placed over it (see later Section 4.4), and a depth obtain a PDMS thickness of 1 mm. As the adhesion between PDMS and PLA was unknown, the mold present holes in the PCB slot so a force can be applied from the backside to help removing sample, if needed. To verify if electrical contact was maintained after PDMS cover and curing, the resistance between terminals of the Wheatstone bridge was measured at the outer ends of the copper wires with a multimeter. Ferromagnetic behavior was verified by moving a permanent magnet on top of the sample and following the output voltage waveform in time domain with an oscilloscope. No more in-depth verification was performed as this sample does not present a clear uniaxial anisotropy, and was used as a dummy. After confirming that wire bonding and soldering resisted the packaging process, PDMS was removed to check its adherence to the sample. Whereas all wire bonds were removed in the process, gold pads and LSMO

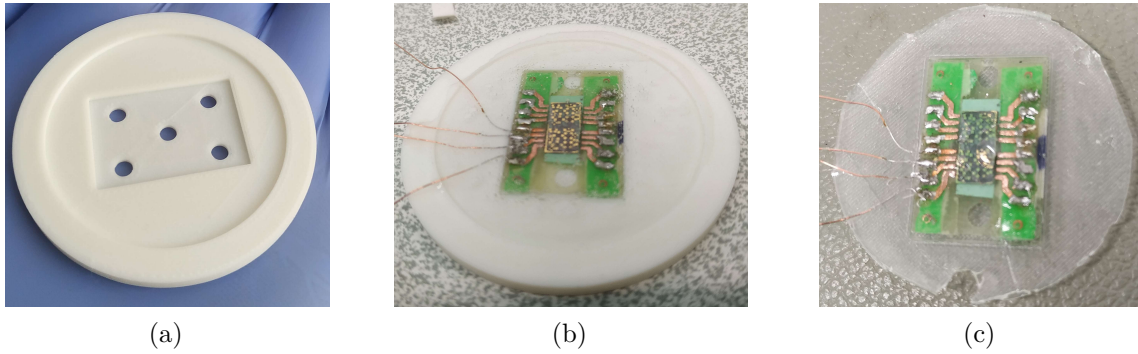


Figure 4.2: First test protecting sample with PDMS. a) 3D printed mold with inner circle presenting 20 mm radius. b) PCB insert in the mold socket after wire bonding and soldering. c) Result after removing from mold.

film remained unaffected. Therefore, the sample can be packaged once again if needed.

In this first case, sample was covered after copper wires were soldered to the PCB. The solder bump may also add some extra height to the PDMS layer, and it may even stay uncovered. It is thus better to perform soldering after PDMS is cured and removed from the extremities of the PCB copper tracks. After the first trials, a smaller mold for PDMS covering was 3D printed, with the dimensions of the PCB. Fortunately, adhesion to PLA is weak, so there is no need for the backside holes. This mold was used to cover sample BA103, a 60 nm thick LSMO film deposited over a 8° vicinal STO substrate at 630°C , and results are shown in Fig. 4.3. A more uniform and flat cover is obtained. To

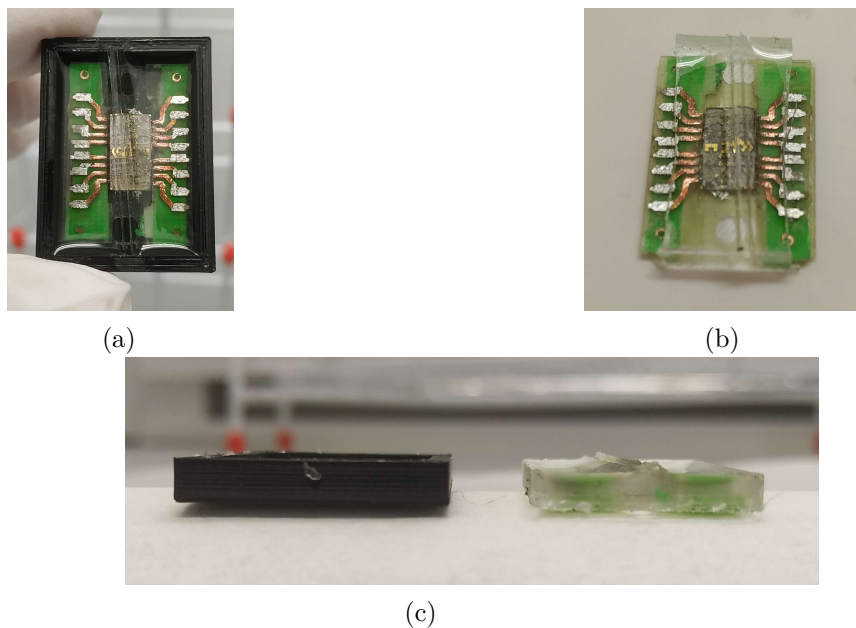


Figure 4.3: Second version of mold for PDMS covering. a) Slow curing at room temperature results in smooth PDMS without air bubbles. b) PDMS removed from extremities of the PCB, allowing the soldering of copper wires. c) Aluminium wires of wire bonding are completely covered, with a total device thickness of 3 mm.

verify if sample noise was degraded due to the packaging process, new measurements were performed. This second run of noise measurements was performed outside the 4-probes station, therefore at room temperature and no shielding. Figure 4.4 shows noise curves for a 45WB structure of BA103. Except for the variations due to sample temperature, similar noise curves are obtained as expected. Covering LSMO with PDMS does not affect the manganite oxide. The $1/f$ noise evolution with voltage bias is also maintained. Therefore

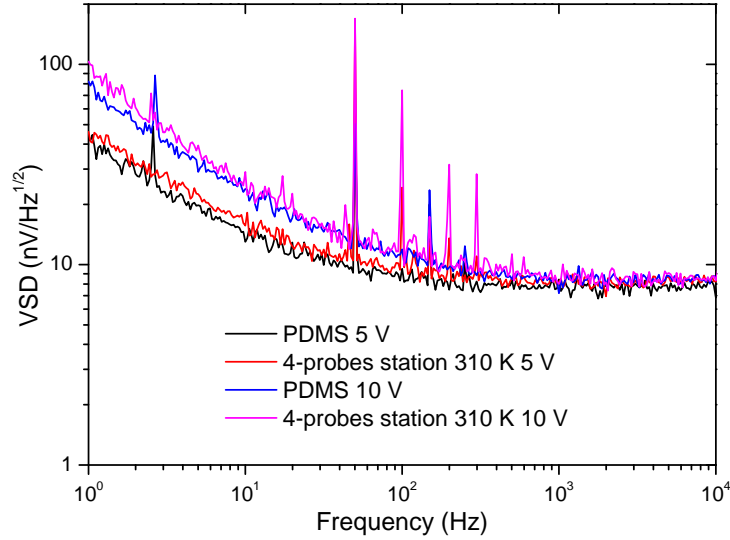


Figure 4.4: Noise comparison of a 45WB structure in sample BA103. Curves before covering with PDMS were obtained with sample at fixed 310 K temperature and inside the 4-probes station. After sample packaging, noise was measured at room temperature.

covering sample with PDMS does not degrade its electrical noise. In fact, it is the quality of the wire bonding and soldering that can have a considerable effect, due to bad electrical contact.

4.2 Characterization with alternating magnetic field

The detectivity curves presented previously indicate the minimum magnetic field amplitude that can be detected by the device at a given frequency. These curves are obtained by dividing the measured spectral noise by the corresponding sensitivity of the sensor. To properly characterize the LSMO samples as a sensing device, it is preferable to apply a magnetic field with known amplitude and frequency and measure the output signal of the device both in time and frequency domains. One possible way to apply a defined alternating field is by employing a pair of Helmholtz coils supplied with electric current from a controllable source. As the amplitude and frequency of the source changes, so does the generated magnetic field. The variation in sensor output is then verified.

A pair of Helmholtz coils can generate an homogeneous magnetic field in their middle point, provided that both coils present the same number of turns n and radius R_c . When the distance between the center of each coil is equal to R_c , the magnetic flux density B at the center of the system is

$$B = \left(\frac{4}{5}\right)^{3/2} \frac{\mu_0 n I}{R_c} \quad (4.1)$$

where I is the electric current through the coils. The pair of coils used at GREYC present $n = 95$ and $R_c = 65$ mm. The expression for B can then be reduced to

$$B = 1.3 \times 10^{-3} I$$

in tesla (T). The first step was to characterize the set of coils itself to obtain its transfer function, as we have interest in applying currents in the frequency range from 1 Hz to 200 Hz. This frequency range was selected due to the nature of the magnetic signals to be detected in the ByAxon project. The characterization of the coils was performed in the magnetic shielded room of the laboratory, using a fluxgate sensor Mag-03 from Bartington Instruments. According to its datasheet, this sensor presents a 3 kHz bandwidth and 143 kV T⁻¹ scale. The sensitive area of the fluxgate was positioned at the middle point

between both coils, and coils were supplied with a sinusoidal voltage signal in series with a 99.4 k Ω resistance. The frequency was swept from 1 Hz to 1 kHz while the peak amplitude was fixed at 10 mV. The output signal of the fluxgate was amplified by a factor of 100 using a Model 5113 Low Noise Voltage Preamplifier from Ametek Scientific Instruments, also configured with a low-pass filter at 1 kHz cut-off frequency and 12 dB attenuation. The spectrum analyzer HP 3562A was used both as source for the coils and measuring the output of the fluxgate. Figure 4.5 shows the flat response of the coils in the desired bandwidth. Using the fluxgate sensor scaling factor and applying a known signal, it is

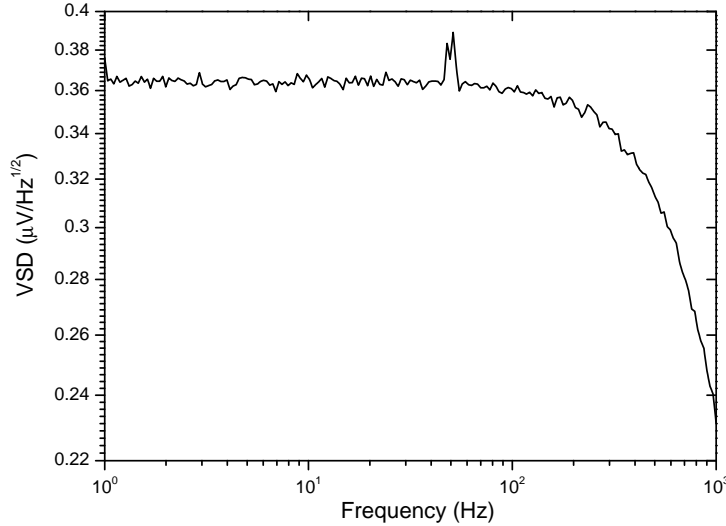


Figure 4.5: Coils frequency response measured with commercial fluxgate. Difference of 2.5% from signal at 16 Hz to 185 Hz.

also possible to obtain the experimental conversion rate of the coils, calculated to be

$$B = 1.22 \times 10^{-3} I$$

It is this conversion rate that was considered for further experiments. After mounting a LSMO sample on a PCB, it can be placed in between the coils for characterization as a proper sensor. The first sample to be tested was BA106, a 60 nm LSMO film deposited over 4° vicinal STO at 680 °C. In Fig. 4.6 the V_{meas} and detectivity curves for both 45WB structures (now referenced as WB1 and WB3) in this sample are presented, all measured using the mentioned 4-probes LakeShore station. The same home-made amplifier based on AD8421 was used for measurements in the shielded room. A low-pass filter at 1 kHz (26 dB attenuation) and 20 dB gain was added between the home-made amplifier and signal reading at spectrum analyzer and oscilloscope. Although 90WB structures present lower detectivity values due to higher sensitivity, a bias DC magnetic field is needed to keep sensor in its linear operation range. Therefore it is much simpler to employ 45WB structures, even though such bias could be done with a DC voltage offset through the coils or correctly positioning some permanent magnets. The first step was to apply a magnetic field with known frequency and amplitude and measure the output of the LSMO device. The signal in V_{rms} can be used to verify the sensitivity value of the Wheatstone bridge, whereas noise curves are in $V \text{ Hz}^{-1/2}$. Noise levels should be similar to those measured inside the 4-probes LakeShore station, with a difference due to operation temperature. Measurements in the station were performed at 310 K whereas sample was kept at room temperature for experiments using Helmholtz coils inside the shielded room. The waveform generator HP 33120A was used to supply coils with a sinusoidal voltage at a given amplitude and frequency. Figure 4.7 shows the V_{rms} curve of BA106 WB3 sensor, biased at 5 V. The applied magnetic field is of 16 Hz frequency and 37 nT root mean square (RMS) amplitude. Measuring a voltage output of 79 nV root mean square, the calculated

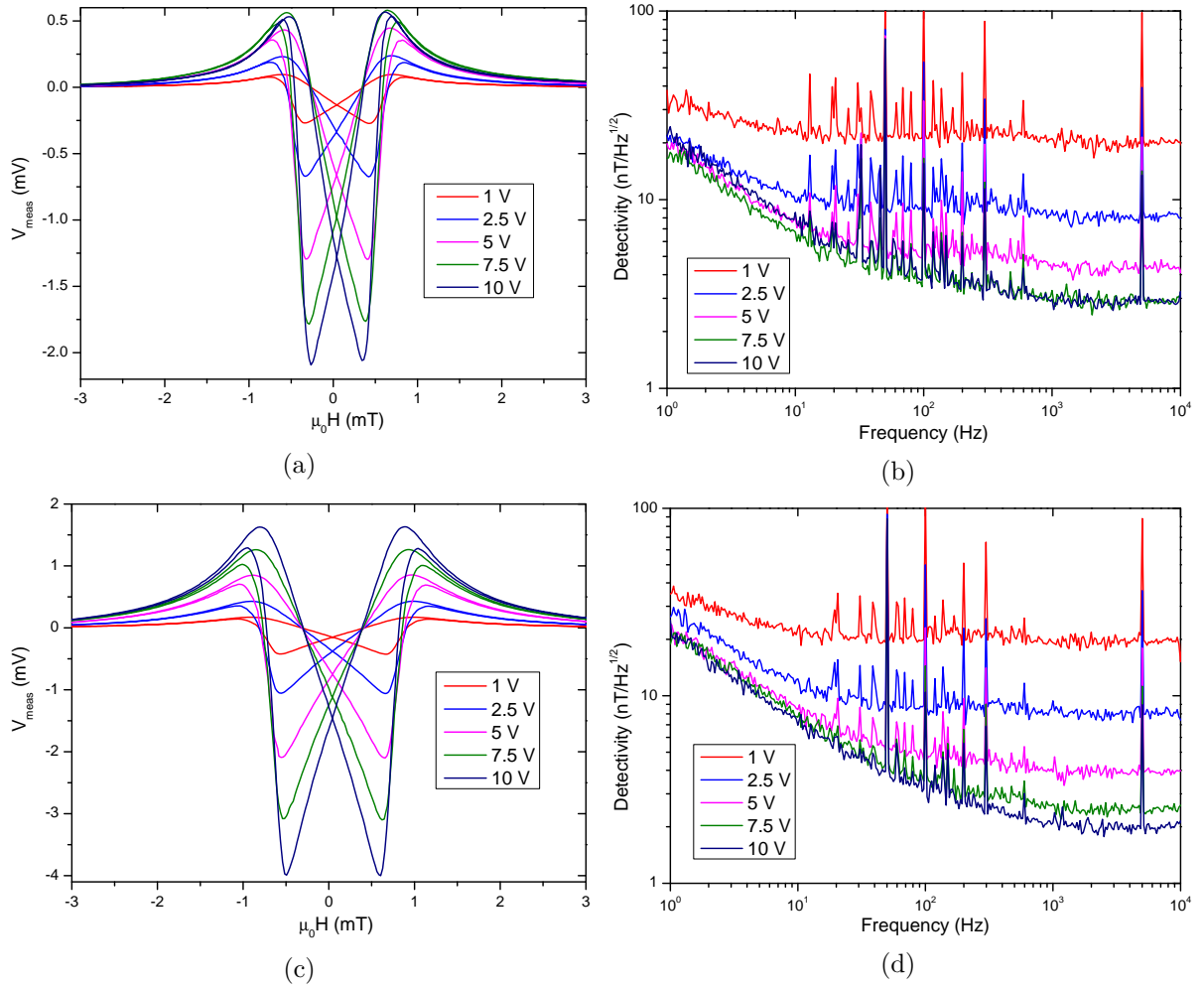


Figure 4.6: Characterization curves at 310 K for a, b) BA106 WB1 bridge and c, d) BA106 WB3 bridge. The 45WB structures present a linear operation around zero applied field and detectivity scales as expected.

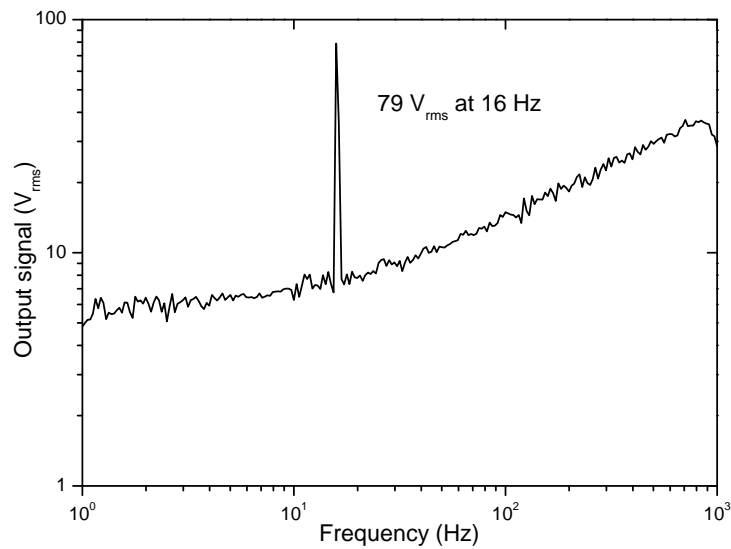


Figure 4.7: Root mean square voltage output signal from BA106 WB3 at 5 V.

sensitivity for this sample is of 2.11 V T^{-1} . This is close to the value obtained through the derivative of V_{meas} around zero applied field. The comparison between noise measured

in LakeShore station and the noise with a given magnetic signal for both 45WB structures is presented in Fig. 4.8, at a 5 V bridge bias. For both Wheatstone bridge structures,

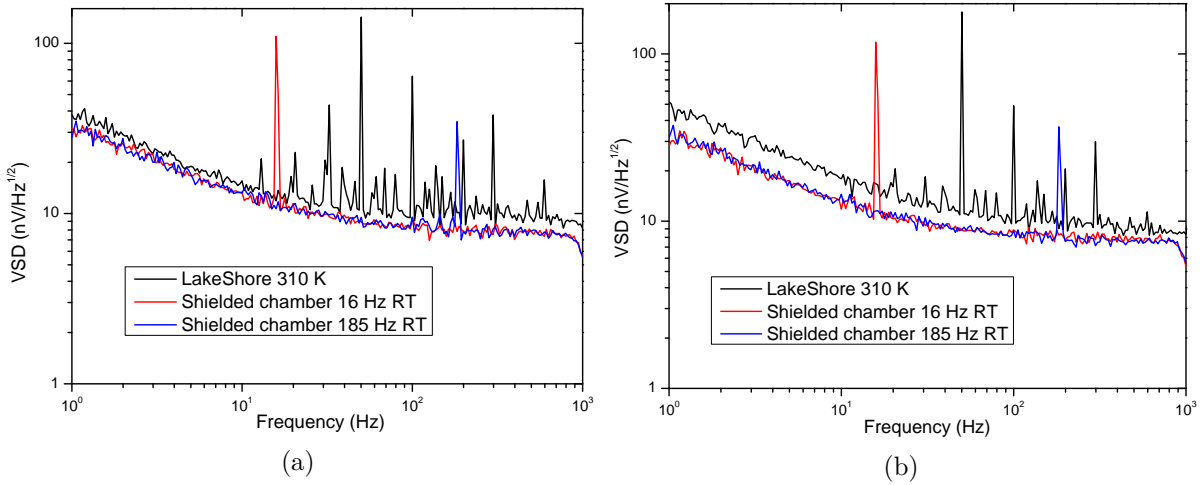


Figure 4.8: Noise levels at 5 V bridge bias, measured in LakeShore station and inside shielded room with Helmholtz coils. a) BA106 WB1 sensor. b) BA106 WB3 sensor.

similar noise levels are obtained, considering the temperature difference and disregarding the peaks due to field generated by the coils and some interference (mostly in LakeShore curves). Noise level is slightly higher in LakeShore station because sample was heated up to 310 K. At higher temperature, the electrical resistance of LSMO increases. This results in higher thermal noise and higher low frequency noise due to amplifier's current noise. The signal going through the coils was either at 16 Hz or 185 Hz, both configured at a 5 V peak amplitude. Using oscilloscope DSOX3014A from Keysight Technologies it was possible to follow the signals in time domain and measure its amplitude. At 16 Hz the reading was at 8.6 V peak-to-peak whereas a 10.7 V peak-to-peak was measured at 185 Hz. Considering the series resistance of 99.4 k Ω and using the coils conversion rate, the root mean square magnetic flux density is of 37 nT and 46 nT at 16 Hz and 185 Hz, respectively. These experiments go beyond a characterization with a sweeping DC magnetic field, and show that our LSMO PHEBs do work as proper sensors. The next step is to verify the detection of inhomogeneous magnetic fields.

4.2.1 Inhomogeneous magnetic field

Out of the shielded room, the pair of Helmholtz coils and LSMO sample were placed inside a mu-metal cylinder, with open extremities. A 0.56 mm diameter copper wire was positioned above the sensor, with a 100 Ω series resistance. By passing electric current through this wire, an inhomogeneous magnetic field is created. As the wire presents a limited length and it is not completely straight, the infinite wire approximation can not be used to predict the generated magnetic field. Figure 4.9 is a photo of the setup, showing the mounted LSMO sample between the pair of Helmholtz coils and the copper wire. The operation of the device can be verified by supplying the coils and the wire with electric currents at known frequencies and recording sensor's output. While coils were supplied with a 16 Hz voltage signal, the wire was given a 183 Hz frequency. The amplitude of the signal in the coils was of 9.25 V peak-to-peak, measured with R&S RTO2000 oscilloscope. This same equipment was used to supply the signals both for coils and wire. Considering the 99.4 k Ω in series with the coils and the calibration obtained in the shielded room, the root mean square amplitude of the flux density is 40 nT. At first, WB1 and WB3 were biased at 5 V, so such amplitude is more than enough. Figure 4.10 shows the voltage spectrum in V_{rms} of both 45WB structures from sample BA106. With a 67 nV $_{rms}$ and 40 nV $_{rms}$ output for structures WB1 and WB3, sensitivities of 33.4 % T $^{-1}$ and 25 % T $^{-1}$

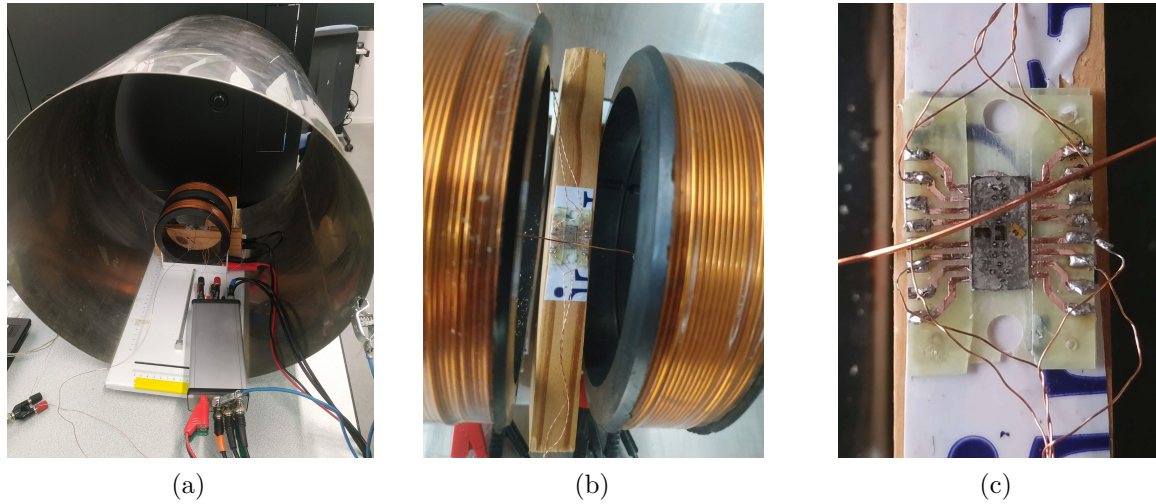


Figure 4.9: Photos of the setup. a) Helmholtz coils and sample inside a mu-metal cylinder. b) Copper wire positioned over the LSMO device. c) Zoomed view of the wire over the sensor.

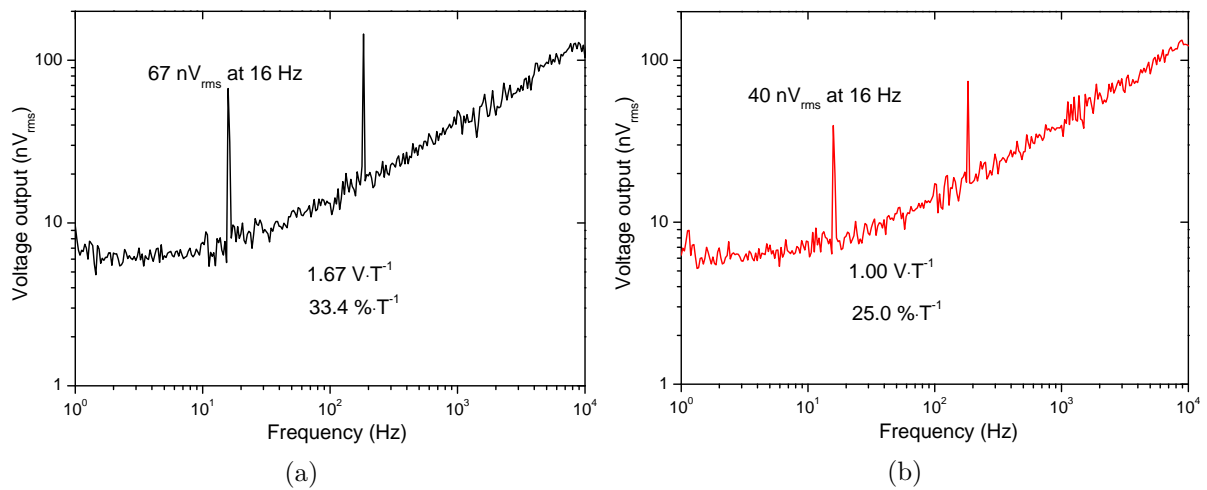


Figure 4.10: 45WB PHEBs working at 5 V bias and room temperature. Coils generate a 40 nT field at 16 Hz, wire generating an inhomogeneous field at 183 Hz. a) Voltage output from WB1. b) Output from WB3.

are respectively calculated. Both bridges do detect the signal from the wire, although there is a difference due to wire placement and the intrinsic sensitivity of each bridge. Actually in this setup, if we follow the right-hand rule, part of the generated magnetic field would be along easy axis. Even so, signal was correctly detected and this did not degrade the detection of the magnetic field from the coils.

In real life applications, we might be interested in obtaining a signal containing only the information of the inhomogeneous magnetic field. One example is the goal of the ByAxon project itself: to detect neural magnetic signals, even in environments with the presence of ambient magnetic field. This can be achieved by using a gradiometer arrangement.

4.3 Gradiometer operation

The goal of a gradiometer arrangement is to remove ambient non-random interference, such as 50 Hz signal coming from the power line. The gradiometer output signal is the difference between two input signals coming from independent sensors. Therefore, correlated signals are suppressed. This configuration is attractive when the signal to be measured is much weaker than ambient noise. While keeping both sensors in the same

environment, only one is close enough to the source of the target signal. The gradiometer output should then present a peak signal only at the frequency of the target, without signals common to both sensors. The difficulty to obtain a proper gradiometer operation is the requirement of very similar sensitivity and noise characteristics for the two sensors.

4.3.1 45WB structure

Each 45WB structure from BA106 (WB1 and WB3 described in previous section) was connected to one of the inputs of the home-made preamplifier. The setup is the same as shown in Fig. 4.9. The goal is to have an output signal with a peak only at the frequency of the magnetic field from the wire, eliminating the homogeneous field from the Helmholtz coils. As each 45WB structure present different sensitivity values, a second Yokogawa GS200 voltage supply was used to properly calibrate sensor's V_{bias} . Bridge named WB3 was kept with $V_{bias} = 5$ V while WB1 was supplied with 2.7 V. The V_{rms} values at 16 Hz for WB1 and WB3 are 35 nV_{rms} and 37 nV_{rms} , respectively. The obtained gradiometer output is presented in Fig. 4.11. With a measured voltage of 10 nV_{rms} , no peak is present

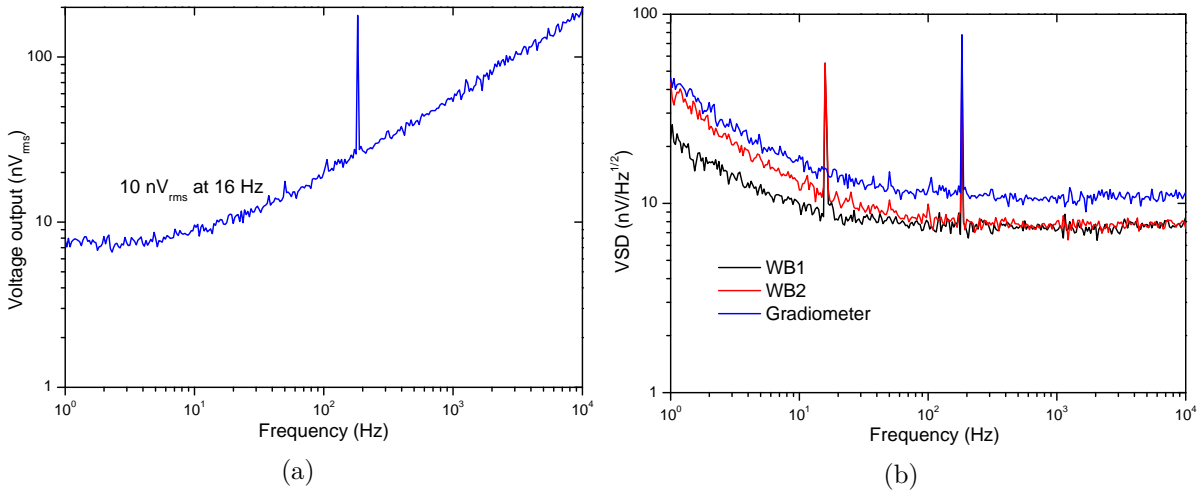


Figure 4.11: Gradiometer output after proper calibration of V_{bias} for each 45WB structure in sample BA106. a) Only the peak corresponding to the magnetic field from the wire at 183 Hz. b) Noise comparison between each individual 45WB bridge and gradiometer. In the latter, signal at 183 Hz is the main contribution.

at 16 Hz, showing that common signal from the Helmholtz coils is completely rejected thanks to the calibrated gradiometer arrangement. And the target field at 183 Hz is clearly seen in the voltage spectrum. This shows that with a correct setup, our LSMO devices work properly in gradiometer arrangement. If a 1 kHz cut off frequency low-pass filter is added, the signal from the wire at 183 Hz will be the main contribution. We see that $1/f$ region in the gradiometer channel is dominated by the sample with the highest low frequency noise.

4.3.2 90WB structure

So far, only sensors in 45WB structure were used due to the linear operation around zero applied field. Wheatstone bridges in 90WB structure require a bias DC field for best sensitivity. After changing the wires soldered to the PCB, both 90WB bridges in LSMO sample BA106 were connected to the inputs of the low noise amplifier. These bridges are named WB2 and WB4. Figure 4.12 presents the V_{meas} and detectivity curves of such sensors, measured inside the 4-probes station, at $V_{bias} = 5$ V and 310 K temperature. Even though bridge WB2 presents a higher sensitivity due to smaller anisotropy field, it also presented a higher $1/f$ noise. That is why a better performance in low frequency region

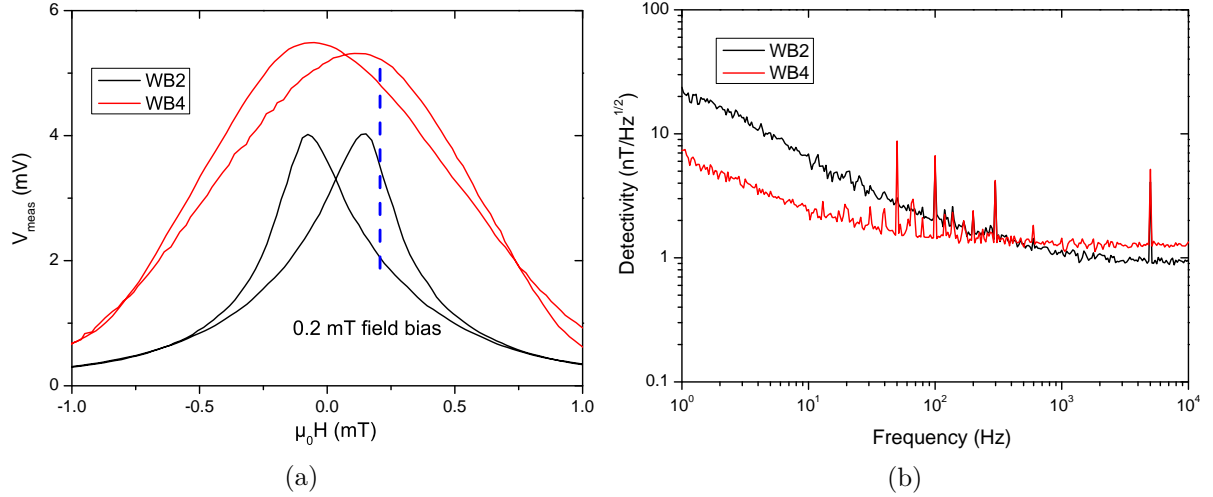


Figure 4.12: Characterization of 90WB structures present on sample BA106, at 5 V bias and 310 K. a) Zoomed view of V_{meas} . A common DC field bias at 310 K may be of 0.2 mT. b) Resulting detectivity using best sensitivity from the derivative of V_{meas} curve.

is obtained with WB4 whereas WB2 has lower detectivity in white noise region. In fact, as sample is 60 nm thick LSMO on top of 4° vicinal STO, some uniaxial anisotropy is lost (as was seen in the thickness investigation in previous chapter), which explains the separated V_{meas} peaks specially for WB2 sensor. This bridge has a non-zero sensitivity around zero applied field. At 310 K temperature, a bias field of 0.2 mT would be needed to place both bridges in a linear operation range. This can be done by a careful placement of permanent magnets or adding a DC component to the signal supplying the Helmholtz coils. Considering the calibration of the coils, a current of 164 mA would be needed to reach 0.2 mT. To increase the maximum current provided to the coils using the RTO2000 waveform generator, the series resistance was changed from 99.4 k Ω to 10 Ω . The output voltage spectrum in V_{rms} for both bridges working at room temperature and 5 V bias is presented in Fig. 4.13. The leftmost graph shows the output signal without any bias DC field. A second measurement with a DC field bias added generated by the coils is also shown. Although due to experimental limitations the constant field value was of 0.04 mT, an increase in output signal is clearly observed. A controllable current source could replace the waveform generator available in RTO to supply the coils with higher current, but this alternative wasn't studied. The smaller V_{rms} value at 16 Hz in WB4 is

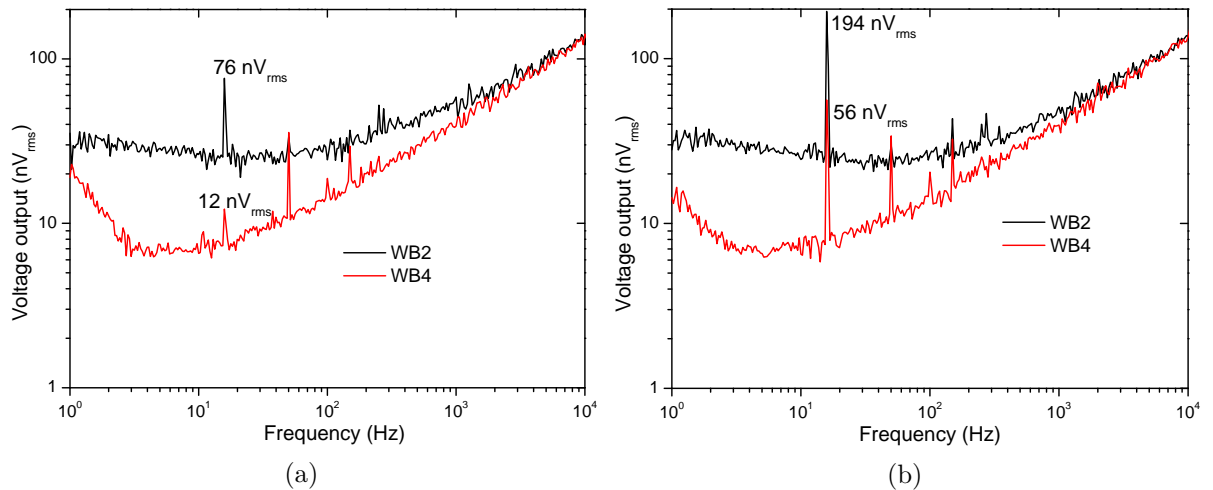


Figure 4.13: Output signal of sample BA106 90WB sensors, operating at room temperature and 5 V bias. a) No bias DC field is present. b) Added a DC field bias of 0.04 mT.

due to a sensitivity much closer to zero around 0 mT than for WB2. When the bias DC field is added, the 16 Hz peak increased by around 2.5 times and 4.7 times for WB2 and WB4, respectively. The DC voltage offset supplied to the coils was then increased to the maximum allowed value, creating a bias field of 0.11 mT. Then a proper calibration of V_{bias} for each Wheatstone bridge was performed to remove the 16 Hz peak in the gradiometer output. While WB4 was kept at 5 V bias, for WB2 it was reduced to 1.7 V. Once this was done, the 183 Hz signal supplying the single copper wire was turned back on. The alternating magnetic fields generated by the pair of Helmholtz coils and single wire were increased, in order to have the 16 Hz signal dominating each individual sensor output and the 183 Hz signal dominating the gradiometer output. This allows a clear visualization of the waveforms in the time domain, as shown in 4.14. Still using the waveform generators available in RTO2000, the signal for the coils was increase to a measured 71 mV peak to peak, corresponding to a root mean square field of 3.06 μT . As the 16 Hz component is

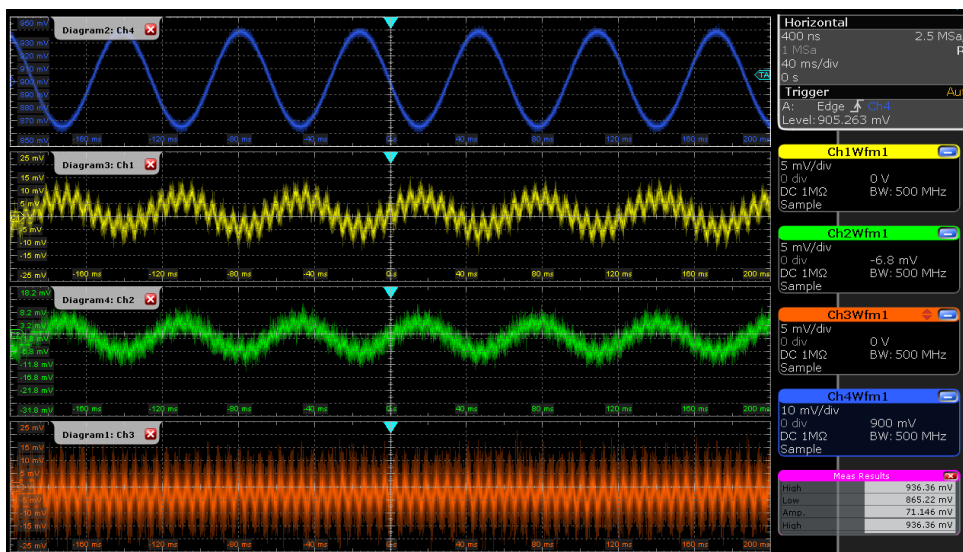


Figure 4.14: Signal supplied to the coils (blue) and outputs of WB2 (yellow), WB4 (green) and gradiometer (orange).

in phase for WB2 and WB4, it is not present in the gradiometer output. The measured voltage spectrum is presented in Fig. 4.15. Table 4.1 presents the V_{rms} values of interest for each curve. Signals from WB2 and WB4 were measured simultaneously, whereas gradiometer output was measured on a second run. In this setup, sensitivity values for

Channel	16 Hz	183 Hz
WB2	1.68 μV	1.01 μV
WB4	1.64 μV	0.31 μV
Gradiometer	57 nV	1.16 μV

Table 4.1: Measured RMS voltage values at frequencies from coils (16 Hz) and single wire (183 Hz).

WB2 and WB4 are 32 % T^{-1} and 11 % T^{-1} , respectively. A better polarization in field could be done to achieve higher performance, but these results serve as a demonstration of operation. The difference when comparing to the maximum values obtained from the derivative of V_{meas} curves is due to the lower working temperature (310 K inside the 4-probes chamber vs room temperature) and the difficulty of polarizing each bridge at the optimal field. To avoid this problem, the sensing bridge and the reference bridge must be farther apart, and a different bias field can be applied to each one. To do so, either a STO substrate can be cut in two, with each half having one 45WB bridge and one 90WB bridge. Another option is to use bridges from different LSMO samples. The setup can be

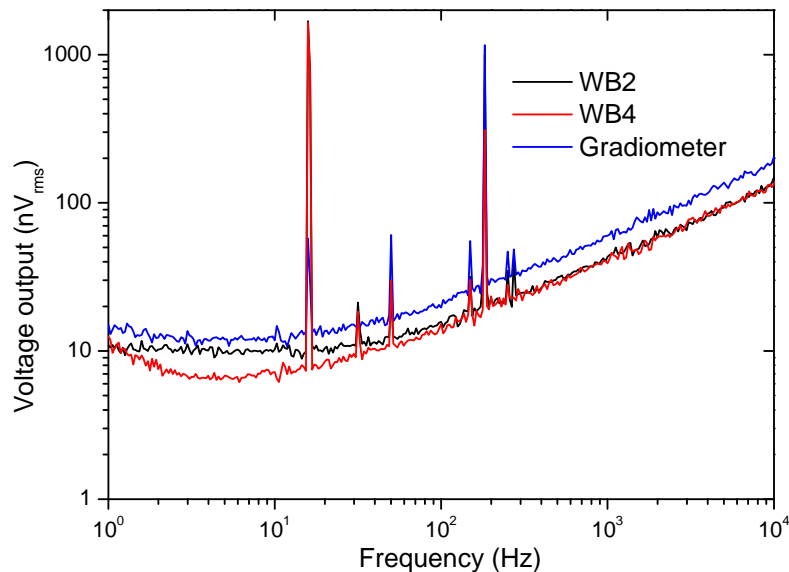


Figure 4.15: Output signals for each individual 90WB structure and gradiometer arrangement, at room temperature and 0.11 mT bias field. Bridge WB2 is supplied with 1.7 V bias and WB4 with 5 V.

simplified further by using one 90WB structure from one sample and a 45WB from another sample. This way, the proper field polarization of only one sensor have to be dealt with. The 90WB bridge is placed closer to the signal of interest, as in general this structure has a better performance. The reduced sensitivity in 45WB structure can be overcome by applying a higher voltage bias. In fact, as the V_{meas} equation for the 45WB structure does not present an offset term, a higher voltage bias than for the 90WB structure can be attained without saturating the first stage amplifier or moving out of the common-mode voltage zone. Eventually, one possibility is to change the gain of the amplifier for each sensor.

4.3.3 Hybrid 90WB and 45WB

For this experiment, a 90WB bridge (from now referenced as WB4) from BA106 and a 45WB bridge (now called WB1) from sample BA103 were connected to the two inputs of the lab-made amplifier. In this trial, any sort of magnetic shielding was used. While WB4 was placed between the Helmholtz coils, WB1 was left around 60 cm apart. A 99.4 k Ω series resistance was used between RTO2000 waveform generator and Helmholtz coils, and a 3 mm height by 4 mm diameter cylinder magnet, placed at an arbitrary position, was responsible for the necessary field polarization of the 90WB bridge. A sinusoidal signal at 129.6 Hz frequency and 12 V peak to peak amplitude was supplied to the coils, generating a RMS field amplitude of 52 nT. WB4 was supplied with 5 V, and the permanent magnet was moved around it in order to have the highest RMS output voltage at 129.6 Hz from the sensor. Using a Hall probe, the field at the LSMO Wheatstone bridge was estimated to be 1.2 mT. Meanwhile, WB1 was supplied with 10 V bias.

As RTO2000 has four input channels, it was used to simultaneously measure the voltage output from each LSMO PHEB and the gradiometer and measure the respective noise. The available fast Fourier transform (FFT) function was used to obtain noise curves. Differently from HP 3562A, only a linear operation mode with fixed resolution bandwidth for the whole frequency range is available. It also does not have a built-in function to reject overload and it has a higher noise floor level, but the 66 dB AC gain of the lab-made amplifier is more than enough to place noise from the sensor above it. Measurement results from 1 Hz to 200 Hz with a 100 mHz resolution bandwidth are presented in Fig. 4.16, with zoomed views around frequencies of interest. The peaks shown in WB1 channel

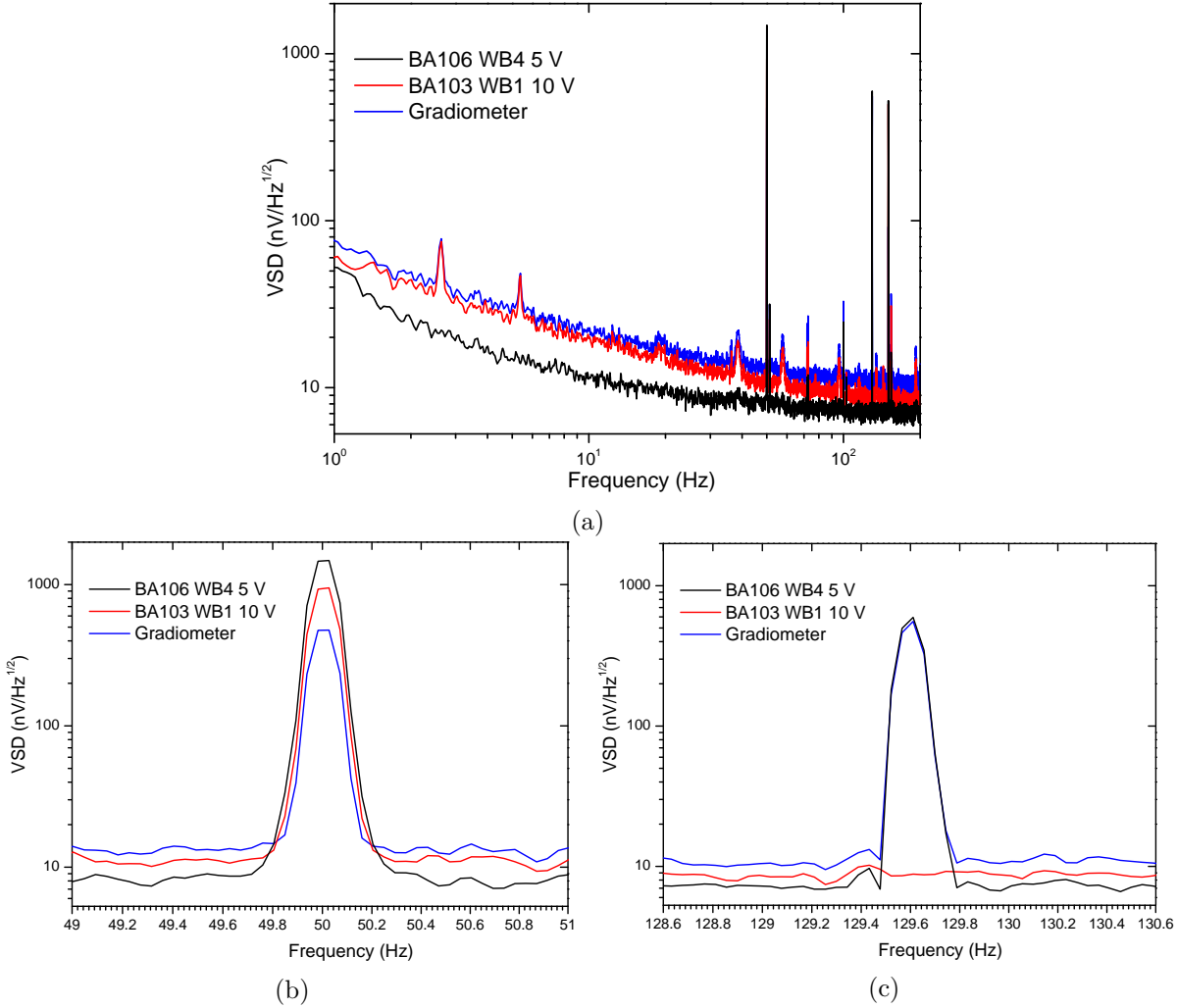


Figure 4.16: Noise curves for the hybrid gradiometer arrangement, at room temperature and without magnetic shielding. A 90WB structure from BA106 is used as the sensing device, polarized at 5 V bias and 1.2 mT static field from a permanent magnet. The reference device is a 45WB bridge from BA103, at 10 V bias. a) Full frequency range. b) Reduction of 50 Hz noise from power line in gradiometer output. c) Field from coils at 129.6 Hz is detected only by WB4, and present in gradiometer.

are probably due to different ambient noise. Placed away from WB4 and Helmholtz coils, this bridge was much closer to other electrical equipment. The measured values of interest are shown in Table 4.2. With the gradiometer arrangement, the noise level at

Channel	50 Hz	129.6 Hz
WB4	1.50 μV	0.60 μV
WB1	0.95 μV	8.8 nV
Gradiometer	0.50 μV	0.56 μV

Table 4.2: Measured RMS voltage values at frequencies from power line (parasite 50 Hz) and coils (129.6 Hz).

50 Hz was reduced to below to that of the the target 129.6 Hz frequency. An improved calibration of V_{bias} for each sensor, such as reducing the WB4 bias, would decrease the 50 Hz peak even further. A proper adjustment of the DC field bias and even gain of each amplification chain would result in a better reduction of common parasitic noise. Even without an optimized setup, these results validate the gradiometer arrangement in the so called hybrid configuration. Only one sensor requires a magnetic field bias, presenting

higher sensitivity. Using the peak value at 129.6 Hz, a sensitivity of $68 \% \text{ T}^{-1}$ for WB4 is calculated. This is more than six times the value obtained when a 0.11 mT field bias was applied with a voltage offset supplied to the pair of Helmholtz coils. Considering the V_{meas} curve measured inside the 4-probes station at 310 K temperature, the highest stable value for sensitivity from the derivative gives $130 \% \text{ T}^{-1}$. Indeed, a proper field bias is crucial for the correct use of 90WB structures.

To improve the verification of this hybrid gradiometer arrangement and achieving a better field bias for the 90WB, a square support was prepared with 3D printer with a central slot to fit the LSMO sample already mounted in the PCB (covered or not with PDMS) and lateral slots to slide cylindrical permanent magnets. This is shown in Fig. 4.17. The PCB sits at 2 mm below the top surface of the support, which allows to place some other piece or device above it without touching the wire bonding connections. A quick

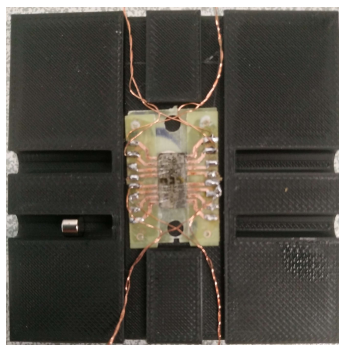


Figure 4.17: Sample BA106 wire bonded to PCB and placed over the 3D printed support. Cylinder magnets can be placed on both sides and distance can be controlled to achieve proper magnetic field bias for 90WB structures.

verification with an alternating field applied by the Helmholtz coils shows how performance of a 90WB structure is improved with proper positioning of permanent magnet. Field was applied at 130 Hz, with a RMS value of 52 nT, and three positions for the cylinder magnet were investigated: no permanent magnet at all, at the middle point of the slot and at the closest position to the LSMO sample. Obtained with RTO2000, corresponding noise curves around the frequency of interest are presented in Fig. 4.18. The sensor is the WB2 structure presented in Section 4.3.2. A gain of one order of magnitude is obtained

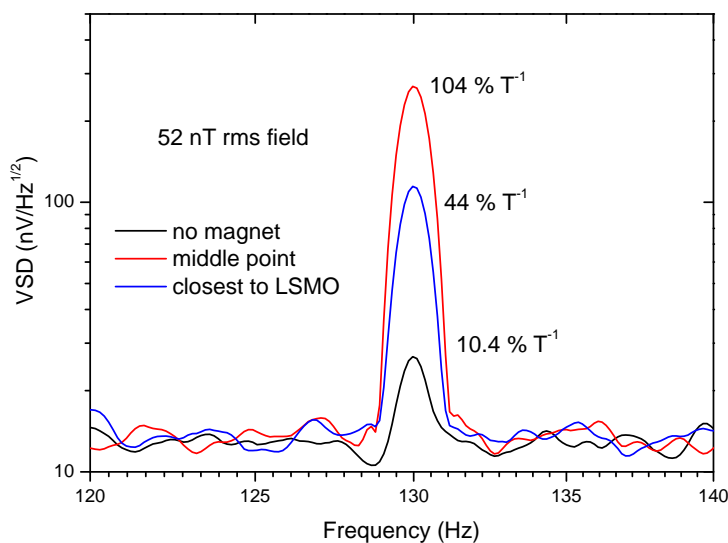


Figure 4.18: FFT with 1 Hz resolution bandwidth of BA106 WB2 bridge at 5 V bias and room temperature. [Sample BA106]

when the permanent magnet is placed in a satisfactory position, comparing to no magnet

at all. If it gets too close to the LSMO sample, sensor is no longer at its working point and sensitivity drops. With a Hall probe, the estimated values for magnetic field due to the permanent magnet were estimated to be of 0.7 mT and 2.5 mT when at middle distance and closest as possible, respectively.

4.4 Experiments with living cells at SISSA

Concerning the goal of the ByAxon project, the detection of magnetic fields from biological origin is required. The Scuola Internazionale Superiore di Studi Avanzati (SISSA) at Trieste, Italy, was a partner in the ByAxon project. With an expertise in neuroscience, they are able to grow organotypical cultures of neuronal cells starting from mouse embryonic stem cells, neural progenitors, hippocampal neurons, spinal cord slices and spinal cord demisections. Samples are placed on top of a PDMS with or without supporting glass or polystyrene (PS) substrate and go for incubation. During this incubation period, a living neuronal tissue grows. As they remain alive, those cells are still active and will spontaneously emit signals [2], which can be detected with electrophysiology or live fluorescence calcium imaging technique. The challenge is then to place the living tissue over a magnetic field sensor and to detect such activity by the associated magnetic signal. This experiment comes with several obstacles. As the shape of magnetic signal from such biological samples is not completely known, investigations with grooved substrates for the neuronal cells were conducted. This grooved substrate induces cell growth in an elongated wire-like geometry, with the goal to have a magnetic field distribution similar to an elongated axon or conducting wire. Another studied option is to incubate two separated spinal cord slices at once, forming an elongated structure between the two. After the incubation period, the biological sample is placed inside a perforated Petri dish, as shown in Fig. 4.19. The perforation is covered by the PDMS or PS substrate of the neuronal culture. An extracellular saline solution must fill the Petri dish, and a constant flow must



Figure 4.19: Double spinal cord slices incubated over a PDMS substrate and placed inside a Petri dish.

be maintained to keep cells alive. The same station for electrophysiology and calcium imaging techniques is used, but in this case the Petri dish will be positioned on top of a magnetic field sensor, properly covered and connected to a PCB for signal readout. Magnetic fields coming from the equipment such as lenses can affect the output of the magnetic sensor, and may even saturate the sensor.

The first tentative to detect biomagnetic signals using our AMR LSMO sensor was performed in November 2019, with the presence of Dr. Isidoro Martinez, Arturo Vera (IMDEA Nanociencia) and Dr. Ivo Calaresu (SISSA). At IMDEA Nanociencia, both 45WB sensor structures from sample BA055 (30 nm LSMO over 4° vicinal STO), from now on referenced as WB1 and WB3, were connected to a PCB via wire bonding and sample was covered with PDMS for protection and biocompatibility. The PDMS layer had an estimated thickness of 650 μm . At SISSA, the PCB was placed over a copper piece on top of a heating table in the electrophysiology/calcium imaging station, which in turn does not allow the use of a XYZ stage for more precise positioning of the magnetic field sensor. The heating table is connected to a MultiChannel Systems TC02, that presents a PI-based temperature control. The 45WB structures were used as they don't require a bias magnetic field to work in linear range, and both were connected to allow a gradiometer configuration. The proportional-integral controller of the heating plate was set to 45 °C, temperature of maximum sensitivity (165 % T^{-1}) for WB3 according to characterization previously performed at IMDEA Nanociencia. A Petri dish containing a double spinal cord slice on top of 150 μm thick PS was positioned over the LSMO device. Photographs of the setup are shown in Fig. 4.20. Signals from PCB to reading electronics were carried using two 4-wires LEMO connectors. To help keeping an operation above room temperature, the saline solution was heated to 38 °C before flowing to the Petri dish through the perfusions. This is the highest possible temperature to keep the neuronal tissue alive. As the saline solution is in constant flow, it does not heat up with the copper plate, and we consider that the biological sample is kept at 38 °C. The glass microelectrode, also known as pipette, is used to obtain electrophysiology readings of the spontaneous activity and compare it with magnetic readings coming from the LSMO sensor. The Wheatstone bridges are side by side, so there was an effort to place the biological sample closer to WB3 for a gradiometer arrangement. Contacting the biological sample with the microelectrode is a very delicate process, and once the microelectrode touches the living tissue, the system can't be repositioned. Therefore it is very difficult to have the microelectrode near the magnetic sensor of interest. After amplification using the lab made amplifier based on AD8421, the outputs of each 45WB PHEB were connected to model SR560 pre-amplifier from Stanford Research Systems in differential mode (at the time this experiment was performed, the lab made amplifier did not have a differential/gradiometer output included). Model SR560 was also configured to a 0.03 Hz to 100 Hz band pass filter, and output went into a National Instruments Data Acquisition (NI DAQ) device for analog to digital conversion at 20 kHz sampling rate for computer monitoring using a LabView Virtual Instrument. The V_{bias} for each PHEB was calibrated around 8.25 V to minimize the 50 Hz peak. Figure 4.21 shows the output voltage during one minute of both electric and magnetic channels, from microelectrodes and LSMO sensor in gradiometer configuration. A solution of bicuculline and strychnine was added to the saline solution in order to increase the synchronization of the spontaneous cells activity, thus creating stronger biological signals. As the system is not thermally stable and the LSMO sensor was not characterized *in situ* to obtain the value of sensitivity in the operating conditions, it was decided to keep the unit of the magnetic signal in voltage. Two clear peaks are present in the electric channel, measured by the glass microelectrodes. This indicates that the biological sample was indeed alive and in activity. Meanwhile, the signal of magnetic origin has variations over time, that can be due to thermal drifts. If we are to correlate the peaks of each channel, the time difference could be accepted as the microelectrode was not placed directly over WB3 and the generation and propagation of magnetic field is not completely understood. But considering the voltage levels reached in the magnetic channel and the estimated sensitivity of the LSMO sensor at the best operating condition, a field amplitude of at least 120 nT would be required. This is a value way above what is expected. Finally, tetrodotoxin was added to the saline solution in order to block completely all electrical activity of the biological sample. While the signal from the microelectrode presented no more peaks, drifts were still present in the magnetic channel.

Even though the spontaneous activity of living cells *in vitro* was not detected with the

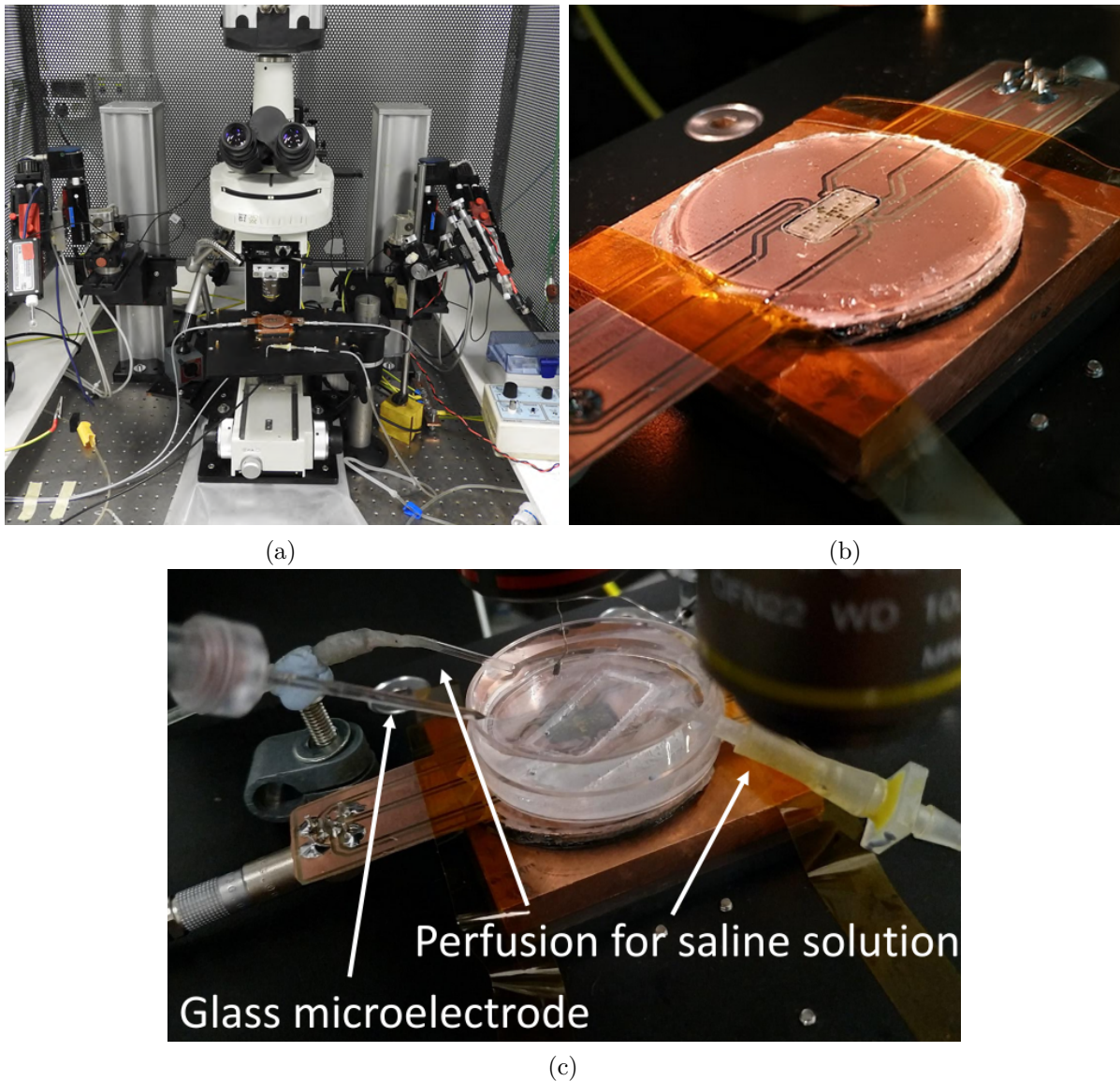


Figure 4.20: Setup to magnetically detect the spontaneous activity of neuronal cells. a) LSMO sample mounted in the statio for electrophysiology and calcium imaging characterization. b) Close up photograph of sensor over heating plate, covered in PDMS and wire bonded to circular PCB. c) Biological sample placed on top.

LSMO sample, this was no doubt a very enriching experience. For future experiments, a more stable system in terms of temperature and even saline solution leakage is strongly advised. LSMO samples with higher performance, obtained after November 2019, should be used. The total distance from neuronal tissue to LSMO sample could be reduced by obtaining a thinner PDMS layer over the sensor and using a thinner substrate for the biological sample, although the latter makes the system more prone to vibrations due to the flow of saline solution. A thin PDMS layer can be achieved with spin coating, but the electrical connection from gold pad to PCB must be more robust and lower in height than wire bonding. To increase the distance between both sensors of the gradiometer arrangement, the two Wheatstone bridges could be on separate substrates, either by cutting a sample in half or using two different samples. It would also be easier to calibrate the sensors in the same environment where the experiment will be conducted. Further experiments were discussed in the scope of the ByAxon project but were not performed before the end of this thesis due to the SARS-CoV-2 global pandemic.

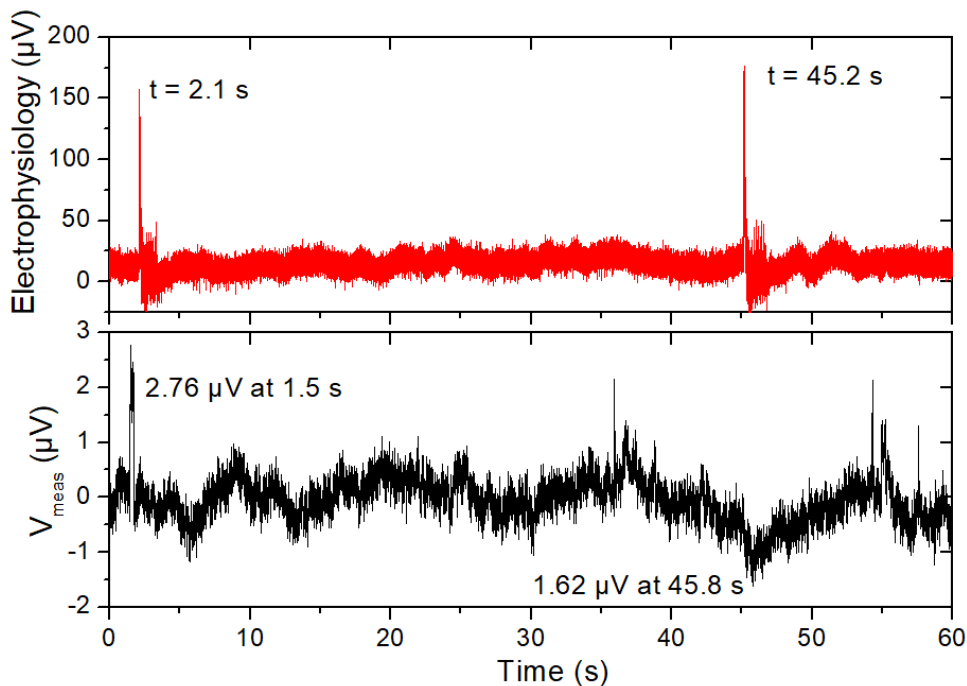


Figure 4.21: Simultaneous acquisition of signals from electric (red) and magnetic (black) origin, using glass microelectrode and sample BA055 LSMO sensor, respectively. Acquisition was performed while a solution of bicuculline and strychnine was added in the saline solution.

4.5 Conclusion

After tweaking sensor performance with different fabrication parameters in Chapter 3, and obtaining V_{meas} , noise and detectivity curves for several samples, experiments as proper sensor in more realistic environment were conducted. Firstly, LSMO sensor had to be mounted on a PCB for portability and perform measurements without the need of electrical probes. Different packaging techniques were discussed in order to obtain a final device as thin as possible. Due to several challenges associated to more complex strategies and time required by other activities, ultimately samples were mounted with wire bonding from gold pads to PCB copper tracks. Some samples were covered using PDMS, a biocompatible polymer, for protection and robustness. After mounting, the performance of selected samples was verified with applied magnetic field of known frequency and amplitude using a pair of Helmholtz coils. Inhomogeneous magnetic field was created by a single copper wire placed on top of the sensor. The metallic wire was supplied with a signal of fixed frequency, although the amplitude of the generated field was not investigated. Different gradiometer configuration were investigated, either using only 45WB structures, only 90WB bridges or both at the same time, on the same LSMO sample or two separate substrates. In all three scenarios, common mode signals, such as parasitic 50 Hz noise from the power line, are reduced in gradiometer output. With proper tuning of voltage bias, it was possible to completely reject the signal contribution from the magnetic field common to both sensors of the gradiometer arrangement. The 45WB structure presents a linear operation around zero applied field, so only alternating fields were applied. On the other hand, the 90WB structure requires a bias DC field to operate in its working point, and this requirement does add some extra steps to the setup. If only 90WB PHEBs are used in the gradiometer arrangement, each may have a different value of static field necessary to stay in the zone of best sensitivity. A static magnetic field was added both by supplying a DC offset voltage to the Helmholtz coils or placing a permanent magnet. So whereas 90WB sensors do present lower detectivity values as was evidenced in previous chapters, an easier and more direct operation in real life applications is obtained with 45WB bridges. Another possibility is to have a gradiometer arrangement in which the reference sensor is a 45WB

device and the “active” sensor a 90WB structure. This way, only one bridge requires a proper biasing with static field. As the 45WB structures present lower sensitivity, a higher voltage bias must be applied to increase the signal from the sensor. In fact, as the V_{meas} equation of 45WB bridges does not present an offset component, V_{bias} can be increase without reaching saturation of the first stage amplifier. Another possibility is to adjust the amplification gain for each sensor, although this was not investigated in this work. Using 3D printing, a sample holder with slots for permanent magnets was prepare, which made easier obtaining a better bias with a static magnetic field.

As the goal of ByAxon project is to bypass signals emitted from the spinal cord, experiments to detect biological signals were conducted at SISSA, a partner laboratory in Trieste, Italy. The source of such signals were incubated neuronal cells. The living tissue was grown from rat hippocampal, progenitor cells or spinal cord slices. The Petri dish containing the biological sample was placed on top of a LSMO sample covered with PDMS, and a microelectrode detects the spontaneous activity of the living tissue. The target fields are of very low amplitude, so a thin cover layer on top of LSMO is advised. If the connection from sample gold pads to PCB copper tracks could be replaced by a more robust alternative than wire bonding, spin coating may be used to obtain a thinner PDMS layer. There is also the added difficulty of keeping the LSMO device above room temperature to increase its sensitivity, and of correctly placing the neuronal cells. Due to the nature of the material, our device work better at 310 K than room temperature, and keeping a constant temperature without drifts is another obstacle in such open system. The only experiment that could be performed with neuronal cells took place in late 2019, before the SARS-CoV-2 pandemic. At that time, our very best LSMO sensors had not been fabricated yet and real time magnetic recordings of neuronal activity were not obtained.

Bibliography

- [1] A. Mata, A. J. Fleischman, and S. Roy. “Characterization of Polydimethylsiloxane (PDMS) Properties for Biomedical Micro/Nanosystems”. In: *Biomedical Microdevices* 7.4 (Dec. 2005), pp. 281–293. ISSN: 1572-8781. DOI: 10.1007/s10544-005-6070-2. URL: <https://doi.org/10.1007/s10544-005-6070-2>.
- [2] M. Giugliano, P. Darbon, M. Arsiero, H. R. Lüscher, and J. Streit. “Single-Neuron Discharge Properties and Network Activity in Dissociated Cultures of Neocortex”. In: *Journal of Neurophysiology* 92.2 (2004). PMID: 15044515, pp. 977–996. DOI: 10.1152/jn.00067.2004. eprint: <https://doi.org/10.1152/jn.00067.2004>. URL: <https://doi.org/10.1152/jn.00067.2004>.

Chapter V

General Conclusions and Future Perspectives

5.1 Conclusions

The goal of this thesis was to optimize the performance of magnetic field sensors based on the anisotropic magnetoresistance (AMR) effect present in semi-metallic manganite oxide $\text{La}_{2/3}\text{Sr}_{1/3}\text{MnO}_3$ (LSMO) thin films, etched in Wheatstone bridge structures. Previous studies performed by the Electronics group at GREYC showed that this ferromagnetic material can be used to fabricate AMR sensors with high performance in the low frequency region, due to its very low normalized Hooke parameter α_H/n . Thanks to such properties, LSMO is a viable candidate to fabricate sensors that target biomedical applications, as in general magnetic biological signals present frequencies below 1 kHz. Respecting the constraints in size and operation temperature, it was then the material of choice for developing the magnetic field sensor to be used in the European project ByAxon. What sets the device here presented apart from other magnetoresistive sensors are the facts that it is a single layer device, it is based on a ferromagnetic functional oxide and that the easy axis arises from a step-induced anisotropy due to epitaxial deposition on top of a vicinal substrate. Therefore, it does not rely on the stacking of multiple materials, exchange bias interaction with other magnetic layers, shape anisotropy or the application of magnetic fields during fabrication process. Although some LSMO Wheatstone bridge samples were fabricated previous to this work, the previous preamplifier was not well adapted to low frequency noise measurements, the working principle of the device was not yet validated, the effects of different fabrication parameters such as film thickness and vicinal angle of the substrate were not investigated and samples were characterized only inside a closed 4-probes station.

Based on the uniaxial magnetic energy equation by Stoner-Wohlfarth and electrical resistance expressions for LSMO stripes etched at 0° , 45° , 90° and 135° to the easy magnetization axis, a numerical model for output signal of two Wheatstone bridge designs was developed. This model was then compared to experimental data obtained from the characterization of LSMO samples. The good agreement between simulation and measurements, along with results from MOKE imaging, showed that the fabricated device behaves as expected with a step-induced magnetic uniaxial anisotropy. Fitting the model to experimental data allows the extraction of physical parameters of the film such as the anisotropy field. The model also predicts the jump in magnetization direction that occurs when the applied field has a small deviation and is not completely perpendicular to the easy axis. This deviation is done on purpose to force the direction of magnetization rotation across all arms of the Wheatstone bridge, which increases the signal from the 45WB structure. Such deviation and its effects were not previously investigated. If each arm presents an independent direction for magnetization rotation, the variation in resistance does not follow the desired behavior and the output signal is degraded. This may give the

impression that 45WB structures have a much worse performance than 90WB counterparts. Still, 45WB bridges present smaller MR ratios, and therefore smaller sensitivity values, due to a lower resistivity variation of the PHE terms in the resistivity tensor, when compared to the standard AMR terms. This difference is not evoked in works concerning permalloys, but arises in LSMO due to the crystalline structure of this oxide. Regarding fabrication parameters, it was verified that a proper balance must be achieved between thin film thickness and vicinal angle of the substrate. A clear uniaxial anisotropy is required for proper operation of the device. High MR ratio and low anisotropy field are desired to obtain high sensitivity values, whereas low electrical resistance reduces the sample thermal noise. It was verified that increasing thickness for a fixed vicinal angle in order to obtain a lower electrical resistance causes a loss of uniaxial anisotropy and increases H_a . And even though thermal noise did reduce, there was an unexpected increase in $1/f$ noise. Employing a substrate with higher vicinal angle does force an uniaxial anisotropy for thicker films, but it also provokes an increase in anisotropy field, which in turn reduces sensor sensitivity. Substrates with increased vicinal angle may also be the cause of an amorphous layer at the LSMO surface. This reduces the effective thickness of the crystalline layer, affecting the electrical resistance, the MR ratio and the anisotropy field. In the end, one should keep a low thickness LSMO film over a substrate with low vicinal angle. This ensures the required uniaxial anisotropy and a low value for H_a , resulting in an improved sensitivity. The sample with the best low frequency performance of this work is a 45 nm LSMO film over 4° vicinal STO, presenting detectivity values of $1.4 \text{ nT Hz}^{-1/2}$ at 1 Hz and $240 \text{ pT Hz}^{-1/2}$ at 1 kHz, while working at 310 K temperature. Although there is a difference of one order of magnitude when comparing to commercial sensors such as HMC1001 and TMR9112, the AMR LSMO sensor here presented is nothing more than one individual Wheatstone bridge, made of a single layer manganite oxide on top of a vicinal substrate. The device mentioned consumes 4.5 mW while occupying a very small surface area of only 2.25 mm^2 . Besides variations on fabrication parameters, another possibility to increase sensor performance is to heat the LSMO sample up to its optimal working point. An increase in sensitivity is obtained thanks to a reduction of H_a , up to a point where ferromagnetic behavior starts to disappear. Performance in the thermal noise region can be improved by increasing the voltage bias supplied to the Wheatstone bridge, with care to avoid self-heating. Damage to the LSMO layer due to higher current values was not verified. As for detectivity in the $1/f$ region, a proper design of the device can reduce the low frequency noise by presenting a more homogeneous current density distribution and avoiding regions of concentration. For portability and protection, some LSMO samples were mounted on PCBs and covered with PDMS. Electrical connection from gold pads to copper tracks of the PCB were done with aluminium wire bonding, and copper wires were soldered to the PCB. While all previous studies at GREYC were conducted with a DC sweep of an homogeneous magnetic field, this simple packaging allows the characterization of the LSMO devices as proper sensors in real environment, under an alternating and inhomogeneous magnetic field. Different arrangements for gradiometer operation were investigated, and all cases showed a rejection of the ambient noise. Presenting linear operation around zero applied field, 45WB structures are easier to use directly. Permanent magnets can be placed closed to the LSMO sample in order to polarize a 90WB bridge with a constant field, and keep it in its linear operation range. The very first trial to detect magnetic signals coming from the spontaneous activity of incubated rat neuronal cells using LSMO sensors was performed at SISSA, a partner laboratory in the ByAxon project. No live recordings of magnetic signals that could be clearly related to the activity indicated by electrophysiology were obtained in this first trial, and unfortunately it was the only round of experiments by the time this thesis was concluded. Additional trials are planned, with better performing LSMO samples and a different design of the measurement setup.

To conclude, this thesis provided some substantial comprehension of the device, along with performance improvement of AMR LSMO samples and use as a real sensor. Although the best LSMO sensor here presented has a performance at 1 Hz about one order of

magnitude below that of HMC1001, a commercially available device, it consumes six times less power. Besides, the LSMO Wheatstone bridge structure occupies a surface area 18 times smaller than that of the packaged permalloy-based sensor. Thus, one can safely affirm that the goals set for this thesis were successfully achieved, while there is still room for improvement, and the work here presented pushes forward the development of oxide-based electronics.

5.2 Future Perspectives

Future work in collaboration with IMDEA Nanociencia is planned, continuing from what was developed in this thesis. Benefiting from the complementary expertise and facilities from both laboratories, investigations on new geometries, the addition of magnetic flux concentrators and perpendicular magnetic anisotropy with a multilayer system will be carried out. The advantage of adding MFCs is that it reduces the effective anisotropy field of the sensor, thus increasing the sensitivity without affecting sample noise. Properly designed MFCs result in gains above one order of magnitude, therefore we can estimate that our LSMO sensors could reach detectivity values under $1 \text{ nT Hz}^{-1/2}$ at 1 Hz. Performance comparable to HMC1001 and TMR9112 is conceivable.

As it was showed that covering LSMO samples does not affect sensor performance, another possible biomedical application is for microfluidics. Channels for liquid flow carrying magnetic beads can be etched in a PDMS structure, to be placed on top of the sensing device. Beyond biomedical, the AMR LSMO sensors can be use in any other application that requires the detection of magnetic fields. Fabrication parameters can be tweaked accordingly to the target field, i.e. obtaining sensors with large linear range of operation for automotive applications. As more samples are fabricated and characterized, a larger dataset becomes available. Using the collection of experimental data and known theories, it might be possible to apply machine learning methods to predict the effect of fabrication parameters on sensor performance. A model can be developed to estimate device characteristics prior to fabrication, and samples with specific target performance can be manufactured. One advantage of our sensors that was not put to use in this work is their robustness to high magnetic fields. As a single layer sensors in which the easy axis is induced by interaction with the substrate, there is no auxiliary layer that might lose its pinned magnetization, no matter the strength of the applied field. Once the field is removed, the sensors returns by itself to proper operation. Also, long term studies would assess the stability of our sensors in repeated magnetization cycles. Considering the ferromagnetic material itself, it would be beneficial to employ a different oxide with a behavior similar to LSMO and with reduced resistivity, thus lowering the thermal noise of the device. In that case, a preamplifier with increased current noise but smaller voltage noise could be employed to achieve a lower noise floor of the system. Another possibility is to use an oxide with a stronger planar Hall effect, which would increase the sensitivity of the 45WB structure. For real use experiments, placing the sensor as close as possible to the origin of the magnetic signal mitigates losses. Thus, developing a packaging with minimal thickness will help detecting very weak signals. With robust electrical connection from the gold pads of the Wheatstone bridge structure to PCB, thinner PDMS cover can be achieved with spin coating. Performing wire bonding very carefully in order to achieve the lowest arcs as possible is an option without the need to change anything in the fabrication process, but difficult to achieve with manual equipment. As they are fixed only at their extremities, they might break during the spin coating. Another discussed possibility is to deposit a secondary gold layer and remove excess material by lift-off, leaving only a metallic path from gold pads of the LSMO structure to the PCB copper tracks. This demands a properly aligned sample mounting, without gaps between STO substrate and second layer of the PCB. A robust connection would also be the direct soldering from a gold track to PCB copper using Wood's metal. The lithography mask for gold layer can be easily modified to extend the metallic tracks all the way to substrate borders. As

photoresist tends to concentrate in the borders and corners, and a careful gold etch is mandatory to avoid any shorts. In the case that Wood's metal is indeed used, a solder bump must be avoided as it would increase the final packaging height. If STO can be pierced through without breaking, vias could be opened to perform electrical connection to gold pads from the backside of the substrate. This presents a much higher complexity and is the most technically challenging option, but would also produce the thinnest packaging height on top of the active LSMO layer.

5.3 Scientific Contributions

During the course of my thesis, I had the opportunity to participate in several scientific events and meetings. As a member of ByAxon, I came in contact with researchers from different fields and participated in discussions to plan further advancements of the project. In September 2019 I participated in the European Summer School at Brno, Czech Republic, where I was awarded the best poster prize. Shortly after, I presented a poster for GDR OXYFUN and an oral presentation for GDR MEETICC, both held in Caen, France. In the same year I had the opportunity to present my research and the ByAxon project to the general public during the Fête de la Science event. I also held an oral presentation for the 2020 edition of the Joint European Magnetic Symposia. Some results obtained during this thesis were also shown in an oral presentation during Intermag 2021, which resulted in a paper published on IEEE Transactions on Magnetics as main author. At the moment of the writing of this thesis, there are more scientific articles in development, both as main and co-author, in GREYC and IMDEA Nanociencia laboratories.

Appendix A

Fabrication Procedure

Samples were fabricated inside GREYC Electronics team's cleanroom. It is divided in two rooms, one class ISO 6 where the lithography process takes places and a class ISO 8 room with the remaining equipment. The cleanroom is well equipped with all the necessary infrastructure to fabricate nanoelectronics devices based on functional oxides and more.

A.1 Thin film deposition

The vicinal SrTiO₃ substrates are acquired from Crystal GmbH (<https://crystal-gmbh.com/>), already cut in rectangular 10 mm by 5 mm geometry, with 0.5 mm thickness. Vicinal angle is ordered from manufacturer, who informs a possible deviation of $\pm 0.5^\circ$, and surface step edges are parallel to the longest side. The LSMO target is obtained from SurfaceNet GmbH (<https://www.surfacenet.de/products.html>) with the desired Sr dopant concentration. The first step in fabrication is the thin film deposition, performed using a pulsed laser deposition (PLD) system from TSST (<https://www.tsstsystems.com/>), shown in Fig. A.1. PLD is a technique used to obtain epitaxial thin films while keeping the same stoichiometry as the target. That is, mono-crystalline films that present the same crystalline structure as the substrate. The system is equipped with a Reflection High-Energy Electron Diffraction (RHEED) option, which allows to monitor the growth of individual mono-layers. The PLD method consists of firing short and high energy pulses of laser, focused on the surface of the target. The material locally evaporates and is ejected in a plume towards the substrate where it will be deposited. Substrate can be heated with a infrared laser, and this thermal energy affects the growth mode of the film. A KrF laser fired against the target has 248 nm wavelength and was adjusted to a 1.5 mm by 1.4 mm spot, with 1.7 J cm^{-1} energy and firing rate of 3 Hz. Chamber is kept at 0.2 mbar O₂ background pressure. Usually substrate was kept at 730 °C temperature but, as presented in the main text, different temperatures were also investigated. Substrate heating is performed by a 980 nm wavelength laser. To control thin film growth, a reference sample is fabricated using flat STO (in other words, 0° vicinal angle). RHEED signal is observed to verify how many laser shots are required to obtain one mono-layer of LSMO. Each peak of the signal, corresponds to one monolayer. This calibration is followed during deposition on vicinal substrates. Due to the miscut angle on STO surface, RHEED signal can't be followed, as a correct alignment with RHEED sensor is required. Performing such tilt in the substrate position would affect thin film deposition, because the PLD plume would arrive at a different angle. After the required number of laser shots is reached, target is changed to a gold disk. Laser firing rate is increased to 5 Hz to speed up deposition. With a higher reflectivity, gold absorbs less energy so less material is evaporated, resulting in a slower deposition rate. It was verified that performing *in-situ* Au deposition yields better quality metal layer, as LSMO is not manipulated and exposed to atmosphere. Then the gold layer is made thicker with Ion Gun Evaporation method by GATAN (<https://www.gatan.com/>).

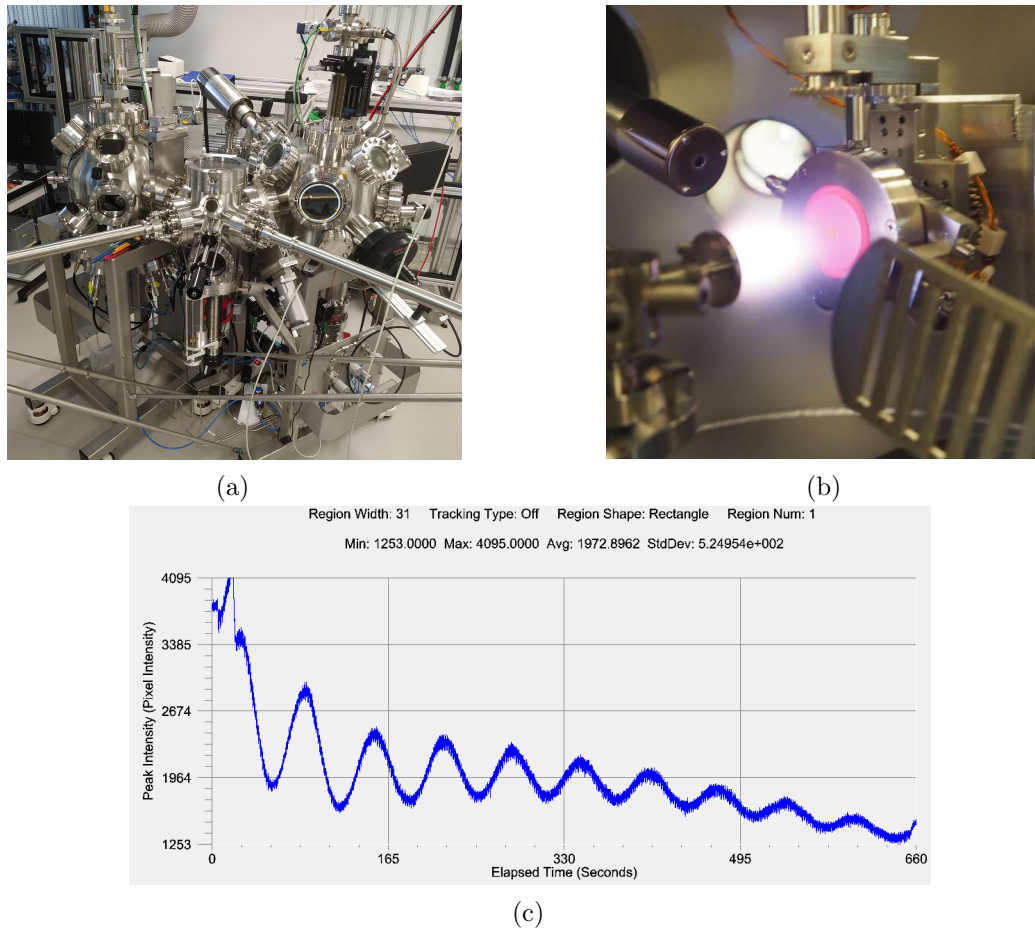


Figure A.1: Deposition of LSMO thin films. a) PLD system installed in the cleanroom. b) Inside of PLD chamber. The plume and heated substrate are visible. c) RHEED signal obtained during LSMO deposition on flat STO.

LSMO thin films and gold deposition for samples used in this thesis were performed by cleanroom engineer Victor Pierron.

A.2 Lithography and etching

Once deposition is completed, two steps of photolithography and etching are performed to obtain the desired structures. First, gold contacts are etched and then the LSMO thin film. Therefore, LSMO is present under the gold pads. Sample is cleaned using a standard process of washing with acetone, ethanol and deionized water, and dried with a N_2 gun. The die is kept at $90^\circ C$ during 5 minutes for drying before covering with positive photoresist MICROPOSITTM S1813TM G2. Spin coating is used during 40 seconds at 4000 RPM, which results in a resist thickness below $1.5 \mu m$ according to the product datasheet. Due to small rectangular size of the STO substrate, there is some border effect and photoresist layer is thicker around borders, specially in the corners. Two lithography machines are available in the cleanroom: Karl Suss MJB3 Mask Aligner (now Suss MicroTec <https://www.suss.com/>), which requires a physical mask, and Durham Magneto Optics Ltd MicroWriter ML3 Pro (<https://www.durhammagnetooptics.com/>). The physical mask used for MJB3 consists of a glass plate patterned with chromium, and must be ordered from a commercial supplier. Ultra-violet lamp is used as light source, and alignment is performed manually. For ML3 Pro only digital mask files are required, which speeds up the prototyping process. The system is equipped with a 385 nm semiconductor light source, and the design is imprinted on top of the sample thanks to the included digital

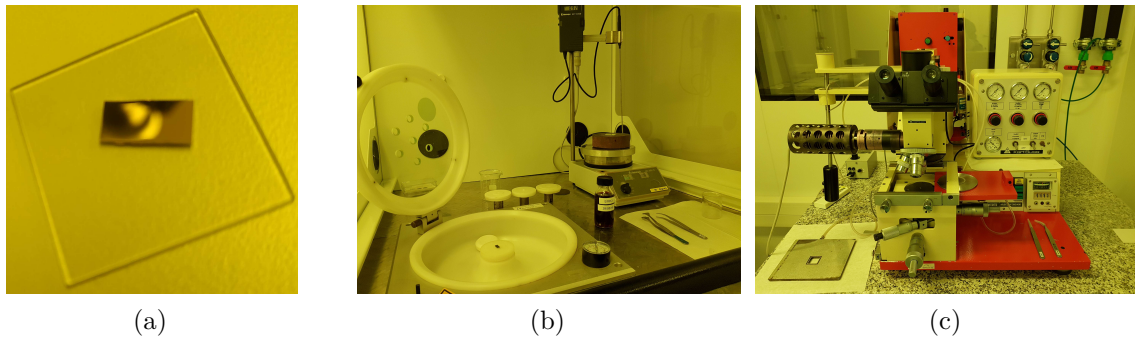


Figure A.2: Lithography room is illuminated with yellow light. a) STO substrate covered with LSMO and gold. b) Spin coating and heating plate. c) MJB3 system with UV lamp and physical mask.

light processor. Other advantages are the automatic alignment for different layers and the possibility to verify where the resist will be exposed over the sample before starting exposition. While the same physical mask for ML3 was used during this work, different masks for ML3 Pro were designed. The software used to draw masks in .cif format file was CleWin 5 (<https://wieweb.com>). While for MJB3 the exposure dose is set by exposure time, the exact dose can be chosen in J cm^{-2} in ML3 Pro. Corresponding values for gold (LSMO) layers are 26 seconds (6 seconds) and 100 J cm^{-2} (150 J cm^{-2}). Resist is then developed using MICROPOSITTM Developer Concentrate at 50 % concentration, diluted in deionized water, during 40 seconds. Figure A.2 shows photographs of sample after deposition, the spin coating equipment and MJB3 lithography inside the cleanroom.

Gold contacts are patterned and etched using I_2 (1.2 g) and KI (4 g) in deionized water (20 mL) liquid solution. Sample stays submerged during approximately 20 seconds, maximum 25 seconds. After the required time, sample is quickly washed in a glass cup filled with deionized water. Result is verified in a microscope and if satisfactory, the remaining resist is removed with standard cleaning process. Sample is once again dried and covered with resist to prepare etching of LSMO structures. After LSMO pattern is developed, sample is glued with silver paste to Ion Beam Etching (IBE) sample holder and left during 10 minutes on heating plate at $90 \text{ }^\circ\text{C}$. The available IBE uses argon ions and etch is performed at a argon pressure of 2×10^{-2} mbar. Sample holder rotates during the process to obtain a more uniform etch. A view of the IBE system is shown in Fig. A.3. Cooling water runs around sample holder, and a shutter can be used to guard sample

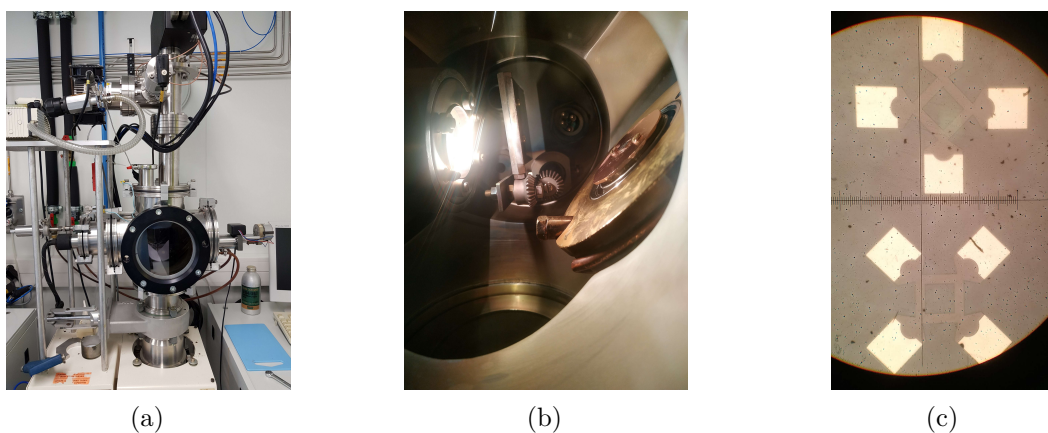


Figure A.3: Dry etching process. a) Outer view of IBE chamber. b) Sample in rotating sample holder being bombarded by Ar ions. c) Two Wheatstone bridge designs are obtained after fabrication is complete.

from incoming ions. To avoid sample overheating and eventually resist burn, etching is

performed with a periodic opening and closing of the shutter, with one minute at each position. An etch time (shutter up) of 20 minutes was verified to be sufficient to remove up to 90 nm of LSMO. When finished, sample is removed and backside is cleaned from excessive silver paste. To achieve better removal of photoresist, sample is kept up to 1 minute in acetone heated at 60 °C, using an ultrasound cleaning system. Nevertheless, while most samples present a clean surface after the procedure, others still had some stains, maybe due to resist burn even following the precautions. After one last cleaning procedure, sample fabrication is completed.

A.3 List of fabricated samples

Below follows a complete list of all samples fabricated during this thesis, informing relevant fabrication parameters. Some samples listed on Table A.1 are not mentioned in the main text due to fabrication issues or use in different experiments.

Sample	Nominal LSMO thickness (nm)	Vicinal angle (°)	Deposition temperature (°C)
BA054	30	2	730
BA055	30	4	730
BA062	30	6	730
BA064	30	10	730
BA068	45	4	730
BA070	60	4	730
BA072	75	4	730
BA074	30	4	730
BA076	90	4	730
BA090	60	4	730
BA097	60	8	730
BA098	30	4	730
BA103	60	8	630
BA104	60	4	730
BA105	60	8	680
BA106	60	4	680
BA114	45	4	730
BA130	45	4	730
BA134	60	flat (001)	730
BA135	60	flat (110)	730
BA136	45	4	730
BA137	60	8 (100)	730
BA138	60	8 (110)	730
BA143	30	4	730
BA144	30	10	730
BA146	45	4	730
BA147	45	8	730
BA154	45	4	730
BA156	45	2	730
BA157	45	6	730
BA158	45	8	730
BA159	45	10	730

Table A.1: List of all LSMO samples fabricated during the thesis.

Appendix B

Characterization Procedure

B.1 Electrical transport and noise

Here, the setup used to obtain electrical resistance measured with a IV curve, magnetoresistance characterization and electrical noise measurements is detailed. For these experiments, sample was loaded into a Lake Shore Model EMPX-HF probe station. This station is equipped with Model 336 Temperature Controller, Model 475 DSP Gaussmeter, Model 642 Magnetic Power Supply and four independent probes for electrical contact. There is also the possibility to perform measurements under vacuum. Each electronic equipment has several configuration parameters as bit resolution, proportional-integral controller and averaging. The reader is invited to read the corresponding manuals for such details.

For resistance measurements, I-V curves were obtained with Hewlett-Packard 4145B Semiconductor Parameter Analyzer. I prepared a *Virtual Instrument* (VI) in LabVIEW to control the range of applied current and measure the output voltage in a 4-probes configuration, and data is saved directly into the controlling computer. For I-V curves of Wheatstone bridges, positive current injection probe and positive voltage measurement probe are in contact with the same gold pad. This also applies for negative probes, so measurement is effectively performed in a 2-probes configuration. Electrical resistance is then estimated by a linear fit in a reduced range of the I-V curve, for current values from -0.3 mA to +0.3 mA. This region is selected to ensure that sample is within its ohmic behavior. Considering the precision for standard deviation of the fit performed in Origin Lab, values down to 0.01Ω could be distinguished at best, as shown in Fig. B.1. As sample resistance gets higher, so does the minimum precision. Uncertainty values are

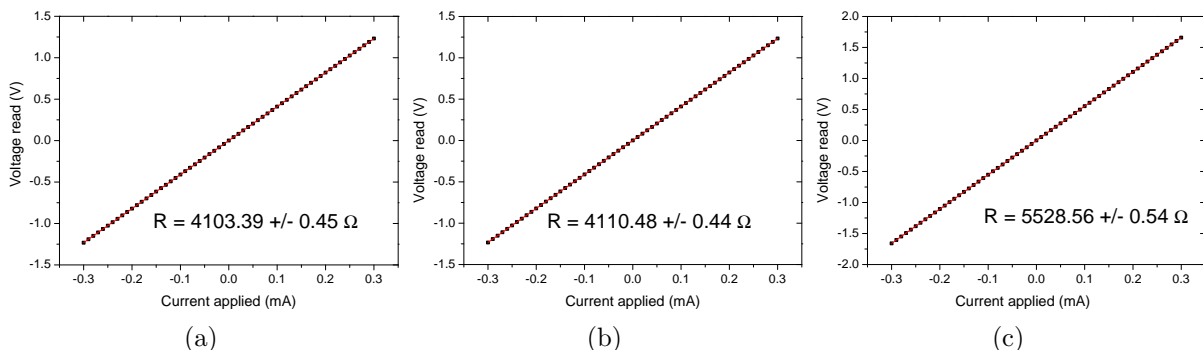


Figure B.1: Example of linear fit to obtain electrical resistance of 45 nm thick LSMO structures on 4° vicinal STO. a) Single stripe 4-probes measurement, magnetization is parallel to current density. b) Same single stripe, but magnetization perpendicular to current density, thus higher value for electrical resistance. c) 2-probes resistance measurement between signal terminals of a Wheatstone bridge.

two times the standard deviation resulting from the linear fit.

Magnetoresistance curves are obtained with VI developed by Dr. Olivier Rousseau, a previous post-Doc who was participating in ByAxon project. The VI sets a target sample temperature with Lake Shore Model 336 and sweeps the current through the coils using Lake Shore Model 642. For each current value, magnetic field measurement is performed with Lake Shore Model 475 and voltage is measured with Keithley 2000 Multimeter. The lab-made preamplifier, described in the main text, increases the signal for a proper read by the voltmeter. Sample is biased either with a home-made low noise current source or with Yokogawa GS200 DC Voltage/Current Source. Finally, Hewlett-Packard 3562A Dynamic Signal Analyzer was used for noise and amplifiers transfer function characterizations. The measured bandwidth is from 1 Hz to 100 kHz, and data is obtained in “log mode” which gives a fixed 80 data points per decade. This mode allows an easy visualization of $1/f$ and thermal components of noise, with a variable bandwidth resolution between each point. It is also possible to perform measurements in “linear mode” with a fixed resolution bandwidth, which results in fewer points in lower frequencies and several data points in higher frequencies. Input channel was configured in AC couple, with a high-pass filter with cut-off frequency below 0.1 Hz. A proper amplitude range for input signal is found with the automatic option, with measurements performed at fixed range. For averaging, the option to reject signals presenting overload of chosen range is kept on. As for n measures the standard deviation reduces by \sqrt{n} , most noise measurements were performed with $n = 16$ or $n = 32$. Characterizations with $2 \times n = 16$ and then the average between the two results were also performed. The built-in source was also used to obtain the transfer function of the amplifiers studied during the thesis. Source was configured in random noise operation with a 5 mV amplitude to avoid amplifier saturation due to high gain. Data is obtained and stored using a VI. Later during the course of this thesis the laboratory acquired a Rohde & Schwarz RTO2000 oscilloscope, that can perform FFT analysis of the input signals and has two waveform generators. Noise measurements performed with this equipment are only in linear mode, and in this thesis a resolution bandwidth down to 100 mHz was selected. This requires an acquisition and processing time of 20 seconds for each sample. The system does not have a built-in function to reject overload signals. Measurement data and screenshots can be directly saved through USB interface, and an Ethernet connection allows for remote control.

In Fig. B.2, it is possible to see the mentioned equipment for electrical characterization of LSMO samples. A top view of the home-made low noise preamplifier is presented

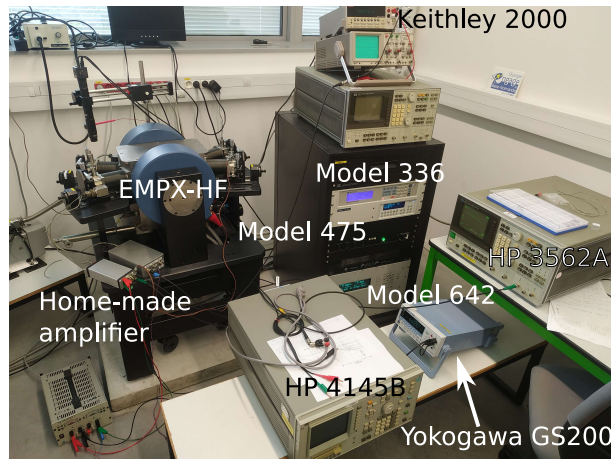


Figure B.2: Available equipment for electrical characterization.

in Fig. B.3. Inputs are on the left side, outputs and supply on the right side. It is possible to see both two-stages channels and the operational amplifier responsible for the gradiometer output. When in use, the circuit is kept in a closed metal box. The schematic is represented in Fig. B.4. After the first stage amplification there is a high-pass RC filter



Figure B.3: Home-made low noise preamplifier based on AD8421.

with 0.16 Hz cutoff frequency, to decouple the AC signal before the second amplification stage. As parasite peaks at high frequency were detected during the development of this amplifier, low-pass RC filters with 16 kHz were added at the output of each second stage amplification. Such peaks would provoke an overload rejection during noise measurements using HP 3562A Dynamic Signal Analyzer.

B.2 Magneto-optical Kerr Effect imaging

Light itself is an electromagnetic wave, with the electric field and magnetic field perpendicular to each other, both transverse to the propagation direction. The plane of the electric field is defined as the polarization plane of the light. When a polarized light interacts with a magnetized material, its polarization direction suffers a rotation. Photons, the quanta of electromagnetic radiation, carry angular momentum and can transmit it to the electron system of a solid. This changes the projection of the magnetic moment along the direction of propagation, causing a rotation in polarization. This connection between light and magnetism was first presented by Michael Faraday in 1845, when he found that polarized light passing through a magnetized material had a rotated polarization plane. Later, John Kerr noticed in 1877 a similar effect for polarized light reflected from a magnetized material. Such effects, know respectively as Faraday rotation and Kerr rotation, allow the imaging of magnetic domains. Two Magneto-optical Kerr Effect (MOKE) systems were used in this work: one available at IMDEA Nanociencia and one developed in GREYC laboratory. The latter will now be further explained.

The MOKE imaging system available at GREYC works in the longitudinal MOKE configuration, allowing the visualization of the magnetization component parallel to applied field direction. One polarizer is placed between light source and sample, and a second one between sample and camera. The two polarizers present a small angle deviation from 90° difference, almost completely blocking the light that reaches the camera sensor. The number of incoming photons at the detector will change according to the Kerr rotation. To increase the contrast of the obtained images for LSMO thin films, a differential method is used. An image corresponding to the initial saturated state at negative applied magnetic field is used to subtract background for following images at different field values. Resulting images are in gray level, and the greater the magnetization component opposite to the initial saturated state, the darker the resulting image. Images showing the evolution of magnetization with applied field are presented in Fig. B.5. It is possible to chose the number of times the image is averaged at each applied field and select the exposure time. Increasing the averaging and exposure time increases the Kerr signal, but the resulting image is also more prone to deviations from mechanical vibrations of the system and temperature drifts. In general, signal is weaker for thinner LSMO films, so a proper balance

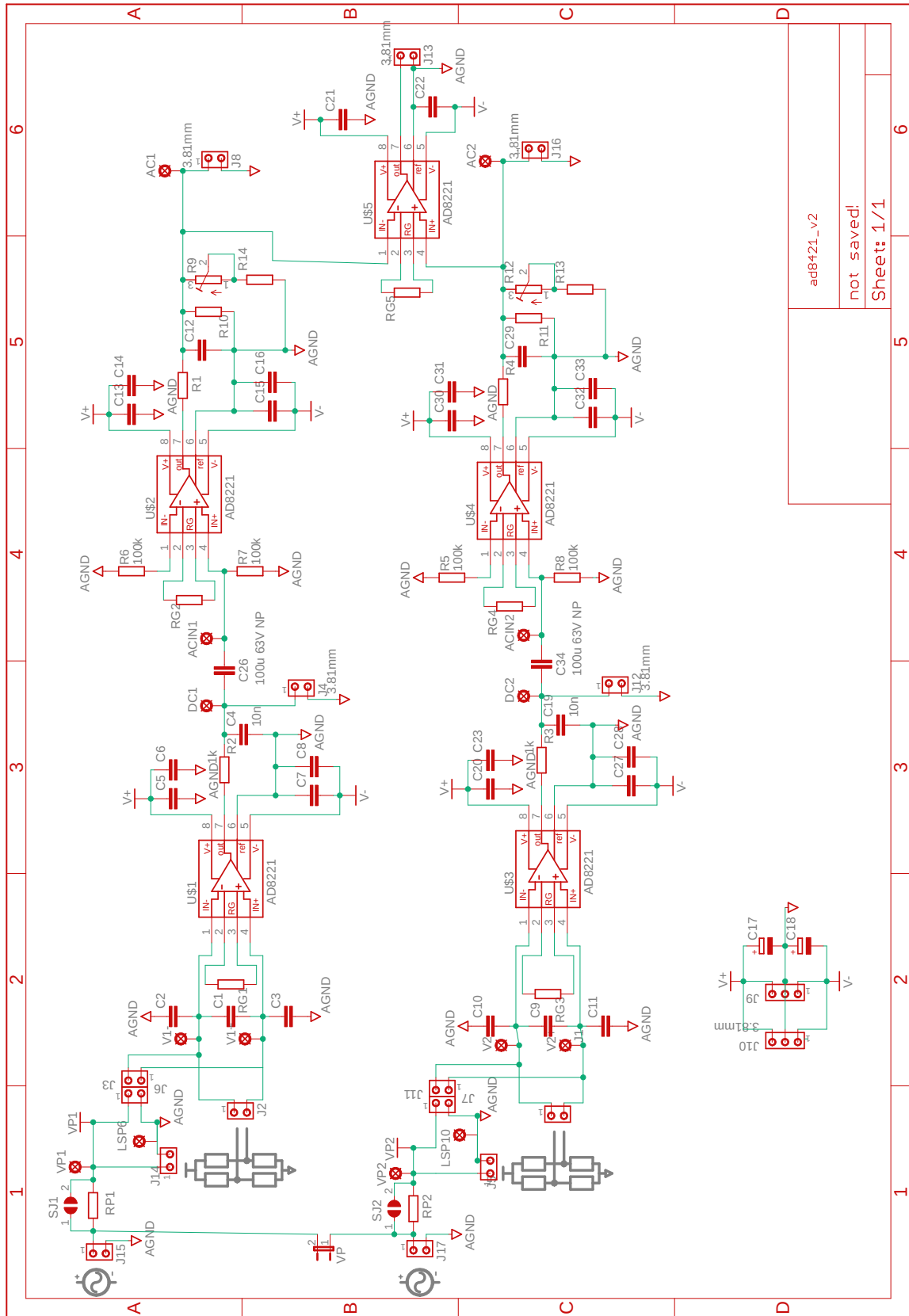


Figure B.4: Schematic of the home-made preamplifier, with two independent channels and a gradiometer output.

must be obtained. The system uses a high power LE B P1W-EZFZ-24 LED from OSRAM

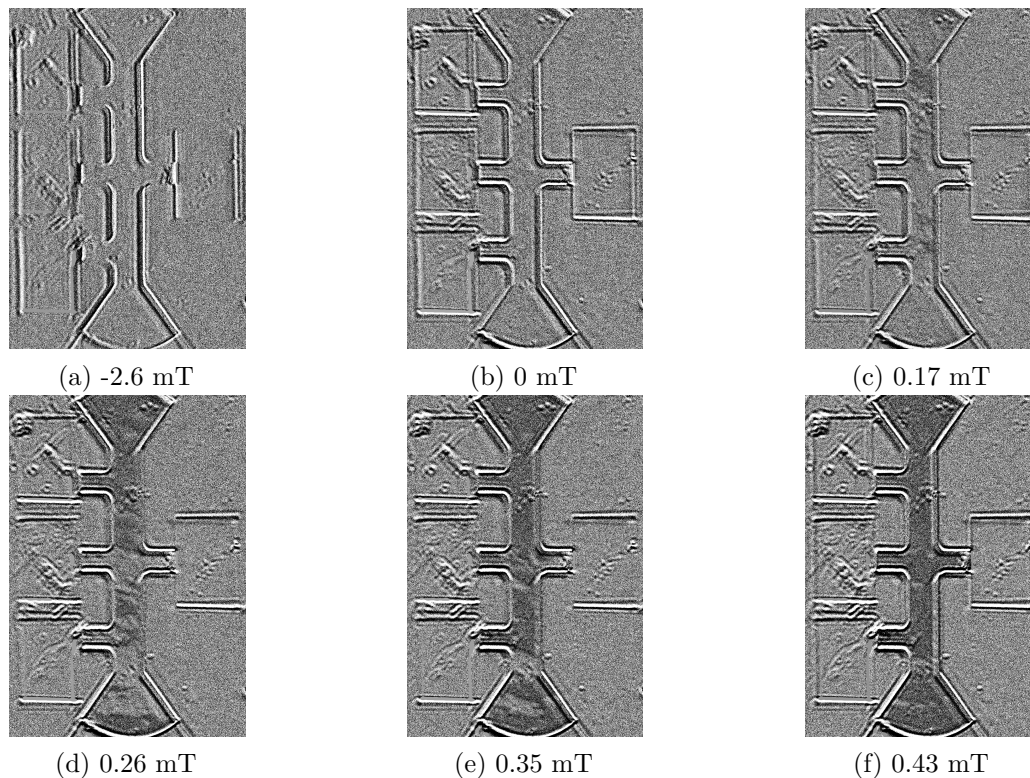


Figure B.5: Examples of MOKE images showing magnetization reversal in a LSMO stripe. [BA146]

Opto Semiconductors at 459 nm wavelength to light the sample. The LED is powered by a SIGLENT SPD1168X Programmable DC Power Supply. Reflected light is captured using Hamamatsu ORCA-Flash 2.8 Scientific CMOS camera. A set of Helmholtz coils with a soft ferrite core and a controllable current source are used to apply the magnetic field. Coils were calibrated using a commercial Hall effect sensors placed at sample position, in the middle of the coils. Sample holder is freely to rotate, allowing to perform MOKE imaging in any desired direction in the plane of the sample. Then, from the obtained images, it is possible to average the gray level of a given area. Dividing this average by the average gray level of a non-magnetic zone of the sample allows to deduce the magnetization cycle of the sample, as shown in Fig. B.6. The system also presents second pair of Helmholtz coils to control a four-quadrant magnetic field along the plane of the sample. Each pair is controlled independently with a SIGLENT SPD3303X Programmable DC Power Supply and a rotational magnetic field can be created. It is thus possible to verify the rotational AMR signal by applying a magnetic field amplitude strong enough to saturate the LSMO film. For proper usage, device must be connected to a PCB with wire bonding. Wires are soldered to said PCB for device biasing and voltage reading. The photographs of the system presented in Fig. B.7 show the available setup.

As the Helmholtz coils were fabricated in the laboratory, a proper calibration was necessary after mounting in the wood support. A Hall effect sensor was used to calibrate independantly each pair of coils, and results are presented in Fig. B.8. For each pair, current was swept 16 times. Black points are the average field value for each requested current, and error bars represent two times the standard deviation. The linear fit was done with Origin Labs built-in function. Due to a different gap between each coil of a pair, the current-to-field transfer is not the same. Whereas pair number 1 has a $11.13 \mu\text{T mA}^{-1}$ transfer, pair number 2 presents $8.91 \mu\text{T mA}^{-1}$. As each pair has its own current supply, the provided current can be adjusted to obtain a circular magnetic field with constant amplitude. This is shown in Fig. B.9. The difference in applied field amplitude reaches a

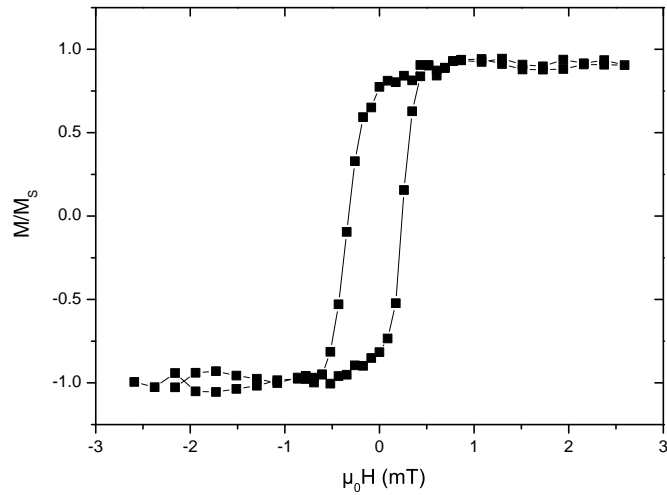


Figure B.6: Magnetization cycle obtained from Fig. B.5 (extra images not shown). [BA146]

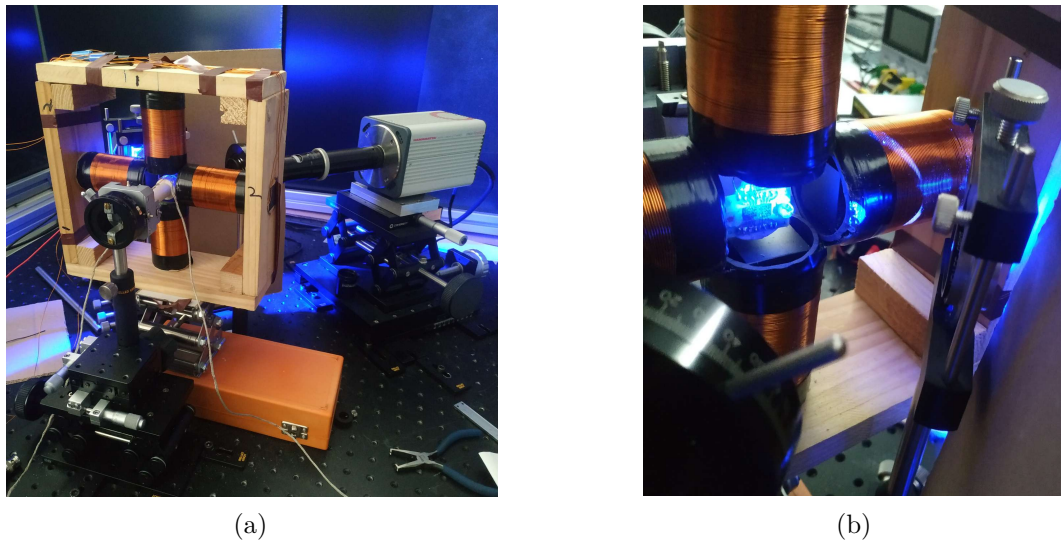


Figure B.7: MOKE system available at GREYC. Pair number 1 applies field in Z-axis and pair number 2 in X-axis. a) Sample holder keeps sample in the middle of two pairs of Helmholtz coils, and camera (far right) captures the reflected light. b) LSMO sample illuminated by high power LED.

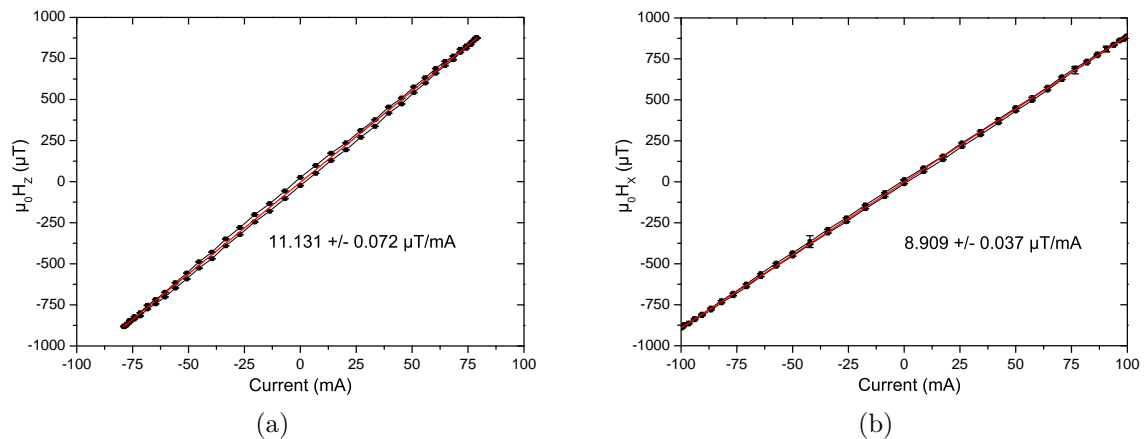


Figure B.8: Calibration of Helmholtz coils for the home-made MOKE imaging system. a) Pair number 1. b) Pair number 2.

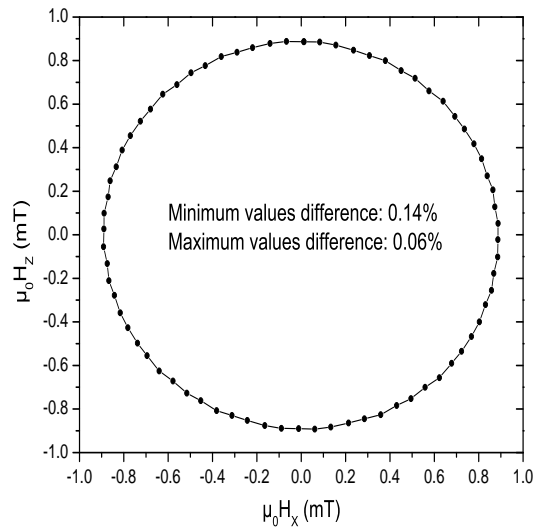


Figure B.9: Resulting circular field with proper adjustment of supplied current for each pair of Helmholtz coils.

maximum error of 0.14%, when one coil is closest to zero applied field while the other is at its most negative current.

B.3 Numerical fit to experimental curves

The script to obtain a numerical curve fitted to experimental data and to extract parameters from the device was written in Python. Available open-source libraries such as SciPy, NumPy and Matplotlib were used to perform calculations and display graphs. The SciPy library provides numerical routines for numerical optimization, such as methods that implement Brent's algorithm, differential evolution and trust region reflective. Those methods are used for curve fitting. Below are key segments of the Python script to fit a curve over experimental V_{meas} data from a 45WB or 90WB structure.

Initially, differential evolution is combined with Brent's method to obtain initial values for the parameters to be adjusted. The initial values can be bounded accordingly from the experimental data. As differential evolution is a stochastic method, it has a considerable computational demand. For each set of values created by this method, the dimensionless magnetic energy is minimized by finding the root of the function. With the obtained θ value, bridge output is calculated and compared to the experimental value. This is repeated until a good set of parameters is obtained, for a small enough error. This set is then used as initial values for the bounded non-linear least squares algorithm implemented by trust region reflective method, which will once again call Brent's method. The final result is optimized parameter values and an array with calculated output voltage for each value of magnetic field. This array is then plotted against the experimental V_{meas} curve.

```
import numpy as np
import matplotlib.pyplot as plt
from scipy.optimize import curve_fit, differential_evolution, minimize_scalar

def uniaxial_energy(theta, ha, h, gamma) -> float:
    return (1/2)*np.sin(theta)**2 - (h/ha)*np.cos(theta-gamma)

def minimize_theta(h, ha, gamma) -> float:
    theta = np.array([])
    for field in h:
        minimization = minimize_scalar(uniaxial_energy,
```



```

        bounds=(-np.pi/2, np.pi), args=(ha, field, gamma),
        method='bounded')
    theta = np.append(theta, minimization.x)
    global theta_minimized
    theta_minimized = theta
    return theta

def calculate_vmeas45(h, ha, amr, gamma) -> float:
    return (vbias/2)*amr*np.sin(2*minimize_theta(h, ha, gamma))

def calculate_vmeas90(h, ha, amr, gamma) -> float:
    return vbias*(amr*np.sin(minimize_theta(h, ha, gamma))**2)

def sumOfSquaredError(parameterTuple):
    val = calculate_vmeas(field_measured, *parameterTuple)
    return np.sum((v_measured - val) ** 2.0)

def generate_Initial_Parameters():
    parameterBounds = []
    parameterBounds.append([0.1, 2]) #bounds for anisotropy field
    parameterBounds.append([-0.01, -1e-4]) #bounds for MR ratio
    parameterBounds.append([np.pi/2,np.pi/2+20*np.pi/180]) #bounds for gamma
    result = differential_evolution(sumOfSquaredError,
                                    parameterBounds,seed=3)
    return result.x

bridge = input('\nBridge design?\n')
vbias = int(input('\nVoltage bias?\n'))
geneticParameters = generate_Initial_Parameters()

if bridge=='45WB':
    fittedParameters, pcov = curve_fit(calculate_vmeas45, field_measured,
    v_measured, geneticParameters,
    bounds=((4,-0.01,np.pi/2),(7,-0.0001,np.pi/2+20*np.pi/180)),maxfev=80000)
elif bridge=='90WB':
    fittedParameters, pcov = curve_fit(calculate_vmeas90, field_measured,
    v_measured, geneticParameters,
    bounds=((0.1,-0.01,np.pi/2),(2,-0.0001,np.pi/2+20*np.pi/180)),maxfev=80000)

```

The above code is not complete but gives the reader an insight into how the method for curve fitting is performed. Limit values for bounds can be changed by the user according to the experimental curve.

Appendix C

Résumé long en Français

C.1 Introduction

Le projet européen ByAxon (Jan. 2017 - Déc. 2020) avait comme objectif une preuve de concept d'un dispositif électronique actif destiné à être implanté au niveau d'une lésion de la moelle épinière. Le dispositif a pour but de restaurer une connexion neuronale au niveau de la zone lésée. Pour cela, la détection du signal émis par les membres doit être assurée. Le mode de détection le moins invasif choisi consiste à détecter le champ magnétique créé par les signaux neuronaux au niveau de la moelle épinière au moyen d'un capteur adapté. Ce capteur doit donc respecter différentes contraintes liées à telle application biomédicale. Il doit fonctionner correctement et de manière optimale à la température du corps humain, être d'une taille réduite et présenter une détectivité de quelques centaines de $\text{pT Hz}^{-1/2}$ dans le domaine basse fréquence (Fig. C.1). À ce jour, seuls les capteurs de

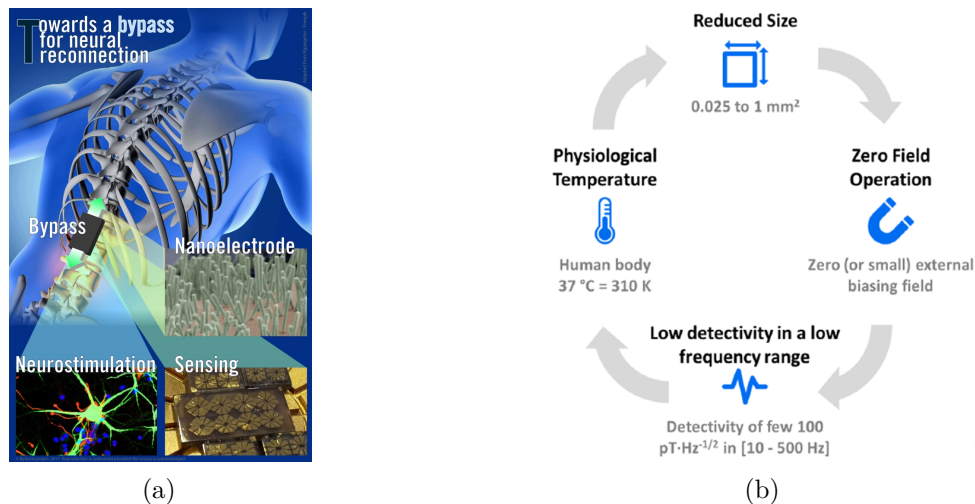


Figure C.1: a) Présentation du projet ByAxon. b) Contraintes imposées au capteur de champ magnétique.

champ magnétique basés sur la magnétorésistance respectent l'ensemble de ces contraintes, si on les compare à d'autres technologies comme *le fluxgate*, *les capteurs à effet Hall*, *les Superconducting Quantum Interference Devices* et *les magnétomètres à pompage optique (Optical Pump Magnetometers)*. Même si la sensibilité des capteurs basés sur l'effet magnétoresistif anisotrope (AMR) n'atteint pas les valeurs obtenus avec les dispositifs basés sur la magnétorésistance géante (GMR) ou la magnétorésistance à effet tunnel (TMR), leur très faible bruit dans le domaine basse fréquence en fait de bons candidats pour répondre au chaper des charges. La caractéristique principale d'un capteur est sa détectivité, c'est-à-dire la valeur la plus petite que le capteur est capable de détecter à une

fréquence donnée. La détectivité d'un capteur de champ magnétique s'exprime de la façon suivante:

$$\text{Détectivité [nT}/\sqrt{\text{Hz}}] = \frac{\text{Totalité de bruit électrique [nV}/\sqrt{\text{Hz}}]}{\text{Sensibilité [V/T]}} \quad (\text{C.1})$$

La Fig. C.2 présente la gamme d'amplitude de champ magnétique détectable avec des différentes technologies de capteurs.

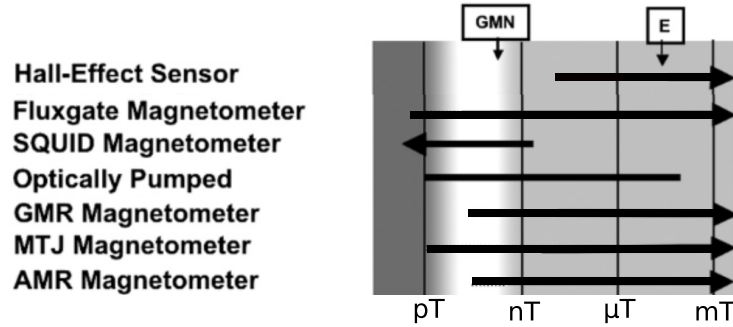


Figure C.2: Amplitude du champ magnétique détectable par différents capteurs. Le terme MTJ désigne les jonctions tunnel magnétiques, E la valeur du champ magnétique terrestre et GMN le bruit géomagnétique.

C.2 LSMO et validation du capteur

La manganite $\text{La}_{1-x}\text{Sr}_x\text{MnO}_3$ (LSMO) est un oxyde à structure pérovskite, dont les propriétés électriques et magnétiques sont une fonction de la concentration du dopant strontium. La structure cristalline pérovskite de ce matériau, qui forme un réseau octaédrique dans le cas idéal sans aucun dopant, est déformée un efois dopée. Avec une concentration de $x = 1/3$, le LSMO est un cristal rhomboédrique semblable à BiFeO_3 , qui peut être considérée comme une structure pseudocubique. Dans cette configuration, le matériau présente un comportement conducteur et ferromagnétique, avec une température de Curie T_C autour de 350 K (Fig. C.3).

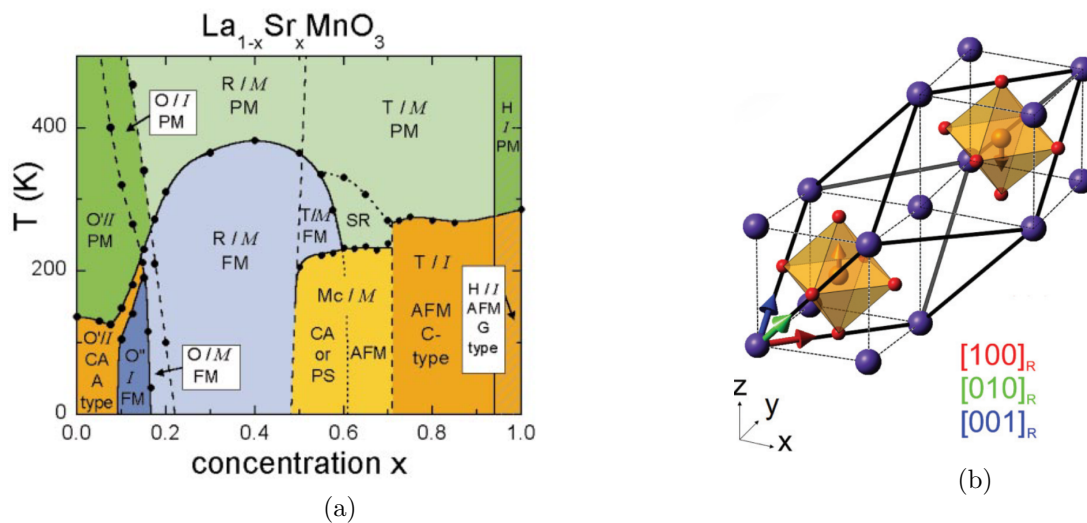


Figure C.3: a) Diagramme de phase du LSMO en fonction de la concentration x du dopant Sr. b) Transformation de la structure rhomboédrique (lignes épaisses) pour une structure cubique (lignes pointillées).

C.2.1 Mécanisme de double échange

Le transport de courant électrique et le comportement ferromagnétique du LSMO sont fortement liés via le mécanisme de double échange proposé par Zener. suite à la substitution d'atomes de La par des atomes de Sr et en raison du fait que l'oxygène garde toujours sa charge 2-, la même proportion d'atomes de Mn doit maintenant présenter un charge 4+ pour garder l'équilibre de charge de la composition. La conduction électrique résulte de la capture d'un électron d'un ion Mn^{3+} par un ion Mn^{4+} . Ce transfert de charge est possible seulement avec la participation d'un anion O^{2-} . Au moment où un électron transite du Mn^{3+} vers l'oxygène, un deuxième électron provenant du O^{2-} est transféré au Mn^{4+} , comme le montre la Fig. C.4. Selon la deuxième règle de Hund, l'état

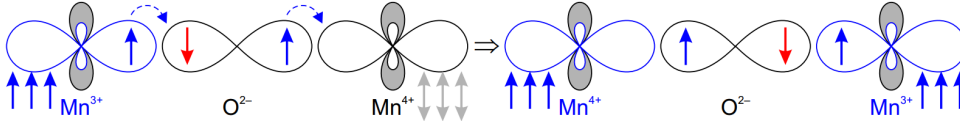


Figure C.4: Transfert de charges simultané entre deux cations Mn et un ion O.

énergétique d'équilibre est celui pour lequel les spins des électrons sont alignés, donc le système cherchera cette configuration naturellement. L'alignement des spins favorise aussi la probabilité de transfert des électrons, ce qui augmente la conductivité électrique. On doit à Zener une expression liant la conductivité électrique σ et le comportement ferromagnétique:

$$\sigma \approx (xe^2/ah)(T_C/T) \quad (\text{C.2})$$

où x est la proportion de Mn^{4+} (dans le cas du LSMO, la proportion du dopant Sr), e la charge de l'électron, a le paramètre de maille, h la constante de Planck, T_C la température de Curie et T la température du matériau. L'augmentation l'énergie thermique supprime l'alignement des spins, le LSMO devient alors isolant à une température proche de celle où il perd son comportement ferromagnétique.

Les contraintes biaxiales présentes dans la couche mince affectent aussi la probabilité du double échange, il s'agit donc là d'un autre paramètre permettant de faire varier la conductivité électrique et la T_C . Dans le cas d'une croissance épitaxiale de LSMO sur des substrats SrTiO_3 (STO), une contrainte de traction de +0.75% apparaît dans la couche mince du manganite. Avec telle contrainte, l'épaisseur de relaxation pour le LSMO se trouve au dessus de 100 nm. C'est l'induction d'une anisotropie uniaxiale dans la couche mince de LSMO par utilisation de substrats vicinaux qui est le fondement du capteur AMR développé dans ce travail de thèse. Les substrats vicinaux sont des substrats qui présentent un angle de coupure par rapport sa surface (l'angle vicinal) et génèrent en surface de la couche mince une structure en plateaux divisés par des marches. La présence des marches provoquera une anisotropie dû la modifications des liaisons atomiques.

C.2.2 Uniaxialité magnétique anisotrope

Le modèle le plus simple pour décrire une uniaxialité magnétique anisotrope est celui développé par Stoner et Wohlfarth. L'énergie magnétique d'une particule présentant une seule direction facile d'aimantation est exprimée par :

$$E = K_u \sin^2 \theta - \mu_0 H M_S \cos(\theta - \gamma) \quad (\text{C.3})$$

où K_u est la constant d'anisotropie uniaxiale, θ est l'angle entre l'axe facile d'aimantation et l'aimantation M , γ est l'angle entre l'axe facile et le champ appliqué H et M_S est la valeur de saturation de l'aimantation. Dans le cas $\gamma = 90^\circ$, la situation d'équilibre s'obtient par la minimisation de l'énergie ce qui conduit à un angle théta inférieur à 90° :

$$\theta = \arcsin\left(\frac{\mu_0 H M_S}{2K_u}\right) \quad (\text{C.4})$$

. Le champ d'anisotropie H_a est alors défini par

$$H_a = \frac{2K_u}{\mu_0 M_S} \quad (\text{C.5})$$

C'est le champ perpendiculaire à l'axe facile nécessaire pour mener l'aimantation à saturation. Si une petite déviation δ autour de $\gamma = 90^\circ$ est présente, cette nouvelle composante selon l'axe facile, aussi faible soit-elle, va déformer les courbes d'énergie. Alors, pour un champ appliqué suffisamment élevé, le point d'équilibre du système bascule dans une situation où $\theta > 90^\circ$, et la direction de l'aimantation M subit une variation brusque, comme présenté dans la Fig. C.5. L'effet AMR est fonction des directions de la densité

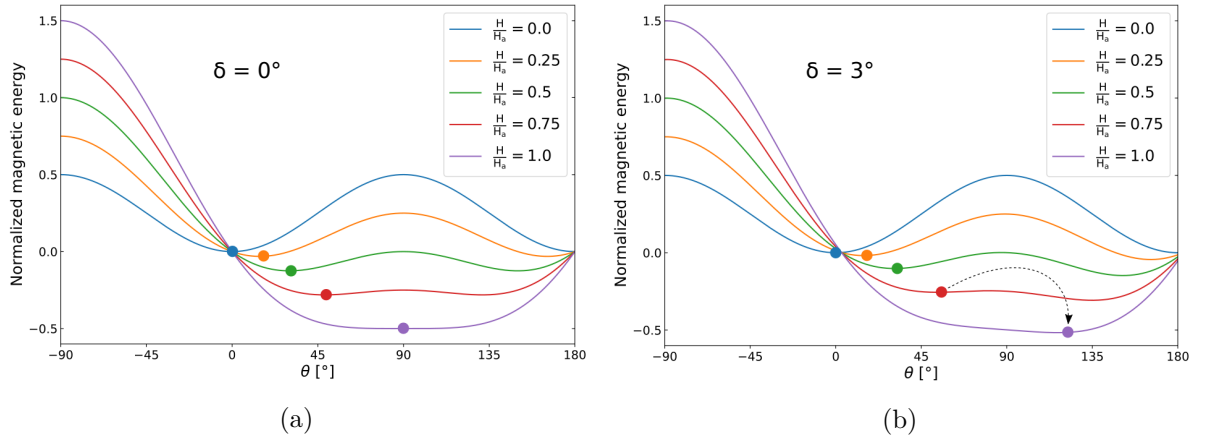


Figure C.5: Point d'équilibre de l'énergie magnétique en fonction du ratio champ appliqué sur champ d'anisotropie. Nous considérons un état initial de saturation en champ appliqué négatif
 a) Champ appliqué parfaitement perpendiculaire à l'axe facile. b) Champ appliqué avec une déviation de 3° par rapport à l'axe difficile.

de courant et de l'aimantation. Un saut sur la valeur de θ est reflété par un saut dans le signal de sortie d'un capteur AMR.

L'imposition d'une seule direction facile d'aimantation dans des couches minces obtenue via la croissance épitaxiale sur des substrats vicinaux peut être décrite via le modèle d'anisotropie de surface de Néel, modifié pour intégrer cette influence :

$$E_{film} = E_{bulk} - 2 \cdot \frac{E_{surface}}{t} - 2 \cdot \frac{E_{edge} + E_{corner}}{t \cdot d} \quad (\text{C.6})$$

où t est l'épaisseur de la couche et d la distance entre deux marches consécutives. Plus l'angle vicinal est grand, plus dense est la concentration des plateaux et plus petit est le terme d . Avec la diminution de d , le système atteindra une constante d'anisotropie uniaxiale K_u plus élevée. Pour vérifier la présence d'une direction facile d'aimantation, des images d'aimantation d'une structure gravée sur une couche de 60 nm de LSMO, déposée sur un substrat vicinal 8° STO, ont été obtenues avec un système d'imagerie magnéto-optique à effet Kerr (MOKE). La Fig. C.6 montre des courbes d'aimantation mesurées quand le champ appliqué est parallèle aux marches, qui est la direction attendue pour l'axe facile, et quand l'échantillon est tourné de 90° . Nous obtenons les formes attendues pour l'évolution de l'aimantation selon l'axe facile et selon l'axe difficile, respectivement.

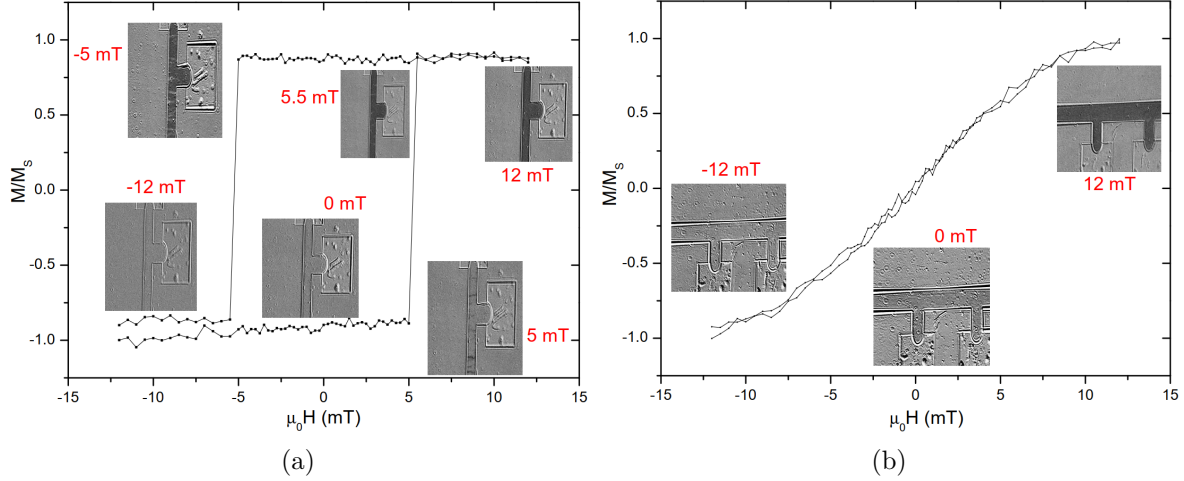


Figure C.6: Courbes d'aimantation obtenues avec un système d'imagerie MOKE. a) Nucléation puis propagation des domaines magnétiques selon la direction de l'axe facile. b) Rotation cohérente de l'aimantation selon l'axe difficile. [échantillon BA137]

C.2.3 Magnétorésistance anisotrope

Considérons une particule magnétique avec une seule direction de l'axe facile dans le plan, et présentant un effet AMR. Le tenseur de résistivité peut être décrit comme

$$\rho = \begin{bmatrix} \rho_{\perp} - \Delta\rho \cdot \cos^2 \theta & -\frac{1}{2}\Delta\rho' \cdot \sin(2\theta) \\ -\frac{1}{2}\Delta\rho' \cdot \sin(2\theta) & \rho_{\perp} - \Delta\rho \cdot \sin^2 \theta \end{bmatrix} \quad (\text{C.7})$$

où $\Delta\rho = \rho_{\perp} - \rho_{\parallel}$, ρ_{\perp} correspond à la résistivité quand les directions de densité de courant J et l'aimantation M sont perpendiculaires et ρ_{\parallel} la résistivité quand elles sont parallèles et $\rho_0 = (\rho_{\perp} + \rho_{\parallel})/2$ désigne la valeur moyenne. Les termes de la diagonale principale sont liés à l'effet "classique" de magnétorésistance anisotrope, tandis que les termes anti-diagonaux sont liés à l'effet Hall planaire. L'utilisation du terme ρ' est utilisée pour prendre en compte une possible différence entre la variation de résistivité pour l'effet Hall planaire et celle de la magnétorésistance anisotrope. La résistivité selon la direction α de la densité de courant J est définie comme:

$$\begin{aligned} \rho_{\alpha}(\theta, \alpha) &= (\rho_{\perp} - \Delta\rho \cdot \cos^2 \theta) \cdot \cos^2 \alpha \\ &+ (\rho_{\perp} - \Delta\rho \cdot \sin^2 \theta) \cdot \sin^2 \alpha \\ &- \frac{1}{2}\Delta\rho' \cdot \sin(2\theta) \cdot \sin(2\alpha) \end{aligned} \quad (\text{C.8})$$

La Fig. C.7 synthétise les directions d'intérêt. Quand la couche mince de LSMO est gravée

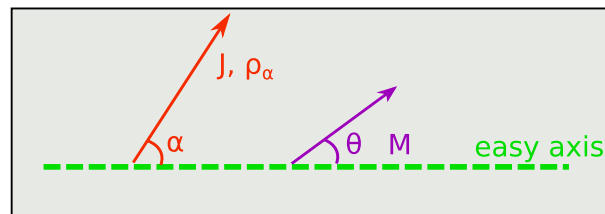


Figure C.7: La densité de courant J présente un angle α avec l'axe facile et l'aimantation M un angle θ .

sous forme de simples lignes, la direction de la densité de courant α est fixée. Dans ce

cas, nous pouvons écrire la résistance électrique de cette ligne en faisant la substitution $R_\alpha(\theta, \alpha) = \rho_\alpha(\theta, \alpha)l(wt)^{-1}$, où w est l'épaisseur de la couche, l et w la longueur et la largeur de la ligne. Dans notre cas, les valeurs choisies pour nos géométries correspondent à α égales 0° , 45° , 90° et 135° . La variation de résistance électrique est donc :

$$\Delta R^{45} = \Delta R^{45^\circ, 135^\circ} = \frac{1}{2} \Delta R' \sin(2\theta) \quad (\text{C.9})$$

et

$$\Delta R^{90} = \Delta R^{0^\circ, 90^\circ} = \frac{1}{2} \Delta R \cos 2\theta \quad (\text{C.10})$$

Dans le cas $\gamma = 90^\circ$ (c'est à dire quand le champ est appliqué selon l'axe difficile), la substitution de l'expression de θ à l'équilibre conduit à :

$$\Delta R^{45} = \Delta R' \frac{H}{H_a} \sqrt{1 - \left(\frac{H}{H_a}\right)^2} \quad (\text{C.11})$$

avec des valeurs de maximum et minimum atteintes lorsque $H \pm H_a/\sqrt{2}$ et

$$\Delta R^{90} = \frac{1}{2} \Delta R - \Delta R \left(\frac{H}{H_a}\right)^2 \quad (\text{C.12})$$

avec la valeur maximale atteinte quand $H = 0$ et la valeur minimale atteinte quand $|H| = H_a$. La variation de résistance peut être détectée en gardant une polarisation en courant fixé pour les lignes de LSMO et en mesurant la tension entre les extrémités de la ligne, comme présenté sur la Fig. C.8 où les lignes ont une longueur $l = 300 \mu\text{m}$, une largeur $w = 100 \mu\text{m}$ et une épaisseur de 60 nm . Ces résultats montrent que les lignes

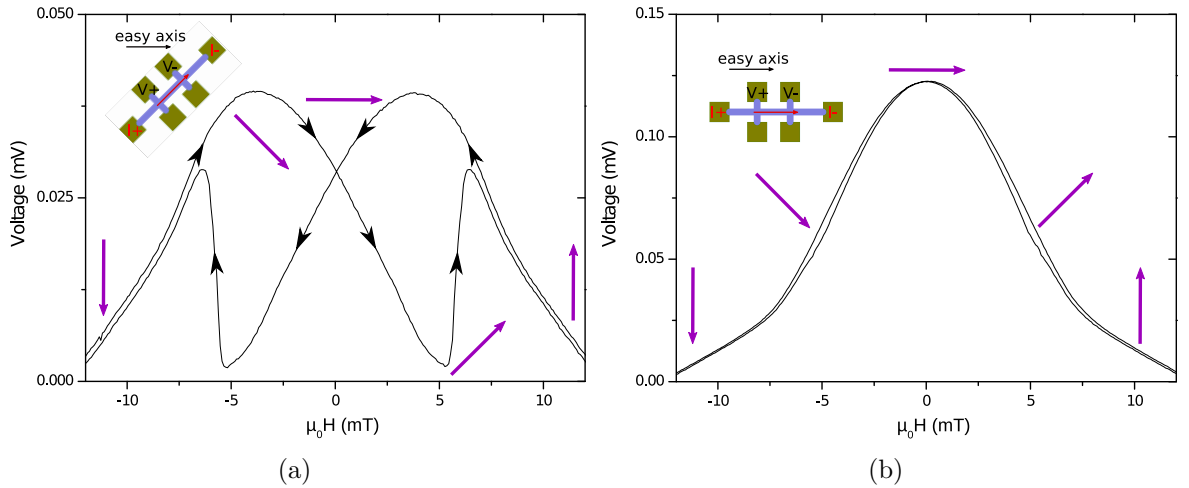


Figure C.8: Variation de la tension mesurée à une température de 310 K avec une polarisation en courant de $25 \mu\text{m}$, l'axe facile étant de direction horizontale. Les flèches en violet sont une représentation visuelle de la direction de l'aimantation pour un cycle depuis un champ négatif vers un champ positif puis retour. a) Ligne $\alpha = 45^\circ$, avec des flèches noires pour indiquer l'évolution du signal de sortie selon le balayage du champ magnétique. b) Ligne $\alpha = 0^\circ$. [échantillon BA097]

gravées dans des couches minces de LSMO déposées sur un substrat STO dit vicinal présentent une uniaxialité magnétique et une magnétorésistance anisotrope conforme à ce qui était attendu.

C.2.4 Validation du dispositif en pont de Wheatstone

Un pont de Wheatstone est une structure largement utilisée pour obtenir des signaux en tension proportionnels à la variation de la résistance des éléments du pont. Il se compose de deux branches liées en parallèle, comportant chacune deux éléments résistifs liés en série, dont la variation vis à vis de la grandeur à mesurer est opposée. C'est une structure avec quatre noeuds de connexion. Entre deux noeuds opposés, nommés les noeuds de polarisation, le pont est alimenté par un courant ou une tension. Les deux autres noeuds, nommés noeuds de signal, sont utilisés pour lire la tension de sortie. La Fig. C.9 présente schématiquement un pont de Wheatstone connecté à une source de tension et un amplificateur d'instrumentation. La tension en sortie de cette structure est

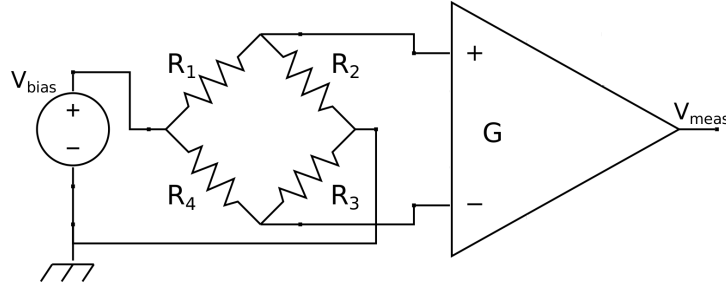


Figure C.9: Pont de Wheatstone alimenté par une source de tension. Le signal de sortie est mesuré avec un amplificateur d'instrumentation.

$$\Delta V_{meas} = V_{bias} \left(\frac{R_2 + \Delta R_2}{R_1 - \Delta R_1 + R_2 + \Delta R_2} - \frac{R_3 - \Delta R_3}{R_3 - \Delta R_3 + R_4 + \Delta R_4} \right) \quad (C.13)$$

Le grand avantage de l'utilisation d'un pont de Wheatstone est la réduction importante des variations de mode commun telles la variation de résistance avec la température ou le bruit de la source.

Deux structures en pont de Wheatstone ont été fabriquées sur des couches minces de LSMO. La Fig. C.10 donne les deux conceptions différentes et comprend un rappel des directions et angles d'intérêt. Une couche d'or est utilisée pour assurer les contacts électriques. Le motif présentant $\alpha = 45^\circ, 135^\circ$ est désormais nommé 45WB, et le deuxième

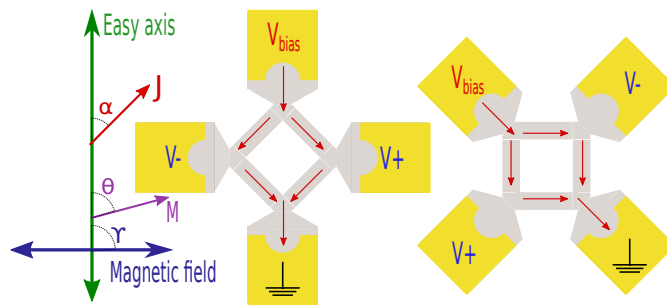


Figure C.10: La direction de l'axe facile est fixée. La densité de courant J et l'aimantation M forment respectivement un angle α et θ . Pour l'un, le pont est formé de lignes en LSMO avec $\alpha = 45^\circ$ et 135° et pour l'autre $\alpha = 0^\circ, 90^\circ$. Les noeuds pour la mesure de la grandeur sont indiqués par $V+$ et $V-$.

motif est nommé 90WB. La Fig. C.11 présente le masque utilisé en photolithographie pour la fabrication des ponts ainsi qu'une image photo d'un pont 90WB fabriqué. Chaque bras du pont de Wheatstone a une longueur $300 \mu\text{m}$ et une largeur de $100 \mu\text{m}$. Le substrat STO sur lequel est épitaxialement déposé le LSMO par ablation laser pulsé, est de 10 mm de longueur et 5 mm de largeur. Pour la structure 45WB, la tension en sortie est

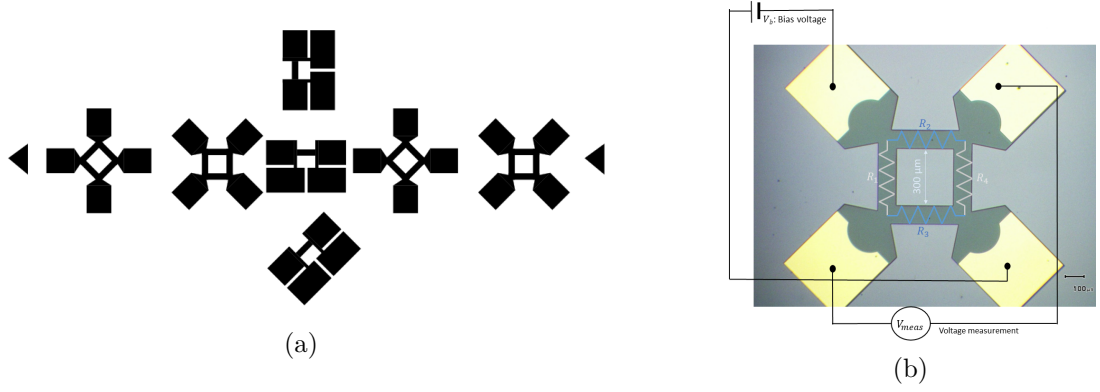


Figure C.11: a) Plan pour le masque physique utilisé en photolithographie. b) Indication du rôle des contacts d'or à partir d'une photo d'un échantillon 90WB fabriqué.

$$V_{meas} = \frac{V_{bias}}{2} \frac{\Delta R'}{R_0} \sin 2\theta \quad (C.14)$$

En y intégrant l'expression de θ à l'équilibre, nous obtenons

$$V_{meas} = V_{bias} \frac{\Delta R'}{R_0} \frac{H}{H_a} \sqrt{1 - \left(\frac{H}{H_a}\right)^2} \quad (C.15)$$

Ce pont présente donc une sortie linéaire autour de zéro et pour de faibles valeurs de champ appliqué. La sensibilité S en $V T^{-1}$ est la dérivée de la sortie V_{meas} par rapport au champ appliqué H . Ainsi, autour du champ nul, son expression est

$$S = V_{bias} \frac{\Delta R'}{R_0} \frac{1}{\mu_0 H_a} \quad (C.16)$$

Pour la structure 90WB, la tension en sortie est

$$V_{meas} = V_{bias} \frac{\Delta R}{R_{\perp} + R_{\parallel}} (1 - 2 \sin^2 \theta) \quad (C.17)$$

qui devient en utilisant l'expression de θ à l'équilibre

$$V_{meas} = V_{bias} \frac{\Delta R}{2R_0} - V_{bias} \frac{\Delta R}{R_0} \left(\frac{H}{H_a}\right)^2 \quad (C.18)$$

Cette deuxième structure nécessite un champ DC de polarisation pour obtenir une zone linéaire de fonctionnement. Sa sensibilité en champ nul est zéro, et pour $H = H_a/2$ nous retrouvons la même expression que l'équation C.16 mais avec la variation de résistance ΔR associée à l'AMR au lieu de $\Delta R'$.

La Fig. C.12 et la Fig. C.13 montrent les courbes d'aimantation obtenues avec le système d'imagerie MOKE, pour un pont 45WB et un pont 90WB. L'échantillon est constitué d'une couche de 60 nm sur substrat vicinal 8° . Ces images confirment l'existence d'une anisotropie uniaxiale pour un film déposé sur substrat vicinal et montrent une rotation cohérente de l'aimantation dans l'ensemble des ponts pour un champ appliqué normal à l'axe facile. Les signaux de tension en sortie présentent les comportements attendus. Les flèches en noir indiquent le cycle des images obtenues en fonction du champ appliqué, et certains points spécifiques des courbes d'aimantation sont colorés pour indiquer son image d'origine. Nous constatons un comportement magnétique comme attendu pour une particule magnétique présentant une anisotropie uniaxiale. La Fig. C.14 affiche les signaux de tension de sortie de chaque structure, avec l'ajustement d'une courbe

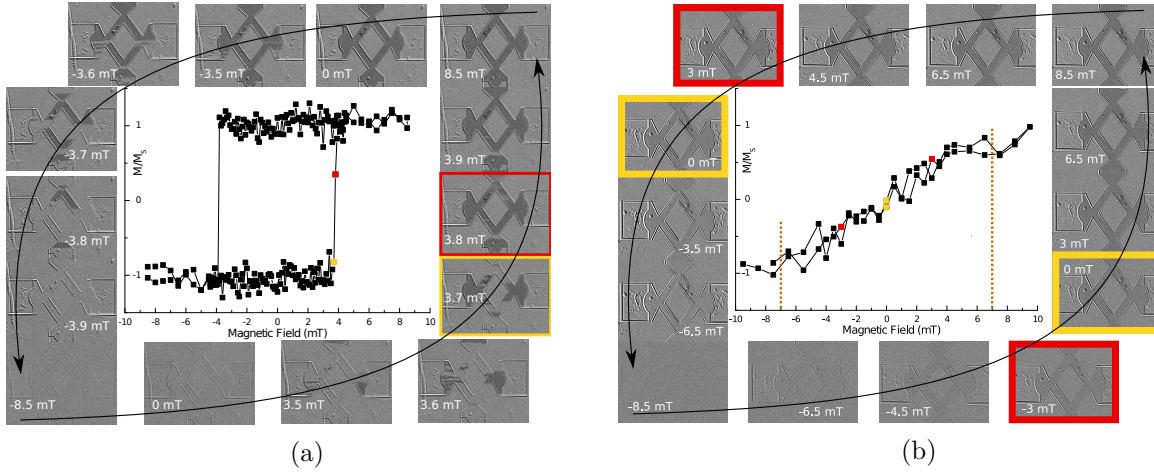


Figure C.12: Cycles d'aimantation pour un pont 45WB selon a) l'axe facile et b) l'axe difficile. [échantillon BA097]

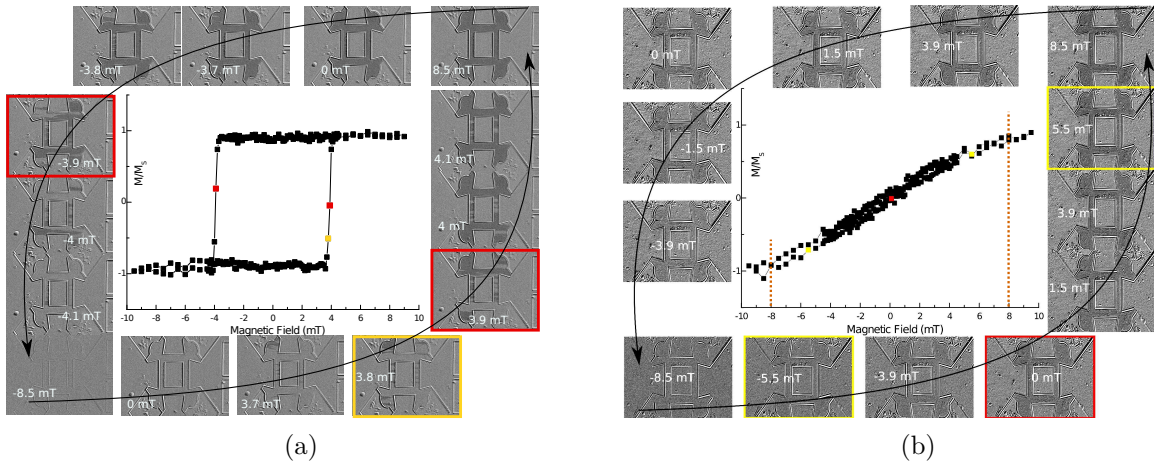


Figure C.13: Cycles d'aimantation pour un pont 90WB selon a) l'axe facile et b) l'axe difficile. [échantillon BA097]

calculée en utilisant un modèle numérique de la réponse des dispositifs. Avec les données expérimentales, ce modèle est capable d'obtenir la direction d'aimantation θ en minimisant l'énergie magnétique, et la valeur trouvée est utilisée pour calculer la sortie des ponts avec les équations Eqs. (C.14) and (C.17). Les paramètres comme le champ d'anisotropie H_a , le rapport MR et la déviation γ peuvent être fixés ou laissés libres pour un ajustement automatique en cherchant à minimiser l'erreur entre la courbe expérimentale et la courbe calculée. Les décrochements sur les courbes V_{meas} sont une conséquence du saut en θ de la direction de l'aimantation M . Comme mentionné précédemment, ce saut est dû à une petite composante du champ magnétique selon l'axe facile. Sa visualisation est facile en suivant les tracés de θ obtenus avec la minimisation de l'énergie magnétique. Nous avons volontairement réalisé une petite déviation du champ appliqué de manière à forcer un sens rotation de l'aimantation identique dans chacune des branches du pont, afin d'éviter une diminution de la variation du signal de sortie pour la structure (notamment pour la structure 45WB) quand le sens de rotation n'est pas identique au sein de chaque branche. Ce saut se produit sur une zone non utilisée du dispositif. Par ailleurs, des tests de stabilité ont garanti la répétabilité du comportement AMR. Au final, l'ensemble de ces caractérisations et résultats montrent la bonne opération du dispositif, et le mode de fonctionnement proposé pour le dispositif est validé.

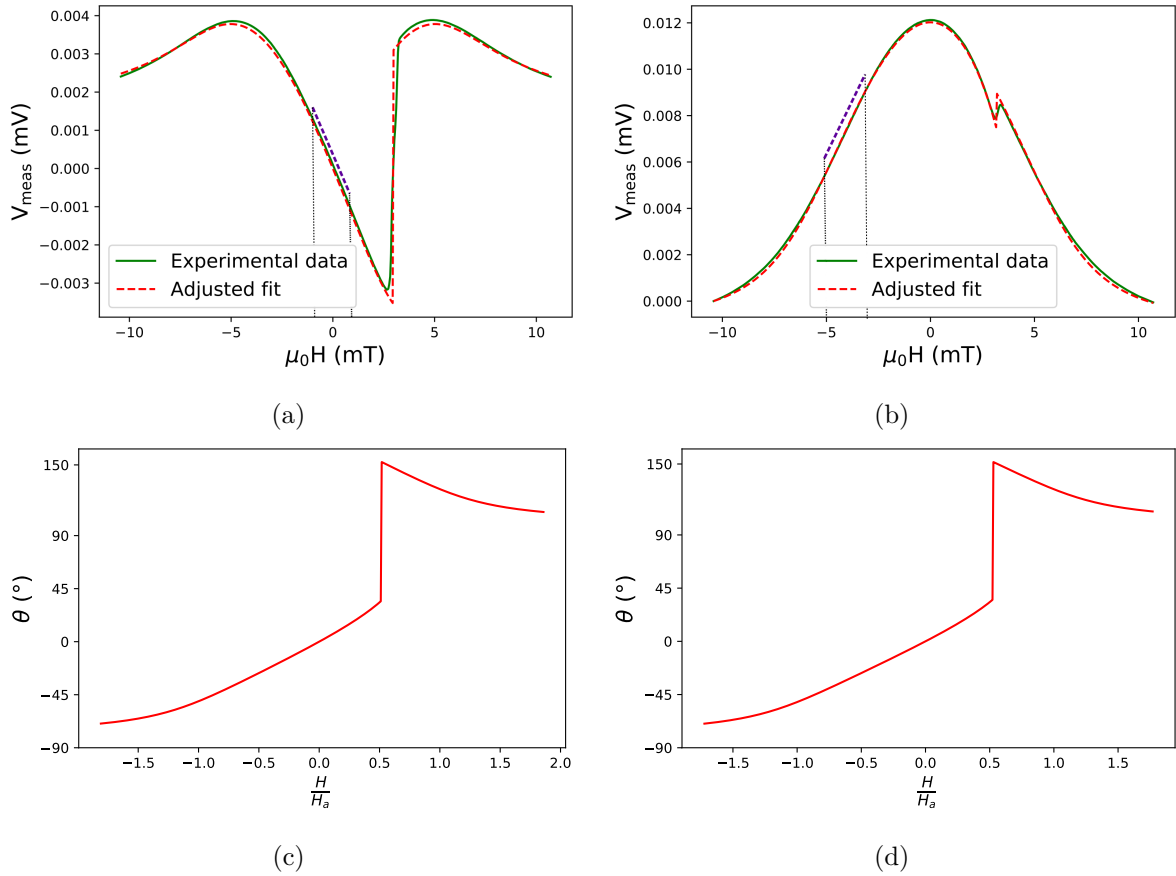


Figure C.14: Signaux de sortie de chaque structure de pont de Wheatstone, comparaison entre les données expérimentales et la courbe ajustée selon le modèle des dispositifs. Le régime d'opération linéaire est indiqué par des pointillés violets. a) V_{meas} pour la structure 45WB. b) V_{meas} pour la structure 90WB. c, d) Les valeurs correspondant de θ pour l'ajustement présenté en a), b) respectivement. [échantillon BA097]

C.2.5 Bruit d'un pont de Wheatstone LSMO et détectivité

Au début de ce document, nous avons présenté l'équation générale pour la détectivité d'un capteur magnétique. Nous disposons des expressions de la sensibilité de chaque structure et le dispositif validé, il convient maintenant de vérifier le bruit intrinsèque d'un pont de Wheatstone basé sur des couches minces de LSMO. Le bruit électrique traduisant peut être exprimé en densité spectrale de puissance (PSD) en $V^2 \text{ Hz}^{-1}$ ou en densité spectrale de tension (VSD) en $V \text{ Hz}^{-1/2}$. Un circuit préamplificateur adapté aux caractéristiques des échantillons a été spécialement conçu afin d'obtenir un bruit électrique total dominé par l'échantillon lui-même. La Fig. C.15 montre un comparatif de bruit entre l'ancien préamplificateur basé sur l'amplificateur d'instrumentation AD743 et le nouveau modèle basé sur l'amplificateur d'instrumentation AD8421. En comparant les courbes quand les entrées sont mises à la masse du système (courbes en noir), nous pouvons vérifier que le modèle utilisant l'AD743 présente un bruit électrique plus élevé, notamment en basse fréquence. En fait, l'amplificateur d'instrumentation AD743 présente un bruit électrique en tension plus élevé que le modèle AD8421 mais un bruit en courant plus petit. L'utilisation du modèle AD743 est adaptée pour des échantillons avec une résistance électrique plus élevée que les valeurs présentées par nos capteurs LSMO. Une mesure du bruit de ce pré-amplificateur nous permet d'écrire une expression pour son bruit intrinsèque

$$S_V^{amp} = \frac{(7.1 \times 10^{-9})^2}{f} + (3.5 \times 10^{-9})^2 + R^2 \left(\frac{(2.7 \times 10^{-12})^2}{f} + (3.3 \times 10^{-13})^2 \right) \quad (\text{C.19})$$

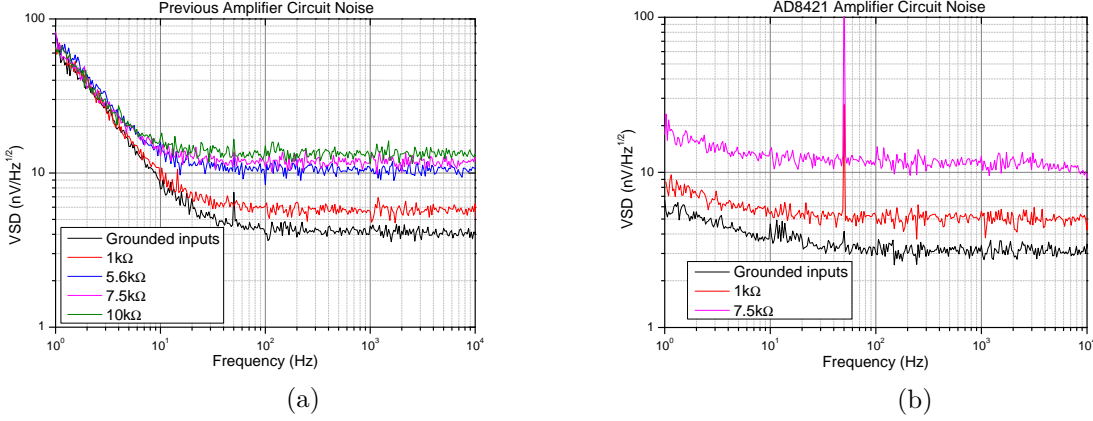


Figure C.15: Mesures de bruit pour différentes valeurs de résistance aux entrées de différents amplificateurs d'instrumentation. a) Préaliminateur basé sur le composant AD743. b) Préaliminateur développé au cours de cette thèse et basé sur le composant AD8421.

où les deux premiers termes sont le bruit en tension, indépendant de la résistance mise à l'entrée, et les deux derniers correspondent au bruit en courant. Nous vérifions aussi que chaque composant du bruit a un terme constant et un terme qui augmente avec la diminution de la fréquence. Ce préamplificateur présente un gain DC de 40 dB et un gain AC de 66 dB, avec un filtre passe-haut à 0.16 Hz pour découpler la composante AC. Le circuit a été conçu avec deux voies indépendantes et une sortie gradiométrique. Une comparaison des valeurs expérimentales et obtenues via une simulation SPICE est présentée en Fig. C.16. La conception d'un tel préamplificateur a été vitale pour la

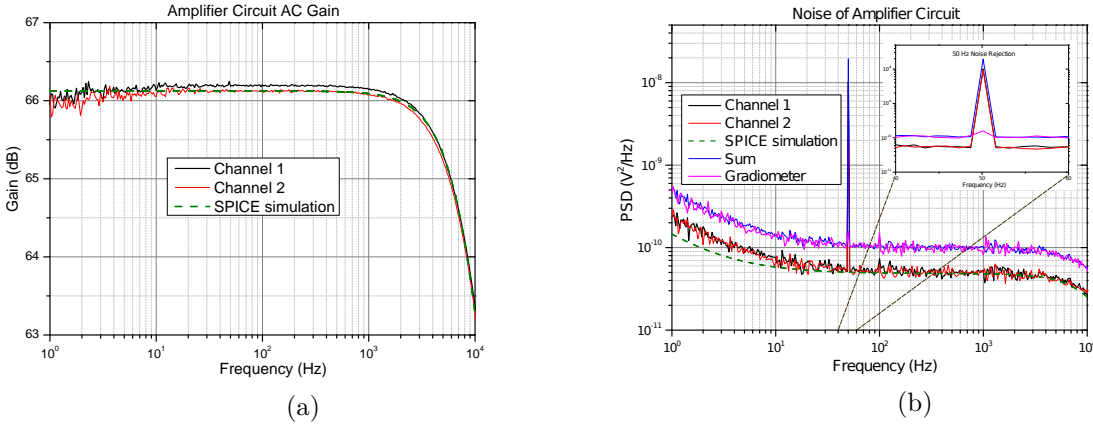


Figure C.16: Caractérisation et simulation SPICE du préamplificateur basé sur AD8421. a) Fonction de transfert avec un gain AC de 66 dB. b) Bruit de chaque voie et sortie gradiométrique, avec une diminution du signal commun à 50 Hz.

caractérisation en bruit des échantillons LSMO, surtout dans la gamme basse fréquence. Le bruit intrinsèque du matériau LSMO peut être modélisé en une composante de bruit thermique selon l'expression de Johnson-Nyquist

$$e_T = 4k_B T R$$

et un bruit excédant à basse fréquence selon l'expression d'Hooge

$$S_V = \frac{\alpha_H}{n} \frac{1}{\Omega f} V_{bias}^2$$

Donc la détectivité, qui est le rapport du bruit total divisé par la sensibilité, s'exprime par :

$$D = \mu_0 H_a \frac{R_0}{\Delta R} \sqrt{\frac{\alpha_H}{n} \frac{1}{4\Omega f} + \frac{4k_B T R_0}{V_{bias}^2}} \quad (C.20)$$

où Eq. (C.16) a été utilisé pour la sensibilité, α_H/n est le paramètre d'Hooge normalisé, Ω le volume d'un bras du pont de Wheatstone LSMO, f la fréquence, k_B la constante de Boltzmann, T la température du dispositif, R_0 la résistance électrique équivalente et V_{bias} la tension de polarisation. L'expression de D est vraie pour un bruit dominé par le LSMO, et servira comme guide pour atteindre des performances encore plus élevées, correspondant à une détectivité plus faible.

C.3 Optimisation de la performance

C.3.1 L'effet de la tension de polarisation et de la température d'opération

Les dépendances de la détectivité vis à vis de la tension de polarisation V_{bias} et de la température d'utilisation T peuvent être facilement vérifiées. L'équation donnant la détectivité montre que lorsque V_{bias} augmente, une performance reste constante à basse fréquences mais s'améliore par contre dans la région du bruit thermique. Les Figs. C.17 and C.18 montrent l'évolution des courbes de V_{meas} , bruit et détectivité pour une structure 45WB et une structure 90WB.

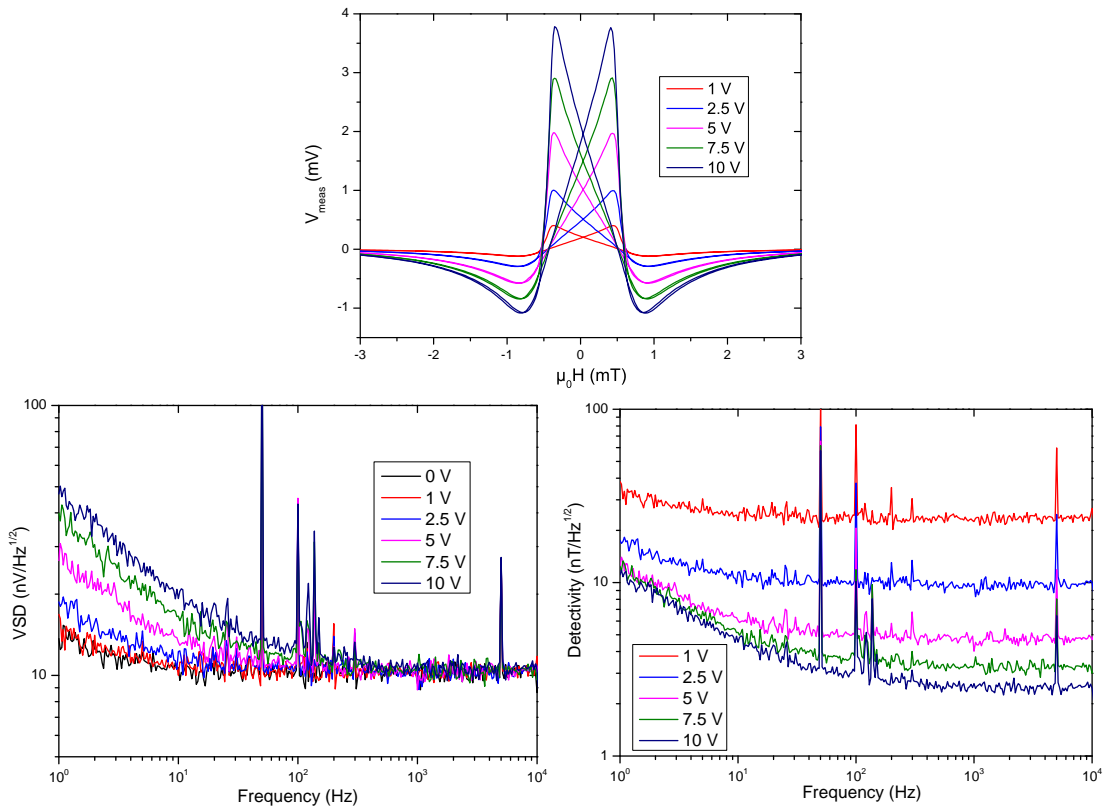


Figure C.17: a) Signal de sortie d'un pont 45WB après recalage des courbes de sorte que le niveau de sortie soit référencé à zéro quand l'aimantation atteint la saturation. b) Bruit mesuré. c) La détectivité résultante. [échantillon BA114]

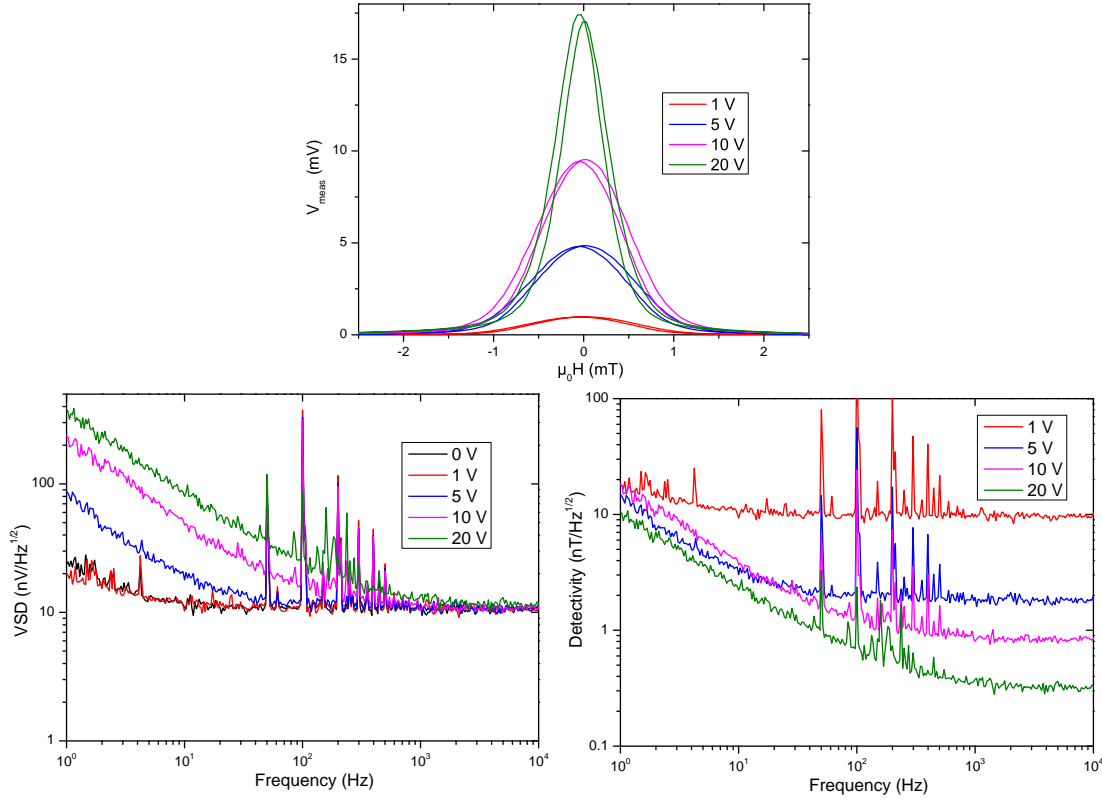


Figure C.18: a) Signal de sortie d'un pont 90WB, après recalage des courbes de sorte que le niveau de sortie soit référencé à zéro quand l'aimantation atteint la saturation. b) Bruit mesuré. c) La détectivité résultante. [échantillon BA055]

Pour les valeurs de V_{bias} plus faibles, le bruit total n'est pas complètement dominé par l'échantillon LSMO. C'est pour cela que ce sont les courbes au dessus de 2.5 V qui suivent le comportement attendu selon l'expression de la détectivité.

Étant donné l'application envisagée du capteur pour le projet ByAxon, la majorité des mesures a été réalisée à la température de 310 K. L'étude de l'effet de la température a été réalisée en chauffant l'échantillon LSMO, en rapprochant le matériau de sa température de Curie T_C . A mesure que la température augmente, la valeur de saturation de l'aimantation M_S diminue. Mais la valeur de la constante d'anisotropie K_u diminue-t-elle aussi, et finalement nous obtenons une dépendance de H_a en M_S^p avec p strictement positif. Donc une diminution de M_S résulte en une diminution du champ d'anisotropie. L'expression Eq. (C.16) montre alors une augmentation de la sensibilité. Des courbes de V_{meas} à une tension de polarisation fixée à 5 V pour différentes températures sont présentées dans la Fig. C.19. L'ajustement avec le modèle permet d'extraire la valeur de H_a pour les températures sélectionnées. Nous pouvons observer visuellement la diminution du champ d'anisotropie par le rétrécissement des courbes. L'échantillon arrive à la saturation avec un valeur de champ appliqué plus faible, jusqu'au point où il perd quasiment la totalité de ses propriétés magnétiques (courbe verte à 330 K). Les valeurs de H_a et sensibilité S sont présentés au Tableau C.1. Des mesures réalisées à IMDEA Nanociencia, un laboratoire

Température d'opération (K)	310	315	320
S de la dérivé de V_{meas} (V/T)	1.67	2.23	3.37
$\mu_0 H_a$ extrait avec le modèle (mT)	1.68	1.26	0.85
S calculé avec Eq. (C.16) (V/T)	1.54	1.97	2.64

Table C.1: Comparaison des valeurs de sensibilité en différentes températures.

partenaire du projet ByAxon, confirment la dépendance du rapport MR et H_a sur la

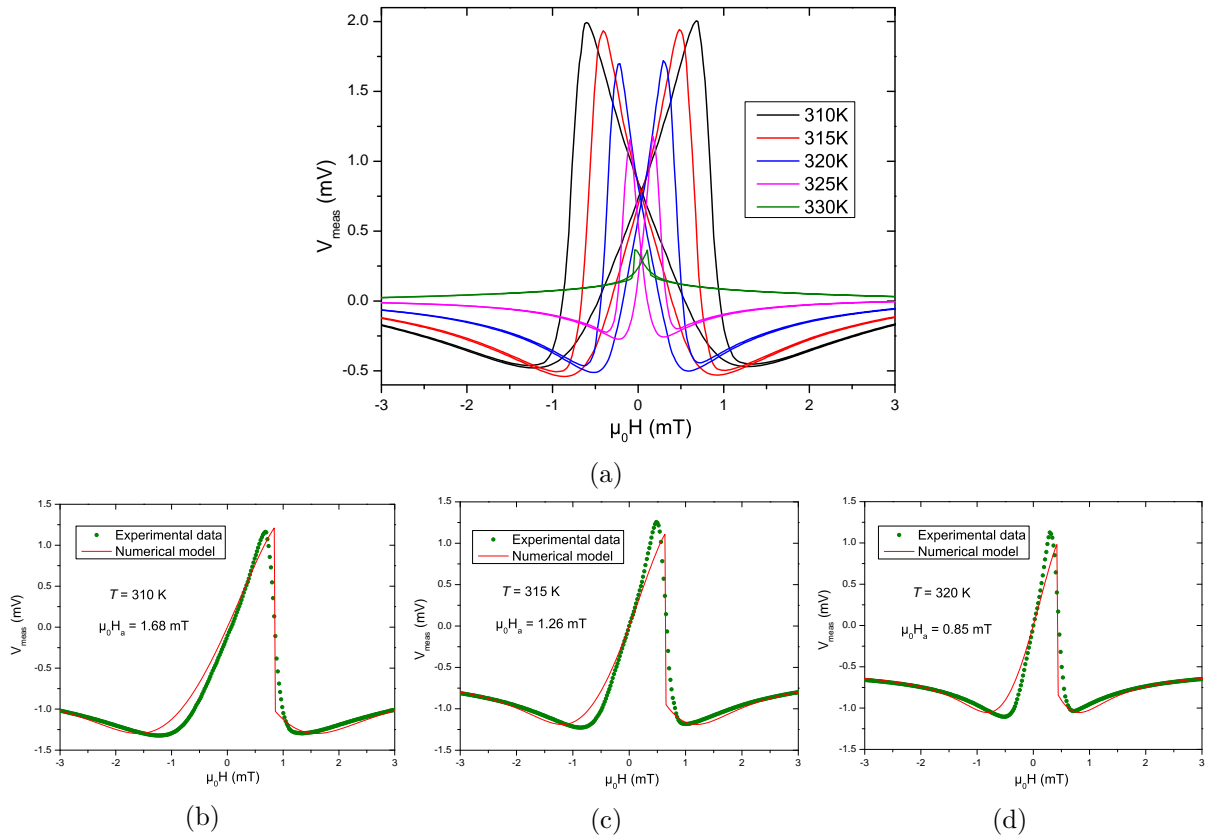


Figure C.19: L'effet de la température d'opération, à une polarisation de 5 V. a) Des courbes de V_{meas} montrent une diminution du H_a . b, c, d) L'application du modèle développé sur les données expérimentales pour extraire des paramètres physiques du dispositif. [échantillon BA104]

température. L'échantillon BA055 montre une sensibilité optimale à 41 °C, même si le rapport MR a diminué (Fig. C.20). Ces mesures montrent que l'effet de la diminution de

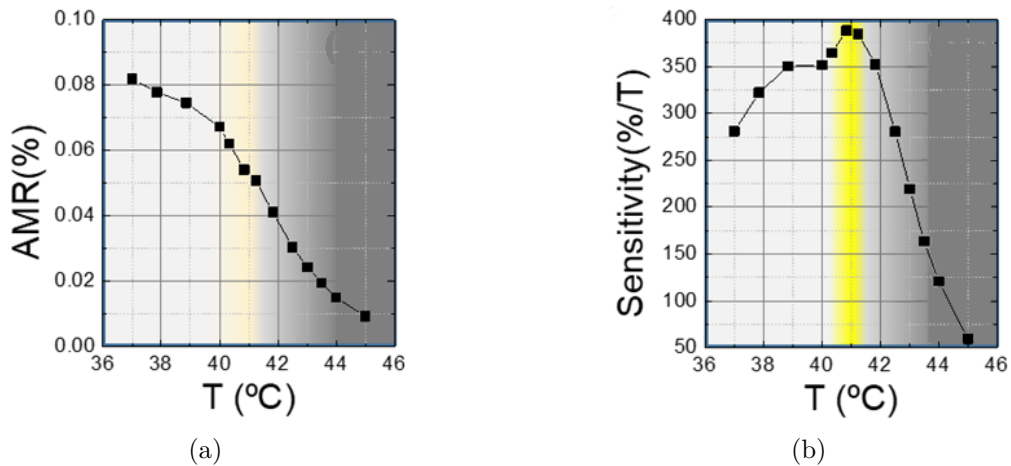


Figure C.20: L'effet de la température mesuré à IMDEA Nanociencia. a) Diminution du rapport MR. b) Température optimale de 41 °C pour la plus haute sensibilité. [échantillon BA055]

H_a est plus fort que celui de la diminution du rapport MR, et la sensibilité augmente.

C.3.2 L'effet de l'épaisseur de la couche mince

Une possibilité d'améliorer la détectivité est de réduire le bruit intrinsèque du dispositif. En augmentant l'épaisseur de la couche mince, nous obtenons un volume plus élevé et une résistance électrique réduite. Une réduction du bruit à basse fréquence et du bruit thermique sont alors attendues. Pour le même substrat STO 4° vicinal, des échantillons de 30 nm à 90 nm d'épaisseur ont été fabriqués. Les courbes de V_{meas} et du bruit pour une structure 90WB sur chaque échantillon sont présentées dans la Fig. C.21, avec une tension de polarisation de 5 V et une température d'opération de 310 K. Nous pouvons observer

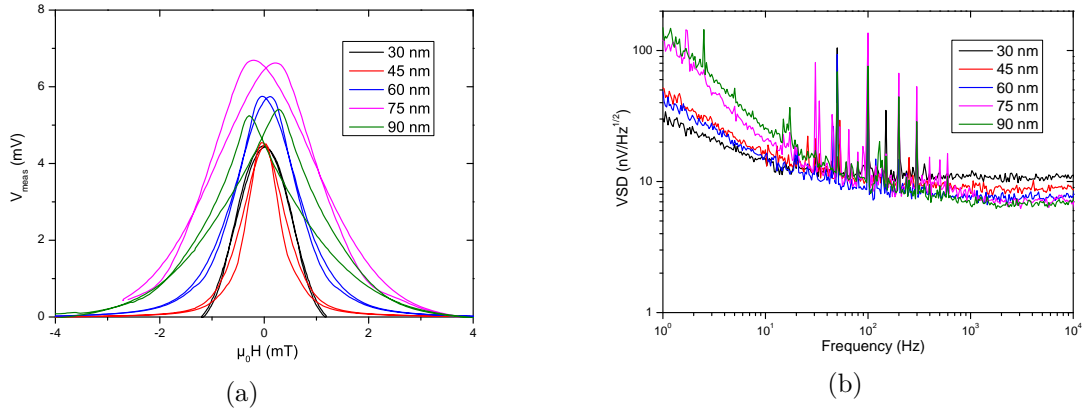


Figure C.21: Caractérisation des structures 90WB pour différentes épaisseurs, à 5 V et 310 K. [échantillons BA055, BA068, BA070, BA072, BA076]

une augmentation du champ d'anisotropie avec l'épaisseur et une augmentation du rapport MR jusqu'à une épaisseur de 60 nm puis une perte de l'anisotropie uniaxiale marquée pour les épaisseurs de 75 nm et 90 nm avec la présence de deux pics pour V_{meas} décalés autour de $\mu_0 H = 0$ mT. Les courbes de bruit montrent une réduction du bruit thermique comme attendu, par contre une augmentation du bruit à basse fréquence. Ces mêmes échantillons ont été envoyés à IMDEA Nanociencia pour une caractérisation magnétique et électrique. Les cycles d'aimantation présentés dans la Fig. C.22 confirment l'augmentation de H_a avec l'épaisseur. Les meilleures performance en bruit à basse fréquence et sensibilité ont

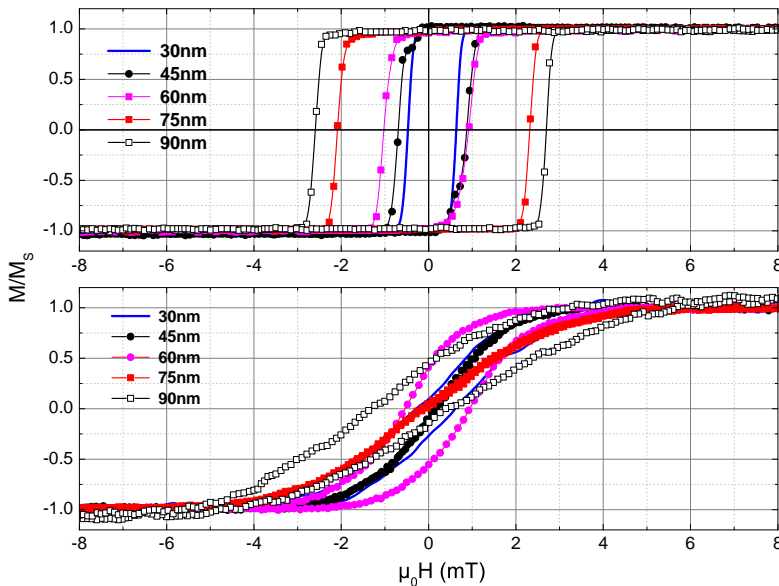


Figure C.22: Cycles d'aimantation selon l'axe facile et l'axe difficile, à température ambiante. [échantillons BA055, BA068, BA070, BA072, BA076]

été atteintes avec les couches les moins épaisses de LSMO.

C.3.3 Angle vicinal du substrat

L'anisotropie uniaxiale étant induite par des marches, nous nous attendons à une anisotropie plus forte quand la distance entre les terrasses du substrat vicinal diminue. Pour étudier l'effet de l'angle vicinal des substrats STO, une série d'échantillons à 30 nm d'épaisseur a été fabriquée sur des substrats à 2°, 4°, 6° et 10° d'angle vicinal. Les courbes à 5 V et 310 K de V_{meas} sont présentées dans Fig. C.23 et le bruit sans polarisation et à 5 V dans Fig. C.24. Nous ne trouvons pas de lien direct du rapport MR et de H_a avec

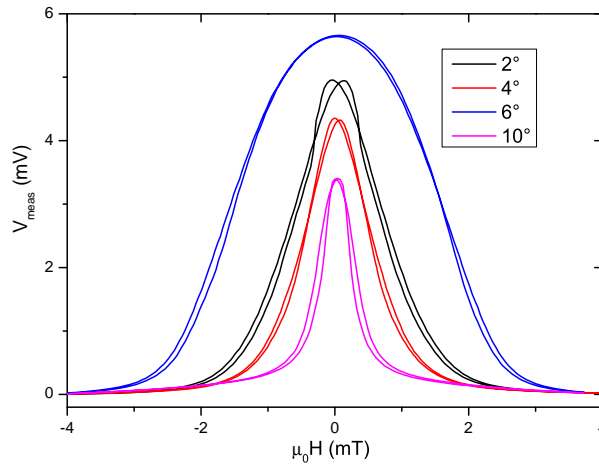


Figure C.23: Courbes V_{meas} pour 30 nm LSMO sur différents angle vicinaux, à 5 V et 310 K. [échantillons BA054, BA098, BA062, BA064]

l'angle vicinal du substrat. C'est l'échantillon à 10° qui présente la plus haute sensibilité, grâce à son champ d'anisotropie réduit. La résistance électrique des échantillons augmente

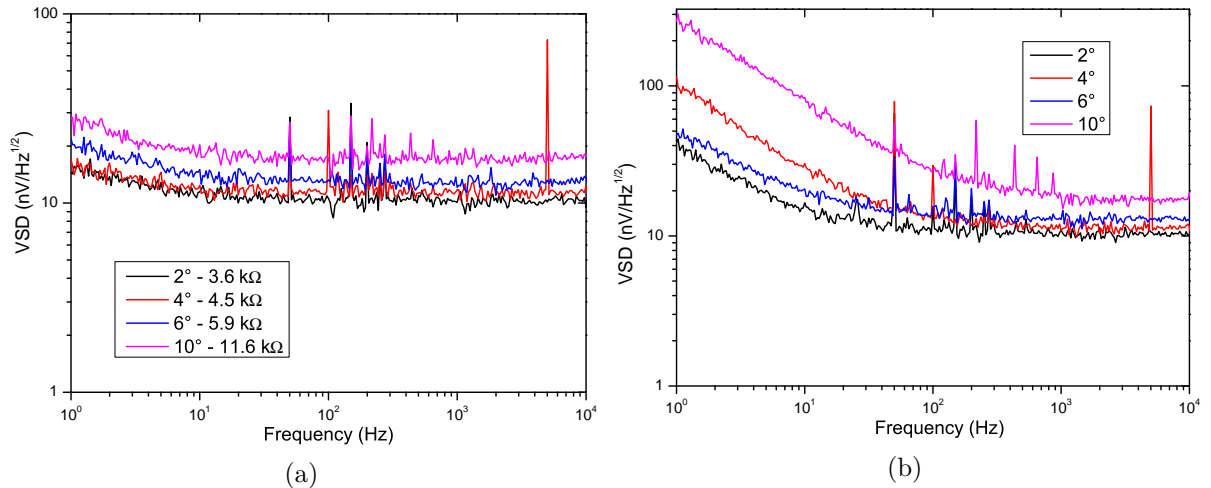


Figure C.24: Bruit électrique à 310 K pour a) polarisation 0 V et b) polarisation 5 V. [échantillons BA054, BA098, BA062, BA064]

avec l'angle vicinal, ce qui conduit à un bruit thermique plus élevé. Avec une polarisation de 5 V, l'échantillon à 10° vicinal présente un bruit à basse fréquence bien au dessus des autres échantillons. C'est alors échantillon à 2° vicinal qui atteint les valeurs les plus basses de détectivité en dessous de 100 Hz. Une vérification de la morphologie de ces échantillons a été réalisé avec un microscope à effet tunnel. L'échantillon à 10° vicinal présente une zone à la surface du LSMO qui devient amorphe. Pour cet échantillon, l'épaisseur effective est seulement 22 nm, ce qui explique parfaitement la résistance électrique élevée.

C.3.4 L'échantillon optimisé

Après les vérifications des effets des paramètres de fabrication sur les performances des dispositifs AMR LSMO, les meilleures performances, présentées sur Fig. C.25, ont été atteintes avec une couche de 45 nm sur un substrat 4° vicinal. L'utilisation d'un substrat à bas angle vicinal conduit à un champ d'anisotropie réduit, sans affecter la structure cristalline du LSMO. Une épaisseur petite assure un comportement magnétique uniaxial. Avec cet échantillon, des valeurs de détectivité de $1.4 \text{ nT Hz}^{-1/2}$ à 1 Hz et $240 \text{ pT Hz}^{-1/2}$

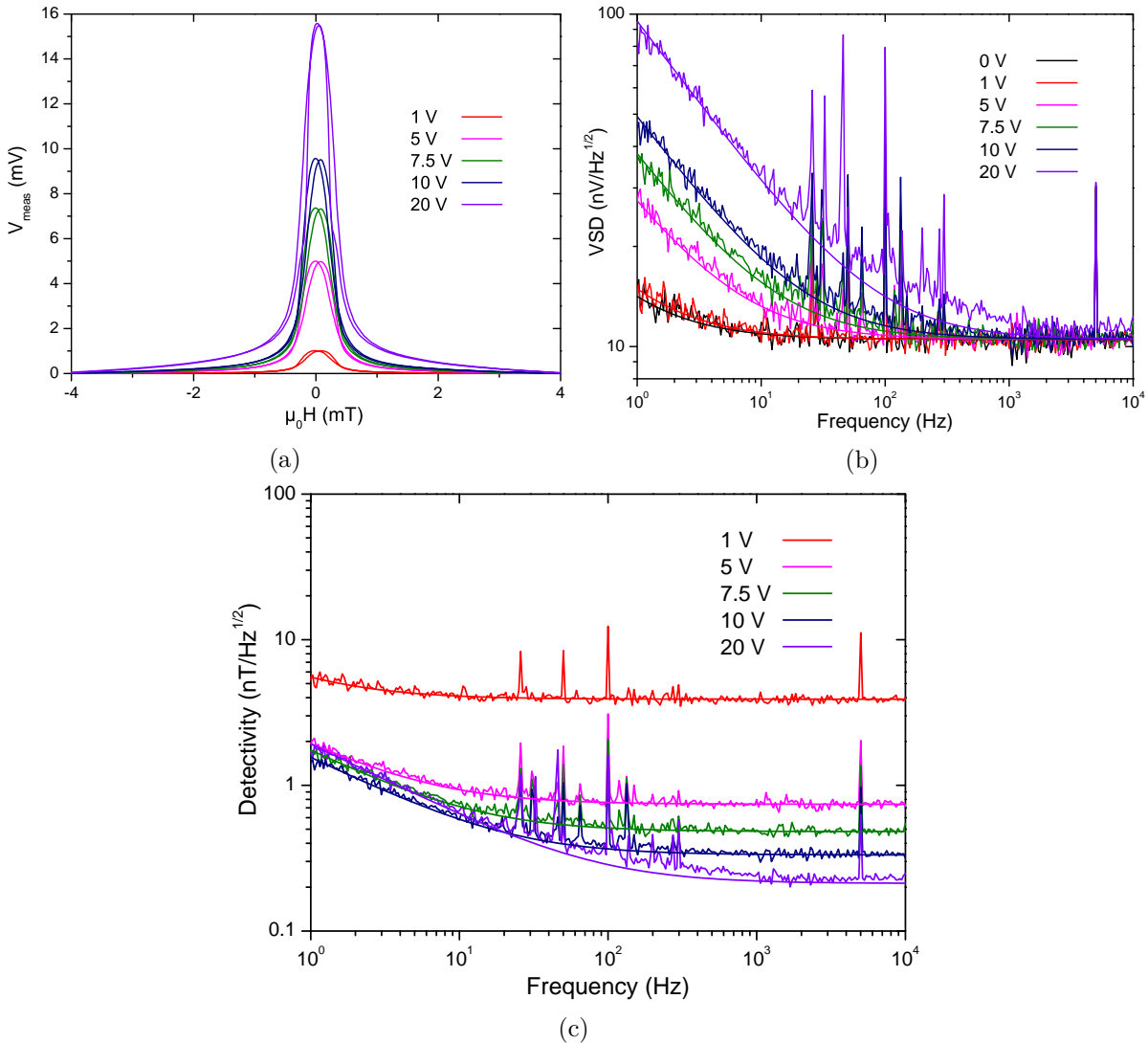


Figure C.25: Caractérisation d'une structure 90WB. a) Courbes de V_{meas} pour obtenir la sensibilité. b) Bruit électrique mesuré et bruit calculé selon les valeurs du paramètre d'Hooge, volume, résistance équivalente. c) Détectivité résultante. [échantillon BA114]

à 1 kHz ont été atteintes 310 K avec un pont de Wheatstone en structure 90WB.

C.3.5 Masques pour lithographie laser

Grâce à l'équipement de lithographie laser, des géométries alternatives pour le dispositif ont été testées. Les motifs des contacts métalliques ont été choisis pour obtenir une distribution plus homogène de la densité de courant. Les ponts de Wheatstone ont été modifiés pour étudier l'effet de forme et l'énergie démagnétisante. Les figures C.26 et C.27 montrent les performances pour trois différents contacts métalliques. C'est le motif dit

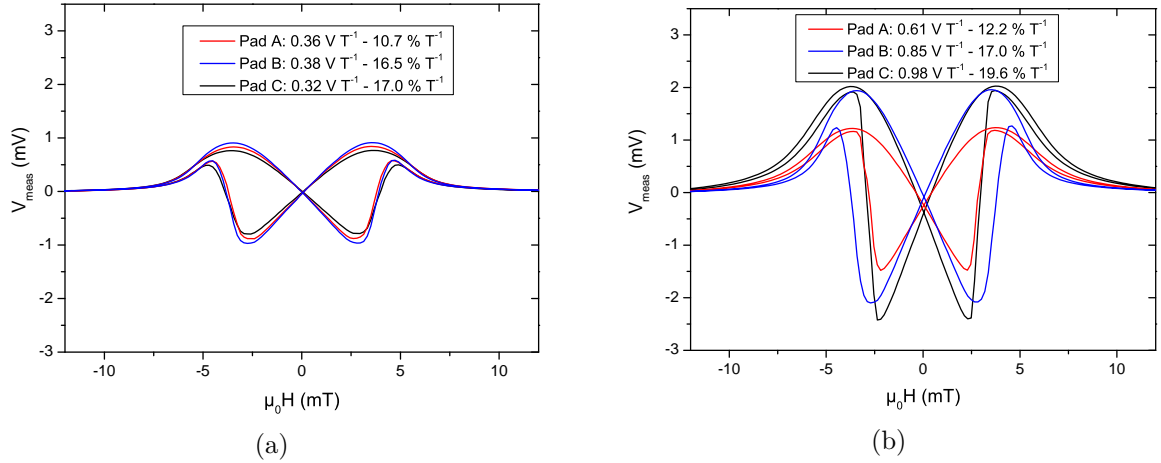


Figure C.26: Courbes V_{meas} obtenues avec une structure 45WB à 310 K. a) Polarisation de 1 mA. b) Polarisation de 5 V. [échantillon BA147]

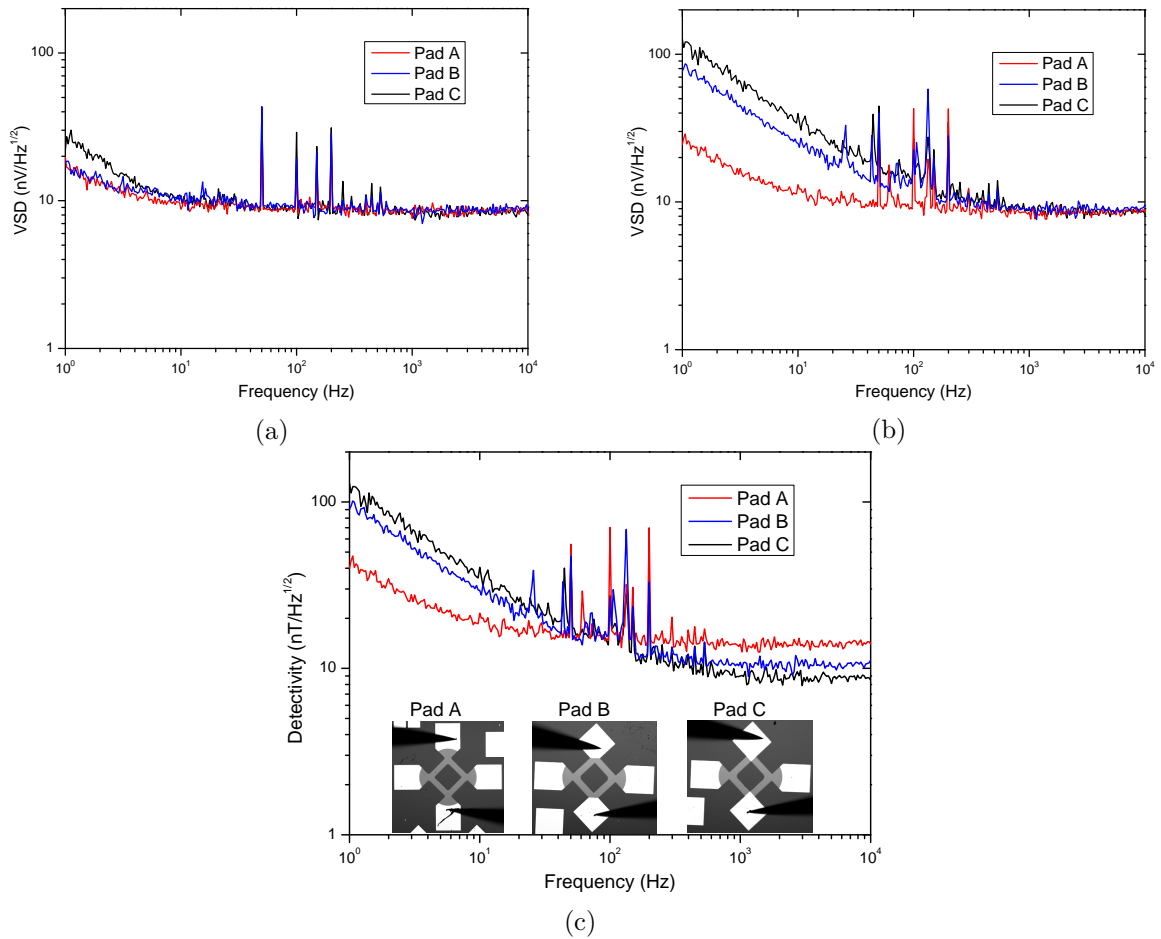


Figure C.27: Bruit et détectivité pour différentes contacts métalliques. a) Bruit pour une polarisation à 0 V. b) Bruit pour une polarisation à 5 V. c) Détectivité à polarisation 5 V. [échantillon BA147]

Pad A qui présente la valeur la plus basse de détectivité en dessous de 10 Hz, même si les autres motifs atteignent des valeurs de sensibilité plus élevées.

Les figures C.28 et C.29 montrent les performances pour trois différents motifs de couche mince LSMO gravée en pont de Wheatstone. La différence pour les courbes de V_{meas} montrent qu'il y a un effet de forme sur l'énergie magnétique, cependant celle-ci reste dominée par l'anisotropie induite par des marches du substrat. La raison du bruit très

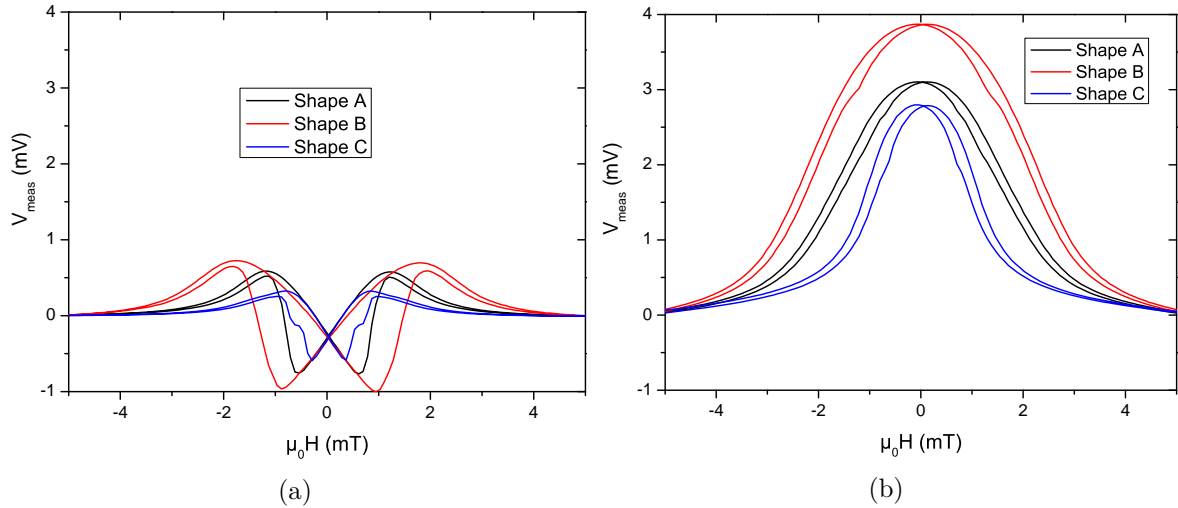


Figure C.28: Courbes V_{meas} pour trois différents motifs de pont de Wheatstone, à 5 V et 310 K. a) Structure 45WB. b) Structure 90WB. [échantillon BA144]

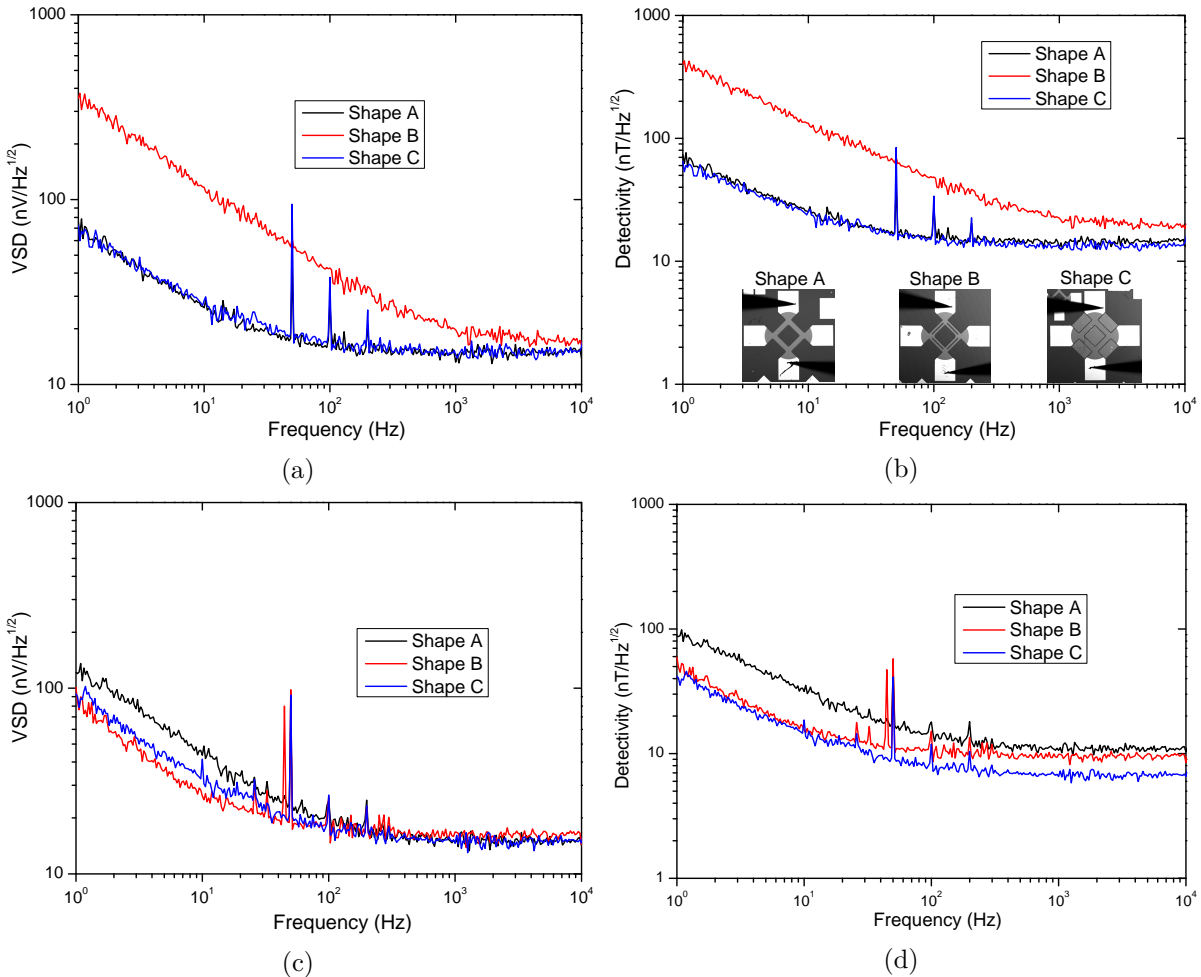


Figure C.29: Bruit et détectivité à 5 V et 310 K. a, b) Structure 45WB. c, d) Structure 90WB. [Sample BA144]

élevé pour le motif dit Shape B de la structure 45WB reste inconnue. Le motif dit Shape C semble intéressant pour une éventuelle étude plus approfondie, vu sa sensibilité supérieure à celle des Shape A et Shape B grâce à un champ d'anisotropie réduit.

C.4 Applications dans des environnements réels

Pour une caractérisation et une utilisation endehors de la station sous pointes, des échantillons LSMO ont été connectés sur des cartes de circuit imprimé (PCB) par wire bonding, en utilisant des fils d'aluminium de 50 μm de diamètre. Pour polariser les dispositifs et mesurer les signaux de sortie, des fils en cuivre ont été soudés aux PCBs. Ce montage est présenté dans la Fig. C.30. Afin de protéger le LSMO de l'environnement

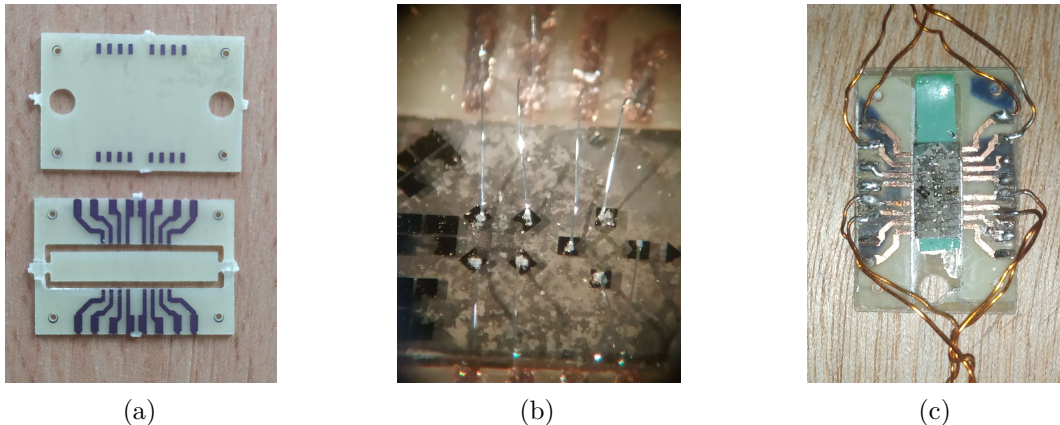


Figure C.30: a) PCB et support pour l'échantillon en époxy. b) Connexion métallique aux ponts de Wheatstone via wire bonding. c) Soudure des fils en cuivre pour polariser les dispositifs et réaliser les mesures.

et en prenant en compte l'application envisagé dans le projet ByAxon, des échantillons sélectionnés ont été recouverts de polydiméthylsiloxane (PDMS), un polymère biocompatible. La Fig. C.31 montre une structure fabriquée en imprimante 3D utilisée comme moule pour recouvrir l'échantillon ainsi que le résultat obtenu. La caractérisation électrique de

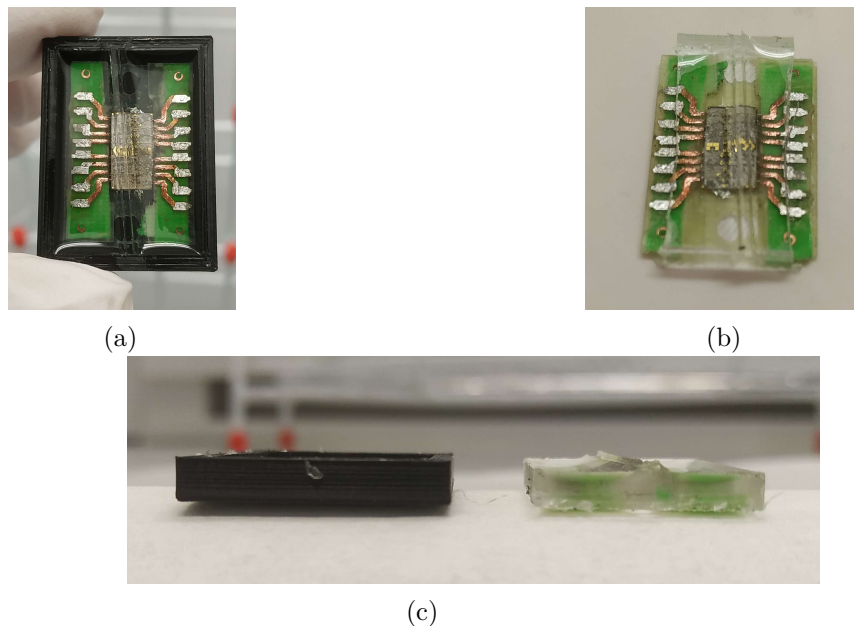


Figure C.31: a) Une surface lisse est obtenue avec un long temps d'endurissement à température ambiante. b) Le polymère peut être coupé pour accéder aux pistes en cuivre du PCB. c) Les fils d'aluminium sont complètement couverts, l'épaisseur totale est de 3 mm.

l'échantillon avant et après le revêtement montrent que les performances du dispositif ne sont pas affectées par le PDMS.

C.4.1 Configuration gradiométrique

Une technique pour réduire l'influence des parasites de l'environnement lors de la mesure et mieux détecter le signal ciblé est d'utiliser une configuration dite gradiométrique. Un capteur est placé près de la source du signal d'intérêt tandis qu'un deuxième capteur est plus éloigné de cette source et détecte ainsi seulement le champ magnétique ambiant, de l'environnement. La sortie gradiométrique est la différence entre les signaux de chaque capteur. Le champ magnétique ambiant étant mesuré par les deux capteurs, la différence ne conserve que le signal d'intérêt. Un échantillon LSMO a été placé à l'intérieur d'une paire de bobines de Helmholtz, et un fil en cuivre a été positionné par dessus l'échantillon. Les bobines et le fil ont été alimentés par des signaux à fréquence différentes. Alors que les deux ponts de Wheatstone de l'échantillon seront soumis au même du champ homogène créé par les bobines, le champ dû au fil métallique généré au niveau d'un capteur sera plus élevé sur l'autre. De cette façon, la détection des champs magnétiques non-homogènes peut être validée. En raison de l'existence d'une différence de sensibilité entre ponts de Wheatstone, il est nécessaire de régler individuellement la tension de polarisation pour chaque capteur, afin d'obtenir le même niveau de tension de sortie pour le champ magnétique généré par les bobines. La Fig. C.32 montre les résultats de mesures en utilisant deux ponts 45WB sur le même échantillon. Les bobines génèrent un champ à 16 Hz et le fil en cuivre génère un champ à 183 Hz. Le pont qualifié 'WB1' a été polarisé avec 2.7 V et le pont 'WB3'

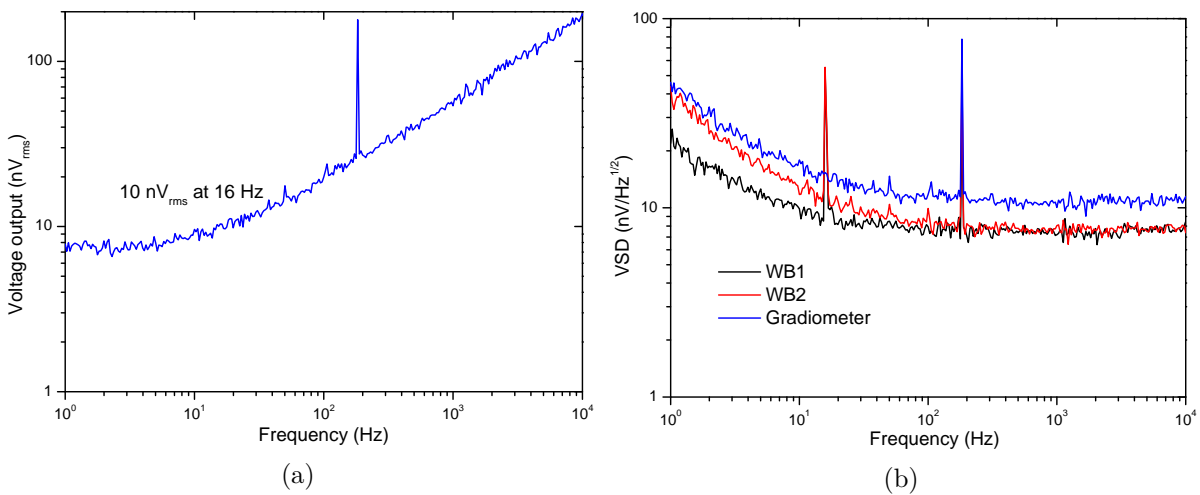


Figure C.32: En bleu, la sortie gradiométrique après réglage des tensions de polarisation de chaque pont. a) Seulement le pic à 183 Hz est observé sur la sortie du gradiomètre. b) Niveau de bruit en tension mesuré au niveau de chaque pont et de la sortie du gradiomètre.

avec 5 V. Cette configuration peut être réalisée en utilisant des ponts 90WB, cependant un champ magnétique DC de polarisation est nécessaire pour placer les capteurs dans leur zone de fonctionnement. Ce qui augmente la complexité de la mesure, vu que chaque pont peut avoir besoin d'une polarisation en champ différente. La Fig. C.33 présente les signaux de sortie dans le domaine temporel pour deux ponts 90WB individuels et la sortie en gradiomètre, ainsi que le signal fourni aux bobines. Le pont WB2 a été polarisé à 1.7 V et le pont WB2 à 5 V. Nous pouvons vérifier que les tensions délivrés par chaque capteur comprend une composante à 16Hz créé par les bobines et une composante à 183Hz produite par le fil placé plus près de WB2 tandis que le signal de la sortie en gradiomètre est dominé par la seule composante à 183 Hz. La configuration en gradiomètre a été validée en utilisant un capteur 90WB et un capteur référence 45WB. La polarisation en champ du pont 90WB a été réalisée avec un aimant permanent. La polarisation correcte de chaque capteur a par ailleurs permis la réduction du signal parasite à 50 Hz de l'alimentation électrique.

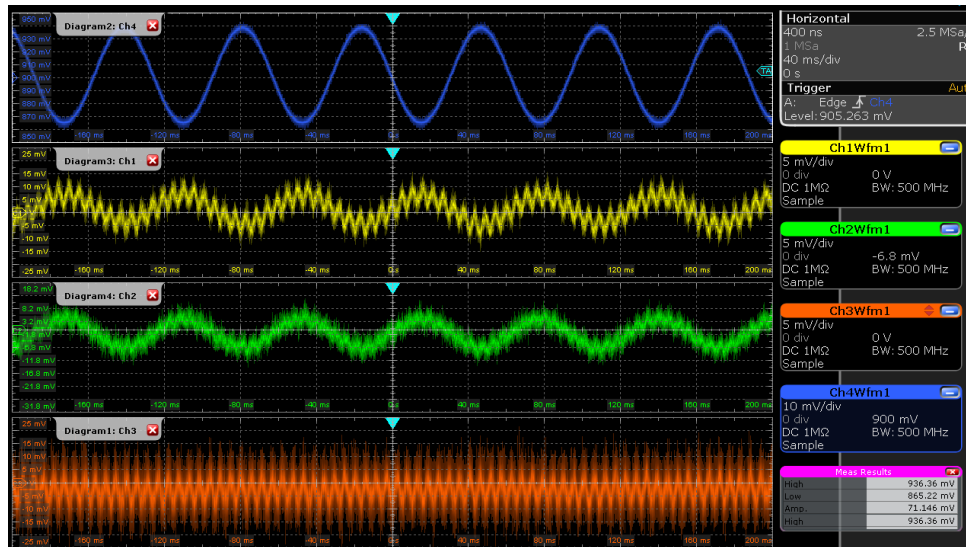


Figure C.33: En bleu, le signal fourni aux bobines. En jaune et en vert, les signaux de sortie des ponts 90WB dits WB2 et WB4, respectivement. La sortie gradiomètre en orange,





C.5 Conclusions

Cette thèse détaille le principe de fonctionnement, le processus de fabrication et l'optimisation des capteurs magnétorésistifs basés sur des couches minces de l'oxyde de manganèse LSMO. Les bases théoriques pour le fonctionnement du dispositif avec deux géométries différentes ont été présentées, et leurs modes d'opération ont été validés par caractérisations magnétique et électrique. Un modèle numérique associé à la physique du capteur a été créé afin d'extraire des mesures expérimentales des paramètres physique du dispositif comme le champ d'anisotropie H_a . Un circuit de pré-amplification à très bas niveau de bruit et adapté à la résistance électrique des échantillons a été conçu. A partir de l'expression théorique de la détectivité du capteur et de la caractérisation d'un grand nombre d'échantillons différents en vue d'améliorer les performances du capteur, l'échantillon le plus performant obtenu atteint une détectivité de $1.4 \text{ nT Hz}^{-1/2}$ à 1 Hz et $240 \text{ pT Hz}^{-1/2}$ à 1 kHz, à une température de 310 K. Ces valeurs sont celles accessibles avec un simple pont de Wheatstone, fabriqué avec une seule couche mince déposée sur un substrat vicinal. Le capteur commercial comme HMC1001 présente une détectivité se situant un ordre de grandeur en dessous, mais il consomme six fois plus de puissance et ce dispositif encapsulé occupe une superficie 18 fois plus grande que le pont de Wheatstone LSMO présenté dans ce manuscrit de thèse. Nous pouvons envisager des développements ultérieurs pour les performances des capteurs AMR LSMO, notamment l'addition des concentrateurs de flux magnétique. Un gain d'un ordre de grandeur est complètement réaliste. Pour conclure, ce travail de thèse présente une application et une réalisation réelle d'un dispositif spintronique performant, à base d'oxyde fonctionnel et constitue une contribution nouvelle et originale au développement des technologies spintroniques.

Appendix D

Sub-nT resolution of Single Layer Sensor Based on the AMR Effect in $\text{La}_{2/3}\text{Sr}_{1/3}\text{MnO}_3$ Thin Films

DOI: 10.1109/TMAG.2021.3089373

Luiz Guilherme Enger¹, Stéphane Flament¹, Imtiaz-Noor Bhatti¹, Bruno Guillet¹, Marc Lam Chok Sing¹, Victor Pierron¹, Sylvain Lebargy¹, Jose Manuel Diez², Arturo Vera², Isidoro Martinez², Ruben Guerrero¹, Lucas Perez^{2,3}, Paolo Perna², Julio Camarero², Rodolfo Miranda², Maria Teresa Gonzalez² and Laurence Méchin¹

¹Normandie Univ, UNICAEN, ENSICAEN, CNRS, GREYC, 14000 Caen, France

²IMDEA Nanociencia, Campus de Cantoblanco, 28049 Madrid, Spain

³Dept. Física de Materiales - Universidad Complutense de Madrid, Av. Complutense s/n 28040 Madrid, Spain

Abstract

Single layer magnetoresistive sensors were designed in a Wheatstone bridge configuration using $\text{La}_{2/3}\text{Sr}_{1/3}\text{MnO}_3$ ferromagnetic oxide thin film. Uniaxial anisotropy was induced by performing epitaxial deposition of the films on top of vicinal SrTiO_3 substrate. X-ray scan confirms high crystalline quality of the films and the magnetic anisotropy was checked by Magneto-optical Kerr Effect measurements. Thanks to the anisotropic magnetoresistive effect and the very low noise measured in the devices, sub-nT resolution was achieved above 100 Hz at 310 K.

D.1 Introduction

Due to low cost, small size and increased performance of magnetoresistive sensors, they can be used in a wide range of applications such as biomedical, flexible electronics, position sensing, human-computer interaction, non-destructive evaluation and monitoring, navigation and transportation [1]. While giant magnetoresistance (GMR) [2] and tunneling magnetoresistance (TMR) [3] devices present electrical resistance variations due to the relative magnetization directions between two separate layers of ferromagnetic material, anisotropic magnetoresistance (AMR) devices have a resistance variation as function of the angle between magnetization and current density directions in the

same layer. GMR and TMR thus required the stacking of different material layers, with a high precision on thickness and composition. Variations at buffer layer level provoke changes in sensor performance [4, 5, 6, 7]. In the present work we fabricated AMR sensors made of a single layer of semi-metallic $\text{La}_{2/3}\text{Sr}_{1/3}\text{MnO}_3$ (LSMO) thin film, an oxide that is ferromagnetic up to 350 K [8] and presents a very low intrinsic noise in low frequencies [9]. Thin films were etched in Wheatstone bridge configuration, forming a device known in literature as Planar Hall Effect Bridge (PHEB) [10, 11, 12]. Usual PHEB sensors based on permalloy use either exchange bias or shape anisotropy to induce a magnetic easy axis. In this paper, such axis is obtained by step-induced magnetic uniaxial anisotropy [13]. To study the viability for biomedical applications of our sensors, samples were kept at 310 K temperature for magnetotransport and noise characterization. A dedicated low noise amplifier was used to qualify the resolution of the sensors which is in the sub-nT range.

D.2 Film and samples characteristics

A Pulsed Laser Deposition system from TSST company was used to grow epitaxial LSMO thin films on top of vicinal SrTiO_3 (STO) substrate. After thin film deposition, LSMO was covered with gold for electrical contact, followed by standard UV lithography. Gold pads

for electrical contact were defined with KI wet etching, and LSMO structure was obtained with Ion Beam Etching. Two Wheatstone bridge geometries were etched over each sample, as shown in Fig. D.1. Wheatstone bridges with arms either parallel or perpendicular to sample easy axis are named 90WB sensor while Wheatstone bridges with arms at 45° to easy axis are named 45WB. In both geometries, each arm is $300 \mu\text{m}$ long and $100 \mu\text{m}$ large.

The vicinal substrates present a surface mis-cut angle regarding the crystallographic plane, forming steps in the crystalline structure. This results in an easy magnetic axis parallel to step edges and enhances AMR effect [14]. In this paper we focus on results obtained with 4° vicinal angle STO substrate and LSMO film thicknesses of 30 nm and 60 nm . The rate of film growth was calibrated following the Reflective High-Energy Electron Diffraction signal using a flat STO substrate. The exact thickness after deposition on vicinal STO was not measured. During film deposition, the laser power was kept at $1.7 \text{ J}\cdot\text{cm}^{-2}$, the fire rate fixed at 3 Hz and the substrate temperature was kept at $730 \text{ }^\circ\text{C}$. Structural analysis of LSMO over 4° vicinal STO was performed with θ - 2θ X-ray diffraction (XRD) technique, as shown in Fig. D.2(a). Peak signals for STO and LSMO were obtained at an offset ω angle of 4.74° . Deviation around the expected 4° angle are within accepted values due to substrate fabrication process and alignment in XRD sample holder. Rocking curve for LSMO with a Full Width at Half Maximum of 0.17° indicates high crystalline quality.

Uniaxial magnetic anisotropy in the etched PHEBs was verified with magnetization loops obtained using a lab-made longitudinal Magneto Optical Kerr Effect (MOKE) imaging setup. Local magnetization was deduced by averaging the MOKE intensity over the arms of the Wheatstone bridge [15]. As exhibited in Fig. D.2(b), a hysteretic behavior typical of easy axis occurs when magnetic field is parallel to step edges while a linear dependence is observed when sample is rotated by 90° , indicating a hard axis magnetization along a direction perpendicular to step edges.

D.3 AMR curves and Detectivity of sensors

For MR and noise characterization, samples were loaded into a chamber with independent temperature and magnetic field control and equipped with four probes for electrical contact. MR curves were obtained with an amplitude sweep for magnetic field applied along hard axis,

from one saturation state to the other and back. Noise measurements were carried out in environmental magnetic field, we did not make use of any magnetic shielded room. Taking advantage of the fact that a balanced Wheatstone bridge reject common-mode signals and noise, a commercial DC voltage source could be used to bias the samples. For signal amplification, we built a low-noise amplifier based on commercially available AD8421. Noise characteristics of this amplifier ensure that it is lower than the noise source of the Wheatstone bridge sensor, with a measured $3.6 \text{ nV}\cdot\text{Hz}^{-1/2}$ broadband voltage noise and a negligible current noise in the resistance range of our samples: $6.1 \text{ k}\Omega$ resistance for the 30 nm thick Wheatstone bridge and $2.5 \text{ k}\Omega$ for the 60 nm sample. Figure D.3 presents the measured noise of the 60 nm thick sample compared to the amplifier voltage noise, obtained at grounded inputs. Curve at 0 V bias includes the contribution from the amplifier voltage and current noises and from the sample thermal noise. As can be seen in the noise curve at 20 V bias, contribution from sample itself dominates the total noise. Both MR and noise were measured for different voltage bias. Magnetoresistance curves for each geometry and for both samples are presented in Fig. D.4. Both geometries present the expected MR curve for PHEB sensors. 45WB presents a linear response and a best sensitivity around zero applied field [10] while 90WB requires a DC magnetic bias to operate in a linear mode and at best sensitivity [16], around half of the maximum of the voltage output. The sensitivity S is deduced from MR measurements in the linear operating mode of the sensors by

$$S = \frac{\partial V_{out}}{\partial \mu_0 H} \quad (\text{C.1})$$

It increases with higher MR ratio and lower anisotropy field [11]. The detectivity at a given bias, which is expressed in $\text{T}\cdot\text{Hz}^{-1/2}$, is given by

$$D = \frac{\text{Noise}}{\text{Sensitivity}} \quad (\text{C.2})$$

and calculated using experimental noise and sensitivity data. Better sensor performance means lower detectivity, therefore lower noise, higher MR ratio and lower anisotropy field. We observed that the thicker sample presents a higher MR ratio, while 30 nm sample has lower anisotropy field. It was reported that film thickness does affect step-induced magnetic anisotropy [13] but a complete theory for the magnetotransport in LSMO thin films at low field is not fully developed. Obtained sensitivity values are $58 \text{ \%}\cdot\text{T}^{-1}$ ($122 \text{ \%}\cdot\text{T}^{-1}$) for

45WB (90WB) structure in 60 nm sample, and $82 \text{ \%} \cdot \text{T}^{-1}$ ($125 \text{ \%} \cdot \text{T}^{-1}$) for 45WB (90WB) design with 30 nm LSMO. While the value of V_{meas} derivative was obtained at zero applied field for 45WB structure, in 90WB bridges an absolute value for bias field of 0.4 mT and 0.2 mT was considered for 60 nm and 30 nm samples, respectively. Ultimately, the thinner sample presents higher sensitivity value and thicker sample yielded a lower noise overall since its resistance is lower. Following (C.2), we plotted detectivity curves for both samples and both geometries, as shown in Fig. D.5. Due to lower MR ratio presented in 45WB geometry, we had to increase the voltage bias of the bridge. In the four cases, we are able to reach sub-nT detectivities above 100 Hz. Even though 30 nm thick sample has higher sensitivity, a better performance is achieved with 60 nm thick sample thanks to lower intrinsic noise. In the low frequency noise domain, a squared dependence of low-frequency noise on bridge voltage bias was obtained. This indicates that our sensor dominates the noise signal and presents a $1/f$ noise that can be modeled after Hooge's empirical equation [17] :

$$S_V = \frac{\alpha_H}{n} \frac{1}{f\Omega} V_{bias}^2 \quad (\text{C.3})$$

where S_V is the spectral noise density expressed in $\text{V}^2 \cdot \text{Hz}^{-1}$, Ω is the volume of the Wheatstone bridge and n is the charge carrier density. In Fig. D.6 we plot $S_V \times f$ for different voltage bias. A linear fit with a fixed slope of 2 shows that the squared dependence is verified. The S_V/V^2 versus f slope can be used as a comparison parameter between sensors. The lower this value, the better. For the 60 nm

thick sample, it is calculated equal to $4.3 \cdot 10^{-17}$. This value is a few orders of magnitude smaller than the one obtained in magnetic tunnel junctions and TMR sensors [18, 19], which explains why the Wheatstone bridge sensors presented in this paper achieve a good detectivity in the low frequency region albeit much lower sensitivity values than TMR sensors.

D.4 Conclusion

By employing vicinal STO substrates and performing epitaxial LSMO deposition, we fabricated single layer AMR sensors based on oxides and without relying on exchange bias interaction or shape anisotropy. θ - 2θ XRD scan and LSMO rocking curve shows a high crystalline quality for the ferromagnetic oxide and an epitaxial growth along the slightly tilted axis of the vicinal substrates. Magnetization curves obtained on etched sample confirms uniaxial magnetic anisotropy, and outputs of the two presented Wheatstone bridge geometries are as expected, with the 45WB geometry being linear around zero field and the 90WB geometry needing a DC bias magnetic field. Noise measurements were carried out with a dedicated lab-made low-noise amplifier. Experimental data show that sub-nanotesla detectivity values is reached above 100 Hz at 310 K for both geometries. Despite its slightly poorer detectivity, the 45WB is preferable since it operates at zero field with a linear range adapted to its detectivity. The performance of the sensors may be improved with the addition of flux concentrators [20], by the use of modulation techniques [21] and with further studies on how tuning fabrication for a better detectivity.

2

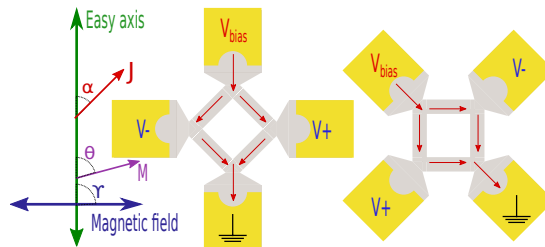
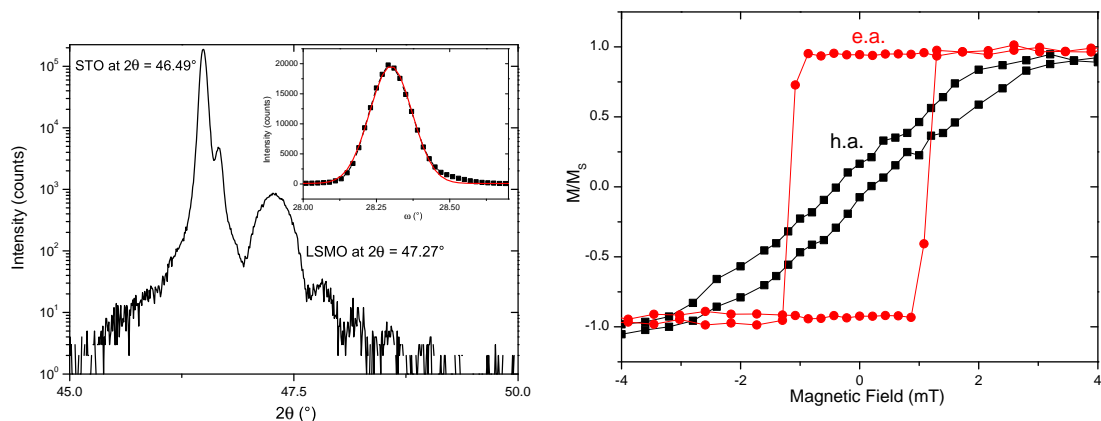


Figure D.1: Easy axis, current density J , magnetization M , applied magnetic field directions and PHEBs designs. 45WB (left) and 90WB (right) geometries.

Bibliography

- [1] C. Zheng, K. Zhu, S. Cardoso de Freitas, J. Chang, J. E. Davies, P. Eames, P. P. Freitas, O. Kazakova, C. Kim, C. Leung, S. Liou, A. Ognev, S. N. Piramanayagam, P. Ripka, A. Samardak, K.



(a) 2θ XRD scan of 30 nm LSMO on 4° vicinal STO. Inset is LSMO rocking curve with gaussian fit. (b) Magnetization loops at room temperature of 60 nm thick LSMO thin film. Easy axis (e.a.) and hard axis (h.a.) along directions parallel and perpendicular to step edges, respectively.

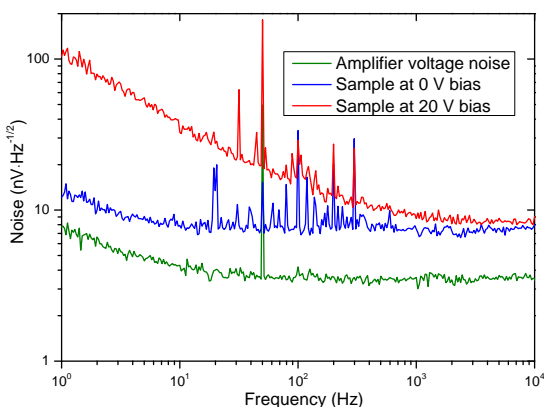


Figure D.3: Noise from 60 nm 45WB sample at 310 K and amplifier at room temperature.

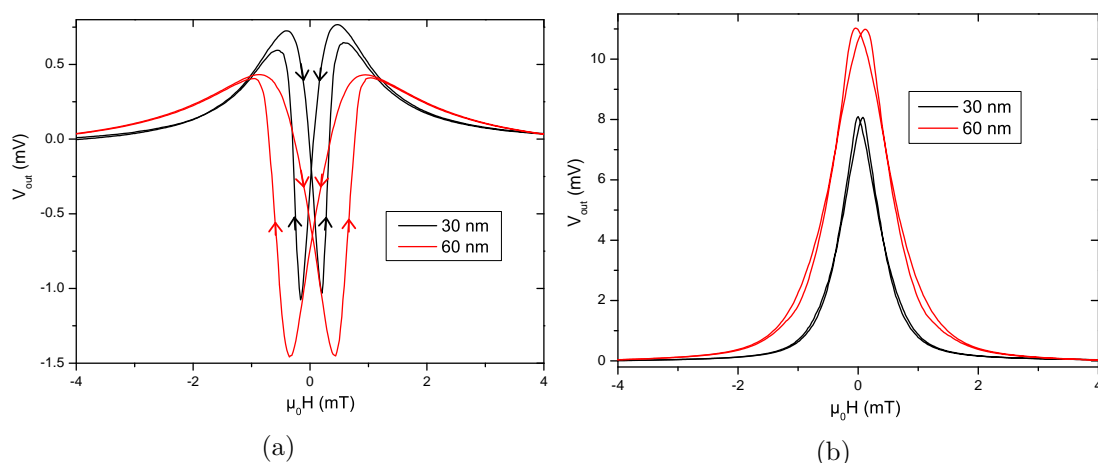


Figure D.4: AMR curves at 310 K sample temperature and 10 V bridge bias. (a) 45WB bridge design. (b) 90WB design.

Shin, S. Tong, M. Tung, S. X. Wang, S. Xue, X. Yin, and P. W. T. Pong. “Magnetoresistive Sensor Development Roadmap (Non-Recording Applications)”. In: *IEEE Transactions on Magnetics* 55.4 (2019), pp. 1–30. DOI: 10.1109/TMAG.2019.2896036.

- [2] M. N. Baibich, J. M. Broto, A. Fert, F. Nguyen Van Dau, F. Petroff, P. Etienne, G. Creuzet, A. Friederich, and J. Chazelas. “Giant Magnetoresistance of (001)Fe/(001)Cr Magnetic Superlattices”. In: *Phys. Rev. Lett.* 61 (21 Nov. 1988), pp. 2472–2475. DOI: 10.1103/PhysRevLett.61.2472. URL: <https://link.aps.org/doi/10.1103/PhysRevLett.61.2472>.

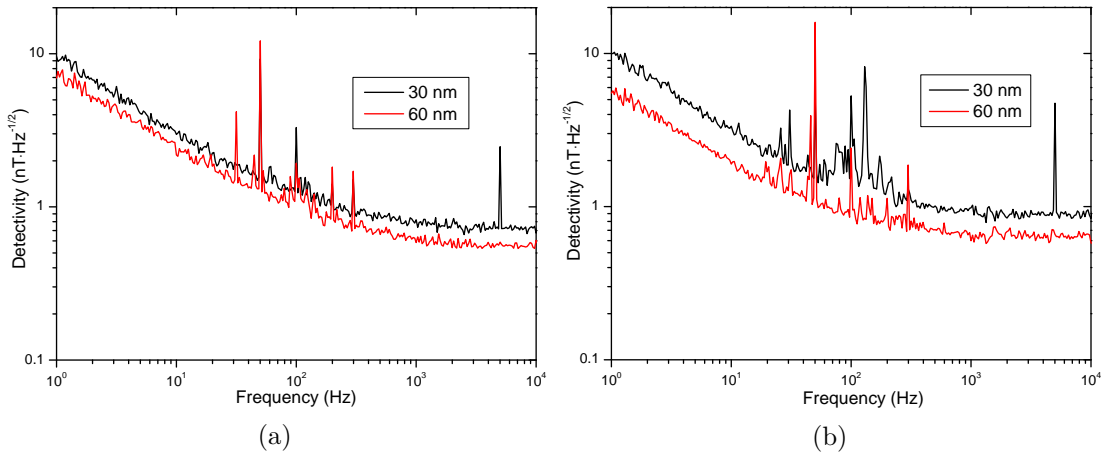


Figure D.5: (a) Detectivity of 45WB PHEB design at 20 V bias. (b) Detectivity of 90WB PHEB design at 10 V bias.

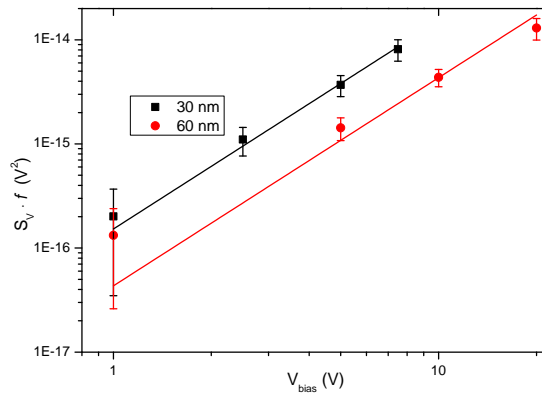


Figure D.6: Each $S_V \times f$ point is the average value from 1 to 10 Hz, error bars correspond to twice the standard deviation.

- [3] M. Julliere. “Tunneling between ferromagnetic films”. In: *Physics Letters A* 54.3 (1975), pp. 225–226. ISSN: 0375-9601. DOI: [https://doi.org/10.1016/0375-9601\(75\)90174-7](https://doi.org/10.1016/0375-9601(75)90174-7). URL: <https://www.sciencedirect.com/science/article/pii/0375960175901747>.
- [4] G. Li, H. Shen, Q. Shen, T. Li, and S. Zou. “Influence of Si buffer layer on the giant magnetoresistance effect in Co/Cu/Co sandwiches”. In: *Sci. China Ser. E-Technol. Sci.* 43.4 (2000), pp. 225–231. DOI: 10.1007/BF02916826.
- [5] T. Li, H. L. Shen, Q. W. Shen, S. C. Zou, K. Tsukamoto, and M. Okutomi. “Effects of Ni buffer layer on giant magnetoresistance in Co/Cu/Co sandwich”. In: *J. Magn. Magn. Mater* 224.1 (2001), pp. 55–60. ISSN: 0304-8853. DOI: [https://doi.org/10.1016/S0304-8853\(00\)01356-1](https://doi.org/10.1016/S0304-8853(00)01356-1). URL: <https://www.sciencedirect.com/science/article/pii/S0304885300013561>.
- [6] M. Sun, T. Kubota, S. Takahashi, Y. Kawato, Y. Sonobe, and K. Takanashi. “Buffer layer dependence of magnetoresistance effects in $\text{Co}_2\text{Fe}_{0.4}\text{Mn}_{0.6}\text{Si}/\text{MgO}/\text{Co}_{50}\text{Fe}_{50}$ tunnel junctions”. In: *AIP Adv.* 8 (2018), p. 055902. DOI: 10.1063/1.5007766. URL: <https://doi.org/10.1063/1.5007766>.
- [7] M. Sun, T. Kubota, Y. Kawato, S. Takahashi, A. Tsukamoto, Y. Sonobe, and K. Takanashi. “Buffer-Layer Dependence of Interface Magnetic Anisotropy in $\text{Co}_2\text{Fe}_{0.4}\text{Mn}_{0.6}\text{Si}$ Heusler Alloy Ultrathin Films”. In: *IEEE Trans. Magn.* 53.11 (2017), pp. 1–4. DOI: 10.1109/TMAG.2017.2728627.
- [8] J. Hemberger, A. Krimmel, T. Kurz, H.-A. Krug von Nidda, V. Yu. Ivanov, A. A. Mukhin, A. M. Balbashov, and A. Loidl. “Structural, magnetic, and electrical properties of single-crystalline $\text{La}_{1-x}\text{Sr}_x\text{MnO}_3$ ($0.4 < x < 0.85$)”. In: *Phys. Rev. B* 66 (9 July 2002), p. 094410. DOI: 10.1103/PhysRevB.66.094410. URL: <https://link.aps.org/doi/10.1103/PhysRevB.66.094410>.
- [9] L. Méchin, S. Wu, B. Guillet, P. Perna, C. Fur, S. Lebargy, C. Adamo, D.G. Schlom, and J. M. Routoure. “Experimental evidence of correlation between $1/f$ noise level and metal-to-insulator transition temperature in epitaxial $\text{La}_{0.7}\text{Sr}_{0.3}\text{MnO}_3$ thin films”. In: *J. Phys. D: Appl. Phys. - Fast*

- Track Communication* 46 (2013), p. 202001. URL: <https://hal.archives-ouvertes.fr/hal-00977721>.
- [10] A. D. Henriksen, B. T. Dalslet, D. H. Skieller, K. H. Lee, F. Okkels, and M. F. Hansen. “Planar Hall effect bridge magnetic field sensors”. In: *Applied Physics Letters* 97.1 (2010), p. 013507. DOI: 10.1063/1.3460290. eprint: <https://doi.org/10.1063/1.3460290>. URL: <https://doi.org/10.1063/1.3460290>.
- [11] A. D. Henriksen, G. Rizzi, and M. F. Hansen. “Experimental comparison of ring and diamond shaped planar Hall effect bridge magnetic field sensors”. In: *Journal of Applied Physics* 118.10 (2015), p. 103901. DOI: 10.1063/1.4930068. eprint: <https://doi.org/10.1063/1.4930068>. URL: <https://doi.org/10.1063/1.4930068>.
- [12] A. Grosz, V. Mor, E. Paperno, S. Amrusi, I. Faivinov, M. Schultz, and L. Klein. “Planar hall effect sensors with subnanotesla resolution”. In: *IEEE Magn. Lett.* 4 (2013), p. 6500104. DOI: 10.1109/LMAG.2013.2276551. URL: <https://doi.org/10.1109/LMAG.2013.2276551>.
- [13] D. S. Chuang, C. A. Ballentine, and R. C. O’Handley. “Surface and step magnetic anisotropy”. In: *Phys. Rev. B* 49 (21 June 1994), pp. 15084–15095. DOI: 10.1103/PhysRevB.49.15084. URL: <https://link.aps.org/doi/10.1103/PhysRevB.49.15084>.
- [14] P. Perna, D. Maccariello, F. Ajejas, R. Guerrero, L. Méchin, S. Flament, J. Santamaria, R. Miranda, and J. Camarero. “Engineering Large Anisotropic Magnetoresistance in $\text{La}_{0.7}\text{Sr}_{0.3}\text{MnO}_3$ Films at Room Temperature”. In: *Advanced Functional Materials* 27.26 (2017), p. 1700664. DOI: <https://doi.org/10.1002/adfm.201700664>. eprint: <https://onlinelibrary.wiley.com/doi/pdf/10.1002/adfm.201700664>. URL: <https://onlinelibrary.wiley.com/doi/abs/10.1002/adfm.201700664>.
- [15] M. Saïb, M. Belmeguenai, L. Méchin, D. Bloyet, and S. Flament. “Magnetization reversal in patterned $\text{La}_{0.67}\text{Sr}_{0.33}\text{MnO}_3$ thin films by magneto-optical Kerr imaging”. In: *J. Appl. Phys.* 103.11 (2008), p. 113905. DOI: 10.1063/1.2938068. eprint: <https://doi.org/10.1063/1.2938068>. URL: <https://doi.org/10.1063/1.2938068>.
- [16] L. K. Quynh, B. D. Tu, D. X. Dang, D. Q. Viet, L. T. Hien, D. T. Huong Giang, and N. H. Duc. “Detection of magnetic nanoparticles using simple AMR sensors in Wheatstone bridge”. In: *Journal of Science: Advanced Materials and Devices* 1.1 (2016), pp. 98–102. ISSN: 2468-2179. DOI: <https://doi.org/10.1016/j.jsamd.2016.04.006>. URL: <https://www.sciencedirect.com/science/article/pii/S2468217916300168>.
- [17] F. N. Hooge. “ $1/f$ noise is no surface effect”. In: *Physics Letters A* 29.3 (1969), pp. 139–140. ISSN: 0375-9601. DOI: [https://doi.org/10.1016/0375-9601\(69\)90076-0](https://doi.org/10.1016/0375-9601(69)90076-0).
- [18] J. Y. Chen, J. F. Feng, and J. M. D. Coey. “Tunable linear magnetoresistance in MgO magnetic tunnel junction sensors using two pinned CoFeB electrodes”. In: *Appl. Phys. Lett.* 100 (2012), p. 142407. DOI: 10.1063/1.4978465. URL: <https://doi.org/10.1063/1.4978465>.
- [19] J. G. Deak, Z. Zhou, and W. Shen. “Tunneling magnetoresistance sensor with pT level $1/f$ magnetic noise”. In: *AIP Advances* 7 (2017), p. 056676. DOI: 10.1063/1.3701277. URL: <http://dx.doi.org/10.1063/1.3701277>.
- [20] X. Zhang, Y. Bi, G. Chen, J. Liu, J. Li, K. Feng, C. Lv, and W. Wang. “Influence of size parameters and magnetic field intensity upon the amplification characteristics of magnetic flux concentrators”. In: *AIP Advances* 8.12 (2018), p. 125222. DOI: 10.1063/1.5066271. URL: <https://doi.org/10.1063/1.5066271>.
- [21] L. Caruso, T. Wunderle, C. M. Lewis, J. Valadeiro, V. Trauchessec, J. Trejo Rosillo, J. P. Amaral, J. Ni, P. Jendritza, C. Fermon, S. Cardoso, P. P. Freitas, P. Fries, and M. Pannetier-Lecœur. “In Vivo Magnetic Recording of Neuronal Activity”. In: *Neuron* 95.6 (2017), pp. 1283–1291. ISSN: 0896-6273. DOI: 10.1016/j.neuron.2017.08.012.